Moveout-based geometrical-spreading correction for converted waves

Xiaoxia Xu[1] and Ilya Tsvankin[2]

[1] *Formerly Colorado School of Mines, Department of Geophysics, Center for Wave Phenomena; presently ExxonMobil Upstream Research Company, Houston, TX 77252.*

[2] *Colorado School of Mines, Department of Geophysics, Center for Wave Phenomena, Golden, CO 80401-1887.*

ABSTRACT

Geometrical-spreading correction is an important component of amplitude-variation-with-offset (AVO) analysis, which provides high-resolution information for anisotropic parameter estimation and fracture characterization. Here, we extend the algorithm of moveout-based anisotropic spreading correction (MASC) to mode-converted PSV-waves in VTI (transversely isotropic with a vertical symmetry axis) media and symmetry planes of orthorhombic media.

While the geometrical-spreading equation in terms of reflection traveltime has the same form for all wave modes in laterally homogeneous media, reflection moveout of PS-waves is more complicated than that of P-waves (e.g., it can become asymmetric in common-midpoint geometry). Still, for models with a horizontal symmetry plane, long-spread reflection traveltimes of PS-waves can be well-approximated by the Tsvankin-Thomsen and Alkhalifah-Tsvankin moveout equations, which are widely used for P-waves. Although the accuracy of the Alkhalifah-Tsvankin equation is somewhat lower, it includes less moveout parameters and helps to maintain the uniformity of the MASC algorithm for P- and PS-waves. The parameters of both moveout equations are obtained by least-squares traveltime fitting or semblance analysis and are different from those for P-waves.

Testing on full-wavefield synthetic data generated by the reflectivity method for layered VTI media confirms that MASC accurately reconstructs the plane-wave conversion coefficient from conventional-spread PS data. Errors in the estimated conversion coefficient, which become noticeable at moderate and large offsets, are mostly caused by offset-dependent transmission loss of PS-waves.

Key words: Mode conversions, AVO analysis, geometrical spreading, VTI media, azimuthal anisotropy, nonhyperbolic moveout

Introduction

AVO analysis of P-wave data can provide essential information for anisotropic parameter estimation and fracture characterization and (e.g., Rüger, 2001; Neves et al., 2003). However, inversion of the wide-azimuth P-wave AVO response for the pertinent anisotropy parameters is generally ambiguous even for the simple HTI (transversely isotropic with a horizontal symmetry axis) model formed by a system of vertical, penny-shaped cracks in isotropic host rock (Rüger and Tsvankin, 1997; Rüger, 2001). In principle, the nonuniqueness of AVO analysis can be overcome by combining the P-wave AVO gradient with the NMO ellipse (Bakulin et al., 2000a), but this approach has serious limitations. First, the NMO ellipse can be reconstructed only for relatively thick reservoirs; second, the difference in vertical resolution between amplitude and traveltime methods can lead to distorted estimates for heterogeneous reservoir formations (Xu and Tsvankin, 2007).

For surveys with multicomponent acquisition, the AVO response of P-waves can be supplemented with that of mode-converted PS-waves. The main advantage

of combining PP and PS amplitude signatures is that they are determined by rock properties on the same scale near the top or bottom of the reservoir. Bakulin et al. (2000a) showed that the azimuthally varying AVO gradients of PP- and PS-waves reflected from an HTI medium constrain both the normal and tangential compliances of the fractures. The compliances can then be related to such physical properties as fracture density and fluid infill. Although this technique was introduced for boundaries between isotropic and HTI media, it remains valid for the lower-symmetry orthorhombic model that describes a vertical fracture system in a VTI background matrix (Bakulin et al., 2000b). A more general methodology for joint inversion of the long-offset, wide-azimuth AVO responses of PP-waves and split PS-waves in azimuthally anisotropic media was developed by Jílek (2002).

Since shear-wave (and, therefore, converted-wave) amplitudes are highly sensitive to the presence of anisotropy along the raypath, robust estimation of PS-wave reflection (conversion) coefficients is impossible without an accurate geometrical-spreading correction. As discussed by Tsvankin (1995, 2005) and Xu et al. (2005), the geometrical spreading of SV-waves in TI media is controlled primarily by the parameter $\sigma \equiv (V_{P0}^2/V_{S0}^2)(\epsilon - \delta)$, which is typically much larger than the Thomsen parameters ϵ and δ responsible for P-wave amplitudes (V_{P0} and V_{S0} are the symmetry-direction P- and S-wave velocities, respectively).

To correct AVO signatures for amplitude distortions in the overburden, it is convenient to represent geometrical spreading through reflection traveltimes. Following paraxial ray theory (Červený, 2001), Xu et al. (2005) obtained geometrical spreading of pure reflection modes (PP or SS) in layered, arbitrarily anisotropic media as a function of traveltime derivatives. Although this equation is strictly valid only for laterally homogeneous models, it remains sufficiently accurate in the presence of moderate dips and mild lateral velocity variation.

By combining this geometrical-spreading formulation with a 3D extension of the Alkhalifah-Tsvankin (1995) nonhyperbolic moveout equation, Xu and Tsvankin (2006a) developed a practical and robust algorithm for moveout-based anisotropic spreading correction ("MASC"). The accuracy of MASC for wide-azimuth, long-spread P-wave data from layered orthorhombic media was confirmed by dynamic ray tracing and full-wavefield synthetic modeling (Xu and Tsvankin, 2006b). The synthetic tests also demonstrate that if the azimuthal variation of geometrical spreading is not negligible, MASC cannot be replaced by empirical gain corrections even in qualitative AVO analysis.

Here, the methodology of MASC is extended to PS-waves converted at the reflector (so-called "C-waves") in laterally homogeneous, anisotropic media. First, we show that despite the asymmetry of the raypath of mode conversions, their geometrical spreading is expressed through reflection traveltime in the same way as that for P-waves. Second, by employing the Tsvankin-Thomsen (1994) and Alkhalifah-Tsvankin (1995) moveout equations, the MASC algorithm is adapted for PSV-waves acquired in vertical symmetry planes of layered TI and orthorhombic media. Finally, we conduct a full-wavefield synthetic study to evaluate the accuracy of MASC in estimating the conversion coefficient and compare its performance with that of empirical gain corrections used in practice.

1 MOVEOUT-BASED GEOMETRICAL-SPREADING EQUATION FOR PS-WAVES

One of the most significant differences between P- and PS-waves is the asymmetry of the raypath and moveout of mode conversions. If the medium is laterally heterogeneous or anisotropic without a horizontal symmetry plane, the traveltime of PS-waves does not stay the same when the source and receiver are interchanged (Thomsen, 1999; Tsvankin and Grechka, 2000; Dewangan, 2004). Because of this moveout asymmetry, PS-wave reflection traveltime on common-midpoint (CMP) gathers may not be an even function of offset and cannot be described by conventional moveout equations for P-waves. Therefore, the two key components of MASC (i.e., the geometrical-spreading and moveout equations) have to be revisited for converted waves.

The general traveltime-based expression for geometrical spreading of pure modes is derived in Appendix A of Xu et al. (2005). Although the derivation assumes reflection moveout to be symmetric (i.e., independent of the sign of offset), the final result turns out to be valid for converted waves. The ray-theory representation of geometrical spreading at the earth's surface (Červený, 2001) includes traveltime derivatives with respect to four variables – the horizontal coordinates of the source and receiver. If the medium is laterally homogeneous, the number of independent variables can be reduced to two (offset x and azimuth α), even for arbitrary anisotropic symmetries. For pure reflection modes, the azimuth varies only from 0° to 180° because their traveltime remains the same when the source and receiver are interchanged.

The only modification required to account for the asymmetric moveout of converted waves is extension of the range of azimuths to 360°. Then the definition of azimuth (equation A-3 of Xu et al., 2005) takes the form

$$\alpha = \begin{cases} \tan^{-1}\left[\frac{x_2^r - x_2^s}{x_1^r - x_1^s}\right] & x_1^r - x_1^s > 0\,, \\ \tan^{-1}\left[\frac{x_2^r - x_2^s}{x_1^r - x_1^s}\right] + \pi & x_1^r - x_1^s < 0\,, \end{cases} \tag{1}$$

where $x_{1,2}^s$ and $x_{1,2}^r$ are the horizontal source and receiver coordinates, respectively. Compared to the orig-

inal definition for pure modes, equation 1 contains an additional constant (π) for $x_1^r - x_1^s < 0$, which does not change traveltime derivatives.

Hence, the moveout-based geometrical-spreading equation given by Xu et al. (2005) is entirely valid for converted waves:

$$L(x,\alpha) = (\cos\phi^s \cos\phi^r)^{1/2} \left[\frac{\partial^2 T}{\partial x^2}\frac{\partial T}{\partial x}\frac{1}{x} + \frac{\partial^2 T}{\partial x^2}\frac{\partial^2 T}{\partial \alpha^2}\frac{1}{x^2} - \left(\frac{\partial T}{\partial \alpha}\right)^2 \frac{1}{x^4}\right]^{-1/2} \quad (2)$$

where T is the traveltime, and ϕ^s and ϕ^r are the angles between the ray and the vertical at the source and receiver locations, respectively. Equation 2 can be used for any reflected wave (pure or converted) in laterally homogeneous, arbitrarily anisotropic media. Application of this equation to events with asymmetric moveout, however, requires certain care because the traveltime derivatives are different for "reciprocal" source-receiver pairs with azimuths $\alpha \pm \pi$.

Note that the only source of moveout asymmetry for converted waves in laterally homogeneous media is the presence of anisotropic layers that do not have a horizontal symmetry plane. Next, we verify that our formalism accurately describes the geometrical spreading of PS-waves in the simplest model of this type, which includes a single homogeneous TI layer with a tilted symmetry axis (TTI; see Figure 1). The TTI parameters used in our test are taken from the physical model of Dewangan et al. (2006).

Figure 1 shows the traveltime surface of the fast PS-wave computed by anisotropic ray tracing. In the symmetry-axis plane (i.e., in the vertical plane that contains the symmetry axis), the fast S-wave represents an SV mode because it has in-plane polarization. Since the horizontal plane in this model is not a plane of symmetry, the traveltime surface in CMP geometry is asymmetric with respect to the global minimum. Also, the minimum traveltime is shifted from the common midpoint to an offset that exceeds 0.5 km.

Since it is difficult to approximate this traveltime surface with a Taylor series, we employed a cubic-spline function. Substituting the traveltime derivatives obtained from this spline function into equation 2, we computed the spreading for the PSV-wave in the symmetry-axis plane. Comparison with dynamic ray tracing in Figure 2 confirms the accuracy of equation 2 for converted waves with asymmetric moveout. Except for the dicrepancies at large $x \to \pm 3$ km and zero offset, which are caused by numerical difficulties in estimating the second-order time derivatives, the spreading computed by our method is close to that obtained by ray tracing.

Although this test proves that MASC can handle arbitary moveout functions, the rest of the paper is focused on models with a horizontal symmetry plane, in which PS-wave moveout is symmetric.

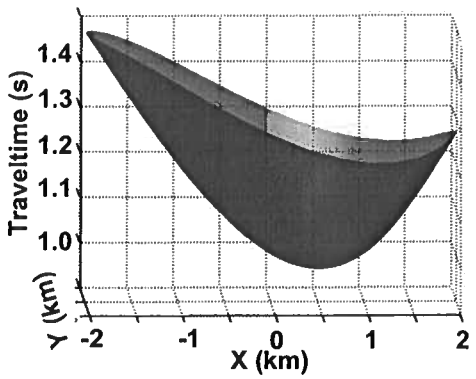

Figure 1. Traveltime surface of the fast PS-wave computed for a horizontal TTI layer in CMP geometry. The model parameters are $V_{P0} = 2.6$ km/s, $V_{S0} = 1.38$ km/s, $\epsilon = 0.46$, $\delta = 0.11$, and $\gamma = 0$. The tilt of the symmetry axis from the vertical is $\nu = 70°$, the layer's thickness is 1 km. Note the asymmetry of the surface with respect to the global traveltime minimum, which does not correspond to zero offset.

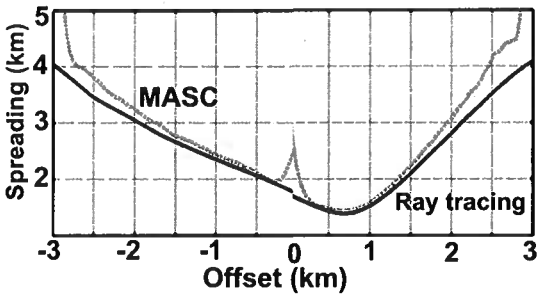

Figure 2. Comparison of the geometrical spreading for the PS-wave computed from equation 2 (dashed line) and ray tracing (solid) in the symmetry-axis plane of the model in Figure 1. The "jitters" in the output of MASC correspond to local errors in approximating the traveltime surface.

2 MASC ALGORITHM FOR PS-WAVES

Outside of the symmetry planes of azimuthally anisotropic media, a P-wave incident upon a horizontal reflector excites two split PS-waves which have to be separated using polarization analysis. To avoid this complication and facilitate AVO analysis, we assume that the acquisition line is confined to a vertical symmetry plane of the model. Then a P-wave source generates only a P-to-SV conversion polarized in the incidence plane. The goal of this section is to extend the MASC methodology of Xu and Tsvankin (2006a) to PSV-waves recorded in vertical symmetry planes of horizontally layered VTI, HTI, and orthorhombic media.

As is the case for P-waves, the key issue in implementing equation 2 for mode conversions is to find a smooth, relatively simple traveltime approximation that

can be used for a wide range of offsets and azimuths. Long-spread reflection moveout of P-waves in layered VTI media is well-described by the Tsvankin-Thomsen (1994) nonhyperbolic equation:

$$T^2(x) = T_0^2 + A_2\,x^2 + \frac{A_4\,x^4}{1 + A\,x^2}\,, \tag{3}$$

where T_0 is the zero-offset time, $A_2 = V_{\rm nmo}^{-2}$ controls hyperbolic moveout ($V_{\rm nmo}$ is the normal-moveout velocity), and A_4 is the quartic coefficient responsible for nonhyperbolic moveout at large offsets. The parameter A depends on the horizontal velocity and is introduced to make $T(x)$ convergent at $x \to \infty$. With an appropriate substitution of the moveout parameters, equation 3 gives sufficient accuracy for PS-wave traveltimes in horizontally-layered VTI media (Tsvankin, 2005).

By taking into account the azimuthal variation of the moveout parameters A_2, A_4, and A, Al-Dajani et al. (1998) extended equation 3 to P-waves in orthorhombic media:

$$T^2(x,\alpha) = T_0^2 + A_2(\alpha)\,x^2 + \frac{A_4(\alpha)\,x^4}{1 + A(\alpha)\,x^2}\,, \tag{4}$$

$$A_2(\alpha) = A_2^{(1)} \sin^2\alpha + A_2^{(2)} \cos^2\alpha\,, \tag{5}$$

$$A_4(\alpha) = A_4^{(1)} \sin^4\alpha + A_4^{(2)} \cos^4\alpha + A_4^{(x)} \sin^2\alpha\,\cos^2\alpha\,. \tag{6}$$

The dependence of A_2 on the azimuth α is described by the NMO ellipse (Grechka and Tsvankin, 1998), and equation 6 for A_4 is derived by Al-Dajani et al. (1998) for a horizontal orthorhombic layer. Note that HTI can be treated as a special case of the more general orthorhombic model. It is assumed in equations 4–6 that $\alpha = 0$ corresponds to the symmetry plane $[x_1, x_3]$, so $A_2^{(1,2)}$ and $A_4^{(1,2)}$ are the symmetry-plane moveout coefficients, while $A_4^{(x)}$ contributes to nonhyperbolic moveout in off-symmetry directions. Because of the difficulties in treating split PS-waves outside of the symmetry planes, equation 4 has not been applied to mode conversions.

Alkhalifah and Tsvankin (1995) proposed a simpler nonhyperbolic moveout equation for P-waves in VTI media that depends on only two parameters, the NMO velocity $V_{\rm nmo}$ and anellipticity coefficient $\eta \equiv (\epsilon - \delta)/(1 + 2\delta)$:

$$T^2(x) = T_0^2 + \frac{x^2}{V_{\rm nmo}^2} - \frac{2\eta\,x^4}{V_{\rm nmo}^2\,[T_0^2\,V_{\rm nmo}^2 + (1 + 2\eta)\,x^2]}\,. \tag{7}$$

Equation 7 is widely used in seismic processing to correct long-spread data for nonhyperbolic moveout and estimate the key anisotropy parameter η. The 3D version of the Alkhalifah-Tsvankin equation provides a close approximation to wide-azimuth P-wave traveltimes in orthorhombic or HTI media (Vasconcelos and Tsvankin, 2006):

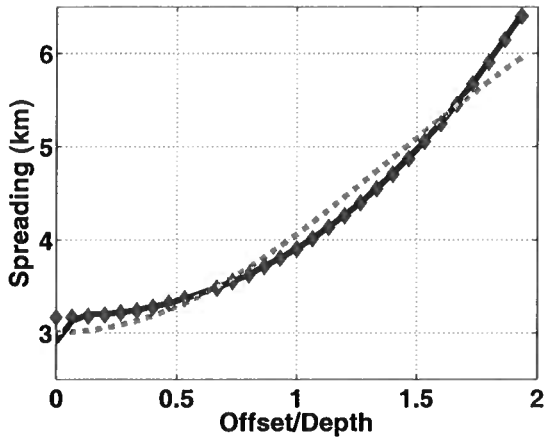

Figure 3. Geometrical spreading of PSV-waves reflected from the bottom of the VTI layer in model 1 (Table 1). Our method was applied with the Tsvankin-Thomsen equation 3 (diamonds) and with the Alkhalifah-Tsvankin equation 7 (dashed line); the solid line is computed by dynamic ray-tracing code ANRAY (Gajewski and Pšenčík, 1987).

$$T^2(x,\alpha) = T_0^2 + \frac{x^2}{V_{\rm nmo}^2(\alpha)} - \frac{2\eta(\alpha)\,x^4}{V_{\rm nmo}^2(\alpha)\,[T_0^2\,V_{\rm nmo}^2(\alpha) + (1 + 2\eta(\alpha))\,x^2]}\,, \tag{8}$$

$$V_{\rm nmo}^{-2}(\alpha) = \frac{\sin^2\alpha}{\left(V_{\rm nmo}^{(1)}\right)^2} + \frac{\cos^2\alpha}{\left(V_{\rm nmo}^{(2)}\right)^2}\,, \tag{9}$$

$$\eta(\alpha) = \eta^{(1)} \sin^2\alpha + \eta^{(2)} \cos^2\alpha - \eta^{(3)} \sin^2\alpha\,\cos^2\alpha\,. \tag{10}$$

Equation 9, which is equivalent to equation 5 discussed above, describes the NMO ellipse with the semi-axes $V_{\rm nmo}^{(1)}$ and $V_{\rm nmo}^{(2)}$; $\eta^{(1,2,3)}$ are the anellipticity parameters in the three mutually orthogonal symmetry planes of the model. Xu and Tsvankin (2006a, 2006b) used equations 8–10 to compute the geometrical spreading of P-waves in horizontally layered, azimuthally anisotropic media.

Although equations 7 and 8 were originally designed for P-waves, it is worthwhile to test them for PS-waves. While we cannot expect the analytic form of the parameters $V_{\rm nmo}$ and η to be the same for P- and PS-waves, the geometrical-spreading correction operates with the best-fit moveout parameters obtained from semblance analysis. Therefore, we need to verify if the fit provided by equations 7 and 8 to converted-wave moveout is sufficient for accurate geometrical-spreading computation using MASC (equation 2).

First, we apply equations 3 and 7 to approximate the moveout of a PSV reflection from the bottom of a VTI layer sandwiched between two isotropic halfspaces (Figure 3 and Table 1). The best-fit moveout parame-

	Layer 1	Layer 2	Layer 3
Symmetry type	ISO	VTI	ISO
Thickness (km)	0.5	1.0	∞
Density (g/cm^3)	2.0	2.1	2.2
V_{P0} (km/s)	1.7	2.2	2.2
V_{S0} (km/s)	0.8	1.1	1.0
ϵ	0	0.23	0
δ	0	0.10	0
γ	0	0.10	0
η	0	0.10	0
σ	0	0.64	0

Table 1. Parameters of a medium that inlcudes a VTI layer sandwiched between two isotropic layers (model 1). The velocities and anisotropy parameters of the VTI layer are taken from the measurements for Dog Creek shale listed in Thomsen (1986).

	Layer 1	Layer 2	Layer 3
Symmetry type	VTI	ORTH	ISO
Thickness (km)	0.5	1.0	∞
Density (g/cm^3)	2.1	2.1	2.2
V_{P0} (km/s)	2.2	2.2	2.2
V_{S0} (km/s)	1.1	1.1	1.0
$\epsilon^{(1)}$	0.23	0.317	0
$\delta^{(1)}$	0.10	-0.054	0
$\gamma^{(1)}$	0.10	0.513	0
$\epsilon^{(2)}$	0.23	0.121	0
$\delta^{(2)}$	0.10	0.046	0
$\gamma^{(2)}$	0.10	0.138	0
$\delta^{(3)}$	0	0.1	0
$\eta^{(1)}$	0.1	0.42	0
$\eta^{(2)}$	0.1	0.07	0
$\eta^{(3)}$	0	0.05	0
$\sigma^{(1)}$	0.64	1.48	0
$\sigma^{(2)}$	0.64	0.31	0

Table 2. Parameters of a medium composed of VTI, orthorhombic, and isotropic layers (model 2). Orthorhombic symmetry can be described by the two vertical velocities (V_{P0} for P-waves and V_{S0} for one of the split S-waves) and seven anisotropy parameters ($\epsilon^{(1)}$, $\epsilon^{(2)}$, $\delta^{(1)}$, $\delta^{(2)}$, $\delta^{(3)}$, $\gamma^{(1)}$, and $\gamma^{(2)}$); the parameter values are based on the measurements of Wang (2002). The anellipticity parameters $\eta^{(1)}$, $\eta^{(2)}$, $\eta^{(2)}$ control P-wave nonhyperbolic moveout, while $\sigma^{(1)}$ and $\sigma^{(2)}$ are largely responsible for the moveout of SV-waves in the vertical symmetry planes. For a detailed explanation of the notation, see Tsvankin (2005).

ters are then substituted into the geometrical-spreading equation 2. In agreement with the results of Tsvankin (2005), equation 3 provides an excellent approximation for PSV-wave moveout and yields a geometrical-spreading factor that is almost identical to that computed by dynamic ray tracing (Figure 3). Although the performance of the Alkhalifah-Tsvankin equation 7 is somewhat inferior, it has the advantage of being consistent with the P-wave formalism while still providing adequate accuracy. It should be mentioned that the best-fit parameter η for PSV-waves is different from its analytic definition [$\eta \equiv (\epsilon - \delta)/(1 + 2\delta)$ in a single VTI layer] for P-waves.

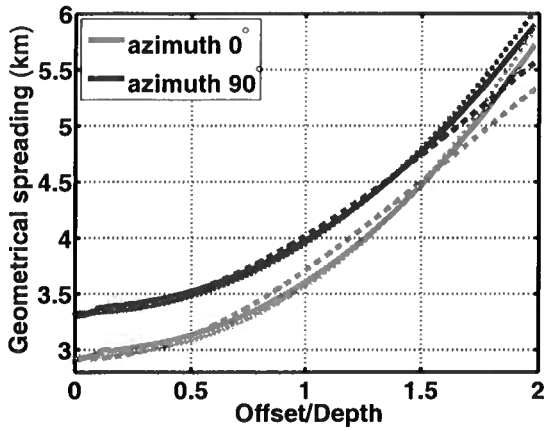

Figure 4. Geometrical spreading of PSV-waves reflected from the bottom of the orthorhombic layer in model 2 (Table 2). The azimuths $\alpha = 0°$ and $\alpha = 90°$ correspond to the symmetry planes $[x_1, x_3]$ and $[x_2, x_3]$, respectively. Our method was applied with the 3D Tsvankin-Thomsen equation 4 (stars) and with the 3D Alkhalifah-Tsvankin equation 8 (dashed lines); the solid lines are computed by dynamic ray tracing.

Next, the moveout approximations and the methodology of MASC are tested for the two vertical symmetry planes of orthorhombic media (Figure 4 and Table 2). Note that P-waves are coupled to two different split S-waves in the symmetry planes $[x_1, x_3]$ and $[x_2, x_3]$ (Tsvankin, 2005). Indeed, if the fast shear wave S_1 is polarized in the x_1-direction at vertical incidence, it represents the SV mode that will produce P-to-SV conversion in the $[x_1, x_3]$-plane. Then the slow shear wave S_2 will be responsible for the converted PSV-wave in the $[x_2, x_3]$-plane.

Since the symmetry planes of orthorhombic models are kinematically equivalent to VTI media, the traveltime fit provided by the moveout approximations in the incidence plane is the same as in VTI media. Geometrical spreading in azimuthally anisotropic media (equation 2), however, also depends on azimuthal traveltime variations away from the incidence plane (Tsvankin, 2005; Xu et al., 2005). Therefore, the accuracy of our method depends on the performance of the 3D versions of the moveout equations in the vicinity of the symmetry planes. As was the case for VTI media, the error of our method with the 3D Tsvankin-Thomsen equation 4 is almost negligible, while the 3D Alkhalifah-Tsvankin equation 8 produces some deviations from the ray-tracing result, especially at far offsets (Figure 4). Still, given relatively a large uncertainty in amplitude

measurements, the accuracy of equation 8 should be acceptable for purposes of AVO analysis.

3 APPLICATION TO AVO ANALYSIS OF SYNTHETIC DATA

In addition to potential problems with moveout approximations, the accuracy of amplitude corrections for mode conversions may be influenced by several other factors. Here, we do not consider PS-wave amplitudes in the anomalous areas near shear-wave cusps (triplications) and singularities, where AVO analysis is not practical. Still, the high sensitivity of S-waves to the presence of anisotropy may lead to rapid amplitude variations along PS wavefronts that are not adequately described by ray theory and, therefore, by MASC (Tsvankin, 2005). Also, even for models with a horizontal symmetry plane, the asymmetry of the PS raypath (i.e., the difference between the P- and S-legs) can result in a significant angular variation of transmission loss and related errors in AVO analysis. Hence, it is essential to test the performance of MASC for PS-waves on 3D full-wavefield synthetic data, as was done by Xu and Tsvankin (2006b) for P-waves.

The main question to be answered in this section is how accurately MASC can reconstruct plane-wave conversion coefficients in layered anisotropic media. An important practical issue is whether or not MASC can be replaced by empirical gain corrections in qualitative AVO analysis. Finally, we evaluate the magnitude of transmission loss (which is not included in MASC) and the related distortions of the PS-wave AVO response.

Due to the difficulties in modeling exact PS-wave amplitudes for layered orthorhombic media, we carried out amplitude processing only for the VTI medium from Table 1 (model 1). Synthetic seismograms were computed with the reflectivity code (ANISYNPA), which generates exact 3D wavefields for horizontally layered anisotropic media (e.g., Fryer and Frazer, 1984). A shot gather of the vertical displacement from a vertical force for model 1 is shown in Figure 5. The processing sequence is similar to that for P-waves described by Xu and Tsvankin (2006b). First, we apply the nonhyperbolic moveout equation 3 to the PS reflection from the bottom of the VTI layer to estimate the parameters A_2, A_4, and A, which serve as the input to the geometrical-spreading correction. Second, the raw amplitudes are picked along the traveltime curve defined by equation 3 with the best-fit parameters. Third, MASC (equation 2) is applied to correct the picked amplitudes for anisotropic geometrical spreading. Fourth, the source and receiver directivity factors are removed using the local horizontal slowness.

To calibrate the P-wave AVO response, we matched the corrected amplitude at normal incidence with the exact reflection coefficient (Xu and Tsvankin, 2006b). This approach is not suitable for PS-waves because the conversion coefficient at normal incidence goes to zero. Since the source factor should be the same for both P- and PS-waves, we normalized the PS conversion coefficient using the scaling factor estimated for the corresponding P-wave reflection.

The high accuracy of MASC with the Tsvankin-Thomsen moveout equation for the model in Figure 5 was confirmed by the test in the previous section (see

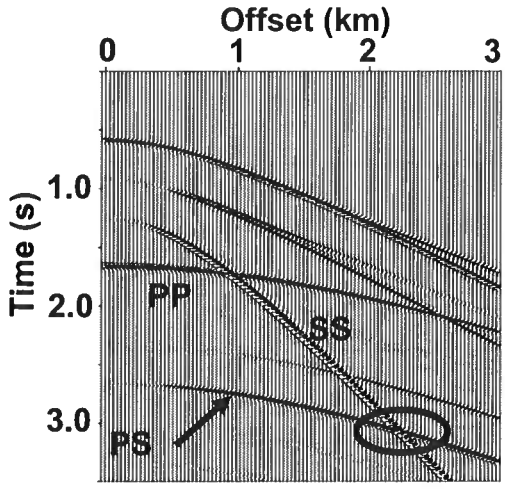

Figure 5. Synthetic shot gather for model 1 (Table 1) computed by the anisotropic reflectivity method. The top layer is specified as a halfspace to eliminate the influence of the free surface. The arrow marks the target PS-wave converted at the bottom of the VTI layer. The ellipse highlights the area of interference between the target event and the SS reflection from the top of the VTI layer.

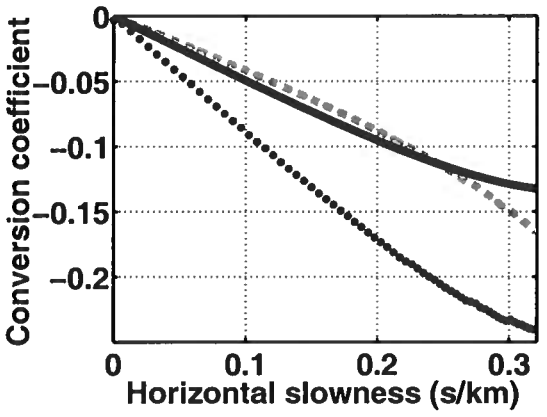

Figure 6. Conversion coefficient at the bottom of the VTI layer in model 1. The estimates obtained with MASC (dashed line) and the t-gain correction (dotted) are compared with the exact conversion coefficient (solid). The incidence angle of the downgoing P-wave corresponding to the maximum horizontal slowness (0.3 s/km) is 30°; for the upgoing SV-wave, the corresponding angle is 15°.

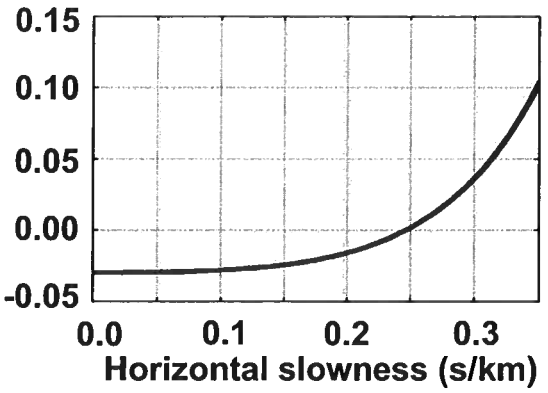

Figure 7. Transmission loss for the target PS-wave from Figure 5. The loss is computed by subtracting from unity the product of the plane-wave transmission coefficients along the raypath.

Figure 3). Still, the VTI layer has a significant value of the parameter σ, which is primarily responsible for SV-wave velocity anisotropy and angle-dependent geometrical spreading. Strong amplitude variations along the wavefront of the PS-wave may cause errors in the ray-theory equations employed in our method. Nevertheless, the conversion coefficient estimated by MASC is close to the exact values for a relatively wide range of horizontal slownesses (Figure 6).

In contrast, application of the conventional t-gain correction results in unacceptable errors even for small offsets. (The accuracy of the t^2-gain correction, not shown here, is lower.) Clearly, the influence of anisotropy significantly distorts geometrical spreading of PS-waves in typical TI models. Hence, AVO analysis for converted waves cannot be implemented without a robust anisotropic spreading correction.

The conversion coefficient reconstructed by MASC deviates from the exact values with increasing offset. This deviation is caused by the combined influence of the transmission loss and interference of the target PS event with the SS reflection from the top of the VTI layer (see the ellipse in Figure 5). Amplitude distortions caused by the interference with the SS-wave become especially severe for horizontal slownesses exceeding 0.3 s/km, which forced us to restrict the slowness range used in Figure 6.

The transmission coefficients for the upgoing and downgoing segments of reflected PP rays compensate for each other in such a way that their product (which determines transmission loss) is almost invariant with offset. For mode conversions, however, the upgoing and downgoing ray segments correspond to different modes, and this raypath asymmetry leads to an increase of the transmission loss for our model with offset (Figure 7). Since the geometrical-spreading correction does not account for transmission coefficients, this offset-dependent transmission loss distorts the reconstructed conversion coefficient in Figure 6.

4 DISCUSSION AND CONCLUSIONS

Geometrical spreading of shear and mode-converted waves typically is more strongly distorted by anisotropy than that of P-waves. Here, we showed that the moveout-based anisotropic spreading correction (MASC), previously developed for P-wave data, can be applied to PS-waves as well. For horizontally layered models, the geometrical-spreading factor of P- and PS-waves can be obtained from the same equation that involves traveltime derivatives with respect to offset and azimuth. This equation remains valid even for models without a horizontal symmetry plane, such as tilted transverse isotropy, in which reflection moveout of PS-waves becomes asymmetric (i.e., traveltime does not stay the same when the source and receiver are interchanged).

Because of the difficulty in dealing with split PS-waves in azimuthally anisotropic media, our implementation of MASC for mode conversions is restricted to VTI media and symmetry planes of orthorhombic and HTI media. To compute the traveltime derivatives required by MASC, we employed the Tsvankin-Thomsen nonhyperbolic moveout equation, which is used almost exclusively for P-waves. Still, numerical testing proves that this equation gives a close approximation for PSV-wave moveout both in layered VTI media and in the vicinity of the vertical symmetry planes of orthorhombic media. The three best-fit parameters of the Tsvankin-Thomsen equation serve as the input to the geometrical-spreading computation. Comparison with dynamic ray tracing shows that the accuracy of MASC for PS-waves is almost as high as for P-waves.

Furthermore, for purposes of geometrical-spreading correction PS-wave traveltimes can be adequately described by the simpler Alkhalifah-Tsvankin moveout equation. Whereas the analytic form of this equation is valid only for P-waves, it can be applied to mode conversions with fitted parameters V_{nmo} and η. The Alkhalifah-Tsvankin equation has the important advantage of making the MASC algorithm for PS-waves fully consistent with that for P-waves at the expense of somewhat lower quality of the traveltime fit.

Application of MASC to full-wavefield synthetic data from layered VTI media yields accurate estimates of the conversion coefficients for conventional-length spreads. The main complication in the reconstruction of conversion coefficients from surface data is related to offset-dependent transmission loss of PS-waves. The product of the transmission coefficients along the asymmetric raypath of mode conversions varies with incidence angle and, therefore, with offset. This variation, which is almost negligible for P-waves, is not accounted

for in the geometrical-spreading correction and can produce significant distortions of the AVO response at moderate and large offsets.

Our results demonstrate that even qualitative AVO analysis of PS-waves in the presence of anisotropy in the overburden requires application of the moveout-based anisotropic spreading correction. A promising direction for future studies is to extend MASC to split PS-waves outside of the symmetry planes of azimuthally anisotropic media. Such an extension is essential for developing robust azimuthal AVO algorithms operating with wide-azimuth mode-converted data.

ACKNOWLEDGMENTS

We are grateful to members of the A(nisotropy)-Team of the Center for Wave Phenomena (CWP), Colorado School of Mines, for helpful discussions. The support for this work was provided by the Consortium Project on Seismic Inverse Methods for Complex Structures at CWP and by the Chemical Sciences, Geosciences and Biosciences Division, Office of Basic Energy Sciences, Office of Science, U.S. Department of Energy.

REFERENCES

Al-Dajani, A., I. Tsvankin, and M. N. Toksöz, 1998, Nonhyperbolic reflection moveout for azimuthally anisotropic media: 68th Annual International Meeting, SEG, Expanded Abstracts, 1479–1482.

Alkhalifah, T., and I. Tsvankin, 1995, Velocity analysis for transversely isotropic media: Geophysics, **60**, 1550–1566.

Bakulin, A., V. Grechka, and I. Tsvankin, 2000a, Estimation of fracture parameters from reflection seismic data – Part I: HTI model due to a single fracture set: Geophysics, **65**, 1788–1802.

Bakulin, A., V. Grechka, and I. Tsvankin, 2000b, Estimation of fracture parameters from reflection seismic data – Part II: Fractured models with orthorhombic symmetry: Geophysics, **65**, 1803–1817.

Červený, V., 2001, Seismic ray theory: Cambridge University Press.

Dewangan, P., 2004, Processing and inversion of mode-converted waves using the PP+PS=SS method: Ph.D. thesis, Colorado School of Mines.

Dewangan, P., I. Tsvankin, M. Batzle, K. van Wijk, and M. Haney, 2006, PS-wave moveout inversion for tilted TI media: A physical-modeling study: Geophysics, **71**, D135–D143.

Fryer, G. J., and L. N. Frazer, 1984, Seismic waves in stratified anisotropic media: Geophysical Journal of the Royal Astronomical Society, **78**, 691–710.

Gajewski, D., and I. Pšenčík, 1987, Computation of high frequency seismic wavefields in 3-D laterally inhomogeneous anisotropic media: Geophysical Journal of the Royal Astronomical Society, **91**, 383–412.

Grechka, V., and I. Tsvankin, 1998, 3-D description of normal moveout in anisotropic inhomogeneous media: Geophysics, **63**, 1079–1092.

Jílek, P., 2002, Modeling and inversion of converted-wave reflection coefficients in anisotropic media: A tool for quantitative AVO analysis: Ph.D. thesis, Colorado School of Mines.

Neves, F. A., A. Al-Marzoug, J. J. Kim, and E. L. Nebrija, 2003, Fracture characterization of deep tight sands using azimuthal velocity and AVO seismic data in Saudi Arabia: The Leading Edge, **22**, 469–475.

Rüger, A., 2001, Reflection coefficients and azimuthal AVO analysis in anisotropic media: Society of Exploration Geophysics.

Rüger, A., and Tsvankin, I., 1997, Using AVO for fracture detection: Analytic basis and practical solutions: The Leading Edge, **16**, 1429–1434.

Thomsen, L., 1986, Weak elastic anisotropy: Geophysics, **51**, 1954–1966.

Thomsen, L., 1999, Converted-wave reflection seismology over inhomogeneous, anisotropic media: Geophysics, **64**, 678–690.

Tsvankin, I., 1995, Body-wave radiation patterns and AVO in transversely isotropic media: Geophysics, **60**, 1409–1425.

Tsvankin, I., 2005, Seismic signatures and analysis of reflection data in anisotropic media, 2nd ed.: Elsevier Science Publ. Co., Inc.

Tsvankin, I., and V. Grechka, 2000, Dip moveout of converted waves and parameter estimation in transversely isotropic media: Geophysical Prospecting, **48**, 257–292.

Tsvankin, I., and L. Thomsen, 1994, Nonhyperbolic reflection moveout in anisotropic media: Geophysics, **59**, 1290–1304.

Vasconcelos, I., and I. Tsvankin, 2006, Non-hyperbolic moveout inversion of wide-azimuth P-wave data for orthorhombic media: Geophysical Prospecting, **54**, 535–552.

Xu, X., I. Tsvankin, and A. Pech, 2005, Geometrical spreading of P-waves in horizontally layered, azimuthally anisotropic media: Geophysics, **70**, D43–D53.

Xu, X., and I. Tsvankin, 2006a, Anisotropic geometrical-spreading correction for wide-azimuth P-wave reflections: Geophysics, **71**, D161–D170.

Xu, X., and I. Tsvankin, 2006b, Azimuthal AVO analysis with anisotropic spreading correction: A synthetic study: The Leading Edge, **24**, 1336–1342.

Xu, X., and I. Tsvankin, 2007, A case study of azimuthal AVO analysis with anisotropic spreading correction: CWP Research Report (this volume).

Wang, Z., 2002, Seismic anisotropy in sedimentary rocks, part 2: Laboratory data: Geophysics, **67**, 1423–1440.

AVO-sensitive semblance analysis for wide-azimuth data

Jia Yan & Ilya Tsvankin
Center for Wave Phenomena, Department of Geophysics, Colorado School of Mines

ABSTRACT

Conventional semblance-based moveout analysis models prestack reflection data with events that have hyperbolic moveout and no amplitude variation with offset (AVO). It has been shown that substantial amplitude variation and even phase change with offset do not significantly compromise the semblance operator. However, polarity reversal associated with a change in the sign of the reflection coefficient may cause conventional semblance to fail. An existing modification of the semblance operator that takes amplitude variations into account (so-called "AK semblance") is limited to narrow-azimuth data and cannot handle nonhyperbolic moveout.

Here, we extend the AK semblance algorithm to long-spread (nonhyperbolic) moveout and 3D multiazimuth data. To preserve velocity resolution in the presence of substantial AVO signature, we keep the ratio K of the AVO gradient and intercept constant within each semblance window. In the presence of azimuthal anisotropy, however, the parameter K has to be azimuthally dependent. In our implementation, the modified semblance operator is combined with a nonhyperbolic moveout inversion algorithm devised for wide-azimuth data.

Synthetic tests confirm that the distortions in moveout analysis caused by polarity reversals are more common for long-spread data. Conventional semblance produces substantial errors in both the NMO ellipse and azimuthally varying parameter η not just for type 2 AVO response, but also for some models with type 1 AVO. In contrast, the AK semblance algorithm gives accurate estimates of the moveout parameters even when the position of the polarity reversal varies with azimuth. The AK method not only helps to flatten wide-azimuth reflection events prior to stacking and azimuthal AVO analysis, but also provides input parameters for the anisotropic geometrical-spreading correction.

Key words: AVO, polarity reversal, semblance, wide-azimuth, anisotropy

1 INTRODUCTION

Semblance-based moveout analysis is routinely employed in seismic data processing to estimate stacking (moveout) velocity $V_{\rm nmo}$ as a function of the zero-offset time t_0 (e.g., Taner and Koehler, 1969). NMO velocity, which typically represents the most stable parameter constrained by surface seismic data, is then used to build the initial velocity model and flatten reflection events for subsequent processing.

The conventional semblance operator can be written as

$$S(V,\ t_0) = \frac{\sum\limits_{t_1}\left[\sum\limits_{x} D_V(t_1,x)\right]^2}{N\sum\limits_{t_1}\sum\limits_{x} D_V^2(t_1,x)}, \qquad (1)$$

where t_1 are the zero-offset times within a time window centered at t_0, x is the source-to-receiver offset, N is the number of traces in a CMP (common mid-

point) gather, and D_V represents the data picked along hyperbolic moveout curves computed with the velocity $V = V_{\text{nmo}}$.

Despite its general robustness, the operator in equation 1 has two serious limitations. First, it does not not account for deviations from hyperbolic moveout, which become significant for offset-to-depth ratios greater than unity. To make equation 1 suitable for long-spread reflection events, the conventional hyperbolic moveout equation is replaced by more complicated nonhyperbolic functions, such as those developed by Tsvankin and Thomsen (1994) and Alkhalifah and Tsvankin (1995).

Second, the semblance operator 1 is devised under the assumption that reflection amplitudes are constant and, therefore, includes no allowance for amplitude variation with offset (AVO). Still, conventional semblance usually estimates moveout velocity with sufficient accuracy even for events with relatively strong AVO, as long as there is no polarity reversal within the recorded offset range. In the presence of polarity reversals, however, the conventional operator often fails and gives a strongly distorted NMO-velocity value (Sarkar et al., 2001). Then the reflection event cannot be properly flattened, which leads to a poor-quality, low-frequency stack.

Figure 1 displays three common types of P-wave AVO behavior for gas sands described in Rutherford and Williams (1989). Classes 1 and 2 correspond to highly or moderately compressed sands beneath shales, while class 3 sands are overlaid by a more compressed overburden. Evidently, for class 1 and class 2 responses a polarity reversal occurs at incidence angles less than 30°. Furthermore, the influence of anisotropy increases the chance of observing polarity reversals on conventional-spread reflection data. Indeed, most shale formations are transversely isotropic (TI), and for typical positive values of the Thomsen (1986) parameter δ in shales the AVO gradient increases by absolute value (Kim et al., 1993; Tsvankin, 2005). As a result, the polarity reversal for the interface between gas sands and VTI (TI with a vertical symmetry axis) shales moves towards lower angles from its "isotropic" position (Figure 1).

Sarkar et al. (2002) developed the so-called "AK semblance" method to make velocity analysis suitable for data with polarity reversals. Their approach is based on introducing into the semblance operator a smooth amplitude variation with offset governed by two parameters (A and K). The existing AK algorithm, however, is designed for 2D data and is restricted to the hyperbolic portion of the moveout curve (i.e., to conventional-length spreads).

Here, we present an extension of the AK semblance method to nonhyperbolic (long-spread) moveout and wide-azimuth data. Our generalized AK algorithm is particularly important for processing of reflection data from anisotropic media because anisotropy usually enhances nonhyperbolic moveout of P-waves (Tsvankin, 2005) and moves the polarity reversal toward smaller offsets (see above). Also, amplitude variations with offset and azimuth may substantially distort the results of moveout analysis for wide-azimuth surveys acquired above fractured formations. Vasconcelos and Tsvankin (2006) presented an efficient technique for nonhyperbolic moveout inversion of wide-azimuth data from layered azimuthally anisotropic media, but their semblance operator does not take amplitude variations into account.

Table 1. Model parameters for the three types of AVO responses in Figure 1.

		V_P(km/s)	V_S(km/s)	ρ (g/cm^3)
Layer 1		3.00	1.32	2.4
Layer 2	type 1	4.40	2.80	2.0
	type 2	3.75	2.40	2.0
	type 3	2.95	1.89	2.0

We begin by reviewing the AK semblance algorithm of Sarkar et al. (2002) and its implementation in moveout analysis. Then we extend the AK semblance operator to long-offset data using the nonhyperbolic moveout equation of Alkhalifah and Tsvankin (1995). To apply the method to wide-azimuth data, we make the AVO gradient azimuthally dependent and incorporate it into the moveout-inversion algorithm of Vasconcelos and Tsvankin (2006). Synthetic tests for VTI and azimuthally anisotropic (orthorhombic) models demonstrate the superior performance of the generalized AK semblance for both class 1 and 2 AVO responses.

2 METHODOLOGY

As discussed above, the conventional semblance operator in equation 1 does not account for amplitude variations within the CMP gather. A more general semblance formulation for 2D data was introduced by Sarkar et al. (2002):

$$S_G(V,\ t_0) = 1 - \frac{\parallel M - D_V \parallel^2}{\parallel D_V \parallel^2}, \qquad (2)$$

where t_0, as before, is the zero-offset time at the center of the semblance window, $D_V = D_V(t_1, x)$ is the data with the zero-offset time t_1 after a hyperbolic moveout correction with the velocity $V = V_{\text{nmo}}$, and $M = M(t_1, x)$ is the modeled variation of the trace amplitudes. The amplitude parameters that govern $M(t_1, x)$ and the velocity V_{nmo} are estimated by matching the model M and data D, which can be achieved by maximizing the semblance (i.e., by minimizing $\parallel M - D_V \parallel^2$). The generalized semblance from equation 2 reduces to the conventional semblance operator (equation 1) when the am-

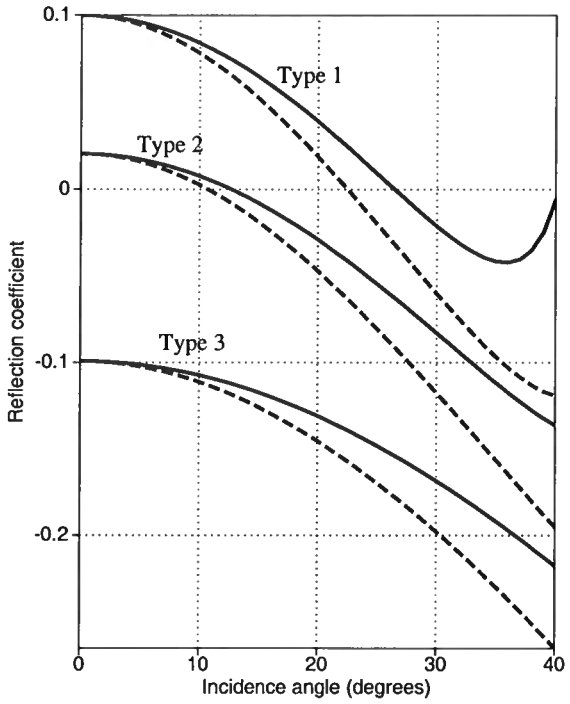

Figure 1. Three types of P-wave AVO responses (reflection coefficients) computed from exact equations (Rüger, 2001) for gas sands overlaid by shale. The solid lines correspond to the three isotropic models from Table 1 (Rutherford and Williams, 1989). The dashed lines are computed for models with the same vertical velocities and densities, but the shale layer is VTI with the Thomsen parameters $\epsilon = \delta = 0.2$. All three models have negative AVO gradients, which become larger by absolute value when the shale is anisotropic.

plitudes associated with model M are independent of offset (Sarkar et al., 2002).

The offset-dependent function M in the AVO-sensitive semblance algorithm can be approximately described by Shuey's (1985) linearized equation for the reflection coefficient:

$$\begin{aligned} M(t_1, x) &= A(t_1) + B(t_1) \sin^2 \theta_x \\ &\approx A(t_1) + B(t_1) \frac{x^2}{x^2 + V_{\text{nmo}}^2 t_0^2}, \end{aligned} \tag{3}$$

where $A(t_1)$ and $B(t_1)$ are the AVO intercept and gradient (respectively) for the reflection event with the zero-offset time t_1, and θ_x is the phase angle of incidence at the reflector, which is expressed through offset x under the assumption that the medium is homogeneous and isotropic.

The exact incidence angle θ_x cannot be computed without knowledge of the velocity model. It should be emphasized, however, that there is no need for an accurate estimate θ_x, because the only role of equation 3 is to introduce a smooth amplitude variation with offset into the semblance operator. Note that Shuey's (1985) equation cannot represent measured reflection amplitudes anyway because it does not include the source directivity and such propagation factors as the geometrical spreading and transmission coefficients along the raypath.

As pointed out by Sarkar et al. (2002), equation 3 (called "AB semblance") allows too much freedom to fit events with various combinations of incorrect parameters A, B, and V_{nmo}, which results in poor velocity resolution. To reduce this interplay, Sarkar et al. (2002) suggested to keep the ratio $A/B = K$ constant inside the semblance window, which implies that the wavelet shape does not change with offset:

$$M(t_1, x) = A(t_1) \left(1 + K \frac{x^2}{x^2 + V_{\text{nmo}}^2 t_0^2}\right). \tag{4}$$

Modeling data using equation 4 with $K = const$ is referred to by Sarkar et al. (2002) as "AK semblance."

The semblance window follows the traveltime trajectory computed from an analytic (hyperbolic in the work by Sarkar et al., 2002) moveout equation and has the width close to the length of the wavelet. For a window with N_t sampling points, the AK semblance operator has only $N_t + 1$ parameters (as compared to $2N_t$ for AB semblance), which mitigates the tradeoffs and increases velocity resolution.

For a given zero-offset time t_0 and a trial velocity V_{nmo}, the parameters A and K can be found analytically by setting the derivatives of S_G with respect to A and K to zero (see Appendix A). The obtained expressions are then substituted back into equation 2 to compute the generalized semblance. As in conventional semblance algorithms, scanning over V_{nmo} is used to maximize the semblance and estimate the best-fit moveout (stacking) velocity.

A key issue in the implementation of the generalized semblance algorithm is the choice of the moveout equation $t(x)$. Reflection moveout on conventional-length spreads (i.e., for offset-to-depth ratios not much larger than unity) typically is close to hyperbolic:

$$t^2(x) = t_0^2 + \frac{x^2}{V_{\text{nmo}}^2}. \tag{5}$$

Although equation 3 is widely used in seismic processing, it breaks down at longer offsets, especially if the medium is anisotropic. A more accurate, nonhyperbolic moveout equation for P-wave data in VTI media was suggested by Alkhalifah and Tsvankin (1995):

$$t^2(x) = t_0^2 + \frac{x^2}{V_{\text{nmo}}^2} - \frac{2\eta x^4}{V_{\text{nmo}}^2 \left[t_0^2 V_{\text{nmo}}^2 + (1 + 2\eta) x^2\right]}, \tag{6}$$

where $\eta \equiv (\epsilon - \delta)/(1 + 2\delta)$ is the "anellipticity" parameter, which controls P-wave time processing for vertical transverse isotropy. The x^4-term in equation 6 is

proportional to η and describes nonhyperbolic moveout for large offsets. Below we employ the Alkhalifah-Tsvankin equation in the AK semblance operator to perform moveout analysis of long-spread 2D P-wave data.

The main goal of the paper, however, is to extend the principle of AK semblance to wide-azimuth surveys, which are often acquired for purposes of fracture detection. Reservoirs with vertical fracture sets are commonly described by an effective anisotropic model with orthorhombic symmetry (Schoenberg and Helbig, 1997; Bakulin et al., 2000; Grechka and Kachanov, 2006). Azimuthally dependent P-wave reflection traveltimes in a horizontal orthorhombic layer can be well-approximated by a generalized version of equation 6, in which both the NMO velocity and parameter η vary with the azimuth α (Xu et al., 2005; Vasconcelos and Tsvankin, 2006):

$$t^2(x,\alpha) = t_0^2 + \frac{x^2}{V_{\rm nmo}^2(\alpha)} - \frac{2\eta(\alpha)\, x^4}{V_{\rm nmo}^2(\alpha)\,[t_0^2\, V_{\rm nmo}^2(\alpha) + (1+2\eta(\alpha))\, x^2]}, \tag{7}$$

where $V_{\rm nmo}$ is obtained from the equation of the NMO ellipse:

$$V_{\rm nmo}^{-2}(\alpha) = \frac{\cos^2(\alpha-\varphi)}{\left[V_{\rm nmo}^{(2)}\right]^2} + \frac{\sin^2(\alpha-\varphi)}{\left[V_{\rm nmo}^{(1)}\right]^2}. \tag{8}$$

Here, φ is the azimuth of the $[x_1, x_3]$ symmetry plane, and $V_{\rm nmo}^{(1)}$ and $V_{\rm nmo}^{(2)}$ are the NMO velocities in the symmetry planes $[x_2, x_3]$ and $[x_1, x_3]$, respectively. [The superscript in $V_{\rm nmo}^{(1)}$ and $V_{\rm nmo}^{(2)}$ refers to the axis orthogonal to the corresponding plane; for a detailed discussion of notation, see Tsvankin (1997, 2005).]

The azimuthal variation of the parameter η is approximately given by (Pech and Tsvankin, 2004)

$$\eta(\alpha) = \eta^{(2)}\cos^2(\alpha-\varphi) + \eta^{(1)}\sin^2(\alpha-\varphi) - \eta^{(3)}\cos^2(\alpha-\varphi)\sin^2(\alpha-\varphi), \tag{9}$$

where $\eta^{(1)}$, $\eta^{(2)}$, and $\eta^{(3)}$ are the anellipticity parameters defined (respectively) in the $[x_2, x_3]$, $[x_1, x_3]$, and $[x_1, x_2]$ symmetry planes.

The accuracy of equation 7 in both vertical symmetry planes is the same as that in the corresponding equivalent VTI medium. Xu et al. (2005) and Vasconcelos and Tsvankin (2006) show that equations 7–9 provide a close approximation for long-spread P-wave traveltimes recorded in all azimuthal directions, even for strongly anisotropic orthorhombic models. Furthermore, if $V_{\rm nmo}^{(1,2)}$ and $\eta^{(1,2,3)}$ are treated as effective parameters, the same formalism can be applied to P-wave moveout from layered orthorhombic media with uniform orientation of the symmetry planes.

Vasconcelos and Tsvankin (2006) used equations 7–9 to develop an efficient semblance-based moveout-inversion algorithm designed to estimate the parameters φ, $V_{\rm nmo}^{(1,2)}$ and $\eta^{(1,2,3)}$ from wide-azimuth P-wave data. Their method, however, does not account for amplitude variation with offset and azimuth and, similar to conventional 2D semblance techniques, can break down in the presence of polarity reversals. Below, we devise a more stable, 3D AK semblance operator by incorporating an azimuthally dependent amplitude function into the semblance computation.

When the medium above or below the reflector is azimuthally anisotropic, the AVO gradient and reflection amplitude as a whole vary with azimuth. For a boundary between two orthorhombic halfspaces with the same orientation of the vertical symmetry planes, the AVO gradient $B(\alpha)$ can be approximated by (Rüger, 2001)

$$B(\alpha) = B^{(2)}\cos^2(\alpha-\varphi) + B^{(1)}\sin^2(\alpha-\varphi), \tag{10}$$

where $B^{(1)}$ and $B^{(2)}$ are the AVO gradients in the $[x_2, x_3]$ and $[x_1, x_3]$ planes, respectively. Then the ratio $K(\alpha)$ of the AVO gradient and intercept also becomes azimuthally dependent and can be written as

$$K(\alpha) = K^{(2)}\cos^2(\alpha-\varphi) + K^{(1)}\sin^2(\alpha-\varphi). \tag{11}$$

Substitution of $K(\alpha)$ from equation 11 into equation 4 yields an azimuthally dependent amplitude function that can be used in the AK semblance computation. In our method, we combine this amplitude function with the moveout equations 7–9 discussed above to devise an AK semblance operator that can handle polarity reversals in wide-azimuth data collected into CMP gathers (see Appendix A). Although equation 11 does not describe geometrical spreading and some other factors that influence recorded amplitudes, it allows us to account for amplitude variation with azimuth $K^{(1)}$, $K^{(2)}$. In particular, it helps to mitigate distortions in the semblance computation related to the azimuthal dependence of the offset that corresponds to the polarity reversal.

Similar to the algorithm of Vasconcelos and Tsvankin (2006), we carry out estimation of $K^{(1)}$, $K^{(2)}$, and the moveout parameters φ, $V_{\rm nmo}^{(1,2)}$ and $\eta^{(1,2,3)}$ in three steps. First, we invert for the NMO ellipse described by φ, $V_{\rm nmo}^{(1)}$, and $V_{\rm nmo}^{(2)}$ using conventional-spread, wide-azimuth data with offsets limited by the reflector depth. If there is an indication of a polarity reversal at the near offsets, we also estimate an azimuthally-invariant value of K along with the NMO ellipse. This step gives initial values of the symmetry-plane azimuths, NMO velocities, and the parameter K. Second, nonhyperbolic AK semblance analysis is carried out in narrow sectors around the identified symmetry planes to find approximate values of $\eta^{(1)}$, $\eta^{(2)}$, $K^{(1)}$, $K^{(2)}$, as well as updated estimates of $V_{\rm nmo}^{(1)}$ and $V_{\rm nmo}^{(2)}$. Third, we carry out 3D nonhyperbolic moveout inversion using the 3D AK semblance operator for all offsets and azimuths in the gather. The search starts with the initial model obtained during the previous steps and scans over φ,

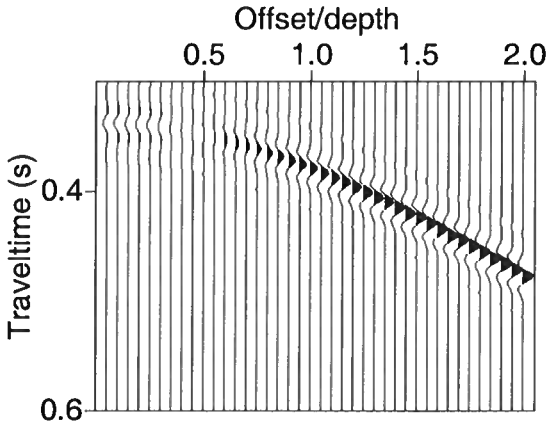

Figure 2. Shot record of a P-wave reflection from an interface between VTI (top) and isotropic (bottom) media. The model parameters are listed in Table 2. The event has a type 2 AVO response with the polarity reversal at an offset-to-depth ratio close to 0.5.

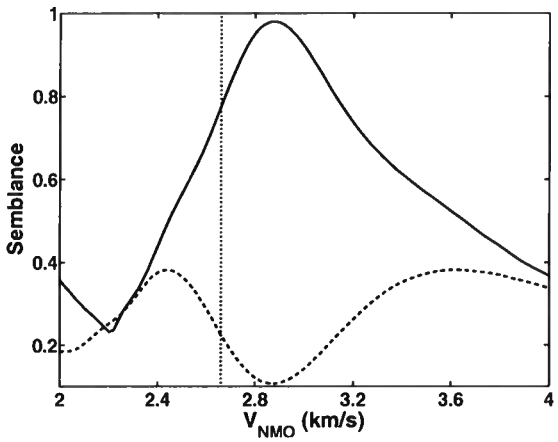

Figure 3. Semblance for the reflection event from Figure 2 computed using the hyperbolic moveout equation 5; the model parameters are listed in Table 2. The dashed curve is produced by the conventional semblance algorithm, and the solid curve is AK semblance. The vertical dotted line marks the actual NMO velocity.

$V_{\text{nmo}}^{(1,2)}$, $\eta^{(1,2,3)}$, and $K^{(1,2)}$ to find the best-fit parameters via Powell minimization (Press et al., 1992).

3 TESTS ON SYNTHETIC DATA

Here, the AK semblance algorithm is applied to 2D and 3D long-offset P-wave data from VTI and orthorhombic media. In addition to type 2 AVO responses, for which the polarity reversal is observed at relatively small offsets, we compare the performance of conventional and AK semblance for type 1 AVO. All synthetic data used below are generated by anisotropic ray tracing code ANRAY developed by Gajewski and Pšenčík (1987).

3.1 2D semblance for VTI media

For layer-cake VTI media, each vertical plane is a plane of symmetry, and the semblance analysis can be performed in 2D, for an arbitrary azimuthal direction. We consider a model that includes an isotropic halfspace beneath a VTI layer with relatively small absolute values of the Thomsen parameters ϵ and δ. The anellipticity parameter η, however, is substantial (0.2), which leads to pronounced nonhyperbolic moveout at offsets approaching two reflector depths (Figure 2). The event has a type 2 AVO response (see the discussion above), with relatively low amplitudes at near offsets and the polarity reversal at an offset close to half the reflector depth.

The first test was carried out using the hyperbolic moveout equation in both the conventional and AK semblance operators (Figure 3). Because of the combined influence of the polarity reversal and nonhyperbolic moveout, the conventional operator produces low semblance values for all trial velocities, with the correct velocity close to the semblance *minimum*. Although our algorithm performs much better and yields higher semblance, the best-fit NMO velocity deviates from the actual value. This error, which is caused by the inaccuracy of the hyperbolic moveout equation, can be reduced by muting out long offsets.

In many applications, such as nonhyperbolic moveout inversion and wide-angle AVO analysis, it is necessary to preserve and flatten the far-offset portion of the gather. To improve the traveltime fit at long offsets, next we employ the nonhyperbolic moveout equation 6 in the semblance computation (Figure 4). Although equation 6 provides a close approximation to the exact traveltimes (Alkhalifah and Tsvankin, 1995; Tsvankin, 2005), the best-fit parameters V_{nmo} and η estimated by the conventional semblance algorithm are severely distorted (e.g., the inverted $\eta = 0.72$, while the actual value is 0.2). Clearly, this error is caused by the polarity reversal because the semblance that corresponds to the correct moveout parameters is relatively low. In contrast, AK semblance gives accurate estimates of both V_{nmo} and η, as well as a high semblance value (0.94).

3.2 3D semblance for type 2 AVO

Here, we apply the 3D AK semblance operator to wide-azimuth P-wave reflections from an interface between

Table 2. Parameters of a model that includes VTI (top) and isotropic (bottom) media. The P-wave reflection for this model has a type 2 AVO response. V_{P0} and V_{S0} are the vertical P- and S-wave velocities, respectively.

	V_{P0}(km/s)	V_{S0}(km/s)	ρ (g/cm^3)	ϵ	δ	$V_{\rm nmo}$(km/s)	η
VTI	2.96	1.38	2.43	0.065	-0.096	2.66	0.2
ISO	3.49	2.29	2.14	0	0	3.49	0

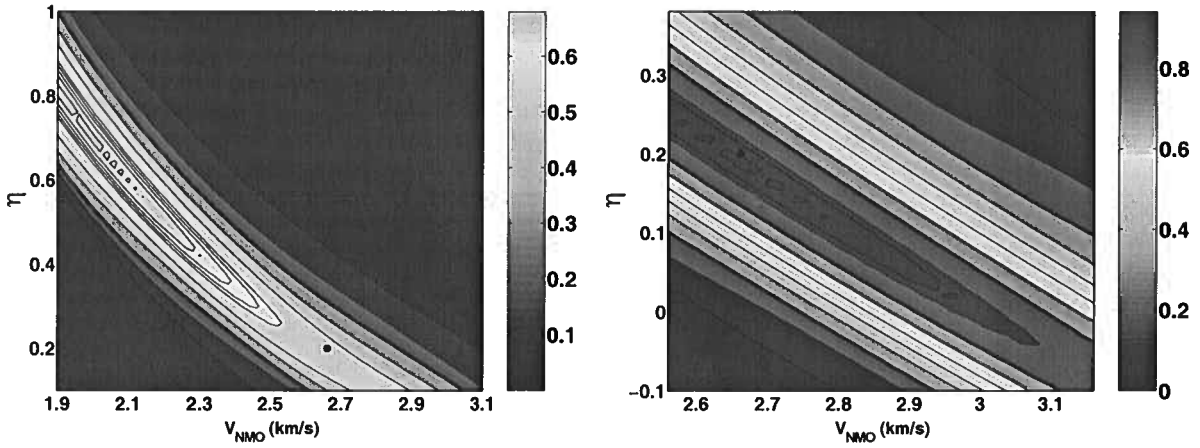

Figure 4. Semblance scans over $V_{\rm nmo}$ and η computed for the event from Figure 2 using the nonhyperbolic moveout equation 6. The scans are generated by the (a) conventional and (b) AK semblance operators. The black dots mark the true model parameters. The best-fit values are $V_{\rm nmo}$ = 1.98 km/s and η = 0.72 for conventional semblance (the maximum semblance is 0.72) and $V_{\rm nmo}$=2.68 km/s, η=0.18 for AK semblance (the maximum semblance is 0.94).

orthorhombic (incidence) and isotropic or orthorhombic (reflecting) media. Since the AVO gradient for this model is azimuthally dependent, the offset of the polarity reversal becomes a function of azimuth as well. If the polarity reversal occurs at relatively small offsets, the corresponding phase incidence angle $\theta_{\rm pr}$ can be estimated by setting $1 + K(\alpha)\sin^2\theta_{\rm pr} = 0$. Using equation 11 with $\varphi = 0$ (i.e., $\alpha = 0$ in the $[x_1, x_3]$-plane), we find

$$\sin^2\theta_{\rm pr} = \frac{-1}{K^{(1)}\sin^2\alpha + K^{(2)}\cos^2\alpha}. \qquad (12)$$

If the medium above the reflector is homogeneous and the difference between the group and phase angles can be neglected, equation 12 provides an estimate of the offset $x_{\rm pr}$ of the polarity reversal:

$$\frac{x_{\rm pr}(\alpha)}{h} \approx 2\tan\theta_{\rm pr} = \frac{2}{\sqrt{-(1 + K^{(1)}\sin^2\alpha + K^{(2)}\cos^2\alpha)}}, \qquad (13)$$

where h is the depth of the reflector.

3.2.1 *Model 1*

The first test was performed for a boundary between orthorhombic (top) and isotropic (bottom) halfspaces (Figure 5). Both media have the same vertical velocities and densities as those in the VTI/isotropic model analyzed above (see Table 2 and Figures 2–4). Also, the anisotropy parameters in the symmetry plane $[x_1, x_3]$ of the orthorhombic medium are taken from the VTI model in Table 2. Although the medium above the reflector is azimuthally anisotropic, the offset of the polarity reversal is weakly dependent on azimuth (Figure 5).

The initial model for 3D analysis of the long-spread gather was obtained by first estimating the NMO ellipse on conventional-spread data and then processing long-offset data (for the maximum offset-to-depth ratio $x_{\rm max}/h = 2$) in narrow sectors centered at the vertical symmetry planes. The NMO ellipse reconstructed by the conventional semblance operator for offset-to-depth ratios limited by unity has the correct orientation but highly distorted semi-axes equal to 3.20 km/s and 3.44 km/s (the actual values are 2.66 km/s and 2.87 km/s); the semblance is only 0.45. Clearly, conventional pro-

Table 3. Parameters of a model that includes orthorhombic (top) and isotropic (bottom) media. The P-wave reflection from this interface has an azimuthally varying type 2 AVO response.

	Layer 1	Layer 2
Symmetry type	ORTH	ISO
Density (g/cm^3)	2.43	2.14
V_{P0} (km/s)	2.96	3.49
V_{S0} (km/s)	1.38	2.29
$\epsilon^{(1)}$	0.065	0
$\delta^{(1)}$	-0.029	0
$\gamma^{(1)}$	0.18	0
$\epsilon^{(2)}$	0.065	0
$\delta^{(2)}$	-0.096	0
$\gamma^{(2)}$	0.05	0
$\delta^{(3)}$	-0.08	0
$V_{\rm nmo}^{(1)}$	2.87	3.49
$V_{\rm nmo}^{(2)}$	2.66	3.49
$\eta^{(1)}$	0.10	0
$\eta^{(2)}$	0.20	0
$\eta^{(3)}$	0.10	0

cessing cannot be used for either stacking of the wide-azimuth data or inversion of NMO ellipses.

The final inversion results for two spreadlengths ($x_{\rm max}/h = 2$ and $x_{\rm max}/h = 3$) are displayed in Figure 6. Note that with both conventional and AK semblance, the parameters for the $[x_1, x_3]$ symmetry plane estimated from the 3D inversion almost coincide with those obtained for the VTI model in Figure 4. Because of the influence of the polarity reversal, conventional semblance produces highly distorted NMO velocities and η values for both spreadlengths and the full range of azimuths. For type 2 AVO with small values of $x_{\rm pr}$, muting out long offsets does not help the conventional algorithm to reconstruct the NMO ellipse. As was the case for the VTI model, AK semblance correctly compensates for the polarity reversal and gives accurate estimates of the azimuthally varying parameters $V_{\rm nmo}$ and η.

3.2.2 Model 2

For the second test we chose another type 2 AVO model, for which the offset $x_{\rm pr}$ of the polarity reversal is larger and varies more strongly with azimuth (Figure 7). The normalized offset $x_{\rm pr}/h$ changes from 0.65 in the $[x_1, x_3]$ symmetry plane ($\alpha = 0°$) to 0.85 in the $[x_1, x_3]$-plane ($\alpha = 90°$).

The NMO ellipse reconstructed by the conventional method for offsets limited by the reflector depth has the correct orientation and the semi-axes 2.43 km/s and 2.11 km/s (the actual values are 2.53 km/s and 2.16 km/s); the semblance is 0.6. The accuracy achieved by the conventional method is explained by the relatively large (for type 2 AVO) offsets $x_{\rm pr}(\alpha)$ of the polarity reversal and low reflection amplitudes for $x > x_{\rm pr}$.

Application of the AK algorithm, however, becomes necessary for long-offset data because conventional semblance yields highly erroneous η values (Figures 8b,d). As discussed above, we obtain the initial model for 3D analysis by first estimating the NMO ellipse on conventional-spread data with $K^{(1)} = K^{(2)} = K$ and then processing long-offset data near the vertical symmetry planes, which gives $K^{(1)} = -5.85$ and $K^{(2)} = -6.21$. The results of 3D nonhyperbolic AK semblance analysis for two long spreads are shown in Figure 8. Since the polarity reversal now occurs in the smaller-offset half of the spread, conventional semblance produces a significant error not only in η, but also in the NMO ellipse. The η values estimated by the conventional algorithm for $x_{\rm max}/h = 2$ even become negative for a wide range of azimuths (Figure 8b).

The AK semblance method, which properly accounts for the azimuthally dependent polarity reversal, gives far superior results. There is practically no error in the reconstruction of the NMO ellipse, while the mild distortion in η for $x_{\rm max}/h = 2$ is caused by the small bias in the nonhyperbolic moveout equation (Tsvankin, 2005) and insufficient spreadlength. Since the parameter η controls nonhyperbolic moveout, it is better constrained for larger spreadlengths. When the maximum offset-to-depth ratio is increased from two to three (Figure 8d), the errors in the function $\eta(\alpha)$ become almost negligible.

3.3 3D semblance for type 1 AVO

Compared to the type 2 AVO response analyzed above, type 1 AVO is typically characterized by a higher normal-incidence reflection coefficient, and the polarity reversal is observed at larger offsets (Figure 1). As long as the polarity reversal does not occur in the recorded offset range, the data can be processed by the conventional semblance algorithm. However, for long-spread reflections with offset-to-depth ratios reaching two, the offset $x_{\rm pr}$ may be close to middle of the spread. Anisotropy, in particular, tends to move the polarity reversal toward smaller offsets (Figure 1).

Figure 9 displays a P-wave reflection from an interface between orthorhombic and isotropic media (see Table 5). The event has a typical type 1 AVO response, with the polarity reversal recorded at offset-to-depth ratios of about 1.2. Although the conventional algorithm performs better than it did for type 2 AVO, the errors in both the NMO ellipse and parameter η are noticeable (Figure 10). A more accurate reconstruction of the NMO ellipse using conventional semblance can be achieved by reducing the maximum offset-to-depth ratio to $x_{\rm max}/h < 1.2$ (i.e., by truncating the spread before the polarity reversal). Despite the presence of

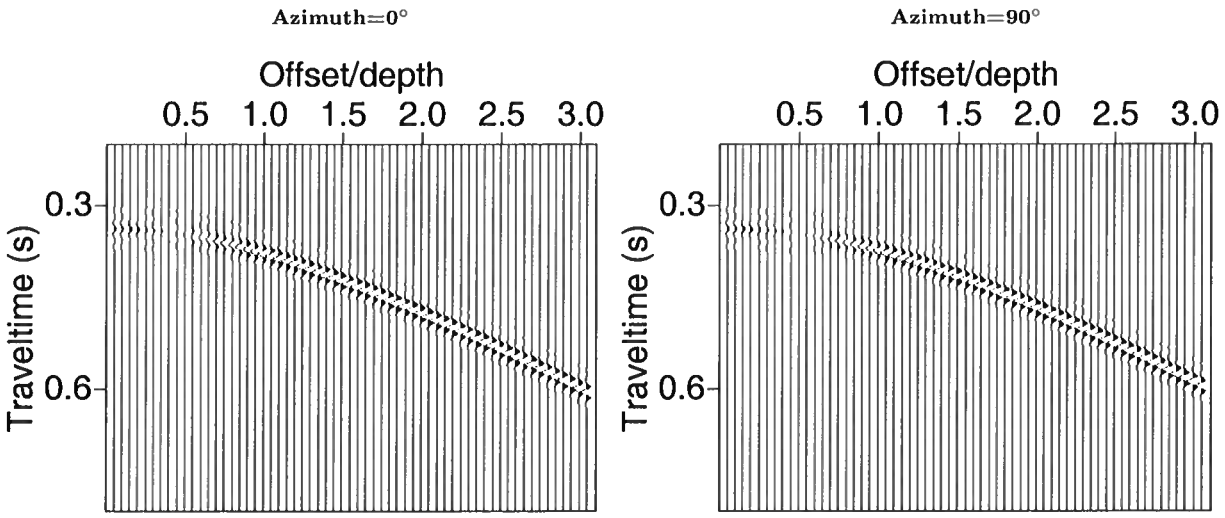

Figure 5. Shot records of a P-wave reflection from an orthorhombic/isotropic interface with a type 2 AVO response (Table 3). The seismograms are computed for the symmetry planes $[x_1, x_3]$ ($\alpha = 0°$) and $[x_2, x_3]$ ($\alpha = 90°$).

Table 4. Orthorhombic/orthorhombic model for which the P-wave reflection has an azimuthally varying type 2 AVO response. The two media have the same orientation of the vertical symmetry planes. Compared to the model from Table 3, the polarity reversal occurs at larger offsets.

	Layer 1	Layer 2
Symmetry type	ORTH	ORTH
Density (g/cm^3)	2.4	2.5
V_{P0} (km/s)	2.35	2.50
V_{S0} (km/s)	1.41	1.83
$\epsilon^{(1)}$	0.20	0.16
$\delta^{(1)}$	0.08	0.09
$\gamma^{(1)}$	0.18	0.05
$\epsilon^{(2)}$	0.13	0.09
$\delta^{(2)}$	-0.08	-0.07
$\gamma^{(2)}$	0.05	0.03
$\delta^{(3)}$	-0.08	-0.09
$V_{\rm nmo}^{(1)}$	2.53	2.72
$V_{\rm nmo}^{(2)}$	2.16	2.32
$\eta^{(1)}$	0.10	0.09
$\eta^{(2)}$	0.25	0.19
$\eta^{(3)}$	0.07	0.14

Table 5. Orthorhombic/isotropic model for which the P-wave reflection has an azimuthally varying type 1 AVO response.

	Layer 1	Layer 2
Symmetry type	ORTH	ISO
Density (g/cm^3)	2.4	2.6
V_{P0} (km/s)	3.30	3.84
V_{S0} (km/s)	1.45	2.46
$\epsilon^{(1)}$	0.20	0
$\delta^{(1)}$	0.10	0
$\gamma^{(1)}$	0.20	0
$\epsilon^{(2)}$	0.13	0
$\delta^{(2)}$	-0.10	0
$\gamma^{(2)}$	0.05	0
$\delta^{(3)}$	0.02	0
$V_{\rm nmo}^{(1)}$	3.61	3.84
$V_{\rm nmo}^{(2)}$	2.95	3.84
$\eta^{(1)}$	0.08	0
$\eta^{(2)}$	0.29	0
$\eta^{(3)}$	0.07	0

the polarity reversal, the error in the NMO ellipse obtained by the AK semblance is almost negligible for both spreadlengths (Figures 10a,c).

As was the case for type 2 AVO (see Figure 8), the AK semblance operator gives a higher accuracy in η for the longer spread ($x_{\rm max}/h = 3$), especially in the $[x_1, x_3]$-plane where $\eta(\alpha)$ reaches its maximum (Figures 10b,d). Somewhat suprisingly, the η estimate produced by the conventional semblance deteriorates with increasing spreadlength. This reduction in accuracy is most likely explained by the increased distortion caused by the polarity reversal on longer spreads, as the semblance becomes more influenced by traces at large (post-reversal) offsets $x > x_{\rm pr}$.

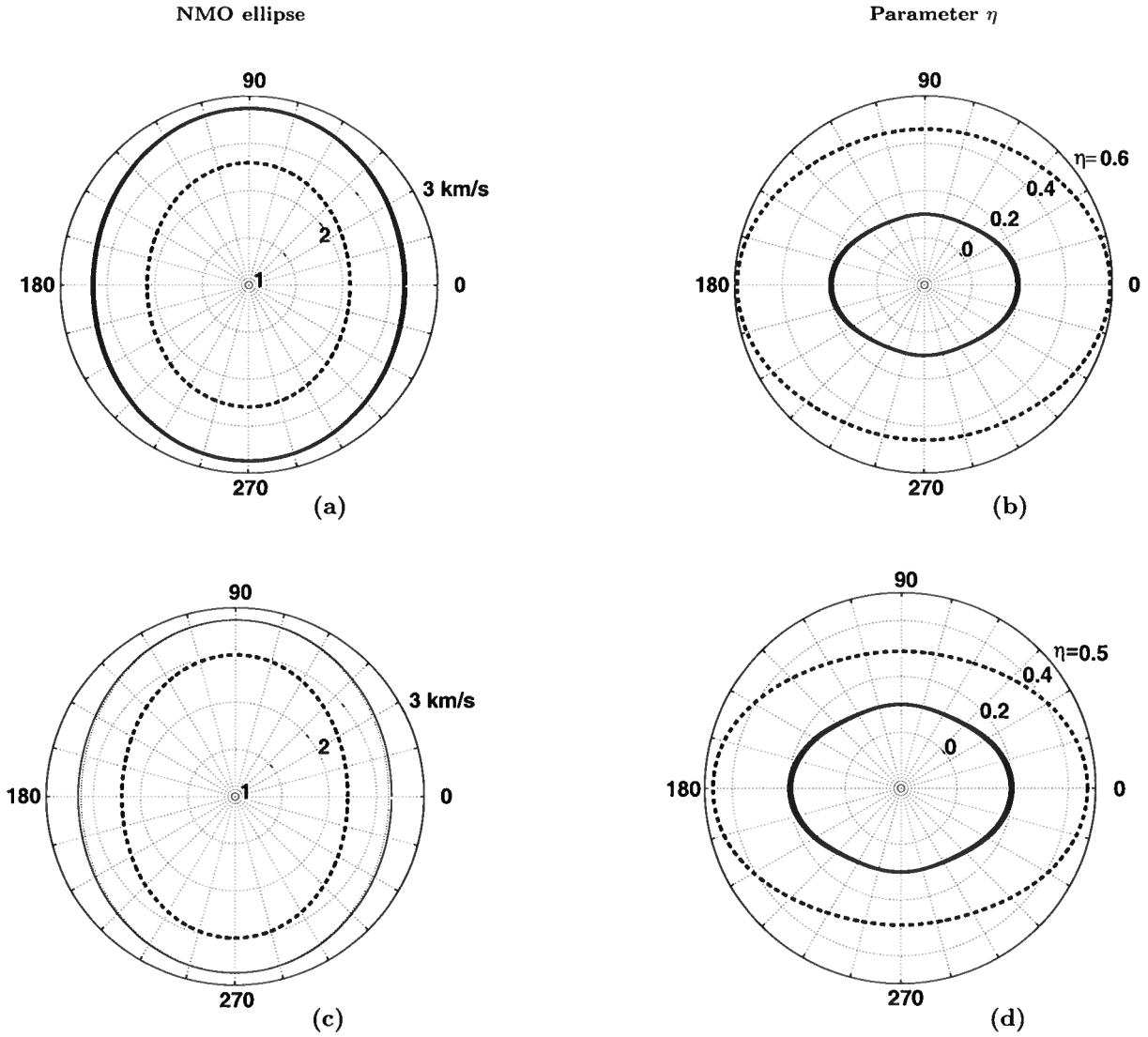

Figure 6. Moveout-inversion results for a wide-azimuth, long-offset P-wave reflection from an orthorhombic/isotropic interface (Table 3). The event has a type 2 AVO response with the polarity reversal at offset-to-depth ratios close to 0.5. (a) and (c) are the NMO ellipses; (b) and (d) are the azimuthally-dependent η values. The maximum offset-to-depth ratio is two for the top row, and three for the bottom row. The solid lines are the actual NMO ellipses and η-curves, the dashed lines are estimated by the conventional semblance algorithm, and the dotted lines by AK semblance. Since the AK semblance algorithm reconstructs the moveout parameters with high accuracy, the dotted lines are almost invisible. The azimuth with respect to the symmetry plane $[x_1, x_3]$ is shown on the perimeter.

4 DISCUSSION

Our results demonstrate that a smooth amplitude function based on Shuey's equation for the AVO gradient is sufficient for removing the influence of polarity reversals on semblance analysis. Still, it should be emphasized that AK semblance should not be regarded as a substitute for 2D or 3D (azimuthal) AVO analysis. Whereas the small-offset AVO equation used in our algorithm is sufficient to correct for the phase change of the wavelet in the presence of polarity reversals, it gives a rather crude approximation for reflection amplitudes on long spreads. Also, it does not properly account for propagation phenomena, such as geometrical spreading and transmission coefficients along the raypath. Therefore, the role of the AK semblance method

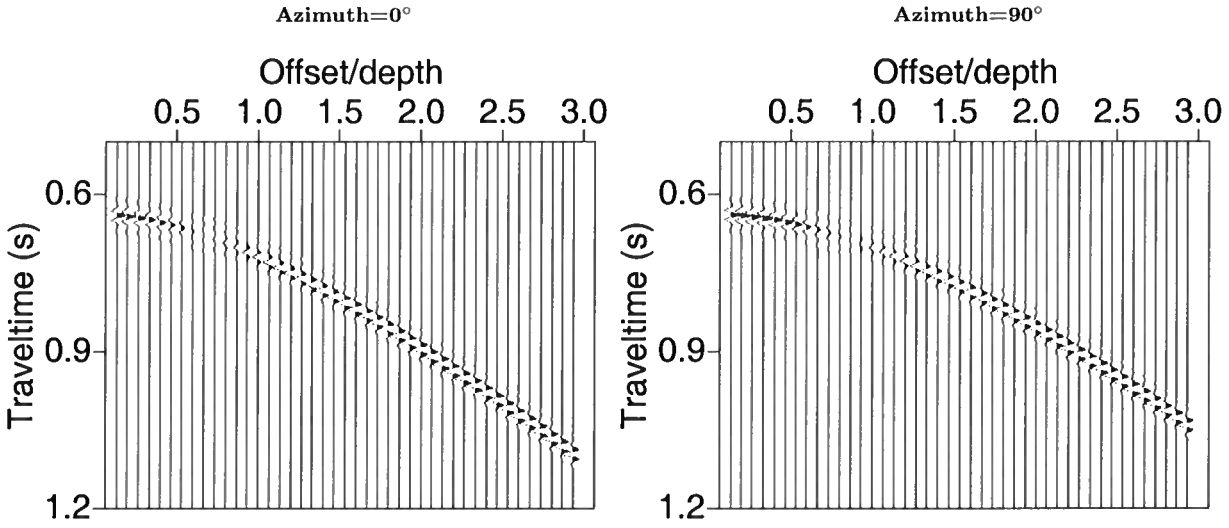

Figure 7. Shot records of a P-wave reflection from an orthorhombic/orthorhombic interface with a type 2 AVO response (Table 4). The seismograms are computed for the symmetry planes $[x_1, x_3]$ ($\alpha = 0°$) and $[x_2, x_3]$ ($\alpha = 90°$). The offset of the polarity reversal for this model noticeably varies with azimuth.

is limited to estimating an accurate set of parameters that control the nonhyperbolic moveout equation. The robust moveout inversion ensures the flatness of multi-azimuth, long-spread events prior to stacking and amplitude picking. The moveout parameters also serve as the input to the anisotropic geometrical-spreading correction (Xu and Tsvankin, 2006a, 2006b) that should be applied prior to AVO analysis.

Far-offset amplitudes needed in our algorithm often are too low to make a meaningful contribution to the semblance operator. Therefore, it may be necessary to gain the whole data set as a prerequisite to stable AK semblance computation. This preprocessing step can be accomplished with any empirical gain function. As mentioned above, a more accurate geometrical-spreading correction can be implemented after the moveout inversion.

In some of our tests for models with large velocity contrasts and type 1 AVO response, the critical angle was small enough for long-spread gathers to include post-critical offsets. As discussed in detail by Landrø and Tsvankin (2007), the critical angle for orthorhombic media varies with azimuth and can be used in anisotropic parameter estimation. According to Sarkar et al. (2002), the phase change with offset at the critical angle does not lead to significant errors in stacking velocity when the hyperbolic moveout equation is used in the semblance computation. However, our numerical tests show that the influence of the critical angle causes severe distortions in the η values estimated by the 3D AK semblance operator. Therefore, it is essential to mute out post-critical offsets in AK nonhyperbolic semblance analysis.

Although the numerical examples here were generated for two-layer models, the AK semblance algorithm can be applied in the same way to multilayered VTI and orthorhombic media. In the presence of vertical heterogeneity, the estimated moveout parameters represent effective quantities for the medium above the reflector (Vasconcelos and Tsvankin, 2006). Also, it should be mentioned that AK semblance cannot help to resolve the tradeoffs between NMO velocities and η parameters discussed in detail by Tsvankin (2005) and Vasconcelos and Tsvankin (2006).

5 CONCLUSIONS

Polarity reversals, which may be quite common for long-spread gathers of reflection events, can produce significant distortions in velocity estimation using conventional semblance analysis. Here, we presented an efficient AVO-sensitive methodology designed to account for the influence of polarity reversals on moveout inversion for long-offset 2D and 3D (wide-azimuth) P-wave reflection data. The 2D algorithm is based on the Alkhalifah-Tsvankin nonhyperbolic moveout equation that accurately describes P-wave traveltimes in vertical symmetry planes of layered anisotropic media. Following the so-called "AK semblance" method of Sarkar et al., the amplitude variation with offset is approximated by a two-parameter function that reduces to Shuey's AVO equation when the overburden is isotropic and homogeneous. To minimize the tradeoffs between the

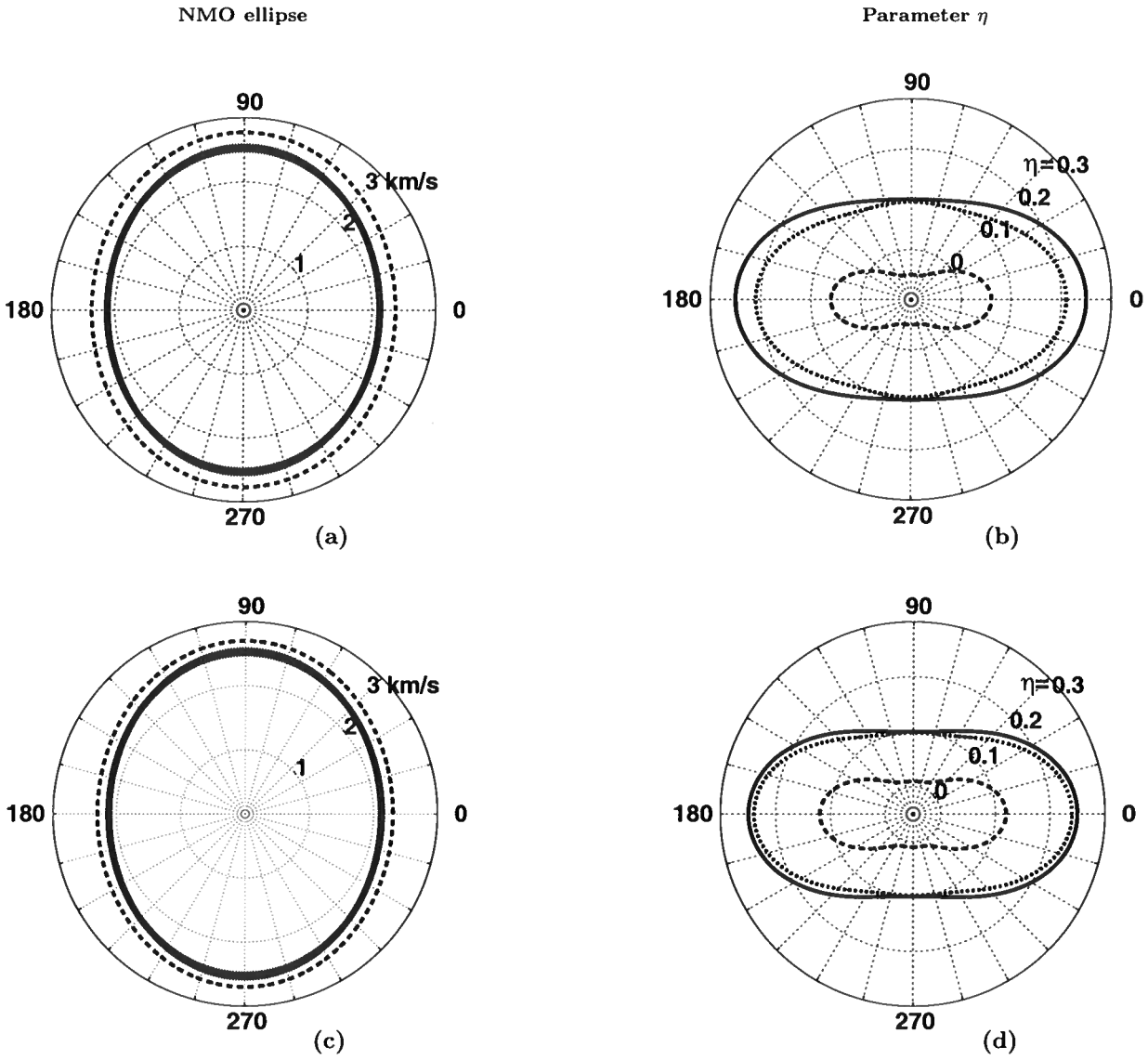

Figure 8. Moveout-inversion results for a wide-azimuth, long-offset P-wave reflection from an orthorhombic/orthorhombic interface (Table 4). The event has a type 2 AVO response with the polarity reversal at offsets between $x/h = 0.65$ and $x/h = 0.85$. The maximum offset-to-depth ratio is two for the top row, and three for the bottom row. The solid lines are the actual NMO ellipses and η-curves, the dashed lines are estimated by the conventional semblance algorithm, and the dotted lines by AK semblance [the dotted and solid curves in plots (a) and (c) almost coincide].

model parameters, the ratio of the AVO gradient and intercept ($K = A/B$) for each reflection event is kept constant.

Although the employed amplitude dependence does not include geometrical spreading and higher-order AVO terms, it proved sufficiently accurate for purposes of moveout inversion. Synthetic tests on long-offset P-wave data from VTI media show that conventional semblance breaks down for type 2 AVO responses with the polarity reversal at relatively small offsets-to-depth ratios (less than unity). Even when combined with the Alkhalifah-Tsvankin equation, the conventional semblance operator produces errors in the NMO velocity and completely distorts the key time-processing parameter η. These errors are practically eliminated by the AK semblance operator, which achieves the same high accuracy in the estimates of $V_{\rm nmo}$ and η as that for AVO-free events.

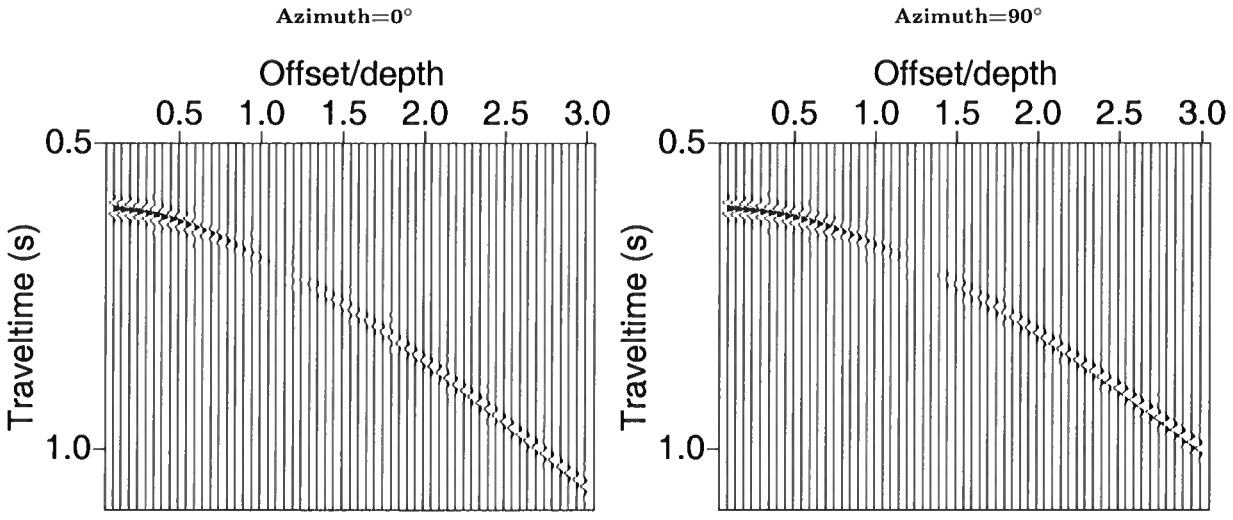

Figure 9. Shot records of a P-wave reflection from an orthorhombic/isotropic interface with a type 1 AVO response (Table 5). The seismograms are computed for the symmetry planes $[x_1, x_3]$ ($\alpha = 0°$) and $[x_2, x_3]$ ($\alpha = 90°$).

Despite the addition of the amplitude parameters (A, which is defined at each time sample, and K), the 2D AK semblance algorithm is computationally efficient because the best-fit values of A and K are obtained analytically by differentiating the semblance function. As a result, the scanning is carried out only over the same two moveout parameters ($V_{\rm nmo}$ and η) as in the conventional method. The only difference between the AK and conventional algorithms in terms of computational cost is in the more complicated form of the AVO-sensitive semblance operator.

For 3D wide-azimuth data, AK semblance needs to handle azimuthally dependent amplitudes, which are largely governed by the AVO gradient. The amplitude function in our 3D AK semblance operator is based on the azimuthal variation of the AVO gradient for orthorhombic media. This amplitude dependence, which is controlled by the symmetry-plane values of K ($K^{(1)}$ and $K^{(2)}$), was incorporated into a nonhyperbolic moveout inversion algorithm for wide-azimuth data that operates with a generalized form of the Alkhalifah-Tsvankin equation. The 3D AK semblance is designed to invert for $K^{(1)}$ and $K^{(2)}$ along with the moveout parameters of orthorhombic media, which include the azimuth of one of the symmetry planes, two symmetry-plane NMO velocities and three η coefficients ($\eta^{(1,2,3)}$). To start the semblance search with an accurate initial model, the multidimensional scan on the full 3D gather is preceded by estimation of the NMO ellipse and by 2D inversion of long-offset data near the symmetry-plane directions.

The improvement achieved by the 3D AK semblance is especially significant for orthorhombic models with type 2 AVO response. The conventional method completely breaks down on long spreads and even produces η values that have the wrong sign. Despite the approximate nature of its amplitude function, the AK semblance algorithm properly accounts for the azimuthally varying polarity reversal in the estimation of both the NMO ellipse and the η-curve. For type 1 AVO, the polarity reversal occurs at larger offsets (typically, at offset-to-depth ratios larger than unity), which makes the conventional method more accurate. Still, since inversion for η requires offsets reaching at least two reflector depths, the polarity reversal distorts the output of the conventional semblance operator. As is the case for AVO-free data, the accuracy of the η parameters computed by the AK semblance algorithm increases for larger spreadlengths. In contrast, conventional semblance for type 1 AVO gives more distorted η estimates with increasing spreadlength, as the influence of the polarity reversal becomes more substantial.

On the whole, nonhyperbolic moveout inversion for both type 1 and type 2 AVO response should be performed with the AVO-sensitive semblance operator. While it may be possible to reconstruct the NMO ellipse by applying conventional semblance to a truncated gather (mostly for type 1 AVO), accurate estimation of the η-parameters requires application of AK semblance. Note that in combination with the symmetry-plane NMO velocities, the parameters $\eta^{(1,2,3)}$ control time processing and geometrical spreading of P-wave data in orthorhombic media.

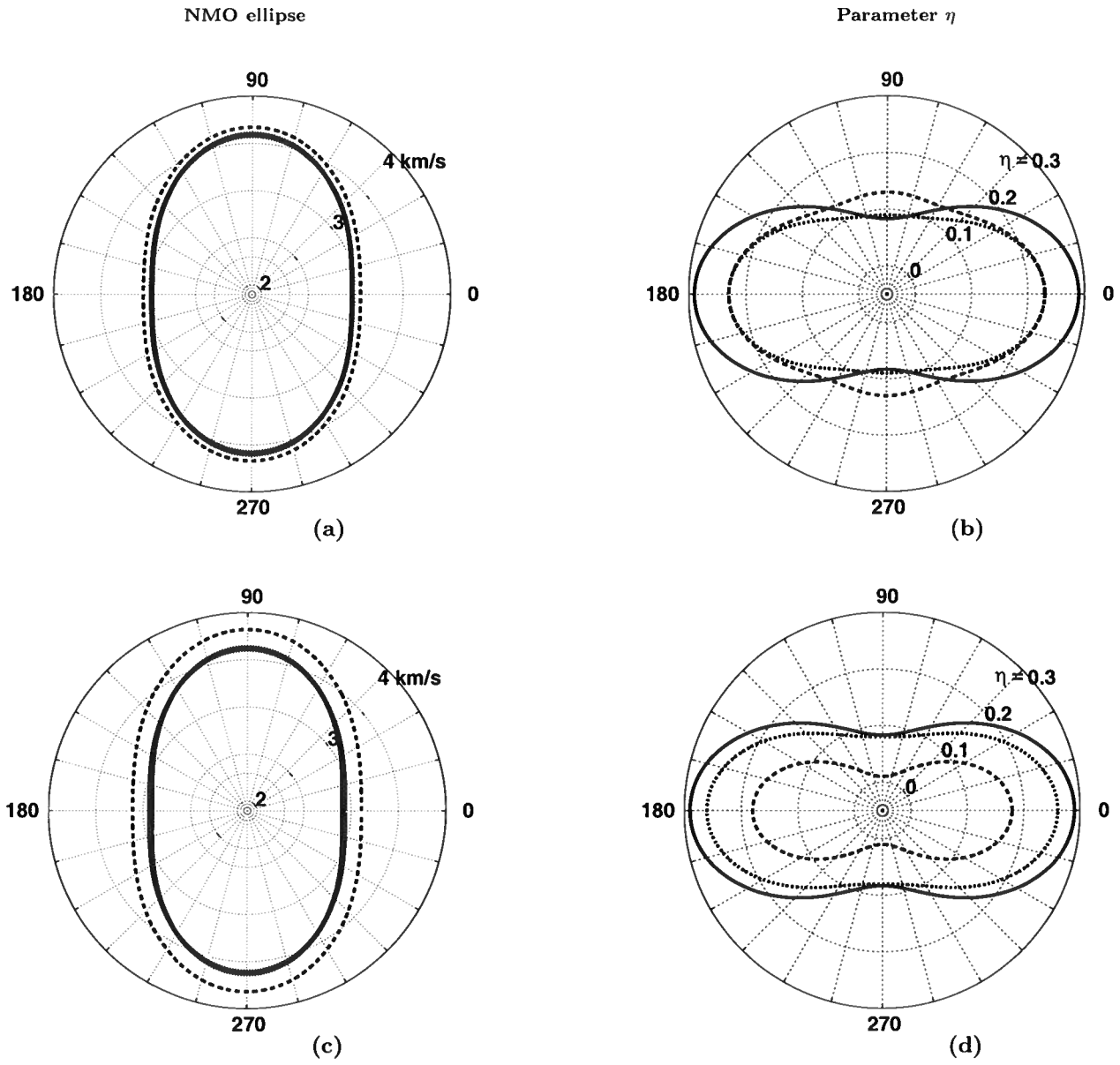

Figure 10. Moveout-inversion results for a wide-azimuth, long-offset P-wave reflection from an orthorhombic/isotropic interface (Table 5). The event has a type 1 AVO response with the polarity reversal at offsets between $x/h = 1$ and $x/h = 1.5$. (a) and (c) are the NMO ellipses; (b) and (d) are the azimuthally-dependent η values. The maximum offset-to-depth ratio is two for the top row, and three for the bottom row. The solid lines are the actual NMO ellipses and η-curves, the dashed lines are estimated by the conventional semblance algorithm, and the dotted lines by AK semblance. As in Figure 6, the dotted lines in plots (a,c) are almost invisible.

6 ACKNOWLEDGMENTS

We are grateful to the A(nisotropy)-Team of the Center for Wave Phenomena (CWP), Colorado School of Mines (CSM), for helpful discussions. We would like to thank Debashish Sarkar (GX Technology) and Ivan Vasconcelos (CSM) for providing their codes, which were critically important for the success of this study. This work was supported by the Consortium Project on Seismic Inverse Methods for Complex Structures at CWP and by the Chemical Sciences, Geosciences and Biosciences Division, Office of Basic Energy Sciences, Office of Science, U.S. Department of Energy.

REFERENCES

Alkalifah, T., and I. Tsvankin, 1995, Velocity analysis for transversely isotropic media: Geophysics, **60**, 1550–1566.

Bakulin, A., V. Grechka, and I. Tsvankin, 2000, Estimation of fracture parameters from reflection seismic data – Part II: Fractured models with orthorhombic symmetry: Geophysics, **65**, 1803–1817.

Gajewski, D., and I. Pšenčík, 1987, Computation of high frequency seismic wavefields in 3-D laterally inhomogeneous anisotropic media: Geophysical Journal of the Royal Astronomical Society, **91**, 383–412.

Grechka, V., and M. Kachanov, 2006, Seismic characterization of multiple fracture sets: Does orthotropy suffice? Geophysics, **71**, D93–D105.

Kim, K. Y., K. H. Wrolstad, and F. Aminzadeh, 1993, Effects of transverse isotropy on P-wave AVO for gas sands: Geophysics, **58**, 883–888.

Landrø, M., and I. Tsvankin, 2007, Seismic critical-angle reflectometry: A method to characterize azimuthal anisotropy?: Geophysics, in print.

Pech, A., and I. Tsvankin, 2004, Quartic moveout coefficient for a dipping azimuthally anisotropic layer: Geophysics, **69**, 699–707.

Press, W. H., S. A. Teukolsky, W. T. Vetterling, and B. P. Flannery, 1992, Numerical Recipes in C: The art of scientific computing: Cambridge University Press.

Rüger, A., 2001, Reflection coefficients and azimuthal AVO analysis in anisotropic media: Society of Exploration Geophysicists.

Rutherford, S., and R. Williams, 1989, Amplitude-versus-offset variations in gas sands: Geophysics, **54**, 680–688.

Sarkar, D., R. T. Baumel, and K. Larner, 2002, Velocity analysis in the presence of amplitude variation: Geophysics, **67**, 1664–1672.

Sarkar, D., J. P. Castagna, and W. Lamb, 2001, AVO and velocity analysis: Geophysics, **66**, 1284–1293.

Schoenberg M. and K. Helbig, 1997, Orthorhombic media: Modeling elastic wave behavior in a vertically fractured earth: Geophysics, **62**, 1954–1974.

Shuey, R. T, 1985, A simplification of the Zoeppritz equations: Geophysics, **50**, 609–614.

Taner, M. T., and F. Koehler, 1969, Velocity spectra – digital computer derivation and applications of velocity functions: Geophysics, **34**, 859–881.

Thomsen, L., 1986, Weak elastic anisotropy: Geophysics, **51**, 1954–1966.

Tsvankin, I., 1997, Anisotropic parameters and P-wave velocity for orthorhombic media: Geophysics, **62**, 1292–1309.

Tsvankin, I., 2005, Seismic signatures and analysis of reflection data in anisotropic media, 2nd edition: Elsevier Science Publ. Co., Inc.

Tsvankin, I., and L. Thomsen, 1994, Nonhyperbolic reflection moveout in anisotropic media: Geophysics, **59**, 1290–1304.

Vasconcelos, I., and I. Tsvankin, 2006, Non-hyperbolic moveout inversion of wide-azimuth P-wave data for orthorhombic media: Geophysical Prospecting, **54**, 535–552.

Xu, X., and I. Tsvankin, 2006a, Anisotropic geometrical-spreading correction for wide-azimuth P-wave reflections: Geophysics, **71**, D161–D170.

Xu, X., and I. Tsvankin, 2006b, Azimuthal AVO analysis with anisotropic spreading correction: A synthetic study: The Leading Edge, **24**, 1336–1342.

Zhu, Y., and I. Tsvankin, 2006, Plane-wave propagation in attenuative transversely isotropic media: Geophysics, **71**, T17–T30.

APPENDIX A: THE 2D AND 3D AK SEMBLANCE OPERATORS

A1 AK semblance in 2D

Conventional semblance operators are based on summation of trace amplitudes along moveout curves (which usually are hyperbolic) within a certain time window. The idea of amplitude-sensitive semblance is to replace this summation with data *modeling* using a moveout equation in combination with an amplitude function $M(t_1, x)$, where t_1 is the zero-offset time and x is the source-receiver offset. The amplitude function for AK semblance is specified as (Sarkar et al., 2002)

$$M_x(t_1) = A(t_1)\left(1 + K\sin^2\theta_x\right), \tag{A1}$$

where $A(t_1)$ is the AVO intercept, K is the ratio of AVO gradient and intercept (K is kept constant inside the semblance window), and θ_x is the incidence angle at offset x approximately given by

$$\sin^2\theta_x = \frac{x^2}{x^2 + V_{\rm nmo}^2 t_0^2}. \tag{A2}$$

Here, $V_{\rm nmo}$ is the NMO velocity and t_0 is the zero-offset time at the center of the semblance window.

Following Sarkar et al. (2002), we define the 2D AK semblance operator as

$$S_G(t_0) = 1 - \frac{\sum_{t_1}\sum_{x}\left[A(t_1)\left(1 + K\sin^2\theta_x\right) - D_V(t_1, x)\right]^2}{\sum_{t_1}\sum_{x} D_V^2(t_1, x)}, \tag{A3}$$

where $D_V = D_V(t_1, x)$ is the moveout-corrected data at the zero-offset time t_1; the summation is carried out over all offsets x and all time samples within the semblance window centered at t_0. The subscript "V" denotes the trial NMO velocity $V_{\rm nmo}$ used by Sarkar et al. (2002) to perform the conventional hyperbolic moveout correction. In our algorithm, the data are modeled using a nonhyperbolic moveout equation parameterized by $V_{\rm nmo}$ and the anellipticity coefficient η (see the main text).

The value of the AVO intercept that corresponds to the maximum of the generalized semblance function can

be found by setting to zero the derivative of equation A3 with respect to $A(t_1)$:

$$A(t_1) = \frac{\sum_x \left[D_V(t_1,x)\ (1 + K\sin^2\theta_x)\right]}{\sum_x (1 + K\sin^2\theta_x)^2}. \quad \text{(A4)}$$

Substituting $A(t_1)$ from equation A4 into equation A3 yields

$$S_G(t_0) = \frac{\sum_{t_1}\left[\sum_x D_V(t_1,x)\ (1 + K\sin^2\theta_x)\right]^2}{\sum_x (1 + K\sin^2\theta_x)^2 \sum_{t_1}\sum_x D_V^2(t_1,x)}. \quad \text{(A5)}$$

Similarly, next we differentiate S_G (equation A5) with respect to K and set the derivative to zero:

$$\alpha K^2 - \beta K + \gamma = 0, \quad \text{(A6)}$$

where

$$\begin{aligned}\alpha &= \sum_x \sin^2\theta_x \sum_{t_1}\left(\sum_x D_V(t_1,x)\sin^2\theta_x\right)^2 \\ &- \sum_x \sin^2\theta_x \\ &\times \sum_{t_1}\left[\sum_x D_V(t_1,x)\sum_x \left(D_V(t_1,x)\sin^2\theta_x\right)\right],\end{aligned} \quad \text{(A7)}$$

$$\begin{aligned}\beta &= \sum_x \sin^2\theta_x \sum_{t_1}\left(\sum_x D_V(t_1,x)\right)^2 \\ &- N\sum_{t_1}\left(\sum_x D_V(t_1,x)\sin^2\theta_x\right)^2,\end{aligned} \quad \text{(A8)}$$

$$\begin{aligned}\gamma &= N\sum_{t_1}\left[\sum_x D_V(t_1,x)\sum_x \left(D_V(t_1,x)\sin^2\theta_x\right)\right] \\ &- \sum_x \sin^2\theta_x \sum_{t_1}\left(\sum_x D_V(t_1,x)\right)^2.\end{aligned} \quad \text{(A9)}$$

The solution of the quadratic equation A6 that always maximizes the semblance for both positive and negative values of α is (Sarkar et al., 2002)

$$K = \frac{\beta - \sqrt{\beta^2 - 4\alpha\gamma}}{2\alpha}. \quad \text{(A10)}$$

Substituting K from equation A10 into equation A5, we obtain the 2D generalized semblance operator that depends only on the parameters of the moveout function.

A2 AK semblance in 3D

Here, the AK semblance operator is extended to long-offset 3D data collected into common-midpoint (CMP) gathers with a wide range of source-receiver azimuths. The 3D AK semblance is computed from equation A3 where the summation is performed not only over all offsets, but also over all azimuths α. Setting the derivative of $S_G(t_0)$ with respect to A_1 to zero, we obtain the generalized 3D semblance in a form similar to equation A5:

$$\begin{aligned}&S_G(t_0) \\ &= \frac{\sum_{t_1}\left[\sum_x\sum_\alpha D_V(t_1,x,\alpha)\ (1 + K(\alpha)\sin^2\theta_x)\right]^2}{\sum_x\sum_\alpha (1 + K(\alpha)\sin^2\theta_x)^2 \sum_{t_1}\sum_x\sum_\alpha D_V^2(t_1,x,\alpha)}.\end{aligned} \quad \text{(A11)}$$

The incidence angle θ_x is expressed through offset using equation A2. As discussed in the main text, the function $K(\alpha)$ is based on the azimuthal dependence of the AVO gradient in orthorhombic media:

$$K(\alpha) = K^{(2)}\cos^2\alpha + K^{(1)}\sin^2\alpha, \quad \text{(A12)}$$

where the azimuth α is defined with respect to the $[x_1, x_3]$ symmetry plane.

Since in the 3D case it is difficult to obtain the best-fit values of $K^{(1)}$ and $K^{(2)}$ analytically, they are estimated from the semblance scan using equation A11. For orthorhombic media, we employ a nonhyperbolic moveout equation parameterized by the azimuth of the $[x_1, x_3]$ symmetry plane, the NMO velocities $V_{\text{nmo}}^{(1)}$ and $V_{\text{nmo}}^{(2)}$, and the anellipticity coefficients $\eta^{(1)}$, $\eta^{(2)}$, and $\eta^{(3)}$. Therefore, semblance scanning is performed over a total of eight independent parameters. The semblance algorithm, which is based on the 3D nonhyperbolic moveout inversion technique of Vasconcelos and Tsvankin (2006), is described in more detail in the main text.

CWP-555P

Retrieving the Green's function of the diffusion equation from the response to a random forcing

Roel Snieder
Center for Wave Phenomena and Department of Geophysics, Colorado School of Mines, Golden CO 80401

ABSTRACT
It is known that the Green's function for non-dissipative acoustic or elastic wave propagation can be extracted by correlating noise recorded at different receivers. This property is often related to the invariance for time-reversal of the acoustic or elastic wave equations. The diffusion equation is not invariant for time-reversal. It is shown in this work that the Green's function of the diffusion equation can also be retrieved by correlating solutions of the diffusion equation that are excited randomly and are recorded at different locations. This property can be used to retrieve the Green's function for diffusive systems from ambient fluctuations. Potential applications include the fluid pressure in porous media, electromagnetic fields in conducting media, the diffusive transport of contaminants, and the intensity of multiply scattered waves.

Key words: interferometry, diffusion, pore pressure, EM

1 INTRODUCTION

The Green's function for acoustic or elastic waves can be extracted by cross-correlating recorded waves that are excited by a random excitation, see ref. (Curtis *et al.*, 2006) for a tutorial. Derivations of this principle have been presented based on normal modes (Lobkis & Weaver, 2001), on representation theorems (Wapenaar, 2004; Weaver & Lobkis, 2004; Wapenaar *et al.*, 2005), on time-reversal invariance (Derode *et al.*, 2003a; Derode *et al.*, 2003b), and on the principle of stationary phase (Snieder, 2004; Roux *et al.*, 2005a; Snieder *et al.*, 2006b). This technique has found applications in ultrasound (Weaver & Lobkis, 2001; Malcolm *et al.*, 2004; Larose *et al.*, 2006), crustal seismology (Campillo & Paul, 2003; Shapiro *et al.*, 2005; Roux *et al.*, 2005b; Sabra *et al.*, 2005a; Sabra *et al.*, 2005b), exploration seismology (Calvert *et al.*, 2004; Bakulin & Calvert, 2004), structural engineering (Snieder & Şafak, 2006; Snieder *et al.*, 2006a), and numerical modeling (van Manen *et al.*, 2005). Recntly the exraction of the Green's function by cross-correlation has been derived for general coupled systems of linear equations (Wapenaar *et al.*, 2006).

The principle of extracting the Green's function of a system from ambient fluctuations creates the possibility to retrieve the impulse response of a system without using controlled point sources. This impulse response can be used for imaging, tomography, or other methods to determine the properties of the medium. For example, models of the crust in California have been constructed using surface wave tomography based on microseismic noise (Shapiro *et al.*, 2005; Sabra *et al.*, 2005b). The autocorrelation of ambient seismic noise has been used for daily monitoring fault zones (Wegler & Sens-Schönfelder, 2006) and volcanoes (Sens-Schönfelder & Wegler, 2006). The Green's function extracted from ambient noise can also be used to model the response of a system to a prescribed excitation without knowing the in-situ properties of the system.

The extraction of the Green's function from ambient noise has been described extensively for wave propagation of acoustic or elastic waves without intrinsic attenuation (e.g., (Curtis *et al.*, 2006)-(Snieder *et al.*, 2006b)). In the absence of intrinsic attenuation, the wave equation is invariant for time-reversal, and several derivations of the reconstruction of the Green's function are indeed based on time-reversal invariance (Derode *et al.*, 2003a; Derode *et al.*, 2003b; Bakulin & Calvert, 2004).

Many physical systems are not invariant under time-reversal. Intrinsic attenuation breaks the symme-

try for time-reversal for acoustic and elastic wave propagation. Electrical conductivity breaks the time-reversal symmetry of Maxwell's equations. It has been shown theoretically (@warning Citation 'Snieder06Atten' on page 141 undefined) and observationally (Snieder & Şafak, 2006; Snieder *et al.*, 2006a) that the impulse response of attenuating acoustic or elastic waves can be retrieved from ambient fluctuations.

Time-reversal invariance is, however, not essential for retrieving the Green's function from ambient noise. This can be seen by considering the diffusion equation

$$\frac{\partial p(\mathbf{r},t)}{\partial t} = \nabla \cdot (D(\mathbf{r}) \nabla p(\mathbf{r},t)) + q(\mathbf{r},t) \; , \tag{1}$$

where the diffusion constant D may depend on position $\mathbf{r}$. The diffusion equation is not invariant for time reversal because the operation $t \rightarrow -t$ changes the sign of the first term. This equation is of practical importance because it describes conductive heat transport, diffusive transport of tracers and contaminants, fluid flow in porous media (Wang, 2000), electromagnetic waves in conducting media (Jackson, 1975), and the energy transport of multiply scattered waves, e.g., (Sheng, 1995).

The derivation in this work is applicable to the frequency domain, and the following Fourier convention is used: $p(\mathbf{r},t) = \int p(\mathbf{r},\omega) \exp(-i\omega t) d\omega$. With this convention, the diffusion equation is, in the frequency domain, given by

$$i\omega p(\mathbf{r},\omega) + \nabla \cdot (D(\mathbf{r}) \nabla p(\mathbf{r},\omega)) = -q(\mathbf{r},\omega) \; . \tag{2}$$

Time-reversal corresponds, in the frequency domain, to complex conjugation. The time-reversed diffusion equation is thus given by

$$-i\omega p^*(\mathbf{r},\omega) + \nabla \cdot (D(\mathbf{r}) \nabla p^*(\mathbf{r},\omega)) = -q^*(\mathbf{r},\omega) \; , \tag{3}$$

where the asterisk denotes complex conjugation. The sign difference in the first terms of expressions (2) and (3) is due to the lack of time-reversal invariance of the diffusion equation.

It is shown here that the Green's function for the diffusion equation can be retrieved by correlating noise recorded at several locations in a diffusive system. One application of this technique is monitoring flow in porous media, we therefore refer to the solution of the diffusion equation as *pressure*, but the results are equally valid for other diffusive systems. In the following all expressions are given in the frequency domain, and the frequency-dependence is not shown explicitly.

2 REPRESENTATION THEOREMS OF THE CONVOLUTION AND CORRELATION TYPE

Following Fokkema and van den Berg (Fokkema & van den Berg, 1993; Fokkema & van den Berg, 1996), we consider representation theorems of the convolution and correlation types by using expressions (2) and (3) for two solutions p_A and p_B with source terms q_A and q_B, respectively. The representation theorem of the convolution type is obtained by computing $\int (p_B(\text{eq. } 2)_A - p_A(\text{eq. } 2)_B) \, dV$, where $(\text{eq. } 2)_A$ denotes equation (2) for state A, and where $\int (\cdots) \, dV$ denotes an integration over a volume V. This gives

$$\int \left(p_B \nabla \cdot (D \nabla p_A) - p_A \nabla \cdot (D \nabla p_B) \right) dV = \int (p_A q_B - p_B q_A) \, dV \; . \tag{4}$$

Note that in the subtraction the $i\omega p$-terms cancel. Applying an integration by parts to the left hand side of expression (4), and using Gauss's theorem gives

$$\oint D \left(p_B \nabla p_A - p_A \nabla p_B \right) \cdot d\mathbf{S} = \int (p_A q_B - p_B q_A) \, dV \; , \tag{5}$$

where the integral $\oint (\cdots) \cdot d\mathbf{S}$ is over the surface that bounds the volume V.

A representation theorem of the correlation type can be obtained by evaluating $\int (p_B^*(\text{eq. } 2)_A - p_A(\text{eq. } 3)_B) \, dV$. Carrying out an integration by parts gives

$$\oint D \left(p_B^* \nabla p_A - p_A \nabla p_B^* \right) \cdot d\mathbf{S} + 2i\omega \int p_A p_B^* dV = \int (p_A q_B^* - p_B^* q_A) \, dV \; . \tag{6}$$

Note that now the $i\omega$-terms in expression (2) and (3) and do not cancel, but combine to give the volume integral in the left hand side. The presence of this term results from the lack of invariance of time-reversal of the diffusion equation.

In the following integration over all space is used. The contribution of the surface integral vanishes because the solution of the diffusion equation $p(\mathbf{r},\omega)$ vanishes exponentially as $r \rightarrow \infty$. Therefore, the representation theorems (5) and (6) reduce to

$$\int (p_A q_B - p_B q_A) \, dV = 0 \; , \tag{7}$$

and

$$\int (p_A q_B^* - p_B^* q_A) \, dV = 2i\omega \int p_A p_B^* dV \; . \tag{8}$$

The contribution of the surface integral also vanishes for a finite volume in case the solution satisfies either Dirichlet conditions ($p = 0$), Neumann conditions ($\partial p / \partial n = 0$), or mixed boundary conditions ($\partial p / \partial n + ap = 0$) at the surface that bounds the volume.

3 REPRESENTATION THEOREMS AND GREEN'S FUNCTIONS

The Green's function for the diffusion equation is the solution to equation (2) when the forcing is a delta function:

$$i\omega G(\mathbf{r},\mathbf{r}_0) + \nabla\cdot(D(\mathbf{r})\nabla G(\mathbf{r},\mathbf{r}_0)) = -\delta(\mathbf{r}-\mathbf{r}_0)\ . \qquad (9)$$

Setting $q_A(\mathbf{r}) = \delta(\mathbf{r}-\mathbf{r}_0)$ in expression (7) implies that $p_A(\mathbf{r}) = G(\mathbf{r},\mathbf{r}_0)$. For this choice of q_A, expression (7) reduces to

$$p(\mathbf{r}) = \int G(\mathbf{r},\mathbf{r}_0)q(\mathbf{r}_0)dV_0\ , \qquad (10)$$

where the subscripts B are dropped. Alternatively, setting

$$q_{A,B}(\mathbf{r}) = \delta(\mathbf{r}-\mathbf{r}_{A,B}) \qquad (11)$$

implies that

$$p_{A,B}(\mathbf{r}) = G(\mathbf{r},\mathbf{r}_{A,B})\ . \qquad (12)$$

For this choice of the states A and B, expression (7) reduces to the reciprocity relation:

$$G(\mathbf{r}_B,\mathbf{r}_A) = G(\mathbf{r}_A,\mathbf{r}_B)\ . \qquad (13)$$

Inserting the states (12) into expression (8) gives

$$G(\mathbf{r}_B,\mathbf{r}_A) - G^*(\mathbf{r}_A,\mathbf{r}_B) = 2i\omega\int G(\mathbf{r},\mathbf{r}_A)G^*(\mathbf{r},\mathbf{r}_B)dV\ . \qquad (14)$$

Using reciprocity, this expression can also be written as

$$G(\mathbf{r}_A,\mathbf{r}_B,\omega) - G^*(\mathbf{r}_A,\mathbf{r}_B,\omega) = 2i\omega\int G(\mathbf{r}_A,\mathbf{r},\omega)G^*(\mathbf{r}_B,\mathbf{r},\omega)dV\ . \qquad (15)$$

The left hand side of this expression corresponds, in the time-domain, to the superposition of the Green's function and the time-reversed Green's function. In the following section we consider how this superposition can be retrieved from the cross-correlation of the pressure generated by uncorrelated sources.

4 RETRIEVING THE GREEN'S FUNCTION

In order to show how the Green's function can be extracted from the correlation of solutions generated by random sources, let us consider spatially uncorrelated sources with power spectrum $|q(\omega)|^2$ that does not depend on location:

$$\langle q(\mathbf{r}_1,\omega)q^*(\mathbf{r}_2,\omega)\rangle = \delta(\mathbf{r}_1-\mathbf{r}_2)\,|q(\omega)|^2\ , \qquad (16)$$

where the brackets $\langle\cdots\rangle$ denote the expectation value. In practical applications this expectation value is usually replaced by using several non-overlapping time windows (e.g., (Shapiro & Campillo, 2004; Sens-Schönfelder & Wegler, 2006)). Multiplying equation (15) with $|q(\omega)|^2$, the volume integral in that expression can be written as

$$\begin{aligned}
&|q(\omega)|^2\int G(\mathbf{r}_A,\mathbf{r})G^*(\mathbf{r}_B,\mathbf{r})dV\\
&= \int G(\mathbf{r}_A,\mathbf{r}_1)\delta(\mathbf{r}_1-\mathbf{r}_2)\,|q(\omega)|^2\,G^*(\mathbf{r}_B,\mathbf{r}_2)dV_1dV_2\\
&= \int G(\mathbf{r}_A,\mathbf{r}_1)\langle q(\mathbf{r}_1,\omega)q^*(\mathbf{r}_2,\omega)\rangle G^*(\mathbf{r}_B,\mathbf{r}_2)dV_1dV_2\\
&= \langle\left(\int G(\mathbf{r}_A,\mathbf{r}_1)q(\mathbf{r}_1,\omega)dV_1\right)\left(\int G(\mathbf{r}_B,\mathbf{r}_2)q(\mathbf{r}_2,\omega)dV_2\right)^*\rangle\ .
\end{aligned} \qquad (17)$$

When we use this result and expression (10), equation (15) after multiplication with $|q(\omega)|^2$ is given by

$$\begin{aligned}
&(G(\mathbf{r}_A,\mathbf{r}_B,\omega) - G^*(\mathbf{r}_A,\mathbf{r}_B,\omega))\,|q(\omega)|^2\\
&\qquad = 2i\omega\langle p(\mathbf{r}_A,\omega)p^*(\mathbf{r}_B,\omega)\rangle\ ,
\end{aligned} \qquad (18)$$

where $p(\mathbf{r},\omega)$ is the pressure at location $\mathbf{r}$ due to the random forcing $q(\mathbf{r},\omega)$.

Equation (18) states that the superposition of the Green's function $G(\mathbf{r}_A,\mathbf{r}_B,\omega)$ and its time-reversed version is, after multiplication with the power spectrum of the excitation, equal to the correlation of the random fields at locations $\mathbf{r}_A$ and $\mathbf{r}_B$, respectively. The pre-factor $2i\omega$ corresponds, in the time domain, with $-2d/dt$. Since multiplication in the frequency domain corresponds, in the time domain to convolution, expression (19) is, in the time domain, given by

$$\begin{aligned}
&(G(\mathbf{r}_B,\mathbf{r}_A,t) - G(\mathbf{r}_B,\mathbf{r}_A,-t)) * C_q(t)\\
&\qquad = -2\frac{d}{dt}\langle p(\mathbf{r}_A,t)\otimes p(\mathbf{r}_B,t)\rangle
\end{aligned} \qquad (19)$$

where $*$ denotes convolution, $\otimes$ denotes correlation, and $C_q(t)$ is the autocorrelation of $q(t)$.

5 DISCUSSION

The Green's function of the diffusion equation can be retrieved by cross-correlating measurements of a diffusive system that is excited by random noise. Since the diffusion equation is not invariant for time-reversal, this shows that invariance for time-reversal is not essential for the retrieval of the Green's function by cross-correlation.

For elastic and acoustic waves, the Green's function can be extracted from waves that are excited randomly at the surface that surrounds the volume (Wapenaar, 2004; Wapenaar *et al.*, 2005). This is not the case for the diffusion equation. For a volume of radius R, the surface area grows with R^2, but for a homogeneous medium the solution of the diffusion equation varies

with the radius as $R^{-1}\exp(-\sqrt{\omega/2D}R)$. The contribution of the surface integral therefore depends on the radius of the volume, and the derivation shown here holds for an infinite volume ($R \rightarrow \infty$), or for a finite volume when Dirichlet, Neumann, or mixed boundary conditions hold at the surface that bounds the volume. In contrast to the retrieval of the Green's function for non-attenuating acoustic or elastic waves, where one needs random sources on a surface that bounds the volume, one needs random sources throughout the volume for the retrieval of the Green's function for the diffusion equation.

The theory presented here provides an example that time-reversal invariance is not required for the extraction of the Green's function from ambient fluctuations. The diffusion equation governs physical systems of practical importance, and the derivation presented here makes it possible to retrieve the impulse response of diffusive systems from measured fluctuations.

In this work the phrase *pressure* is used for the solution of the diffusion equation because the pore-pressure in a porous medium follows the diffusion equation. The theory of this work makes it possible to retrieve the Green's function for fluid flow in an aquifer or hydrocarbon reservoir from recorded pressure fluctuations. This Green's function can be used to estimate parameters such as hydraulic conductivity, and it can be used to model the fluid transport in the subsurface without explicit knowledge of the in-situ hydraulic conductivity. Similarly, the impulse response for the diffusive transport of contaminants can be retrieved from observations of ambient fluctuations in the concentration. The Green's function thus obtained can then be used to predict the diffusive transport of a localized release of the contaminant.

Electromagnetic fields in a conducting media satisfy the diffusion equation. This has been used in the magnetotelluric method where the ambient fluctuations in the electric and magnetic fields observed at one location are used to determine the electrical conductivity (Weidelt, 1972). The theory presented here makes it possible to retrieve the Green's function for electromagnetic fields for non-coincident points from observed electromagnetic fluctuations.

The intensity of multiply scattered waves satisfies, for late times, the diffusion equation. Controlled intensity fluctuations of multiply scattered waves have been used to create images of the spatial distribution of the diffusion constant. This has found application in medical imaging, e.g., (Yodh & Chance, 1995). Instead of using controlled, spatially localized, sources for the intensity of scattered waves, one may use the theory of this work to use random spatially distributed sources instead.

As always, the application of the theory to these, and other, applications faces implementation issues. The assumption that the sources of the ambient fluctuations have a homogeneous spatial distribution may not be satisfied in practical applications. For applications where this condition is satisfied, the theory can be used to extract the impulse response of diffusive systems without using a controlled, localized, source.

Acknowledgments: I appreciate the comments of Ken Larner. This research was supported by the Gamechanger Program of Shell International Exploration and Production Inc.

Note: This paper has been accepted for publication in Phys. Rev. E, PACS: 43.20.+g, 05.40.Ca, 82.56.Lz

REFERENCES

Bakulin, A., & Calvert, R. 2004. Virtual source: new method for imaging and 4D below complex overburden. *Expanded abstracts of the 2004 SEG-meeting*, 2477–2480.

Calvert, R.W., Bakulin, A., & Jones, T.C. 2004. Virtual sources, a new way to remove overburden problems. *Expanded abstracts of the 2004 EAGE-meeting.*

Campillo, M., & Paul, A. 2003. Long-range correlations in the diffuse seismic coda. *Science*, **299**, 547–549.

Curtis, A., Gerstoft, P., Sato, H., Snieder, R., & Wapenaar, K. 2006. Seismic interferometry – turning noise into signal. *The Leading Edge*, **25**, 1082–1092.

Derode, A., Larose, E., Campillo, M., & Fink, M. 2003a. How to estimate the Green's function for a heterogeneous medium between two passive sensors? Application to acoustic waves. *Appl. Phys. Lett.*, **83**, 3054–3056.

Derode, A., Larose, E., Tanter, M., de Rosny, J., Tourin, A., Campillo, M., & Fink, M. 2003b. Recovering the Green's function from far-field correlations in an open scattering medium. *J. Acoust. Soc. Am.*, **113**, 2973–2976.

Fokkema, J.T., & van den Berg, P.M. 1993. *Seismic applications of acoustic reciprocity.* Amsterdam: Elsevier.

Fokkema, J.T., & van den Berg, P.M. 1996. 4D Geophysical monitoring as an application of the reciprocity theorem. *Pages 99–108 of:* van den Berg, P.M., Blok, H., & Fokkema, J.T. (eds), *Wavefields and reciprocity.* Delft: Delft University Press.

Jackson, J.D. 1975. *Classical electrodynamics.* 2nd edn. New York: John Wiley.

Larose, E., Montaldo, G., Derode, A., & Campillo, M. 2006. Passive imaging of localized reflectors and interfaces in open media. *Appl. Phys. Lett.*, **88**, 104103.

Lobkis, O.I., & Weaver, R.L. 2001. On the emergence of the Green's function in the correlations of a diffuse field. *J. Acoust. Soc. Am.*, **110**, 3011–3017.

Malcolm, A., Scales, J., & van Tiggelen, B.A. 2004. Extracting the Green's function from diffuse, equipartitioned waves. *Phys. Rev. E*, **70**, 015601.

Roux, P., Sabra, K.G., Kuperman, W.A., & Roux, A. 2005a. Ambient noise cross correlation in free space: Theoretical approach. *J. Acoust. Soc. Am.*, **117**, 79–84.

Roux, P., Sabra, K.G., Gerstoft, P., & Kuperman, W.A. 2005b. P-waves from cross correlation of seismic noise. *Geophys. Res. Lett.*, **32**, L19303, doi: 10.1029/2005GL023803.

Sabra, K.G., Gerstoft, P., Roux, P., Kuperman, W.A., & Fehler, M.C. 2005a. Extracting time-domain Green's function estimates from ambient seismic noise. *Geophys. Res. Lett.*, **32**, L03310, doi: 10.1029/2004GL021862.

Sabra, K.G., Gerstoft, P., Roux, P., Kuperman, W.A., & Fehler, M.C. 2005b. Surface wave tomography from microseisms in Southern California. *Geophys. Res. Lett.*, **32**, L14311, doi:10.1029/2005GL023155.

Sens-Schönfelder, C., & Wegler, U. 2006. Passive image interferometry and seasonal variations at Merapi volcano, Indonesia. *Geophys. Res. Lett.*, **33**, L21302, doi:10.1029/2006GL027797.

Shapiro, N.M., & Campillo, M. 2004. Emergence of broadband Rayleigh waves from correlations of the ambient seismic noise. *Geophys. Res. Lett.*, **31**, L07614, doi10.1029/2004GL019491.

Shapiro, N.M., Campillo, M., Stehly, L., & Ritzwoller, M.H. 2005. High-resolution surface-wave tomography from ambient seismic noise. *Science*, **307**, 1615–1618.

Sheng, P. 1995. *Introduction to Wave Scattering, Localization, and Mesoscopic Phenomena.* San Diego: Academic Press.

Snieder, R. 2004. Extracting the Green's function from the correlation of coda waves: A derivation based on stationary phase. *Phys. Rev. E*, **69**, 046610.

Snieder, R., & Şafak, E. 2006. Extracting the building response using seismic interferometry; theory and application to the Millikan Library in Pasadena, California. *Bull. Seismol. Soc. Am.*, **96**, 586–598.

Snieder, R., Sheiman, J., & Calvert, R. 2006a. Equivalence of the virtual source method and wavefield deconvolution in seismic interferometry. *Phys. Rev. E*, **73**, 066620.

Snieder, R., Wapenaar, K., & Larner, K. 2006b. Spurious multiples in seismic interferometry of primaries. *Geophysics*, **71**, SI111–SI124.

van Manen, D.J., Robertson, J.O.A., & Curtis, A. 2005. Modelling of wave propagation in inhomogeneous media. *Phys. Rev. Lett.*, **94**, 164301.

Wang, H.F. 2000. *Theory of linear poroelasticity, with applications to geomechanics and hydrogeology.* Princeton: Princeton Univ. Press.

Wapenaar, K. 2004. Retrieving the elastodynamic Green's function of an arbitrary inhomogeneous medium by cross correlation. *Phys. Rev. Lett.*, **93**, 254301.

Wapenaar, K., Fokkema, J., & Snieder, R. 2005. Retrieving the Green's function by cross-correlation: a comparison of approaches. *J. Acoust. Soc. Am.*, **118**, 2783–2786.

Wapenaar, K., Slob, E., & Snieder, R. 2006. Unified Green's function retrieval by cross-correlation. *Phys. Rev. Lett.*, **97**, 234301.

Weaver, R.L., & Lobkis, O.I. 2001. Ultrasonics without a source: Thermal fluctuation correlations and MHz frequencies. *Phys. Rev. Lett.*, **87**, 134301.

Weaver, R.L., & Lobkis, O.I. 2004. Diffuse fields in open systems and the emergence of the Green's function. *J. Acoust. Soc. Am.*, **116**, 2731–2734.

Wegler, U., & Sens-Schönfelder, C. 2006. Fault zone monitoring with passive image interferometry. *Geophys. J. Int., in press.*

Weidelt, P. 1972. The Inverse Problem of Geomagnetic Induction. *J. Geophys.*, **38**, 257–289.

Yodh, A., & Chance, B. 1995. Spectroscopy and Imaging with Diffusing Light. *Physics Today*, **48**(3), 34–40.

CWP-556

Extracting the Green's function of attenuating heterogeneous acoustic media from uncorrelated waves

Roel Snieder
Center for Wave Phenomena and Department of Geophysics, Colorado School of Mines, Golden CO 80401

ABSTRACT
The Green's function of acoustic or elastic wave propagation can, for loss-less media, be retrieved by correlating the wave field that is excited by random sources and is recorded at two locations. Here the generalization of this idea to attenuating acoustic waves in an inhomogeneous medium is addressed, and it is shown that the Green's function can be retrieved from waves that are excited throughout the volume by spatially uncorrelated injection sources with a power spectrum that is proportional to the local dissipation rate. For a finite volume, one needs both volume sources and sources at the bounding surface for the extraction of the Green's functions. For the special case of a homogeneous attenuating medium defined over a finite volume, the phase and geometrical spreading of the Green's function is correctly retrieved when the volume sources are ignored, but the attenuation is not.

Key words: interferometry, attenuation

1 INTRODUCTION

The extraction of the Green's function by correlating waves excited by random sources that are recorded at two locations has recently received much attention. There are numerous derivations of this principle that are valid for closed systems (Lobkis & Weaver, 2001) and for open systems (e.g., (Derode *et al.*, 2003b; Derode *et al.*, 2003a; Weaver & Lobkis, 2004)). Formulations of this principle are based either on random sources placed throughout a volume (Lobkis & Weaver, 2001; Snieder, 2004) or on sources that are located at a surface (Wapenaar, 2004; Wapenaar *et al.*, 2005; Snieder *et al.*, 2006b). The extraction of the Green's function using random wave fields has been applied to ultrasound (Weaver & Lobkis, 2001; Weaver & Lobkis, 2003; Malcolm *et al.*, 2004; Larose *et al.*, 2006), in seismic exploration (Bakulin & Calvert, 2004; Bakulin & Calvert, 2006; Zhou *et al.*, 2006), in crustal seismology (Campillo & Paul, 2003; Shapiro *et al.*, 2005; Sabra *et al.*, 2005b; Paul *et al.*, 2005), in ocean acoustics (Roux *et al.*, 2004; Sabra *et al.*, 2005a; Sabra *et al.*, 2005c), to buildings (Snieder & Şafak, 2006; Snieder *et al.*, 2006a), and in helioseismology (Rickett & Claerbout, 1999; Rickett & Claerbout, 2000; Rickett & J.F., 2001). The recent supplement of seismic interferometry (Wapenaar *et al.*, 2006a) in Geophysics gives an overview of this field of research. Phrases that include passive imaging, correlation of ambient noise, extraction of the Green's function, and seismic interferometry have been proposed for this line of research. Recently the theory has been developed for the extraction of the Green's function for more general linear systems than acoustic or elastic waves (Wapenaar *et al.*, 2006b; Snieder *et al.*, 2007; Weaver, 2006).

Many derivations of this principle are valid for systems that are invariant under time reversal. Several derivations invoke time-reversal invariance explicitly (Derode *et al.*, 2003b; Derode *et al.*, 2003a; Calvert *et al.*, 2004; Bakulin & Calvert, 2004). For acoustics waves in a flowing medium the time-reversal invariance is broken by the flow; this broken symmetry has been incorporated in the theory for the extraction of the Green's function (Godin, 2006; Wapenaar, 2006). Attenuation also breaks the invariance for time reversal. For homogeneous acoustic media (Snieder, 2004; Roux *et al.*, 2005) and for a homogeneous oceanic waveguide (Sabra *et al.*, 2005a) attenuation has been incorporated into the theory for the extraction of the Green's funciton. Weaver and Lobkis (Weaver & Lobkis, 2004) use

complex frequency as a tool to force convergence on an integral over all sources.

Here I derive the principle of seismic interferometry for general attenuating, acoustic media, and extend earlier formulations for homogeneous media to include arbitrary heterogeneity in density, compressibility, and intrinsic attenuation. In section 2 I introduce the basic equations and re-derive a representation theorem of the correlation type for attenuating media. I show in section 3 that for an unbounded volume, or for a volume that is bounded by a surface where the pressure or normal component of the velocity vanishes, the Green's function can be extracted from waves excited by uncorrelated volume sources with a source strength that is proportional to the local dissipation rate. In section 4 I show that for a bounded volume one needs, in general, both volume sources and surface sources in order to retrieve the correct Green's function. In section 5 I illustrate the relative roles of the volume sources and surface sources by analyzing the special case of a homogeneous, attenuating medium, with a single reflector. In this special case, when volume sources are ignored, the phase and geometrical spreading of the Green's function are correctly reproduced by seismic interferometry, but the attenuation is not.

2 BASIC EQUATION FOR ACOUSTIC WAVES

Using the Fourier convention $f(t) = \int f(\omega) \exp(-i\omega t)\, d\omega$, the pressure p and particle velocity $\mathbf{v}$ for acoustic waves satisfy, in the frequency domain, the following coupled equations:

$$\nabla p - i\omega\rho \mathbf{v} = 0 \,, \tag{1}$$

$$(\nabla \cdot \mathbf{v}) - i\omega\kappa p = q \,. \tag{2}$$

In these expressions ω is the angular frequency, ρ the mass density, and κ the compressibility. All expressions in this work are given in the frequency domain; for brevity I do not denote this frequency-dependence explicitly. I assume that only injection sources q are present. Body forces would render the right hand side of expression (1) nonzero. For attenuating media, the compressibility κ is complex, this quantity can be decomposed in a real and imaginary part:

$$\kappa = \kappa_r(\mathbf{r},\omega) + i\kappa_i(\mathbf{r},\omega) \,. \tag{3}$$

Because of the Kramers-Kronig relation (e.g., (Aki & Richards, 2002; Jackson, 1975)), the real and imaginary part of the compressibility depend on frequency. In contrast to the treatment of de Hoop (de Hoop, 1988), I presume that the mass density is real. In this general derivation the density and compressibility can be arbitrary functions of location and frequency.

Following de Hoop, Fokkema, and van den Berg (de Hoop, 1995; Fokkema & van den Berg, 1993), expressions (1) and (2) can be used to derive a representation theorem of the correlation type. The treatment given here generalizes earlier descriptions of the extraction of the Green's function (Wapenaar *et al.*, 2005; Wapenaar, 2006) to include dissipation. I consider two wave states, labeled A and B, that both satisfy expressions (1) and (2), and that are excited by forcing functions q_A and q_B, respectively. The subscripts A and B indicate the state for each quantity. A representation theorem of the correlation type is obtained by integrating the combination $(1)_A \cdot \mathbf{v}_B^* + (1)_B^* \cdot \mathbf{v}_A + (2)_A p_B^* + (2)_B^* p_A$ over volume, and applying Gauss' theorem. (The asterisk denotes complex conjugation, and $(1)_B^*$ stands, for example, for the complex conjugate of expression (1) for state B.) This gives

$$\oint (p_A \mathbf{v}_B^* + p_B^* \mathbf{v}_A) \cdot d\mathbf{S} = \int (q_B^* p_A + q_A p_B^*)\, dV - i\omega \int (\kappa^* - \kappa)\, p_A p_B^* dV \,, \tag{4}$$

where $\oint (\cdots) \cdot d\mathbf{S}$ denotes the surface integral over the surface that bounds the volume. Note that the last term is due to the attenuation; for loss-less media κ is real, and $\kappa^* - \kappa = 0$. The relative roles of the surface integral in the left hand side and the volume integral in the last term play a crucial role in the following treatment. In the following the "surface" refers to the surface that bounds the volume. In the presence of cavities this surface may consists of disconnected pieces.

These representation theorems can be used to derive several properties of the Green's function $G(\mathbf{r},\mathbf{r}_0)$ that is the pressure response to an injection source $q(\mathbf{r}) = \delta(\mathbf{r}-\mathbf{r}_0)$. Setting

$$q_{A,B}(\mathbf{r}) = \delta(\mathbf{r}-\mathbf{r}_{A,B}) \tag{5}$$

implies that the corresponding pressure states are given by

$$p_{A,B}(\mathbf{r}) = G(\mathbf{r},\mathbf{r}_{A,B}) \,, \tag{6}$$

respectively.

Inserting the excitations (5) into expression (4), and using equation (1) to eliminate the velocity, one obtains

$$G^*(\mathbf{r}_A,\mathbf{r}_B) + G(\mathbf{r}_B,\mathbf{r}_A) = 2\omega \int \kappa_i(\mathbf{r},\omega) G(\mathbf{r},\mathbf{r}_A) G^*(\mathbf{r},\mathbf{r}_B) dV + \oint \frac{1}{i\omega\rho} (G^*(\mathbf{r},\mathbf{r}_B)\nabla G(\mathbf{r},\mathbf{r}_A) - G(\mathbf{r},\mathbf{r}_A)\nabla G^*(\mathbf{r},\mathbf{r}_B)) \cdot d\mathbf{S} \,. \tag{7}$$

For brevity the frequency-dependene of G is suppresed. In the presence of intrinsic attenuation, reciprocity of acoustic waves still holds, hence

$$G(\mathbf{r}_A,\mathbf{r}_B) = G(\mathbf{r}_B,\mathbf{r}_A) \,. \tag{8}$$

Expression (7) can therefore be written as

$$G^*(\mathbf{r}_B,\mathbf{r}_A) + G(\mathbf{r}_B,\mathbf{r}_A)$$
$$= 2\omega \int \kappa_i(\mathbf{r},\omega) G(\mathbf{r}_A,\mathbf{r}) G^*(\mathbf{r}_B,\mathbf{r}) dV + \oint \frac{1}{i\omega\rho}$$
$$(G^*(\mathbf{r}_B,\mathbf{r}) \nabla G(\mathbf{r}_A,\mathbf{r}) - G(\mathbf{r}_A,\mathbf{r}) \nabla G^*(\mathbf{r}_B,\mathbf{r})) \cdot d\mathbf{S} \,. \quad (9)$$

Note that for loss-less media, because of the complex conjugates, the surface integral does not vanish when the system satisfies radiation boundary conditions at the surface. A similar relation has been derived for electromagnetic fields in conducting media (Slob *et al.*, 2006).

The left-hand side of expression (9) is the sum of the causal and acausal Green's functions. Wapenaar *et al.* (Wapenaar *et al.*, 2005) use this expression for loss-less media ($\kappa_i = 0$) to show that the sum of the causal and acausal Green's function can be obtained by cross-correlating the pressure fields that are due to uncorrelated random sources at the surface. The pressure field caused by these sources is transmitted to the points $\mathbf{r}_A$ and $\mathbf{r}_B$ in the interior by the Green's functions in the surface integral in equation (9). For attenuating media ($\kappa_i(\mathbf{r}) \neq 0$), this analysis is complicated by the presence of the volume integral in this expression.

3 INTERFEROMETRY WHEN THE SURFACE INTEGRAL VANISHES

In this section I analyze the special case where the surface integral in expression (9) vanishes. This is the case when one of the following conditions is satisfied:

C1: The volume integration is over all space. For attenuating media the wave field vanishes exponentially at infinity, and the surface integral vanishes.

C2: The pressure vanishes at the surface ($G = 0$).

C3: The normal component of the velocity perpendicular to the surface vanishes at the surface. Because of expression (1) this implies that $\nabla G \cdot d\mathbf{S} = 0$.

When one of the conditions C1-C3 is satisfied, the pressure is related to the excitation by

$$p(\mathbf{r}_0) = \int G(\mathbf{r}_0,\mathbf{r}) q(\mathbf{r}) dV \quad (10)$$

and the representation theorem of the correlation type (9) reduces to

$$G^*(\mathbf{r}_B,\mathbf{r}_A) + G(\mathbf{r}_B,\mathbf{r}_A)$$
$$= 2\omega \int \kappa_i(\mathbf{r},\omega) G(\mathbf{r}_A,\mathbf{r}) G^*(\mathbf{r}_B,\mathbf{r}) dV \,. \quad (11)$$

Consider the situation where random pressure sources are present throughout the volume, and that these sources at different locations are uncorrelated:

$$q(\mathbf{r}_1,\omega) q^*(\mathbf{r}_2,\omega) = \kappa_i(\mathbf{r}_1,\omega) \delta(\mathbf{r}_1 - \mathbf{r}_2) |S(\omega)|^2 \,, \quad (12)$$

where $|S(\omega)|^2$ denotes the power spectrum of the random excitation. The excitation (12) is proportional to $\kappa_i(\mathbf{r},\omega)$, the imaginary part of the compressibility, which in turn is proportional to the local attenuation. This means that the excitation (12) supplies a random excitation of the pressure field that locally compensates for the attenuation. Multiplying expression (11) with $|S(\omega)|^2$ gives

$$(G^*(\mathbf{r}_B,\mathbf{r}_A) + G(\mathbf{r}_B,\mathbf{r}_A)) |S(\omega)|^2$$
$$= 2\omega \int \kappa_i(\mathbf{r},\omega) |S(\omega)|^2 G(\mathbf{r}_A,\mathbf{r}) G^*(\mathbf{r}_B,\mathbf{r}) dV$$
$$= 2\omega \int\int \kappa_i(\mathbf{r}_1,\omega) \delta(\mathbf{r}_1 - \mathbf{r}_2) |S(\omega)|^2$$
$$G(\mathbf{r}_A,\mathbf{r}_1) G^*(\mathbf{r}_B,\mathbf{r}_2) dV_1 dV_2$$
$$= 2\omega \int G(\mathbf{r}_A,\mathbf{r}_1) q(\mathbf{r}_1) dV_1 \left(\int G(\mathbf{r}_B,\mathbf{r}_2) q(\mathbf{r}_2) dV_2 \right)^*$$
$$= 2\omega p(\mathbf{r}_A) p^*(\mathbf{r}_B) \,. \quad (13)$$

Expression (12) is used for the 3rd identity, above, and expression (10) for the last one. The sum of the causal and acausal Green's function thus follows from correlating the pressure fields caused by the random volume sources:

$$G^*(\mathbf{r}_B,\mathbf{r}_A) + G(\mathbf{r}_B,\mathbf{r}_A) = \frac{2\omega}{|S(\omega)|^2} p(\mathbf{r}_A) p^*(\mathbf{r}_B) \,. \quad (14)$$

As in seismic interferometry for loss-less media (Lobkis & Weaver, 2001; Weaver & Lobkis, 2004; Wapenaar *et al.*, 2005), one needs to divide by the power spectrum of the excitation to remove the imprint of this excitation on the recorded pressure $p(\mathbf{r}_A)$ and $p(\mathbf{r}_B)$.

4 WHEN THE SURFACE INTEGRAL IS NONZERO

In practical applications, none of the conditions C1-C3 might be satisfied. This is, in fact, the case in formulations of seismic interferometry where the Green's function is extracted by correlating pressure fields that are excited by uncorrelated sources at the surface that bounds the volume (e.g., (Wapenaar *et al.*, 2005)). In this section I investigate the relative roles of the surface and volume integrals in expression (9). For simplicity, I use, following Wapenaar *et al.* (Wapenaar *et al.*, 2005), that the surface is far from the region of interest and that $\nabla G(\mathbf{r},\mathbf{r}_0) \cdot d\mathbf{S} = ikG(\mathbf{r},\mathbf{r}_0) dS = (i\omega/c) G(\mathbf{r},\mathbf{r}_0) dS$. Inserting this in equation (9) gives

$$G^*(\mathbf{r}_B,\mathbf{r}_A) + G(\mathbf{r}_B,\mathbf{r}_A) = I_V(\mathbf{r}_B,\mathbf{r}_A) + I_S(\mathbf{r}_B,\mathbf{r}_A) \,, \quad (15)$$

where the volume integral $I_V(\mathbf{r}_B,\mathbf{r}_A)$ is given by

$$I_V(\mathbf{r}_B,\mathbf{r}_A) = 2\omega \int \kappa_i(\mathbf{r},\omega) G(\mathbf{r}_A,\mathbf{r}) G^*(\mathbf{r}_B,\mathbf{r}) dV \,, \quad (16)$$

and the surface integral $I_S(\mathbf{r}_B,\mathbf{r}_A)$ by

$$I_S(\mathbf{r}_B,\mathbf{r}_A) = 2 \oint \frac{1}{\rho c} G(\mathbf{r}_A,\mathbf{r}) G^*(\mathbf{r}_B,\mathbf{r}) dS \,. \quad (17)$$

In many applications, the attenuation is weak

($\kappa_i \ll \kappa_r$), and one might think that the volume integral is small compared to the surface integral. This, however, is not the case. Because of the attenuation, the surface integral decreases exponentially with increasing surface area, and goes to zero while the volume integral is finite. According to expression (15) the sum of the volume integral and the surface integral is independent of the size of the volume. This implies that the volume integral and the surface integral are, in general, both needed for the extraction of the Green's function. The stationary phase analysis of section 5 shows that, for the special case of a homogeneous medium, this is indeed the case.

5 STATIONARY PHASE ANALYSIS OF THE SURFACE INTEGRAL AND VOLUME INTEGRAL

To better understand the relative roles of the volume and surface integrals of expressions (16) and (17), I analyze in this section the special case of a homogeneous, attenuating medium, and solve the volume and surface integrals in the stationary phase approximation. For a homogeneous medium, equations (1) and (2) can be combined to give

$$\nabla^2 p + \omega^2 \kappa \rho p = i\omega\rho q \; . \tag{18}$$

The wave number is therefore given by

$$k = \omega\sqrt{\kappa\rho} \; . \tag{19}$$

I consider weak attenuation; in this case the wavenumber is to first order in κ_i/κ_r given by

$$k = \omega\sqrt{\kappa_r\rho}\left(1 + \frac{i\kappa_i}{2\kappa_r}\right) \; . \tag{20}$$

The phase velocity thus is given by

$$c = \frac{\omega}{k_r} = 1/\sqrt{\kappa_r\rho} \; , \tag{21}$$

and the imaginary component of the wave number by

$$k_i = \omega\kappa_i\rho c/2 \; . \tag{22}$$

The Green's function solution for expression (18) is equal to

$$G(R) = -i\omega\rho \exp(-k_i R)\,\frac{e^{ikR}}{4\pi R} \; . \tag{23}$$

The geometry for the stationary phase analysis is shown in figure 1.

I use a coordinate system whose origin is at the midpoint of the receiver positions $\mathbf{r}_A$ and $\mathbf{r}_B$ and whose z-axis points along the receiver line. The distance between these points is denoted by R; hence $\mathbf{r}_A = (0, 0, -R/2)$, and $\mathbf{r}_B = (0, 0, R/2)$. I consider a volume that is bounded by a surface at distance L from the origin. The stationary phase analysis follows the treatment of ref. (Snieder, 2004). The stationary phase point of the integrals in expressions (16) and (17) is located on the z-axis

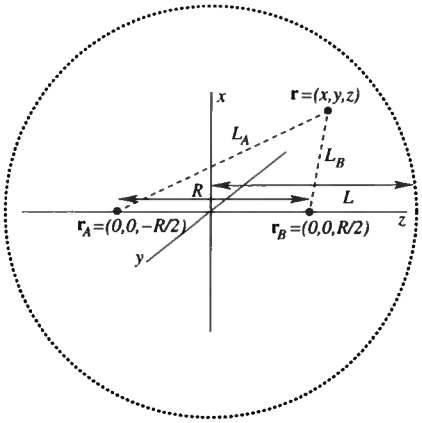

Figure 1. Definition of geometric variables for the stationary phase evaluation of integrals $I_V(\mathbf{r}_B, \mathbf{r}_A)$ and $I_S(\mathbf{r}_B, \mathbf{r}_A)$. The volume is bounded by a sphere with radius L, as denoted by the dotted line.

($x = y = 0$). Following ref. (Snieder, 2004), the points to the right of $\mathbf{r}_B$ (for which $z > R/2$) give the causal Green's function $G(\mathbf{r}_B, \mathbf{r}_A)$, while the points to the left of $\mathbf{r}_A$ (for which $z < -R/2$) give the acausal Green's function $G^*(\mathbf{r}_B, \mathbf{r}_A)$. In the following I only treat the contribution of integration points for which $z > R/2$; this gives only the causal Green's function. Because of this limitation, the corresponding surface and volume integrals are denoted with the superscript $(+)$.

Both the surface and volume integrals contain a double integration over the transverse x- and y-coordinates. As shown in the appendix, the stationary phase approximation of the surface and volume integrals gives

$$I_V^{(+)}(\mathbf{r}_B, \mathbf{r}_A) = -i\omega\rho\left[\exp(-k_i R) - \exp(-2k_i L)\right]\frac{e^{ikR}}{4\pi R} \; , \tag{24}$$

and

$$I_S^{(+)}(\mathbf{r}_B, \mathbf{r}_A) = -i\omega\rho \exp(-2k_i L)\,\frac{e^{ikR}}{4\pi R} \; . \tag{25}$$

The sum of the surface and volume integrals indeed gives the causal Green's function:

$$I_S^{(+)}(\mathbf{r}_B, \mathbf{r}_A) + I_V^{(+)}(\mathbf{r}_B, \mathbf{r}_A) = -i\omega\rho \exp(-k_i R)\,\frac{e^{ikR}}{4\pi R} = G(\mathbf{r}_B, \mathbf{r}_A) \; . \tag{26}$$

Expressions (24) and (25) show that neither the volume integral nor the surface integral gives the Green's function, but that the sum does. Equation (16) suggests that for weak attenuation the volume integral can be ignored, because this integral is proportional to $\kappa_i << \kappa_r$. Expressions (24) and (25) show, however, for the special case of a homogeneous medium that as long as $k_i L = O(1)$, the volume integral and the surface integral in general have comparable strength. (As shown

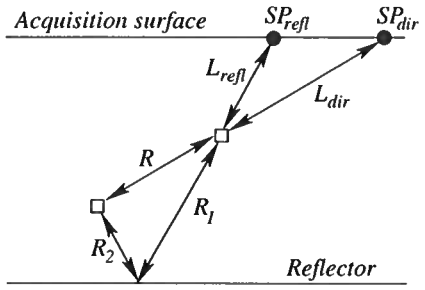

Figure 2. Two receivers (open squares) that are located between the acquisition surface and a reflector, and the stationary phase points SP_{dir} and SP_{refl} of the direct and reflected waves, respectively.

in expression (A5) of Appendix A, the volume integral $I_V^{(+)}$ is proportional to κ_i/k_i, which according to expression (22) has a finite value as $\kappa_i \rightarrow 0$.) The relative contribution of the surface integral and the volume integral is weighted by $\exp(-2k_iL)$. As the volume occupies all space ($L \rightarrow \infty$), the surface integral vanishes ($I_S^{(+)} \rightarrow 0$) and the volume integral is given by $I_V^{(+)}(\mathbf{r}_B, \mathbf{r}_A) = -i\omega\rho \exp(-k_iR)\, e^{ikR}/4\pi R = G(\mathbf{r}_B, \mathbf{r}_A)$. This is the special case treated in section 3 because in this limit the surface integral vanishes because of the large distance L traversed by the attenuating waves that are correlated.

Equation (26) shows that in the frequency domain the Green's function can be retrieved from the cross-correlation of waves excited by a combination of volume sources and surface sources. A similar result was obtained in the frequency domain in expression (10) of ref. (Snieder, 2004) where an infinite volume is needed. Expression (26) of ref. (Roux *et al.*, 2005) gives a time-domain formulation of the retrieval of the Green's function. In the latter studies sources in a homogeneous attenuating medium were integrated over an infinite volume. Because of the infinite integration region, the surface integral (25) did not contribute in those studies. The relative role of the surface integral and the volume integral is important because in some applications sources are present only on a finite surface (e.g., (Bakulin & Calvert, 2006)).

In this example, only the direct wave arrives, and ignoring the volume integral leads to an overall amplitude error. Next, I consider the example of interferometry for both the direct wave and a reflected wave. Sources are placed on the acquisition surface shown in figure 2. Both the direct wave and a reflected wave propagate to receivers indicated with open squares. The points SP_{dir} and SP_{refl} shown in that figure indicate the stationary phase source locations for the direct and reflected waves, respectively (Snieder *et al.*, 2006b).

The direct wave contains contributions $\exp(-k_iL_{dir}) \times exp(-k_i(L_{dir} + R))$ from the attenuation at the stationary points. Following the stationary phase analysis of ref. (Snieder *et al.*, 2006b), and taking the attenuation terms into account gives a contribution of the surface integral to the direct wave that is given by

$$u_{dir} \propto e^{-2k_iL_{dir}} e^{-k_iR}\, \frac{e^{ikR}}{R}\,. \tag{27}$$

The reflected waves has a contribution at the stationary phase point from the attenuation $\exp(-k_iL_{refl})$ $\times exp(-k_i(L_{refl}+R_1+R_2))$, the reflected wave obtained from the surface integral satisfies in the stationary phase approximation (Snieder *et al.*, 2006b)

$$u_{refl} \propto e^{-2k_iL_{refl}} r e^{-k_i(R_1+R_2)}\, \frac{e^{ik(R_1+R_2)}}{R_1+R_2}\,, \tag{28}$$

where r is the reflection coefficient of the interface. Both the direct and reflected waves thus obtained have the correct phase and geometrical spreading, but both contain an amplitude term ($\exp(-2k_iL_{dir})$ and $\exp(-2k_iL_{refl})$, respectively) that is due to neglecting the volume integrals. Since these amplitude terms are different for the direct wave and the reflected waves, neglecting the contribution of the volume integrals disrupts the relative amplitude of the different arrivals.

It is interesting to compare this result with expressions (1) and (18) of Sabra *et al.* (Sabra *et al.*, 2005a) who show that for an homogeneous attenuating oceanic wave guide with source placed at a surface of constant depth that the phase of the different arrivals is correctly produced by the cross-correlation, but the amplitude is not in the presence of attenuation. Expressions (27) and (28) presented here describe what happens when the sources are placed on a surface only. It is the absence of volume sources in ref. (Sabra *et al.*, 2005a) that leads to an incorrect estimate attenuation in the Green's function estimated from cross-correlation.

6 DISCUSSION

The derivation in this work shows that the Green's function of attenuating acoustic waves in a heterogeneous medium can be extracted by cross-correlating measurements of the pressure that is excited by random sources. As shown in sections 3 and 4, the Green's function can, however, be computed from the cross-correlation when the random pressure field is excited by sources that are distributed throughout the volume, and that have a source strength that is proportional to the local dissipation rate (which is proportional to κ_i). Volume sources are also required for the extraction of the Green's function of the diffusion equation (Snieder, 2006), which is another example of a system that is not invariant for time-reversal.

The physical reason that the excitation must be proportional to the local dissipation rate is that the extraction of the Green's function is based on the equilibration of energy. This condition is necessary for the

fluctuation-dissipation theorem, which relates the response of a dissipative system (the Green's function) to the fluctuations of that system around the equilibrium state (Callen & Welton, 1951; Kubo, 1966). Acoustic, dissipative, waves can be in equilibrium only when the excitation of the waves matches the local dissipation rate. If this were not the case, there would be a net energy flow, and the system would not be in equilibrium. The equilibrium of energy (Weaver, 1982), also referred to as equipartitioning, has been shown to be essential for the accurate reconstruction of the Green's function (e.g., (Malcolm *et al.*, 2004; Snieder *et al.*, 2007; Sánchez-Sesma *et al.*, 2006)).

When none of the conditions C1-C3 of section 3 is satisfied, the sum of the causal and acausal Green's function is, according to expression (15) given by the sum of the volume integral and a surface integral. The physical reason is that in equilibrium, the sources at the surface must be supplemented with sources within the volume that are proportional to the local dissipation rate if the system is to be in equilibrium. In some applications this condition can be realized. For example, Weaver and Lobkis (Weaver & Lobkis, 2001) extract the Green's function from the wavefield that is excited by thermal fluctuations throughout the volume of their sample. The need to have sources throughout the volume in addition to sources at the surface, is impractical in applications where one seeks to extract the Green's function for two points in the interior by placing sources at the bounding surface only (e.g., (Bakulin & Calvert, 2004; Bakulin & Calvert, 2006)).

Roux *et al.* (Roux *et al.*, 2005) show that for a homogeneous infinite acoustic medium one needs to correct for a factor ω^{-1}. They note that this term is due to their assumed attenuation mechanism ($Im(c) = constant$). In the formulation of this work, such a correction term is hidden in condition (12) which states that the power of the sources is proportional to the local attenuation rate. In this work, $\kappa_i(\mathbf{r}, \omega)$ can be an arbitrary function of position and frequency, but, as long as condition (12) is satisfied the Green's function can be extracted by cross correlation. In practical applications the source spectrum may not satisfy this condition. In that case there is no energy balance, and the Green's function is not correctly retrieved. This may be an important limitation in practical applications.

In practical situations, attenuation is present, and the contribution of the volume integral is often ignored, yet seismic interferometry seems to be able to retrieve the Green's function well (e.g., (Bakulin & Calvert, 2004; Bakulin & Calvert, 2006)). For the special case of a homogeneous medium, the contribution of the surface integral to the Green's function is given by expression (25). This contribution has the correct phase and geometrical spreading ($\exp(ik_r R)/R$), but incorrect attenuation ($\exp(-2k_i L)$ instead of $\exp(-k_i R)$). This suggests that when seismic interferometry for attenuating systems is used by summing over sources at the surface only, the correct phase and geometrical spreading are recovered, but that the attenuation is not. According to expressions (15)-(17) one needs for a general inhomogeneous attenating medium both volume sources and surface sources for the extraction of the Green's function. It is not known that multiple scattering by a boundary (Draeger & Fink, 1997) or by internal scatterers (Derode *et al.*, 1995) can compensate for a deficit of sources needed for focusing by time-reversal. This raises the unsolved question to what extent multiple scattering can compensate for the lack of volume sources.

Acknowledgments: I thank Ken Larner, Kees Wapenaar, and Richard Weaver for their valuable insights and comments. I appreciate the numerous comments of two anonymous reviewers who also pointed out an error in the presentation of the original manuscript. This research was supported by the Gamechanger Program of Shell International Exploration and Production Inc.

Note: This paper is in press, J. Acoust. Soc. Am., PACS: 43.20-f, 43.20.Bi, 43.60.Tj

REFERENCES

Aki, K., & Richards, P.G. 2002. *Quantitative Seismology.* Second edn. Sausalito: Univ. Science Books.

Bakulin, A., & Calvert, R. 2004. Virtual source: new method for imaging and 4D below complex overburden. *Expanded abstracts of the 2004 SEG-meeting*, 2477–2480.

Bakulin, A., & Calvert, R. 2006. The virtual source method: Theory and case study. *Geophysics*, **71**, SI139–SI150.

Bleistein, N., & Handelsman, R.A. 1975. *Asymptotic expansions of integrals.* New York: Dover.

Callen, H.B., & Welton, T.A. 1951. Irreversibility and generalized noise. *Phys. Rev.*, **83**, 34–40.

Calvert, R.W., Bakulin, A., & Jones, T.C. 2004. Virtual sources, a new way to remove overburden problems. *Expanded abstracts of the 2004 EAGE-meeting.*

Campillo, M., & Paul, A. 2003. Long-range correlations in the diffuse seismic coda. *Science*, **299**, 547–549.

de Hoop, A.T. 1988. Time-domain reciprocity theorems for acoustic wave fields in fluids with relaxation. *J. Acoust. Soc. Am.*, **84**, 1877–1882.

de Hoop, A.T. 1995. *Handbook of Radiation and Scattering of Waves: Acoustic Waves in Fluids, Elastic Waves in Solids, Electromagnetic Waves.* San Diego: Academic Press.

Derode, A., Roux, P., & Fink, M. 1995. Robust Acoustic Time Reversal with High-Order Multiple Scattering. *Phys. Rev. Lett.*, **75**, 4206–4209.

Derode, A., Larose, E., Campillo, M., & Fink, M. 2003a. How to estimate the Green's function for a heterogeneous medium between two passive sensors? Application to acoustic waves. *Appl. Phys. Lett.*, **83**, 3054–3056.

Derode, A., Larose, E., Tanter, M., de Rosny, J., Tourin, A., Campillo, M., & Fink, M. 2003b. Recovering the Green's

function from far-field correlations in an open scattering medium. *J. Acoust. Soc. Am.*, **113**, 2973–2976.

Draeger, C., & Fink, M. 1997. One-Channel Time Reversal of Elastic Waves in a Chaotic 2D-Silicon Cavity. *Phys. Rev. Lett.*, **79**, 407–410.

Fokkema, J.T., & van den Berg, P.M. 1993. *Seismic applications of acoustic reciprocity.* Amsterdam: Elsevier.

Godin, O.A. 2006. Recovering the acoustic Green's function from ambient noise cross correlation in an inhomogeneous medium. *Phys. Rev. Lett.*, **97**, 054301.

Jackson, J.D. 1975. *Classical electrodynamics.* 2nd edn. New York: John Wiley.

Kubo, R. 1966. The fluctuation-dissipation theorem. *Rep. Prog. Phys.*, **29**, 255–284.

Larose, E., Montaldo, G., Derode, A., & Campillo, M. 2006. Passive imaging of localized reflectors and interfaces in open media. *Appl. Phys. Lett.*, **88**, 104103.

Lobkis, O.I., & Weaver, R.L. 2001. On the emergence of the Green's function in the correlations of a diffuse field. *J. Acoust. Soc. Am.*, **110**, 3011–3017.

Malcolm, A., Scales, J., & van Tiggelen, B.A. 2004. Extracting the Green's function from diffuse, equipartitioned waves. *Phys. Rev. E*, **70**, 015601.

Paul, A., Campillo, M., Margerin, L., Larose, E., & Derode, A. 2005. Empirical synthesis of time-asymmetrical Green functions from the correlation of coda waves. *J. Geophys. Res.*, **110**, B08302, doi:10.1029/2004JB003521.

Rickett, J.E., & Claerbout, J.F. 1999. Acoustic daylight imaging via spectral factorization; helioseismology and reservoir monitoring. *The Leading Edge*, **18**, 957–960.

Rickett, J.E., & Claerbout, J.F. 2000. Calculation of the sun's acoustic impulse response by multidimensional spectral factorization. *Solar Physics*, **192**, 203–210.

Rickett, J.E., & J.F., Claerbout. 2001. Calculation of the acoustic solar impulse response by multidimensional spectral factorization. *In:* Duvall, T.L., Harvey, J.W., Kosovichev, A.G., & Svestka, Z. (eds), *Helioseismic Diagnostics of Solar Convection and Activity.* Dordrecht: Kluwer Academic Publishers.

Roux, P., Kuperman, W.A., & Group, NPAL. 2004. Extracting coherent wave fronts from acoustic ambient noise in the ocean. *J. Acoust. Soc. Am.*, **116**, 1995–2003.

Roux, P., Sabra, K.G., Kuperman, W.A., & Roux, A. 2005. Ambient noise cross correlation in free space: Theoretical approach. *J. Acoust. Soc. Am.*, **117**, 79–84.

Sabra, K.G., Roux, P., & Kuperman, W.A. 2005a. Arrival-time structure of the time-averaged ambient noise cross-correlation in an oceanic waveguide. *J. Acoust. Soc. Am.*, **117**, 164–174.

Sabra, K.G., Gerstoft, P., Roux, P., Kuperman, W.A., & Fehler, M.C. 2005b. Extracting time-domain Green's function estimates from ambient seismic noise. *Geophys. Res. Lett.*, **32**, L03310, doi: 10.1029/2004GL021862.

Sabra, K.G., Roux, P., Thode, A.M., D'Spain, G.L., & Hodgkiss, W.S. 2005c. Using ocean ambient noise for array self-localization and self-synchronization. *IEEE J. of Oceanic Eng.*, **30**, 338–347.

Sánchez-Sesma, F.J., Pérez-Ruiz, J.A., Campillo, M., & Luzón, F. 2006. Elastodynamic 2D Green function retrieval from cross-correlation: Canonical inclusion problem. *Geophys. Res. Lett.*, **33**, L13305, doi:10.1029/2006GL026454.

Shapiro, N.M., Campillo, M., Stehly, L., & Ritzwoller, M.H. 2005. High-resolution surface-wave tomography from ambient seismic noise. *Science*, **307**, 1615–1618.

Slob, E., Draganov, D., & Wapenaar, K. 2006. GPR without a source. *GPR 2006: Eleventh International Conference on Ground Penetrating Radar, Columbus Ohio,*, paper no. ANT.6.

Snieder, R. 2004. Extracting the Green's function from the correlation of coda waves: A derivation based on stationary phase. *Phys. Rev. E*, **69**, 046610.

Snieder, R. 2006. Retrieving the Green's function of the diffusion equation from the response to a random forcing. *Phys. Rev. E*, **74**, 046620.

Snieder, R., & Şafak, E. 2006. Extracting the building response using seismic interferometry; theory and application to the Millikan Library in Pasadena, California. *Bull. Seismol. Soc. Am.*, **96**, 586–598.

Snieder, R., Sheiman, J., & Calvert, R. 2006a. Equivalence of the virtual source method and wavefield deconvolution in seismic interferometry. *Phys. Rev. E*, **73**, 066620.

Snieder, R., Wapenaar, K., & Larner, K. 2006b. Spurious multiples in seismic interferometry of primaries. *Geophysics*, **71**, SI111–SI124.

Snieder, R., Wapenaar, K., & Wegler, U. 2007. Unified Green's function retrieval by cross-correlation; connection with energy principles. *Phys. Rev. E, in press.*

Wapenaar, K. 2004. Retrieving the elastodynamic Green's function of an arbitrary inhomogeneous medium by cross correlation. *Phys. Rev. Lett.*, **93**, 254301.

Wapenaar, K. 2006. Nonreciprocal Green's function retrieval by cross correlation. *J. Acoust. Soc. Am.*, **120**, EL7–EL13.

Wapenaar, K., Fokkema, J., & Snieder, R. 2005. Retrieving the Green's function by cross-correlation: a comparison of approaches. *J. Acoust. Soc. Am.*, **118**, 2783–2786.

Wapenaar, K., Dragonv, D., & Robertsson, J. 2006a. Introduction to the supplement on seismic interferometry. *Geophysics*, **71**, SI1–SI4.

Wapenaar, K., Slob, E., & Snieder, R. 2006b. Unified Green's function retrieval by cross-correlation. *Phys. Rev. Lett.*, **97**, 234301.

Weaver, R., & Lobkis, O. 2003. On the emergence of the Green's function in the correlations of a diffuse field: pulse-echo using thermal phonons. *Ultrasonics*, **40**, 435–439.

Weaver, R.L. 1982. On Diffuse Waves in Solid Media. *J. Acoust. Soc. Am.*, **71**, 1608–1609.

Weaver, R.L. 2006. Ward identties and he retrieval of Green's functions in the correlations of a diffuse field. *Submitted.*

Weaver, R.L., & Lobkis, O.I. 2001. Ultrasonics without a source: Thermal fluctuation correlations and MHz frequencies. *Phys. Rev. Lett.*, **87**, 134301.

Weaver, R.L., & Lobkis, O.I. 2004. Diffuse fields in open systems and the emergence of the Green's function. *J. Acoust. Soc. Am.*, **116**, 2731–2734.

Zhou, M., Jiang, Z. ad Yu, J., & Schuster, G.T. 2006. Comparison between interferometric migration and reduced-time migration of common-depth-point data. *Geophysics*, **71**, SI189–SI196.

APPENDIX A: STATIONARY PHASE ANALYSIS OF THE INTEGRATION OVER THE TRANSVERSE COORDINATES

The integrals $I_V(\mathbf{r}_B, \mathbf{r}_A)$ and $I_S(\mathbf{r}_B, \mathbf{r}_A)$ of expressions (16) and (17) contain, in the geometry of figure 1, an integration over the x- and y-coordinates. In this appendix I consider the contribution from integration points $z > R/2$. These points lead to the causal Green's function. The contribution from integration points $z < -R/2$ leads to the acausal Green's function, which can be obtained by complex conjugation of the results derived here.

For the Green's function of the homogeneous medium of expression (23),

$$G(\mathbf{r}_A, \mathbf{r})G^*(\mathbf{r}_B, \mathbf{r}) = \left(\frac{\rho\omega}{4\pi}\right)^2 e^{-k_i(L_A+L_B)} \frac{e^{ik_r(L_A+L_B)}}{L_A L_B} , \tag{A1}$$

where $L_{A,B} = |\mathbf{r} - \mathbf{r}_{A,B}|$, as shown in figure 1. The phase term $\exp(ik_r(L_A + L_B))$ of expression (A1) is oscillatory as a function of the transverse coordinates x and y. The phase is stationary along the z-axis ($x = y = 0$). For fixed z, near the stationary phase point, the lengths L_A and L_B are, to second order in x and y, given by

$$L_A = \sqrt{x^2 + y^2 + (z + R/2)^2} \approx (z + R/2) + \frac{1}{2}\frac{x^2 + y^2}{(z + R/2)} , \tag{A2}$$

and

$$L_B = \sqrt{x^2 + y^2 + (z - R/2)^2} \approx (z - R/2) + \frac{1}{2}\frac{x^2 + y^2}{(z - R/2)} . \tag{A3}$$

These expressions are valid for integration points $z > R/2$. In the stationary phase approximation (Bleistein & Handelsman, 1975) of the integration of expression (A1) over x and y, these approximations for L_A and L_B are used in the phase term $\exp(ik_r(L_A + L_B))$. In the stationary phase approximation, the attenuation and geometrical spreading terms $\exp(-k_i(L_A + L_B))/L_A L_B$ are evaluated at the stationary phase point $x = y = 0$, where $L_{A,B} = z \pm R/2$. The integral of expression (A1) over the transverse coordinates is, in the stationary phase approximation, given by (Bleistein & Handelsman, 1975)

$$\begin{aligned} \iint G(\mathbf{r}_A, \mathbf{r})G^*(\mathbf{r}_B, \mathbf{r})dxdy &= \left(\frac{\rho\omega}{4\pi}\right)\frac{e^{-2k_i z}}{z^2 - R^2/4}e^{ik_r R}\iint \exp\left(-\frac{ik_r}{2}\left(\frac{R}{z^2 - R^2/4}\right)(x^2 + y^2)\right)dxdy \\ &= \left(\frac{\rho\omega}{4\pi}\right)\frac{e^{-2k_i z}}{z^2 - R^2/4}e^{ik_r R}\left(e^{-i\pi/4}\sqrt{\frac{2\pi\left(z^2 - R^2/4\right)}{k_r R}}\right)^2 \\ &= -\frac{i\rho^2\omega c}{8\pi}e^{-2k_i z}\frac{e^{ik_r R}}{R} . \end{aligned} \tag{A4}$$

Inserting this result in equation (17), and setting $z = L$, gives expression (25) for the contribution of the surface $z = L$ to the surface integral $I_S(\mathbf{r}_B, \mathbf{r}_A)$. In order to obtain the contribution of the region $R/2 < z < L$ to the volume integral of expression (16), one needs to integrate equation (A4) over z:

$$\begin{aligned} I_V^{(+)}(\mathbf{r}_B, \mathbf{r}_A) &= 2\omega\kappa_i\frac{-i\rho^2\omega c}{8\pi}\frac{e^{ik_r R}}{R}\int_{R/2}^{L} e^{-2k_i z}dz \\ &= -\frac{i\rho^2\omega^2 c\kappa_i}{2k_i}\frac{e^{ik_r R}}{R}\left(e^{-k_i R} - e^{-2k_i L}\right) . \end{aligned} \tag{A5}$$

Using equation (22) to eliminate κ_i/k_i gives expression (24).

CWP-559P

Unified Green's function retrieval by cross-correlation; connection with energy principles

Roel Snieder[1], Kees Wapenaar[2], and Ulrich Wegler[3]
[1] *Center for Wave Phenomena and Department of Geophysics, Colorado School of Mines, Golden CO 80401*
[2] *Department of Geotechnology, Delft University of Technology, 2600 GA Delft, The Netherlands*
[3] *Institut für Geophysik und Geologie, Universität Leipzig, Leipzig, Germany*

ABSTRACT
It has been shown theoretically and observationally that the Green's function for acoustic and elastic waves can be retrieved by cross-correlating fluctuations recorded at two locations. We extend the concept of the extraction of the Green's function to a wide class of scalar linear systems. For systems that are not invariant under time reversal, the fluctuations must be excited by volume sources in order to satisfy the energy balance (equipartitioning) that is needed to extract the Green's function. The general theory for retrieving the Green's function is illustrated with examples that include the diffusion equation, Schrödinger's equation, a vibrating string, the acoustic wave equation, a vibrating beam, and the advection equation. Examples are also shown of situations where the Green's function cannot be extracted from ambient fluctuations. The general theory opens up new applications for the extraction of the Green's function from field correlations that include flow in porous media, quantum mechanics, and the extraction of the response of mechanical structures such as bridges.

Key words: interferometry, general scalar systems, energy

1 INTRODUCTION

The extraction of the Green's function from ambient fluctuations for acoustic and elastic waves has recently received much attention: see recent tutorials and reviews (Curtis *et al.*, 2006; Larose *et al.*, 2006), and the special supplement on seismic interferometry in Geophysics (Wapenaar *et al.*, 2006a). Derivations of this principle have been based on normal modes (Lobkis & Weaver, 2001), on representation theorems (Wapenaar, 2004; Wapenaar *et al.*, 2005), on the superposition of incoming plane waves (Weaver & Lobkis, 2004; Sánchez-Sesma *et al.*, 2006; Sánchez-Sesma & Campillo, 2006), on time-reversal invariance (Derode *et al.*, 2003b; Derode *et al.*, 2003a), and on the principle of stationary phase (Snieder, 2004a; Roux *et al.*, 2005; Sabra *et al.*, 2005a; Snieder *et al.*, 2006b). The extraction of the Green's function has been applied to ultrasound (Weaver & Lobkis, 2001; Weaver & Lobkis, 2003; Malcolm *et al.*, 2004), to crustal seismology (Campillo & Paul, 2003; Shapiro & Campillo, 2004; Shapiro *et al.*, 2005; Sabra *et al.*, 2005c; Sabra *et al.*, 2005b), to exploration seismology (Bakulin & Calvert, 2004; Bakulin & Calvert, 2006; Schuster *et al.*, 2004), to helioseismology (Rickett & Claerbout, 1999; Rickett & Claerbout, 2000; Rickett & J.F., 2001), to structural engineering (Snieder & Şafak, 2006; Snieder *et al.*, 2006a; Thompson & Snieder, 2006), to ocean acoustics (Roux *et al.*, 2004; Sabra *et al.*, 2005a; Sabra *et al.*, 2005d), to earthquake data recorded in a borehole (Mehta *et al.*, 2007), and to monitoring of volcanoes and fault zones (Sens-Schönfelder & Wegler, 2006; Wegler & Sens-Schönfelder, 2006).

Wapenaar et al. (Wapenaar *et al.*, 2006b) derived the extraction of the Green's function for systems of coupled first-order differential equations that describe general linear systems that include acoustic and elastic waves, the Maxwell's equations, and diffusive systems. The general applicability of the extraction of the Green's function is reminiscent to the fluctuation-dissipation theorem, e.g., (Callen & Welton, 1951; Kubo, 1966; Le Bellac *et al.*, 2004), which states that the response of a linear system in thermodynamic

equilibrium to an external force is related to the fluctuations in the system. The application of the fluctuation dissipation theorem to macroscopic systems such as the Earth's crust or ocean is, however, not trivial. The energy of macroscopic systems is large compared to the thermal energy; hence these systems are, in general, not in thermodynamic equilibrium. The extraction of the Green's function for acoustic and electromagnetic waves was derived earlier for stationary random media (Barabanenkov, 1969; Barabanenkov, 1971; Rytov *et al.*, 1989a). These treatments rely on an ensemble average, and therefore give the Green's function of the mean field only. In this work we average neither over thermal fluctuations, nor over an ensemble, but use an averaging over sources instead.

In this work we explore the general formulation of the extraction of the Green's function for linear scalar systems and explore the requirements that such a system must satisfy in order to retrieve the Green's function from fluctuations. Section 2 illustrates the central role of the concept of equipartitioning in the extraction of the Green's function. We introduce linear systems with symmetric spatial differential operators in section 3 and derive in section 4 a general theory for the extraction of the Green's function from fluctuations for such systems. Several examples are shown that are either of a didactic nature, or because they provide new applications. This general formalism is applied to systems that are invariant under time-reversal (section 5), to the diffusion equation (section 6), to a string with either an open end or fixed ends (sections 7 and 8), to acoustic waves (section 10), to Schrödinger's equation (section 11), and to a vibrating beam (section 12). We extend the general theory to anti-symmetric differential operators in section 13, and apply this in section 14 to the one-dimensional advection equation. In section 9 we show that the Green's function cannot always be retrieved by cross-correlation, and relate this to the lack of equipartitioning. We explain in section 15 why energy transport plays such a central role in the retrieval of the Green's functions from ambient fluctuations. In the appendix we show that the requirement of equipartitioning is stronger than the condition that the net energy current vanishes.

2 A HEURISTIC EXPLANATION OF THE ROLE OF EQUIPARTITIONING

The concept of *equipartitioning* plays a central role in the retrieval of the Green's function. The word equipartitioning is often used to mean that all modes (Larose *et al.*, 2006; Weaver, 1982), or degrees of freedom (Goldstein, 1980), of the system are excited with equal energy. It has also been used to indicate that the energy current is equal in all directions (Malcolm *et al.*, 2004). We use the latter definition of equipartitioning. Figure 1 serves

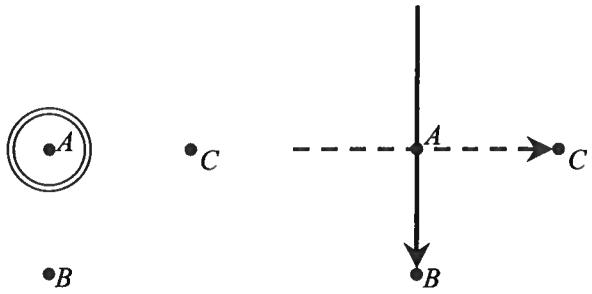

Figure 1. Left panel: a point source in a homogeneous acoustic medium at point A that emits equal amounts of energy toward points B and C. Right panel: equal energy transport along the solid and dashed arrows is needed to retrieve the Green's function for the propagation from the source point A to the points B and C.

to illustrate heuristically the central role of equipartitioning. In this example we consider acoustic waves in a homogeneous medium. A pressure source at location A excites acoustic waves. As shown in the left panel, these waves propagate with equal amplitude to receivers at points B and C.

Next, we consider the retrieval of the Green's function from cross-correlation. In the right panel of figure 1 there is no physical source at point A, and incoming waves turn into outgoing waves from point A as they pass through that location. Because of the absence of a physical source in the right panel of figure 1, the term *virtual source* has been used (Bakulin & Calvert, 2004; Bakulin & Calvert, 2006). Since the outgoing waves for the physical source in the left panel have the same amplitude for all propagation directions, the same must be true for the virtual source in the right panel. The outgoing wave at point A in the right panel has the same energy as the incoming wave, because the waves simply move through point A. The equivalence of the real source in the left panel, and the virtual source in the right panel, implies that the incoming waves in the right panel must have the same energy for all propagation directions. In other words: the waves must be equipartitioned. For the sake of argument we used a homogeneous acoustic medium. This is, however, not essential. A scalar source in an inhomogeneous medium also radiates waves isotropically (Chapman, 2004).

As another case consider the situation that point B is a diffractor. The direct wave that travels from A to C should be excited by the virtual source with the same strength as that of the diffracted wave that travels from A through the diffractor B to point C. In order to retrieve the correct amplitude ratio of the direct and diffracted waves from cross-correlation, the energy currents along the solid and dashed arrows in the right panel of figure 1 must be identical.

For vector equations, such as for elastic waves, the energy is usually not radiated isotropically. For exam-

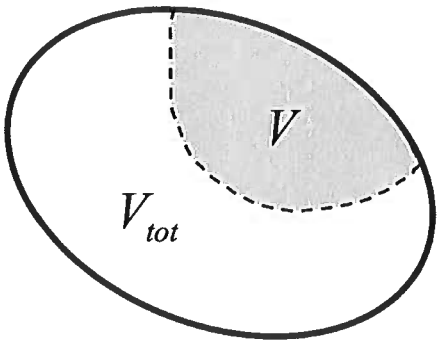

Figure 2. Definition of the total volume V_{tot} (bounded by the solid line), and the sub-volume V defined by the shaded region.

ple, a point force in an elastic medium radiates energy with a dipole pattern (Aki & Richards, 2002). For such a vector problem, one retrieves the Green's function by cross-correlating the displacement fields recorded at two receivers (Wapenaar, 2004). The projection of the displacement field onto the component used for the cross-correlation, gives the same dependence on the direction of propagation as does the radiation pattern of a point force. Therefore, one also needs the energy current to be independent of direction for such a vector problem.

In general, the extraction of the Green's function by cross-correlation gives the superposition of the causal Green's function and its time-reversed version (usually called the acausal Green's function.) In observational studies the causal Green's function as estimated by cross-correlation, and its acausal counterpart, often have different amplitudes. This asymmetry has been linked to the lack of equipartitioning (e.g., (Malcolm *et al.*, 2004; Paul *et al.*, 2005)). We give a more quantitative discussion of equipartitioning in section 15.

The requirement that the energy current is independent of direction implies that the net energy current vanishes. The net energy current vanishes when the energy current for every pair of opposing directions vanishes, but the energy current can still vary with direction. We show in the appendix explicitly that a vanishing net energy current does not necessarily imply equipartitioning.

3 A GENERAL DYNAMIC SYSTEM WITH A SYMMETRIC OPERATOR

Consider a scalar field u that is governed by the equation

$$\left(a_N(\mathbf{r},t) * \frac{\partial^N}{\partial t^N} + \cdots + a_2(\mathbf{r},t) * \frac{\partial^2}{\partial t^2} + a_1(\mathbf{r},t) * \frac{\partial}{\partial t}\right) u(\mathbf{r},t) = H(\mathbf{r},t) * u(\mathbf{r},t) + q(\mathbf{r},t)\,. \tag{1}$$

In this expression the asterisk denotes temporal convolution, $q(\mathbf{r},t)$ is the forcing, and H is a symmetric operator with properties that are defined in equation (3). Later we provide examples of physical systems that are described by equation (1). For Schrödinger's equation, the wave function is complex in the time domain, hence $u(\mathbf{r},t)$, and the time-domain Green's function, may be complex. In this work we analyze this system in the frequency domain, using the Fourier convention, $h(t) = \int h(\omega) \exp(-i\omega t)\, d\omega$. With this convention, expression (1) corresponds, in the frequency domain, to

$$\sum_{n=1}^{N} a_n(\mathbf{r},\omega)\,(-i\omega)^n\, u(\mathbf{r},\omega) = H(\mathbf{r},\omega)u(\mathbf{r},\omega) + q(\mathbf{r},\omega)\,. \tag{2}$$

Henceforth we suppress the frequency dependence of these quantities. The operator $H(\mathbf{r},\omega)$ and the coefficients $a_n(\mathbf{r},\omega)$ are not necessarily real.

Symmetry of H means that for any two functions f and g

$$\int_{V_{tot}} f\,(Hg)\,dV = \int_{V_{tot}} (Hf)\,g dV\,. \tag{3}$$

where the integration is over the total volume V_{tot} over which the system is defined. For example, in seismology the total volume could be the solid earth, which is bounded by a stress-free surface. Because of property (3), the system satisfies reciprocity. To show this we derive a representation theorem of the convolution type by considering expression (2) for two states that we label with the subscripts A and B, by evaluating $(2)_A u_B - u_A (2)_B$. In this notation $(2)_A$ denotes expression (2) for state A. This subtraction gives

$$u_A(Hu_B) - (Hu_A)\,u_B - q_A u_B + q_B u_A = 0\,. \tag{4}$$

Integrating this equation over the total volume V_{tot}, and using equation (3) gives

$$\int_{V_{tot}} q_A u_B dV = \int_{V_{tot}} q_B u_A dV\,. \tag{5}$$

Consider an impulsive forcing at location $\mathbf{r}_A$ for state A and at location $\mathbf{r}_B$ for state B:

$$q_{A,B}(\mathbf{r}) = \delta(\mathbf{r} - \mathbf{r}_{A,B})\,, \tag{6}$$

The response to such a forcing is, by definition, the Green's function

$$u_{A,B}(\mathbf{r}) = G(\mathbf{r}, \mathbf{r}_{A,B})\,. \tag{7}$$

Inserting these expressions into equation (5) gives

$$G(\mathbf{r}_A, \mathbf{r}_B) = G(\mathbf{r}_B, \mathbf{r}_A)\,, \tag{8}$$

which states that reciprocity is satisfied.

As stated in expression (3), the operator is symmetric when integrated over the total volume V_{tot}. In this work we limit the integration in several examples to a sub-volume V of the total volume V_{tot}, see figure 2. For example, in seismology the sub-volume may be the region that is investigated in a seismic survey.

Its boundary ∂V is not necessarily a physical boundary where homogeneous boundary conditions apply. For integration over this sub-volume the operator H is not necessarily symmetric, and we define the bilinear form $L(f,g)$ by

$$\int_V \left(f\,(Hg) - (Hf)\,g\right) dV \equiv \oint_{\partial V} L(f,g) dS\,. \tag{9}$$

Examples of the bilinear form L are shown in later sections. From definition (9), L is anti-symmetric:

$$L(f,g) = -L(g,f)\,. \tag{10}$$

Integrating expression (4) over the volume V, and using definition (9), gives

$$\oint_{\partial V} L(u_A,u_B) dS + \int_V \left(q_B u_A - q_A u_B\right) dV = 0\,. \tag{11}$$

Consider a state B that is excited by an impulsive excitation at location $\mathbf{r}_0$, i.e., $q_B(\mathbf{r}) = \delta(\mathbf{r}-\mathbf{r}_0)$; hence u_B is given by the Green's function: $u_B(\mathbf{r}) = G(\mathbf{r},\mathbf{r}_0)$. Dropping the subscript A, expression (11) is then given by

$$\oint_{\partial V} L(u(\mathbf{r}),G(\mathbf{r},\mathbf{r}_0)) dS - \int_V G(\mathbf{r},\mathbf{r}_0) q(\mathbf{r}) dV + u(\mathbf{r}_0) = 0\,. \tag{12}$$

Using reciprocity, expression (8), this gives the representation theorem that relates the field to the excitation and its values on the boundary

$$u(\mathbf{r}_0) = \int_V G(\mathbf{r}_0,\mathbf{r}) q(\mathbf{r}) dV - \oint_{\partial V} L(u(\mathbf{r}),G(\mathbf{r}_0,\mathbf{r})) dS\,. \tag{13}$$

4 GENERAL EXPRESSION FOR THE EXTRACTION OF THE GREEN'S FUNCTION

In this section we derive a general expression for the extraction of the Green's function using a representation theorem of the correlation type. Following Fokkema and van den Berg (Fokkema & van den Berg, 1993; Fokkema & van den Berg, 1996) we evaluate $(2)_A u_B^* - u_A (2)_B^*$, where $(2)_B^*$ denotes, for example, the complex conjugate of expression (2) for state B. Integrating the result over the volume V gives

$$\begin{aligned}\sum_{n=1}^{N} \int_V \left((-i\omega)^n a_n - (i\omega)^n a_n^*\right) u_A u_B^* dV \\ = \int_V \left(u_B^*\,(Hu_A) - (H^* u_B^*)\,u_A\right) dV \\ + \int_V \left(q_A u_B^* - q_B^* u_A\right) dV\,.\end{aligned} \tag{14}$$

For even values of n, $a_n(-i\omega)^n - a_n^*(i\omega)^n = 2iIm(a_n)(i\omega)^n$, while for odd values of n, $a_n(-i\omega)^n - a_n^*(i\omega)^n = -2Re(a_n)(i\omega)^n$. Writing $H^* = H + (H^* - H) = H - 2i\,\mathrm{Im}(H)$, and using definition (9) gives

$$\begin{aligned}-2 \sum_{n\ odd} \int_V (i\omega)^n\, Re(a_n) u_A u_B^* dV \\ +2i \sum_{n\ even} \int_V (i\omega)^n\, Im(a_n) u_A u_B^* dV \\ = 2i \int_V u_A\,\mathrm{Im}(H) u_B^* dV + \oint_{\partial V} L(u_B^*,u_A) dS \\ + \int_V \left(q_A u_B^* - q_B^* u_A\right) dV\,.\end{aligned} \tag{15}$$

The general expression for the extraction of the Green's function follows by choosing expression (6) for the excitations $q_{A,B}$. According to expression (7), the fields $u_{A,B}$ are then given by the Green functions. Using reciprocity (equation (8)), we can write the result as

$$\begin{aligned}G(\mathbf{r}_A,\mathbf{r}_B) - G^*(\mathbf{r}_A,\mathbf{r}_B) \\ = 2 \sum_{n\ odd} (i\omega)^n \int_V Re(a_n(\mathbf{r})) G(\mathbf{r}_A,\mathbf{r}) G^*(\mathbf{r}_B,\mathbf{r}) dV \\ -2i \sum_{n\ even} (i\omega)^n \int_V Im(a_n(\mathbf{r})) G(\mathbf{r}_A,\mathbf{r}) G^*(\mathbf{r}_B,\mathbf{r}) dV \\ + \oint_{\partial V} L(G^*(\mathbf{r}_B,\mathbf{r}),G(\mathbf{r}_A,\mathbf{r})) dS \\ +2i \int_V G(\mathbf{r}_A,\mathbf{r})\,\mathrm{Im}(H) G^*(\mathbf{r}_B,\mathbf{r}) dV\,.\end{aligned} \tag{16}$$

In the following sections we give examples of how this expression can be used to extract the Green's function from the correlation of fields. The left-hand side is the difference of the Green's function and its complex conjugate. Since complex conjugation in the frequency domain corresponds in the time domain to time-reversal, the left-hand side corresponds in the time domain to $G(\mathbf{r}_A,\mathbf{r}_B,t) - G^*(\mathbf{r}_A,\mathbf{r}_B,-t)$, the difference of the causal Green's function and the complex conjugate of the acausal Green's function. In many applications, such as acoustics or diffusion, the field is real in the time domain. In quantum mechanics, the wave function, and the associated time domain Green's function, is complex. For this reason we retain the complex conjugation of the time domain acausal Green's function.

The minus sign in the left-hand side of equation (16) is a matter of convention only. Multiplying expression (16) with $-i\omega$, and defining

$$G^{(v)} \equiv -i\omega G\,, \tag{17}$$

gives

$$G^{(v)}(\mathbf{r}_A,\mathbf{r}_B)+G^{(v)*}(\mathbf{r}_A,\mathbf{r}_B)$$
$$=2\sum_{n\ odd}(i\omega)^{n-1}\int_V Re(a_n(\mathbf{r}))G^{(v)}(\mathbf{r}_A,\mathbf{r})G^{(v)*}(\mathbf{r}_B,\mathbf{r})dV$$
$$-2i\sum_{n\ even}(i\omega)^{n-1}\int_V Im(a_n(\mathbf{r}))G^{(v)}(\mathbf{r}_A,\mathbf{r})G^{(v)*}(\mathbf{r}_B,\mathbf{r})dV$$
$$+\frac{1}{i\omega}\oint_{\partial V}L(G^{(v)*}(\mathbf{r}_B,\mathbf{r}),G^{(v)}(\mathbf{r}_A,\mathbf{r}))dS$$
$$+\frac{2}{\omega}\int_V G^{(v)}(\mathbf{r}_A,\mathbf{r})\,\mathrm{Im}(H)G^{(v)*}(\mathbf{r}_B,\mathbf{r})dV\ . \qquad (18)$$

This equation is equivalent to expression (16), but has a plus sign in the left-hand side, as in several other derivations, e.g., (Weaver & Lobkis, 2005; Snieder, 2004a; Wapenaar *et al.*, 2005). When G denotes, for example, the displacement Green's function, $G^{(v)}$ corresponds to the Green's function for the velocity. The sign in the left-hand side of expressions (16) and (18) is thus defined by the choice of the Green's function that one uses. Note that the right-hand sides of these equations differ by a factor $1/i\omega$. Since, with the employed Fourier convention, $-i\omega$ corresponds, to differentiation in the time domain, expressions (16) and (18) differ, in the time domain, by an additional time derivative.

5 EXAMPLE: INVARIANT SYSTEMS UNDER TIME-REVERSAL

Consider systems that are invariant under time reversal. This invariance has explicitly been used in some derivations for extraction of the Green's function (Derode *et al.*, 2003b; Derode *et al.*, 2003a). An example of systems that are invariant under time reversal is, for example, the acoustic wave equation without attenuation:

$$\frac{1}{\rho c^2}\frac{\partial^2 u}{\partial t^2}-\nabla\cdot\left(\frac{1}{\rho}\nabla u\right)=q\ , \qquad (19)$$

with ρ the mass density and c the speed of sound. In the notation of expression (1), $a_2=1/\rho c^2$, and $H=\nabla\cdot\rho^{-1}\nabla$. For this problem only a_2 is nonzero, and both a_2 and H are real. Another example is Schrödinger's equation (Merzbacher, 1970)

$$i\hbar\frac{\partial\psi}{\partial t}=-\frac{\hbar^2}{2m}\nabla^2\psi+V\psi\ , \qquad (20)$$

which is invariant under time reversal and complex conjugation. Since the complex conjugation does not change expectation values (Merzbacher, 1970), the complex conjugate wave function corresponds to the same physical state. In this case only a_1 is nonzero, H is real, and $a_1=i\hbar$ is purely imaginary.

For these examples the first two terms in the right-hand side of expression (16) vanish. Since time-reversal corresponds, in the frequency domain, to complex conjugation, time reversal invariance of equation (2) implies that $a_n(-i\omega)^n$ is real. For even n this means that a_n is real, while for odd n, a_n is imaginary. Under these conditions the first two terms in the right-hand side of equation (16) are equal to zero, while the condition that H is real implies that the last term vanishes as well. In this case, expression (16) reduces to

$$G(\mathbf{r}_A,\mathbf{r}_B)-G^*(\mathbf{r}_A,\mathbf{r}_B)=\oint_{\partial V}L(G^*(\mathbf{r}_B,\mathbf{r}),G(\mathbf{r}_A,\mathbf{r}))dS\ . \qquad (21)$$

This expression contains a surface integral, but no volume integral. In later sections we show that this allows for the extraction of the Green's function by cross-correlation of fields that are excited by sources on the surface ∂V only. The general expression (16) contains both a surface integral and volume integrals. The presence of volume integrals indicates that for systems that are not invariant under time reversal, one needs sources throughout the volume to extract the Green's function. We analyze the acoustic wave equation and Schrödinger's equation in more detail in sections 10 and 11.

6 EXAMPLE: THE DIFFUSION EQUATION

The general expression (16) is also valid for systems that are not invariant under time-reversal. As an example of such a system consider the diffusion equation

$$\frac{\partial u(\mathbf{r},t)}{\partial t}=\nabla\cdot(D(\mathbf{r})\nabla u(\mathbf{r},t))+q(\mathbf{r},t)\ , \qquad (22)$$

where the diffusion constant $D(\mathbf{r})$ can vary with location. In the notation of expression (1), $a_1=1$, and $a_n=0$ for $n\neq 1$. The operator H is real and is defined by

$$H=\nabla\cdot D\nabla\ . \qquad (23)$$

In this section we show how the Green's function of the diffusion equation can be extracted from the correlation of fields excited by random sources. This derivation is equivalent to an earlier derivation (Snieder, 2006b).

For operator H of expression (23), $fHg=f\nabla\cdot(D\nabla g)=\nabla\cdot(Df\nabla g)-D\nabla f\cdot\nabla g$. Integrating this over the volume V, applying Gauss's theorem, and subtracting the same expression with f and g interchanged, gives Green's theorem:

$$\int_V(fHg-(Hf)\,g)\,dV=\oint_{\partial V}D\left(f\frac{\partial g}{\partial n}-\frac{\partial f}{\partial n}g\right)dS\ , \qquad (24)$$

where $\partial/\partial n$ denotes the derivative normal to the boundary ∂V. The bilinear form L for this problem is thus given by

$$L(f,g)=D\left(f\frac{\partial g}{\partial n}-\frac{\partial f}{\partial n}g\right)\ . \qquad (25)$$

Consider the special case, where on the boundary, either the field, its normal derivative, or a superposition of these quantities vanishes. This means that f satisfies one of the following boundary conditions:

$$f = 0 \quad \text{or} \quad \frac{\partial f}{\partial n} = 0 \quad \text{or} \quad \frac{\partial f}{\partial n} + \alpha f = 0 \,, \quad (26)$$

with α a real number. The same boundary condition holds for g. In this case

$$L(f,g) = 0 \,, \quad (27)$$

and expression (16), for the diffusion equation, is given by

$$G(\mathbf{r}_A,\mathbf{r}_B) - G^*(\mathbf{r}_A,\mathbf{r}_B) = 2i\omega \int_V G(\mathbf{r}_A,\mathbf{r}) G^*(\mathbf{r}_B,\mathbf{r}) dV \,. \quad (28)$$

Also, using expression (27), representation theorem (13) reduces to

$$u(\mathbf{r}_0) = \int_V G(\mathbf{r}_0,\mathbf{r}) q(\mathbf{r}) dV \,. \quad (29)$$

Suppose that the field is excited by spatially uncorrelated sources that have a power spectrum $|S(\omega)|^2$:

$$\langle q(\mathbf{r}_1) q^*(\mathbf{r}_2)\rangle = |S(\omega)|^2 \, \delta(\mathbf{r}_1 - \mathbf{r}_2) \,. \quad (30)$$

The brackets $\langle \cdots \rangle$ denote an average of all sources. Expression (30) states that the excitation at two different spatial locations is uncorrelated when averaged over all sources. This happens for quasi-random continuous sources whose source signature is uncorrelated for sources at different locations. Equation (30) is also applicable when controlled, impulsive, sources fire sequentially at different locations, and when a summation over these sources is applied (e.g., (Bakulin & Calvert, 2004; Bakulin & Calvert, 2006)). In practical applications the source average for continuous sources is implemented by averaging over multiple non-overlapping time windows, e.g., (Shapiro & Campillo, 2004; Sens-Schönfelder & Wegler, 2006). Multiplying expression (28) with $|S(\omega)|^2$, and using that $\int_V G(\mathbf{r}_A,\mathbf{r}) G^*(\mathbf{r}_B,\mathbf{r}) dV = \int_V \int_V G(\mathbf{r}_A,\mathbf{r}_1) \delta(\mathbf{r}_1 - \mathbf{r}_2) \, G^*(\mathbf{r}_B,\mathbf{r}_2) dV_1 dV_2$ gives

$$\begin{aligned}
&\left(G(\mathbf{r}_A,\mathbf{r}_B) - G^*(\mathbf{r}_A,\mathbf{r}_B)\right) |S(\omega)|^2 \\
&= 2i\omega \int_V \int_V G(\mathbf{r}_A,\mathbf{r}_1) \, |S(\omega)|^2 \, \delta(\mathbf{r}_1 - \mathbf{r}_2) \, G^*(\mathbf{r}_B,\mathbf{r}_2) dV_1 dV_2 \\
&= 2i\omega \langle \int_V G(\mathbf{r}_A,\mathbf{r}_1) q(\mathbf{r}_1) dV_1 \left(\int_V G(\mathbf{r}_B,\mathbf{r}_2) q(\mathbf{r}_2) dV_2 \right)^* \rangle \\
&= 2i\omega \langle u(\mathbf{r}_A) u^*(\mathbf{r}_B) \rangle \,, \quad (31)
\end{aligned}$$

where expression (29) is used in the last identity. This result can be written as

$$G(\mathbf{r}_A,\mathbf{r}_B) - G^*(\mathbf{r}_A,\mathbf{r}_B) = \frac{2i\omega}{|S(\omega)|^2} \langle u(\mathbf{r}_A) u^*(\mathbf{r}_B) \rangle \,. \quad (32)$$

The difference of the causal and acausal Green's function thus follows from the cross-correlation of fields excited by spatially uncorrelated sources. The factor $i\omega$ corresponds, in the time domain, to a (negative) time derivative $-\partial/\partial t$. A stronger excitation leads to stronger field, but the Green's functions in the left-hand side must be independent of the strength of the excitation of the fields that are correlated. The division by the power spectrum in the right hand side of expression (32) provides the required normalization.

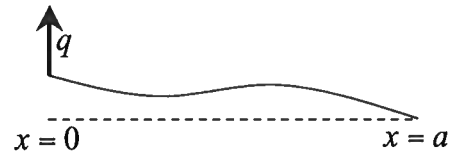

Figure 3. A string with an open, forced, end at $x = 0$ and a fixed end at $x = a$.

The reason why volume sources are needed for the extraction of the Green's function can be explained as follows. The diffusion equation is of a dissipative nature. A continuous injection of energy within a volume is needed to overcome the dissipation inherent with diffusive systems. In this way an energy balance is established, and the system is equipartitioned when averaged over all sources.

7 EXAMPLE: A STRING WITH MOVING END

In order to clarify the essential role of an energy balance for retrieving the Green's function, we first present a simple one-dimensional system. Consider a string extending from $x = 0$ to $x = a$ with mass-density $\rho(x)$ per unit length, and is under constant tension T, see figure 3. The left end of the string is excited at $x = 0$, while the right end is fixed at $x = a$. There is no dissipation in the string. The motion of the string is governed by

$$\rho(x) \frac{\partial^2 u}{\partial t^2} - T \frac{\partial^2 u}{\partial x^2} = q(x,t) \,. \quad (33)$$

The string has a fixed end at $x = a$ and is being shaken by a force $F(t)$ at $x = 0$

$$q(x,t) = F(t) \delta(x) \,. \quad (34)$$

In the notation of expression (1), $a_2(x) = \rho(x)$, all other a_n are equal to zero, and $H = T\partial^2/\partial x^2$. Using definition (9)

$$L(f,g) = T \left(f \partial_x g - g \partial_x f \right) \,. \quad (35)$$

Inserting these results into expression (16) gives

$$\begin{aligned}
G(x_A,x_B) - G^*(x_A,x_B) = T \, &[G^*(x_B,x) \partial_x G(x_A,x) \\
&- G(x_A,x) \partial_x G^*(x_B,x)]_{x=0}^{x=a} \,. \quad (36)
\end{aligned}$$

(For one-dimensional systems the surface integral in expression (16) reduces to the difference of the integrand at the ends of the integration interval.) The contribution from the point $x = a$ on the right-hand side vanishes because the string is fixed at this point. In order to use this

expression for the extraction of the Green's function, we need to eliminate the derivative of the Green's function at the left endpoint ($x = 0$) from this expression. This can be achieved by imposing a radiation boundary condition at the left side of the string. Together with the condition that the right side is fixed, this means that $u(x)$ and $G(x, x_0)$ satisfy the following boundary conditions

$$\frac{\partial f(x=0)}{\partial x} = -ikf(x=0) \qquad \text{and} \qquad f(x=a) = 0\,, \tag{37}$$

with the local wave number k at the left side of the string given by

$$k = \frac{\omega}{c(x=0)}\,, \tag{38}$$

where $c = \sqrt{T/\rho}$. Note that for radiation boundary condition (37) the parameter α in expression (26) is imaginary. Inserting these results in expression (36) then gives

$$G(x_A, x_B) - G^*(x_A, x_B) = 2iTk\, G(x_A, x=0) G^*(x_B, x=0)\,. \tag{39}$$

Using boundary condition (37) the motion of string is according to expression (13) given by

$$u(x_0) = G(x_0, x=0) F(\omega)\,. \tag{40}$$

Multiplying equation (39) with $|F(\omega)|^2$, and using expression (40), then gives

$$\begin{aligned}(G(x_A, x_B) - G^*(x_A, x_B))\,|F(\omega)|^2 \\ = 2iTk\, G(x_A, x=0) F(\omega)\,(G(x_B, x=0) F(\omega))^* \\ = 2iTk\, u(x_A) u^*(x_B)\,.\end{aligned} \tag{41}$$

Using expression (38), this result can also be written as

$$G(x_A, x_B) - G^*(x_A, x_B) = \frac{2i\omega\sqrt{\rho(x=0)T}}{|F(\omega)|^2} u(x_A) u^*(x_B)\,. \tag{42}$$

In expression (41), the cross-correlation is multiplied with Tk. The power in a vibrating string is proportional to $Tk|u|^2$ (Butkov, 1968). This means that the reconstructed Green's function depends on the power that is injected into the string by the shaking at its end point.

We used the radiation boundary condition (37) to eliminate the x-derivative of the Green's function. The physical reason for this choice is that the radiation boundary condition corresponds to an energy sink by outward radiation at the same point where energy is supplied to the system (the left side of the string that is shaken). This creates a state of equipartitioning in the string.

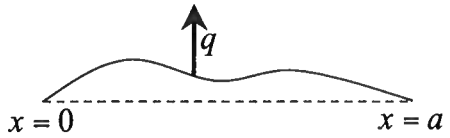

Figure 4. A string that is fixed at both endpoints that is forced internally.

8 EXAMPLE: A STRING WITH FIXED ENDPOINTS AND DISSIPATION

In the previous example the string was not damped, and the radiation from the left end provided an energy sink. In this section we show a damped string with fixed endpoints, where the damping acts as an energy sink. The damped string with fixed endpoints satisfies

$$\rho(x)\frac{\partial^2 u}{\partial t^2} + a_1(x)\frac{\partial u}{\partial t} - T\frac{\partial^2 u}{\partial x^2} = q(x,t)\,, \tag{43}$$

where $a_1(x)$ is the damping parameter. Because of the fixed endpoints

$$u(x=0) = u(x=a) = 0\,. \tag{44}$$

According to expression (35), for these boundary conditions the bilinear boundary term vanishes:

$$L(f,g) = 0\,, \tag{45}$$

and expression (16) is given by

$$\begin{aligned}G(x_A, x_B) - G^*(x_A, x_B) \\ = 2i\omega \int_0^a a_1(x) G(x_A, x) G^*(x_B, x) dx\,.\end{aligned} \tag{46}$$

For a given loading, the response according to equation (13) is given by

$$u(x_0) = \int_0^a G(x_0, x) q(x) dx\,. \tag{47}$$

Next consider a spatially uncorrelated excitation that satisfies

$$\langle q(x_1) q^*(x_2)\rangle = a_1(x_1)\,|S(\omega)|^2\,\delta(x_1 - x_2)\,. \tag{48}$$

Note that this source strength locally is proportional to the attenuation, as described by the damping parameter $a_1(x)$. Multiplying expression (46) with the power spectrum gives

$$\begin{aligned}&(G(x_A, x_B) - G^*(x_A, x_B))\,|S(\omega)|^2 \\ &= 2i\omega \int_0^a \int_0^a G(x_A, x_1)\,|S(\omega)|^2\, a_1(x_1)\delta(x_1 - x_2) \\ &\quad G^*(x_B, x_2) dx_1 dx_2 \\ &= 2i\omega \langle \int_0^a G(x_A, x_1) q(x_1) dx_1 \left(\int_0^a G(x_B, x_2) q(x_2) dx_2\right)^* \rangle \\ &= 2i\omega \langle u(x_A) u^*(x_B)\rangle\,;\end{aligned} \tag{49}$$

hence the sum of the causal and acausal Green's functions follows from cross-correlation of the fields excited by spatially uncorrelated sources.

Note the presence of the damping $a_1(x)$ in expression (48). The Green's function can be extracted from the cross-correlation only when the excitation is locally proportional to the damping. This creates an energy balance because the source of energy by the excitation is locally compensated by the attenuation, which acts as an energy sink. In section 15 we use the equation of radiative transfer to show that in a state of equipartitioning the excitation locally balances the dissipation due to intrinsic attenuation. When the excitation would not be proportional to the damping, there would be a net energy flux from the regions with strong excitation and weak damping to the areas of weak excitation and strong damping. The associated net energy flux violates the requirement of equipartitioning.

9 EXAMPLE: FAILURE TO EXTRACT THE GREEN'S FUNCTION

In this work numerous examples are presented of the extraction of the Green's function by cross-correlation. We now use the string, as presented in sections 7 and 8, to illustrate situations where the Green's function cannot be extracted by cross-correlation. First consider the string with internal excitation, as analyzed in section 8, but now without dissipation. This corresponds to the case $a_1 = 0$. Inserting this value in the right-hand side of expression (46) gives $G(x_A, x_B) - G^*(x_A, x_B) = 0$, which implies that the Green's function cannot be retrieved by cross-correlation.

The physical reason for the inability to extract the Green's function in this case is that energy is continuously supplied by the excitation, but there is no dissipation to act as a sink for this energy. The string thus is not in equilibrium, violating equipartitioning. Consequently, the Green's function cannot be retrieved from the fluctuations. In this case attenuation is needed to break the invariance for time-reversal in order to retrieve the Green's function.

As a second example consider the string that is excited at one of its endpoints, and whose motion is dissipative as described by a nonzero value for $a_1(x)$. Following expression (16), and modifying equation (39) to include the attenuation gives

$$\begin{aligned} &G(x_A, x_B) - G^*(x_A, x_B) \\ &\quad = 2iTk\, G(x_A, x=0) G^*(x_B, x=0) \\ &\qquad +2i\omega \int_0^a a_1(x) G(x_A, x) G^*(x_B, x) dx \,. \end{aligned} \tag{50}$$

Extending the steps leading to expression (41) then gives

$$\begin{aligned} &(G(x_A, x_B) - G^*(x_A, x_B))\, |F(\omega)|^2 \\ &\quad = 2iTk\, u(x_A) u^*(x_B) + 2i\omega\, |F(\omega)|^2 \\ &\qquad \int_0^a a_1(x) G(x_A, x) G^*(x_B, x) dx \,. \end{aligned} \tag{51}$$

The last term prevents the Green's function from being retrieved by cross-correlation. Again, this is caused by a non-equilibrium state of this string. The string is being supplied with energy on its left endpoint while energy is being dissipated throughout the string. There is thus a net energy flux from the endpoint into the string. This net energy flux violates equipartitioning.

If in addition to the force at the endpoint, there also is a continuous excitation within the string, then the Green's function can be retrieved by cross-correlation. This can be achieved, however, only when the internal excitation compensates for the dissipation. Experimentally this may be difficult to realize.

10 EXAMPLE: THE ACOUSTIC WAVE EQUATION

The previous examples are for one-dimensional systems. The same principles hold for more dimensions. We show this by analyzing the acoustic wave equation (19) in more detail. This derivation is equivalent to earlier treatments (Wapenaar *et al.*, 2005; Weaver & Lobkis, 2004). A comparison with expression (23) shows that $H = \nabla \cdot \rho^{-1} \nabla$ is the same operator as that for the diffusion equation when D is replaced by ρ^{-1}. Making this substitution in equation (25) and inserting these results in (16) gives

$$\begin{aligned} &G(\mathbf{r}_A, \mathbf{r}_B) - G^*(\mathbf{r}_A, \mathbf{r}_B) = \oint_{\partial V} \frac{1}{\rho} \\ &\left(G^*(\mathbf{r}_B, \mathbf{r}) \frac{\partial G(\mathbf{r}_A, \mathbf{r})}{\partial n} - \frac{\partial G^*(\mathbf{r}_B, \mathbf{r})}{\partial n} G(\mathbf{r}_A, \mathbf{r}) \right) dS \,. \end{aligned} \tag{52}$$

Note that in contrast to equation (28) for the diffusion equation, this expression contains a surface integral rather than a volume integral. Following ref. (Wapenaar *et al.*, 2005) we use a spherical surface far away from the points $\mathbf{r}_A$ and $\mathbf{r}_B$ and impose a radiation boundary condition:

$$\frac{\partial G(\mathbf{r}_0, \mathbf{r})}{\partial n} = ikG(\mathbf{r}_0, \mathbf{r}) \,. \tag{53}$$

Using the relation $k = \omega/c$, expression (52) is then given by

$$\begin{aligned} &G(\mathbf{r}_A, \mathbf{r}_B) - G^*(\mathbf{r}_A, \mathbf{r}_B) \\ &\quad = 2i\omega \oint_{\partial V} \frac{1}{\rho c} G(\mathbf{r}_A, \mathbf{r}) G^*(\mathbf{r}_B, \mathbf{r}) dS \,. \end{aligned} \tag{54}$$

For spatially uncorrelated sources at the boundary that satisfy

$$\langle q(\mathbf{r}_1) q^*(\mathbf{r}_2) \rangle = \frac{|S(\omega)|^2}{\rho(\mathbf{r}_1) c(\mathbf{r}_1)} \delta(\mathbf{r}_1 - \mathbf{r}_2) \,, \tag{55}$$

expression (54) reduces to

$$G(\mathbf{r}_A, \mathbf{r}_B) - G^*(\mathbf{r}_A, \mathbf{r}_B) = \frac{2i\omega}{|S(\omega)|^2} \langle u(\mathbf{r}_A) u^*(\mathbf{r}_B) \rangle \,. \tag{56}$$

In this case, energy is supplied to the system at the

boundary by the sources, and the energy loss due to the radiation boundary condition establishes the equilibrium condition required for equipartitioning.

The presence of the factors $1/\rho c$ in expression (55) can be explained as follows. The power in an acoustic medium is proportional to pv, with v the particle velocity. The ratio of the pressure to the velocity is given by the acoustic impedance (Snieder, 2004b), $p/v = \rho c$; hence the power is proportional to $p^2/\rho c$. The excitation of expression (55) thus dictates that the power supplied at all points on the surface is constant, this establishes equipartitioning.

According to expression (56) the Green's function can indeed be extracted by cross-correlation. A similar problem has been formulated for acoustic waves that are attenuated (Snieder, 2006a), as described by a complex-valued compressibility $\kappa = 1/\rho c^2$. In this case $\mathrm{Im}(H) \neq 0$, and, as a result, an additional volume integral is present in the right-hand side of expression (52). In that case the Green's function can be recovered when the volume is chosen in such a way that either the surface integral vanishes (i.e., a free surface) and volume sources are present, or the volume sources and the surface sources are in the right proportion as in the case of the string in section 9.

11 EXAMPLE: SCHRÖDINGER'S EQUATION

The extraction of the Green's function can also be carried out for quantum systems. The extraction of the Green's function for Schrödinger's equation is almost the same as that for acoustic waves. (In quantum mechanics, the term *propagator* is often used for the Green's function (Merzbacher, 1970).) For Schrödinger's equation (20), $H = -(\hbar^2/2m)\nabla^2 + V$. A comparison with the acoustic wave equation (19) shows that in expression (52), $1/\rho$ must be replaced by $-\hbar^2/2m$. Expression (54) generalizes for Schrödinger's equation to

$$G(\mathbf{r}_A, \mathbf{r}_B) - G^*(\mathbf{r}_A, \mathbf{r}_B) = -\frac{ik\hbar^2}{m} \oint_{\partial V} G(\mathbf{r}_A, \mathbf{r}) G^*(\mathbf{r}_B, \mathbf{r}) dS \,. \tag{57}$$

Suppose that the excitation on ∂V is spatially uncorrelated, and is given by

$$\langle q(\mathbf{r}_1) q^*(\mathbf{r}_2) \rangle = |S(\omega)|^2 \, \delta(\mathbf{r}_1 - \mathbf{r}_2) \,. \tag{58}$$

Taking the same steps as in the derivation of expression (56), and denoting the field by ψ, the Green's function for Schrödinger's equation can be retrieved by cross-correlation:

$$G(\mathbf{r}_A, \mathbf{r}_B) - G^*(\mathbf{r}_A, \mathbf{r}_B) = -\frac{ik\hbar^2}{m|S(\omega)|^2} \langle \psi(\mathbf{r}_A) \psi^*(\mathbf{r}_B) \rangle \,. \tag{59}$$

Extraction of the Green's function for Schrödinger's equation experimentally requires that the cross-correlation of the wave function be measured experimentally and that waves are excited at the bounding surface. The condition that sources are present on the surface can be relaxed by using the derivation of Weaver and Lobkis (Weaver & Lobkis, 2004), which shows for acoustic waves in a medium that is homogeneous outside the surface ∂V, that the sources on the surface can be replaced by distributed volume sources outside the surface. In the frequency domain, the acoustic wave equation for a homogeneous medium and Schrödinger's equation for a free particle both reduce to the Helmholtz equation. The arguments of Weaver and Lobkis therefore also are applicable for Schrödinger's equation when the potential vanishes outside the surface ∂V. The continuous source distribution is more realistic than sources on the surface for quantum-mechanical scattering problems.

The right hand side of expression (59) contains the correlation of the fields at locations $\mathbf{r}_A$ and $\mathbf{r}_B$. This quantity can be measured when these points coincide: $\mathbf{r}_A = \mathbf{r}_B = \mathbf{r}$. In that case

$$G(\mathbf{r}, \mathbf{r}) - G^*(\mathbf{r}, \mathbf{r}) = -\frac{ik\hbar^2}{m|S(\omega)|^2} \langle |\psi(\mathbf{r})|^2 \rangle \,. \tag{60}$$

The right hand side is the expectation value of the intensity fluctuations as a function of frequency. The left hand side is the sum of the causal and acausal Green's function for waves to return to their starting point. This quantity contains phase information that is related to the time needed for a wave to return to the point $\mathbf{r}$ after it has left this point. The counterpart of expression (60) for elastic waves has been applied to recorded fluctuations in the displacement to determine the elastic waves that travel from a receiver into the subsurface of the Earth and then return to the receiver (Sens-Schönfelder & Wegler, 2006; Wegler & Sens-Schönfelder, 2006).

12 EXAMPLE: A VIBRATING BEAM

In the previous examples, the operator H was a second-order differential operator. This operator, however, need not be of second order. As an example, consider an unclamped beam that is supported at its end points $x = 0$ and $x = a$; see figure 5. The beam satisfies a differential equation that is of fourth order in the space variable

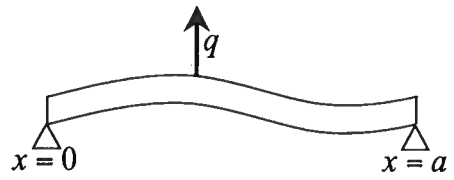

Figure 5. A beam that is supported at both endpoints that is forced internally.

(Chopra, 1995)

$$m(x)\frac{\partial^2 u}{\partial t^2} + a_1(x)\frac{\partial u}{\partial t} + \frac{\partial^2}{\partial x^2}\left(D(x)\frac{\partial^2 u}{\partial x^2}\right) = q\,. \qquad (61)$$

In this expression $m(x)$ is the mass of the beam per unit length, and $D(x)$ denotes the flexural rigidity. In the notation of expression (1), $a_2(x) = m(x)$, and $H = -\partial_{xx}\,(D\partial_{xx})$. Since the endpoints of the beam are fixed and unclamped, the beam satisfies the following boundary conditions

$$u(x=0) = u(x=a) = 0 \qquad \text{and} \qquad \partial_{xx}u(x=0) = \partial_{xx}u(x=a) = 0\,. \qquad (62)$$

Using repeated integration by parts, the operator L defined in expression (9) is given by

$$L(f,g) = D\,(f_x g_{xx} - f_{xx} g_x) + g\partial_x\,(Df_{xx}) - f\partial_x\,(Dg_{xx})\,. \qquad (63)$$

Because of boundary conditions (62), $[L(f,g)]_{x=0}^{x=a} = 0$. In this case, expression (16) is given by

$$G(x_A,x_B) - G^*(x_A,x_B) = 2i\omega\int_0^a a_1(x)G(x_A,x)G^*(x_B,x)dx\,. \qquad (64)$$

This expression is identical to equation (46) for the string with internal loading and attenuation. This means that for the beam the Green's function can be determined from the motion excited by the spatially uncorrelated source defined in equation (48) using the cross-correlation of expression (49). This example is of practical importance because the beam is a model for mechanical structures such as bridges.

13 SYSTEMS DEFINED BY AN ANTI-SYMMETRIC OPERATOR

The theory of the preceding sections is based on an operator H that is symmetric when considered over the volume V_{tot}. Some systems are defined by an operator that is anti-symmetric. This happens when H contains an odd order of spatial derivatives, as in the flow problem presented in the next section. For such an operator

$$\int_{V_{tot}} f\,(Hg)\,dV = -\int_{V_{tot}} (Hf)\,g dV\,. \qquad (65)$$

Reciprocity does not hold in this case because the symmetry property of H is essential in the derivation of expression (8). Equation (65) is not necessarily satisfied when the integration is carried out over a sub-volume V. By analogy with expression (9) we define a bilinear form M by

$$\int_V (f\,(Hg) + (Hf)\,g)\,dV \equiv \oint_{\partial V} M(f,g)dS\,. \qquad (66)$$

A representation theorem of the correlation type follows by considering two states labeled with the subscripts A and B, and by integrating the combination $(2)_A u_B^* + u_A(2)_B^*$ over the volume V to give

$$\sum_{n=1}^{N}\int_V ((-i\omega)^n a_n + (i\omega)^n a_n^*)\,u_A u_B^* dV = \int_V (u_B^*\,(Hu_A) + (H^* u_B^*)\,u_A)\,dV + \int_V (q_A u_B^* + q_B^* u_A)\,dV\,. \qquad (67)$$

Applying steps similar to those for the derivation of expression (16) gives

$$\begin{aligned} G(\mathbf{r}_B,\mathbf{r}_A) + G^*(\mathbf{r}_A,\mathbf{r}_B) &= 2\sum_{n\ even}(i\omega)^n\int_V Re(a_n(\mathbf{r}))G(\mathbf{r},\mathbf{r}_A)G^*(\mathbf{r},\mathbf{r}_B)dV \\ &\quad -2i\sum_{n\ odd}(i\omega)^n\int_V Im(a_n(\mathbf{r}))G(\mathbf{r},\mathbf{r}_A)G^*(\mathbf{r},\mathbf{r}_B)dV \\ &\quad -\oint_{\partial V} M(G^*(\mathbf{r},\mathbf{r}_B),G(\mathbf{r},\mathbf{r}_A))dS \\ &\quad +2i\int_V G(\mathbf{r},\mathbf{r}_A)\,\mathrm{Im}(H)G^*(\mathbf{r},\mathbf{r}_B)dV\,. \end{aligned} \qquad (68)$$

Note that now for real a_n only the even order coefficients contribute. Also, because of the lack of reciprocity, the arguments of the Green's function differ from those in the corresponding expression (16) for the case of a symmetric operator.

14 EXAMPLE: THE ADVECTION EQUATION

As a simple one-dimensional example of the extraction of the Green's function for a system that is described by an anti-symmetric operator H, we study one-dimensional advection of a fluid. In this case the governing equation is

$$\frac{1}{c(x)}\frac{\partial u}{\partial t} + \frac{\partial u}{\partial x} = q\,, \qquad (69)$$

with the field u advected by the flow. This field could denote, for example, the temperature for advective heat transport or the concentration of a non-reactive contaminant. Consider the case in which the field is determined by its value at a point upstream, rather than by an explicit source term; hence $q = 0$ in expression (69). As shown in figure 6, flow is between two endpoints $x = 0$

Figure 6. Advective transport in a single direction.

and $x = a$, first with flow towards the right, as shown by the solid arrow. Because of the varying width of the channel, as in a venturi, the flow velocity may depend on the x-coordinate. For this system, $a_1(x) = 1/c(x)$, all other a_n are equal to zero, and $H = -\partial/\partial x$. Using integration by parts, the bilinear form M defined in equation (66) is given by

$$M(f,g) = -fg\ . \tag{70}$$

We denote the Green's function which depends on the velocity c, by $G^{(c)}$. For this special case the general expression (68) reduces to

$$G^{(c)}(x_B,x_A) + G^{(c)*}(x_A,x_B) = \Big[G^{(c)}(x,x_A)G^{(c)*}(x,x_B)\Big]_{x=0}^{x=a}\ . \tag{71}$$

Since H is anti-symmetric, reciprocity does not hold. For this type of flow problem, the flow-reversal theorem (Lyamshev, 1961; Brekhovskikh & Godin, 1992; Wapenaar & Fokkema, 2004) states that the arguments of the Green's function can be reversed when the flow is reversed as well:

$$G^{(c)}(x_1,x_2) = -G^{(-c)}(x_2,x_1)\ . \tag{72}$$

Applying this to expression (71) gives

$$G^{(-c)}(x_A,x_B) + G^{(-c)*}(x_B,x_A) = -\Big[G^{(-c)}(x_A,x)G^{(-c)*}(x_B,x)\Big]_{x=0}^{x=a}\ . \tag{73}$$

Note that the velocity c is replaced everywhere by $-c$. Since the sign of the velocity is not important, we drop the superscript $-c$, and consider a flow towards the left as shown by the dashed arrow in figure 6. For the advection equation a source has an influence downstream only; hence the Green's function for a leftward moving flow satisfies

$$G(x,x_0) = 0 \qquad \text{for} \qquad x > x_0\ . \tag{74}$$

Consider two points between the endpoints of the flow ($0 < x_{A,B} < a$). Because of condition (74), the contribution of endpoint $x = 0$ to expression (73) vanishes

$$G(x_A,x_B)+G^*(x_B,x_A) = -G(x_A,x=a)G^*(x_B,x=a)\ . \tag{75}$$

Let u at the right endpoint have power spectrum $|S(\omega)|^2$. Multiplying expression (75) with this power spectrum, and taking the same steps as those leading to expression (41) gives

$$G(x_A,x_B) + G^*(x_B,x_A) = \frac{-1}{|S(\omega)|^2}u(x_A)u^*(x_B)\ . \tag{76}$$

This shows that the sum of the causal and acausal Green's functions can be found by correlating the field recorded at two locations that are generated by a source upstream.

For this problem, the sum of the causal and acausal Green's functions can be reformulated. Consider first the situation where x_B is upstream from x_A; hence $x_B > x_A$. Because of condition (74), the second term in the left hand side of expression (76) vanishes, so that

$$G(x_A,x_B) = \frac{-1}{|S(\omega)|^2}u(x_A)u^*(x_B) \qquad (x_B > x_A)\ . \tag{77}$$

When x_B is downstream from x_A, the first term of expression (76) vanishes by virtue of condition (74), and

$$G^*(x_B,x_A) = \frac{-1}{|S(\omega)|^2}u(x_A)u^*(x_B) \qquad (x_B < x_A)\ . \tag{78}$$

Taking the complex conjugate changes this result into

$$G(x_B,x_A) = \frac{-1}{|S(\omega)|^2}u(x_B)u^*(x_A) \qquad (x_B < x_A)\ . \tag{79}$$

Expressions (77) and (79) can be combined into the general expression

$$G(x_{downstream},x_{upstream}) = \frac{-1}{|S(\omega)|^2}u(x_{downstream})u^*(x_{upstream})\ , \tag{80}$$

where $x_{downstream}$ denotes the downstream point and $x_{upstream}$ the upstream. This means that for the advection equation, the Green's function can be retrieved by cross-correlating the fields generated by a source upstream from both observation points. The extraction of the Green's function for acoustic waves in a medium with flow is described in refs. (Wapenaar *et al.*, 2006b; Wapenaar, 2006; Godin, 2006)

15 RECONSTRUCTING THE GREEN'S FUNCTION AND EQUIPARTITIONING

As shown in the examples, an energy balance is necessary for extracting the Green's function by cross-correlation. This confirms the heuristic arguments of section ??. In this section we explore the requirement of equipartitioning. Let us first consider why the energy current, rather than another current such as the momentum current, plays such a central role in the extraction of the Green's function.

In the derivation of the general expression for extracting the Green's function in section 4, a central step is to multiply the field equation for state A with the complex conjugate of field for state B, and to integrate the result over volume, leading to expression (14). The field equation contains the forcing q. The product of the forcing and the field gives the power supplied by the excitation. This means that expression (14), and subsequent expression, really *are* energy equations. Fokkema, and van den Berg (Fokkema & van den Berg, 1993) use

the phrase *power reciprocity* for the representation theorems of the correlation type.

For random media, a connection between the correlation and the energy transport is made through the Wigner distribution (Wigner, 1932). This distribution is the spatial Fourier transform of the field-field correlation function. Ryzhik et al. (Ryzhik *et al.*, 1996) show for acoustic waves, elastic waves, electromagnetic waves, and matter waves, that in random media the Wigner distribution leads to the equation of radiative transfer, which governs energy transport. Other derivations also used the Wigner distribution to show that for stationary random media, the Green's function of the mean field can be retrieved from the field correlations (Barabanenkov, 1969; Barabanenkov, 1971; Rytov *et al.*, 1989a). Larose *et al.* (Larose *et al.*, 2006) discuss the relation between the Wigner distribution and the extraction of the Green's function in more detail.

We have stressed the importance of equipartitioning as defined by an energy current that is independent of direction. The energy current $J(\mathbf{r},t,\hat{\mathbf{n}})$ satisfies the equation of radiative transfer, which, in the time domain, is given by (Chandrasekhar, 1960; Özisik, 1973; Rytov *et al.*, 1989b)

$$\frac{\partial J(\mathbf{r},t,\hat{\mathbf{n}})}{\partial t} + c\hat{\mathbf{n}}\cdot\nabla J(\mathbf{r},t,\hat{\mathbf{n}}) + (\mu_{in}+\mu_{scat})J(\mathbf{r},t,\hat{\mathbf{n}}) = \int S(\hat{\mathbf{n}},\hat{\mathbf{n}}')J(\mathbf{r},t,\hat{\mathbf{n}}')d^2\hat{\mathbf{n}}' + Q(\mathbf{r},t,\hat{\mathbf{n}}) \; . \tag{81}$$

In this expression μ_{in} and μ_{scat} are damping coefficients due to intrinsic attenuation and scattering losses, respectively. $S(\hat{\mathbf{n}},\hat{\mathbf{n}}')$ accounts for the transfer of energy propagating in the $\hat{\mathbf{n}}'$-direction to the $\hat{\mathbf{n}}$-direction by scattering, and $Q(\mathbf{r},t,\hat{\mathbf{n}})$ denotes energy sources.

In our derivation of the extraction of the Green's function, we use source averaging. Since the source average does not depend on time, its time derivative vanishes. When the energy propagation is the same in all directions, the energy current does not depend on the direction of propagation: $J = J(\mathbf{r},t)$. Consider the source-averaged intensity, which is defined as

$$I(\mathbf{r}) = \langle \int J(\mathbf{r},t)d^2\hat{n}\rangle = 4\pi\langle J(\mathbf{r},t)\rangle \; . \tag{82}$$

When J does not depend on the direction of propagation, the second term of the left-hand side of expression (81) integrates to zero; hence the average intensity satisfies in this case

$$(\mu_{in}+\mu_{scat})I(\mathbf{r}) = \int S(\hat{\mathbf{n}},\hat{\mathbf{n}}')d^2\hat{n}'\; I(\mathbf{r}) + \langle Q(\mathbf{r})\rangle \; , \tag{83}$$

where $\langle Q\rangle$ is the source average of Q averaged over all directions. The damping coefficient for scattering losses follows from the requirement that for lossless media ($\mu_{in} = 0$) in the absence of sources ($\langle Q\rangle = 0$), expression (83) reduces to

$$\mu_{scat} = \int S(\hat{\mathbf{n}},\hat{\mathbf{n}}')d^2\hat{n}' \; , \tag{84}$$

This expression relates the scattering attenuation to $S(\hat{\mathbf{n}},\hat{\mathbf{n}}')$. This relation also holds in the presence of attenuation. Using the previous expression in equation (83) gives

$$\mu_{in}I(\mathbf{r}) = \langle Q(\mathbf{r})\rangle \; . \tag{85}$$

This means that for the source average in a equipartitioned state, the intrinsic attenuation is balanced by the energy sources. This is precisely the requirement that is obtained in sections 8 and 12 for the damped string with fixed ends and for the damped vibrating beam. This condition is also required for attenuating acoustic waves (Snieder, 2006a).

16 DISCUSSION

The theory presented here shows that for a general class of scalar linear systems, the Green's function can be extracted from field correlations. This makes it possible to extract the Green's function for systems other than those for acoustic or elastic waves. Of particular interest are Schrödinger's equation and the diffusion equation, because the theory accounts for the extraction of the Green's function by cross-correlation in quantum mechanics, for the pore fluid pressure in porous media, the diffusive transport of tracers and contaminants, and for electromagnetic waves in attenuating media. The example of the vibrating beam has applications in monitoring bridges, buildings, and other mechanical structures.

The examples shown illustrate the importance of equipartitioning. This condition implies, in particular, that in systems that are not invariant under time-reversal, the sources of the field must be distributed throughout the volume and have a strength proportional to the local attenuation rate. Depending on the application, it might be difficult to realize such a distribution of sources experimentally.

It is not clear what happens when the requirement of equipartitioning is not satisfied. Figure 1 helps understand what happens in that case. Suppose the energy transport along the solid arrow is larger than the energy transport along the dashed arrow. The correlation of the field at the points A and B is larger than the correlation of the fields at the points A and C. The extracted Green's function for the propagation from A to B is therefore stronger than those from A to C. The arrival time, or phase, of the Green's function, however, is not influenced by this mismatch in the energy flow. This suggests that when the condition of equipartitioning is violated, the kinematic properties of the extracted Green's function is correct, although the dynamic properties are not. Experiments with ultrasound (Malcolm *et al.*, 2004) and crustal surface waves (Paul *et al.*, 2005) support this conclusion. This conclusion is also supported by analytic models which show that for elastic waves in a homogeneous medium, the amplitude of the

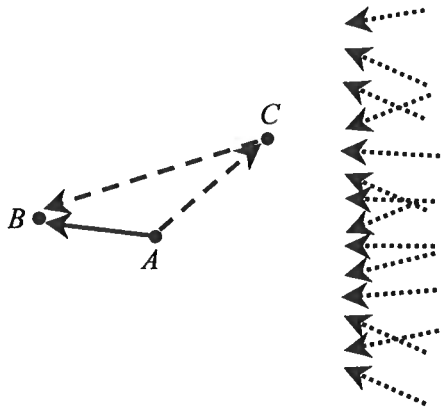

Figure 7. An example in which the direct can be retrieved by cross correlation, but the diffracted wave cannot. Solid arrow: the direct wave propagating from A to B. Dashed arrow: the diffracted wave traveling from A through C to B. Dotted arrows: direction of the the incoming ambient waves used for the extraction of the Green's function.

P and S-waves in the extracted Green's function is correct only when the ratio of the P-wave energy to the S-wave energy equals the value required by equipartitioning, but the phase of the extracted P and S-waves is correct for any value of this ratio (Sánchez-Sesma *et al.*, 2006; Sánchez-Sesma & Campillo, 2006).

Two caveats should be made about the need for equipartitioning. First, note that in the advection example of section 14 there is no need to excite the field on the downstream side. All transport is in the flow direction only; hence equipartitioning is unnecessary in that example. Second, the formalism for the extraction of the Green's function given here gives the superposition of the causal and acausal Green's function. In some situations, such as a homogeneous medium, one-sided energy transport is sufficient to give either the causal or the acausal Green's function. This is illustrated in figure 7 showing incoherent waves are propagating towards the left (dotted arrows). Here, the direct wave propagating from A to B, as indicated by the solid arrow, can be retrieved by cross-correlation, but the direct wave traveling in the opposite direction cannot. This does not mean, however, that the full Green's function for wave propagation from A to B can be retrieved. Suppose a diffractor is present at point C. The diffracted wave traveling from A through C to B, as shown by the dashed arrows, cannot be extracted from the waves coming in from the right. Cross correlation here gives only part of the Green's function (the direct wave).

The words equipartitioning and ensemble average have a well-defined meaning in statistical mechanics that does not necessarily carry over to the macroscopic systems considered here. Note that we have not assumed thermodynamic equilibrium, as used in derivations of the fluctuation-dissipation theorem (Callen & Welton, 1951; Kubo, 1966; Le Bellac *et al.*, 2004). In thermodynamic equilibrium, a state with energy E is weighted by $\exp(-\beta E)$ in the ensemble average, where $\beta^{-1} = kT$ is the thermal energy. In this work, the fields are characterized by a power spectrum $|S(\omega)|^2$ that can be any function of frequency, as long as it is known. The fact that thermodynamic equilibrium is not required is no surprise because the field energy in the macroscopic systems considered here is usually much larger than the thermal energy.

This implies that source average in the context of this paper does not refer to a thermodynamic average. This means, in particular, that at any given moment in time, the system need not be close to a state of equilibrium. Consider, for example, a string that is excited at both endpoints. It does not matter whether the two endpoints are simultaneously excited with an uncorrelated forcing, or one first shakes one endpoint and then the other endpoint. In fact, in the virtual source method (Bakulin & Calvert, 2004; Bakulin & Calvert, 2006) one excites elastic waves sequentially by different sources, and extracts the Green's function by summing over all the sources. Averaging in the context of this work implies an averaging over all sources that are used for the extraction of the Green's function, and equipartitioning is required after averaging over these sources.

Acknowledgments: We appreciate critical and illuminating discussions with Ken Larner and Rodney Calvert, and the comments and corrections of two anonymous reviewers. **Note:** This paper has been published in *Phys. Rev. E.*, **75**, 2007: Pacs 43.20.+g, 46.40.Cd, 03.65.-w, 46.65.+g.

REFERENCES

Aki, K., & Richards, P.G. 2002. *Quantitative Seismology.* Second edn. Sausalito: Univ. Science Books.

Arfken, G.B., & Weber, H.J. 2001. *Mathematical methods for physicists.* 5th edn. Amsterdam: Harcourt.

Bakulin, A., & Calvert, R. 2004. Virtual source: new method for imaging and 4D below complex overburden. *Expanded abstracts of the 2004 SEG-meeting*, 2477–2480.

Bakulin, A., & Calvert, R. 2006. The virtual source method: Theory and case study. *Geophysics*, **71**, SI139–SI150.

Barabanenkov, Yu.N. 1969. Correlation function of a random field at the great optical depth. *Izv. Vyssch. Uchebn. Zaved. Radiofiz.*, **12**(6), 894–899.

Barabanenkov, Yu.N. 1971. The depth regime of the electromagnetic field in a scattering medium. *Izv. Vyssch. Uchebn. Zaved. Radiofiz.*, **14**(6), 887–891.

Brekhovskikh, L.M., & Godin, O.A. 1992. *Acoustics of layered media II. Point sources and boudary beams.* Springer Verlag.

Butkov, E. 1968. *Mathematical Physics.* Reading MA: Addison-Wesley.

Callen, H.B., & Welton, T.A. 1951. Irreversibility and generalized noise. *Phys. Rev.*, **83**, 34–40.

Campillo, M., & Paul, A. 2003. Long-range correlations in the diffuse seismic coda. *Science*, **299**, 547–549.

Chandrasekhar, S. 1960. *Radiative transfer.* New York: Dover.

Chapman, C. 2004. *Fundamentals of seismic wave propagation.* Cambridge, UK: Cambridge Univ. Press.

Chopra, A.K. 1995. *Dynamics of structures; theory and applications to earthquake engineering.* Second edn. Prentice Hall.

Curtis, A., Gerstoft, P., Sato, H., Snieder, R., & Wapenaar, K. 2006. Seismic interferometry – turning noise into signal. *The Leading Edge*, **25**, 1082–1092.

Derode, A., Larose, E., Campillo, M., & Fink, M. 2003a. How to estimate the Green's function for a heterogeneous medium between two passive sensors? Application to acoustic waves. *Appl. Phys. Lett.*, **83**, 3054–3056.

Derode, A., Larose, E., Tanter, M., de Rosny, J., Tourin, A., Campillo, M., & Fink, M. 2003b. Recovering the Green's function from far-field correlations in an open scattering medium. *J. Acoust. Soc. Am.*, **113**, 2973–2976.

Fokkema, J.T., & van den Berg, P.M. 1993. *Seismic applications of acoustic reciprocity.* Amsterdam: Elsevier.

Fokkema, J.T., & van den Berg, P.M. 1996. 4D Geophysical monitoring as an application of the reciprocity theorem. *Pages 99–108 of:* van den Berg, P.M., Blok, H., & Fokkema, J.T. (eds), *Wavefields and reciprocity.* Delft: Delft University Press.

Godin, O.A. 2006. Recovering the acoustic Green's function from ambient noise cross correlation in an inhomogeneous medium. *Phys. Rev. Lett.*, **97**, 054301.

Goldstein, H. 1980. *Classical Mechanics, 2nd Ed.* Reading MA: Addison-Wesley.

Kubo, R. 1966. The fluctuation-dissipation theorem. *Rep. Prog. Phys.*, **29**, 255–284.

Larose, E., Margerin, L., Derode, A., van Tiggelen, B., Campillo, M., Shapiro, N., Paul, A., Stehly, L., & Tanter, M. 2006. Correlation of random wavefields: an interdisciplinary review. *Geophysics*, **71**, SI11–SI21.

Le Bellac, M., Mortessagne, F., & Batrouni, G.G. 2004. *Equilibrium and non-equilibrium statistical thermodynamics.* Cambridge, UK: Cambridge Univ. Press.

Lobkis, O.I., & Weaver, R.L. 2001. On the emergence of the Green's function in the correlations of a diffuse field. *J. Acoust. Soc. Am.*, **110**, 3011–3017.

Lyamshev, L.M. 1961. On some integral relationships in acoustics of moving medium. *Dokl. Akad. Nauk SSSR*, **138**, 575–578.

Malcolm, A., Scales, J., & van Tiggelen, B.A. 2004. Extracting the Green's function from diffuse, equipartitioned waves. *Phys. Rev. E*, **70**, 015601.

Mehta, K., Snieder, R., & Graizer, V. 2007. Extraction of near-surface properties for lossy layered medium using propagator matrix. *Geophys. J. Int., in press.*

Merzbacher, E. 1970. *Quantum Mechanics (2nd Ed.).* New York: Wiley.

Özisik, M.N. 1973. *Radiative transfer and interaction with conduction and convection.* New York: John Wiley.

Paul, A., Campillo, M., Margerin, L., Larose, E., & Derode, A. 2005. Empirical synthesis of time-asymmetrical Green functions from the correlation of coda waves. *J. Geophys. Res.*, **110**, B08302, doi:10.1029/2004JB003521.

Rickett, J.E., & Claerbout, J.F. 1999. Acoustic daylight imaging via spectral factorization; helioseismology and reservoir monitoring. *The Leading Edge*, **18**, 957–960.

Rickett, J.E., & Claerbout, J.F. 2000. Calculation of the sun's acoustic impulse response by multidimensional spectral factorization. *Solar Physics*, **192**, 203–210.

Rickett, J.E., & J.F., Claerbout. 2001. Calculation of the acoustic solar impulse response by multidimensional spectral factorization. *In:* Duvall, T.L., Harvey, J.W., Kosovichev, A.G., & Svestka, Z. (eds), *Helioseismic Diagnostics of Solar Convection and Activity.* Dordrecht: Kluwer Academic Publishers.

Roux, P., Kuperman, W.A., & Group, NPAL. 2004. Extracting coherent wave fronts from acoustic ambient noise in the ocean. *J. Acoust. Soc. Am.*, **116**, 1995–2003.

Roux, P., Sabra, K.G., Kuperman, W.A., & Roux, A. 2005. Ambient noise cross correlation in free space: Theoretical approach. *J. Acoust. Soc. Am.*, **117**, 79–84.

Rytov, S.M., Kravtsov, Yu.A., & Tatarskii, V.I. 1989a. *Principles of statistical radiophysics. Vol. 3, elements of random fields.* Berlin: Springer.

Rytov, S.M., Kravtsov, Yu.A., & Tatarskii, V.I. 1989b. *Principles of statistical radiophysics. Vol. 4, wave propagation.* Berlin: Springer.

Ryzhik, L., Papanicolaou, G., & Keller, J. B. 1996. Transport equations for elastic and other waves in random media. *Wave Motion*, **24**, 327–370.

Sabra, K.G., Roux, P., & Kuperman, W.A. 2005a. Arrival-time structure of the time-averaged ambient noise cross-correlation in an oceanic waveguide. *J. Acoust. Soc. Am.*, **117**, 164–174.

Sabra, K.G., Gerstoft, P., Roux, P., Kuperman, W.A., & Fehler, M.C. 2005b. Extracting time-domain Green's function estimates from ambient seismic noise. *Geophys. Res. Lett.*, **32**, L03310, doi: 10.1029/2004GL021862.

Sabra, K.G., Gerstoft, P., Roux, P., Kuperman, W.A., & Fehler, M.C. 2005c. Surface wave tomography from microseisms in Southern California. *Geophys. Res. Lett.*, **32**, L14311, doi:10.1029/2005GL023155.

Sabra, K.G., Roux, P., Thode, A.M., D'Spain, G.L., & Hodgkiss, W.S. 2005d. Using ocean ambient noise for array self-localization and self-synchronization. *IEEE J. of Oceanic Eng.*, **30**, 338–347.

Sánchez-Sesma, F.J., & Campillo, M. 2006. Retrieval of the Green's funciton from cross correlation: The canonical elastic problem. *Bull. Seismol. Soc. Am.*, **96**, 1182–1191.

Sánchez-Sesma, F.J., Pérez-Ruiz, J.A., Campillo, M., & Luzón, F. 2006. Elastodynamic 2D Green function retrieval from cross-correlation: Canonical inclusion problem. *Geophys. Res. Lett.*, **33**, L13305, doi:10.1029/2006GL026454.

Schuster, G.T., Yu, J., Sheng, J., & Rickett, J. 2004. Interferometric/daylight seismic imaging. *Geophys. J. Int.*, **157**, 838–852.

Sens-Schönfelder, C., & Wegler, U. 2006. Passive image interferometry and seasonal variations at Merapi volcano, Indonesia. *Geophys. Res. Lett.*, **33**, L21302, doi:10.1029/2006GL027797.

Shapiro, N.M., & Campillo, M. 2004. Emergence of broadband Rayleigh waves from correlations of the ambient seismic noise. *Geophys. Res. Lett.*, **31**, L07614, doi10.1029/2004GL019491.

Shapiro, N.M., Campillo, M., Stehly, L., & Ritzwoller, M.H. 2005. High-resolution surface-wave tomography from ambient seismic noise. *Science*, **307**, 1615–1618.

Snieder, R. 2004a. Extracting the Green's function from the correlation of coda waves: A derivation based on stationary phase. *Phys. Rev. E*, **69**, 046610.

Snieder, R. 2004b. *A Guided Tour of Mathematical Methods for the Physical Sciences*. 2nd edn. Cambridge, UK: Cambridge Univ. Press.

Snieder, R. 2006a. Extracting the Green's function of attenuating acoustic media from uncorrelated waves. *Submitted to J. Acoust. Soc. Am.*

Snieder, R. 2006b. Retrieving the Green's function of the diffusion equation from the response to a random forcing. *Phys. Rev. E*, **74**, 046620.

Snieder, R., & Şafak, E. 2006. Extracting the building response using seismic interferometry; theory and application to the Millikan Library in Pasadena, California. *Bull. Seismol. Soc. Am.*, **96**, 586–598.

Snieder, R., Sheiman, J., & Calvert, R. 2006a. Equivalence of the virtual source method and wavefield deconvolution in seismic interferometry. *Phys. Rev. E*, **73**, 066620.

Snieder, R., Wapenaar, K., & Larner, K. 2006b. Spurious multiples in seismic interferometry of primaries. *Geophysics*, **71**, SI111–SI124.

Thompson, D., & Snieder, R. 2006. Seismic anisotropy of a building. *The Leading Edge*, **25**, 1093.

Wapenaar, K. 2004. Retrieving the elastodynamic Green's function of an arbitrary inhomogeneous medium by cross correlation. *Phys. Rev. Lett.*, **93**, 254301.

Wapenaar, K. 2006. Nonreciprocal Green's function retrieval by cross correlation. *J. Acoust. Soc. Am.*, **120**, EL7–EL13.

Wapenaar, K., & Fokkema, J. 2004. Reciprocity theorems for diffusion, flow and waves. *J. Appl. Mech.*, **71**, 145–150.

Wapenaar, K., Fokkema, J., & Snieder, R. 2005. Retrieving the Green's function by cross-correlation: a comparison of approaches. *J. Acoust. Soc. Am.*, **118**, 2783–2786.

Wapenaar, K., Dragonv, D., & Robertsson, J. 2006a. Introduction to the supplement on seismic interferometry. *Geophysics*, **71**, SI1–SI4.

Wapenaar, K., Slob, E., & Snieder, R. 2006b. Unified Green's function retrieval by cross-correlation. *Phys. Rev. Lett.*, **97**, 234301.

Weaver, R., & Lobkis, O. 2003. On the emergence of the Green's function in the correlations of a diffuse field: pulse-echo using thermal phonons. *Ultrasonics*, **40**, 435–439.

Weaver, R.L. 1982. On Diffuse Waves in Solid Media. *J. Acoust. Soc. Am.*, **71**, 1608–1609.

Weaver, R.L., & Lobkis, O.I. 2001. Ultrasonics without a source: Thermal fluctuation correlations and MHz frequencies. *Phys. Rev. Lett.*, **87**, 134301.

Weaver, R.L., & Lobkis, O.I. 2004. Diffuse fields in open systems and the emergence of the Green's function. *J. Acoust. Soc. Am.*, **116**, 2731–2734.

Weaver, R.L., & Lobkis, O.I. 2005. Fluctuations in diffuse field-field correlations and the emergence of the Green's function in open systems. *J. Acoust. Soc. Am.*, **117**, 3432–3439.

Wegler, U., & Sens-Schönfelder, C. 2006. Fault zone monitoring with passive image interferometry. *Geophys. J. Int., in press.*

Wigner, E. 1932. On the quantum correction for thermodynamic equilibrium. *Phys. Rev.*, **40**, 749–759.

APPENDIX A: AN EXAMPLE THAT A VANISHING NET ENERGY CURRENT DOES NOT IMPLY EQUIPARTITIONING

The net energy transport $\mathbf{J}^{(net)}$ is the energy current averaged over all directions

$$\mathbf{J}^{(net)} = \oint J(\hat{\mathbf{n}})\hat{\mathbf{n}}\, d^2n \,, \tag{A1}$$

where $\oint(\cdots)d^2n$ denotes an integration over all directions. At every point in space the energy current can be expanded in spherical harmonics

$$J(\theta,\varphi) = \sum_{l,m} J_{l,m} Y_{l,m}(\theta,\varphi) \,, \tag{A2}$$

where the angles θ and φ are the polar angles of the propagation direction $\hat{\mathbf{n}}$:

$$\hat{\mathbf{n}} = \begin{pmatrix} \sin\theta\cos\varphi \\ \sin\theta\sin\varphi \\ \cos\theta \end{pmatrix} . \tag{A3}$$

Rather than considering the Cartesian components of $\hat{\mathbf{n}}$, we consider for brevity (Arfken & Weber, 2001)

$$n_x \pm i n_y = \sin\theta \exp(\pm i\varphi) = \mp\sqrt{\frac{8\pi}{3}} Y_{1,\pm 1}(\theta,\varphi) \,, \tag{A4}$$

and

$$n_z = \cos\theta = \sqrt{\frac{4\pi}{3}} Y_{1,0}(\theta,\varphi) \,. \tag{A5}$$

The corresponding components of the net energy current are given by

$$J_x^{(net)} \pm i J_y^{(net)} = \sum_{l,m} J_{l,m} \oint Y_{l,m}(\theta,\varphi) \sin\theta e^{\pm i\varphi} d^2n \,, \tag{A6}$$

and

$$J_z^{(net)} = \sum_{l,m} J_{l,m} \oint Y_{l,m}(\theta,\varphi) \cos\theta \, d^2n \,, \tag{A7}$$

Because of the orthogonality of the spherical harmonics (Arfken & Weber, 2001)

$$J_x^{(net)} \pm i J_y^{(net)} = \mp\sqrt{\frac{8\pi}{3}} J_{1,\mp 1} \,, \; J_z^{(net)} = \sqrt{\frac{4\pi}{3}} J_{1,0} \,. \tag{A8}$$

The condition that the net energy current vanishes thus implies that

$$J_{l=1,m} = 0 \,, \; m = 0, \pm 1 \,. \tag{A9}$$

A vanishing energy current thus requires only that the coefficients $J_{l=1,m}$ vanish. For a vanishing net energy current $\mathbf{J}^{(net)} = 0$, all coefficients $J_{l,m}$ with $l \neq 1$ can be nonzero. This means that an energy current given by expansion (A2) with nonzero coefficients $J_{l,m}$ for $l > 1$ gives a vanishing net energy current, while the energy current $J(\hat{\mathbf{n}})$ varies with direction. In this case the net energy current vanishes, but there is no equipartitioning.

CWP-571

Unified Green's function retrieval by cross-correlation

Kees Wapenaar[1], Evert Slob[1] & Roel Snieder[2]
[1] *Department of Geotechnology, Delft University of Technology, 2600 GA Delft, The Netherlands*
[2] *Center for Wave Phenomena, Colorado School of Mines, Golden CO 80401, USA*

ABSTRACT
It has been shown by many authors that the cross-correlation of two recordings of a diffuse wave field at different receivers yields the Green's function between these receivers. Recently the theory has been extended for situations where time-reversal invariance does not hold (e.g. in attenuating media) and where source-receiver reciprocity breaks down (in moving fluids). Here we present a unified theory for Green's function retrieval which captures all these situations and, due to the unified form, readily extends to more complex situations, such as electrokinetic Green's function retrieval in poro-elastic or piezoelectric media. The unified theory has a wide range of applications in 'remote sensing without a source'.

Key words: interferometry, general vector systems

1 INTRODUCTION

Since the pioneering work of Weaver and Lobkis (Weaver & Lobkis, 2001; Weaver & Lobkis, 2002), Campillo and Paul (Campillo & Paul, 2003) and others, the literature on retrieving the acoustic Green's function from the cross-correlation of two recordings of a diffuse wave field has expanded spectacularly. Apart from the many successful demonstrations of the method on ultrasonic, geophysical and oceanographic data, many theoretical developments have been published as well (Lobkis & Weaver, 2001); (Derode *et al.*, 2003); (van Tiggelen, 2003); (Malcolm *et al.*, 2004); (Snieder, 2004); (Roux *et al.*, 2005); (Weaver & Lobkis, 2005); (Sánchez-Sesma *et al.*, 2006). One particular branch of theory is based on the reciprocity principle (Wapenaar *et al.*, 2002); (Wapenaar, 2004); (Weaver & Lobkis, 2004); (van Manen *et al.*, 2005). This theory applies to arbitrary inhomogeneous anisotropic media and therefore not only accounts for the reconstruction of the ballistic wave but also for the primary and multiply scattered waves present in the coda of the Green's function. Recent developments in this branch of research are the extension for situations where time-reversal invariance does not hold (as for electromagnetic waves in conducting media (Slob *et al.*, 2006a); (Slob *et al.*, 2006b); (Slob & Wapenaar, 2006), acoustic waves in attenuating media (Snieder, 2006a), or general scalar diffusion phenomena (Snieder, 2006b)), as well as for situations where source-receiver reciprocity breaks down (as in moving fluids (Wapenaar, 2006b); (Godin, 2006)). In this Letter we develop a unified representation of Green's functions in terms of cross-correlations that covers all these cases. Due to the unified formulation, the theory readily extends to more complex situations, such as electrokinetic Green's function retrieval in poro-elastic or piezoelectric media. From this extension it follows, for example, that the cross-correlation of passive elastodynamic and electric noise observations at two different receivers yields the elastodynamic response that would be observed at one of the receiver positions as if there were an impulsive electric current source at the other. Hence, cross-correlating passive measurements may lead to the remote sensing response of the electrokinetic coupling coefficient, which, in case of a porous medium, contains relevant information about the permeability of the medium under investigation.

2 GENERAL MATRIX-VECTOR EQUATION

Diffusion, flow and wave phenomena can each be captured by the following differential equation in matrix-vector form (de Hoop & de Hoop, 2000); (Wapenaar & Fokkema, 2004), $\mathbf{A}\frac{D\mathbf{u}}{Dt} + \mathbf{B}\mathbf{u} + \mathbf{D}_\mathbf{x}\mathbf{u} = \mathbf{s}$, where

$\mathbf{u} = \mathbf{u}(\mathbf{x},t)$ is a vector containing space- and time-dependent field quantities, $\mathbf{s} = \mathbf{s}(\mathbf{x},t)$ is a source vector, $\mathbf{A} = \mathbf{A}(\mathbf{x})$ and $\mathbf{B} = \mathbf{B}(\mathbf{x})$ are matrices containing space-dependent material parameters and $\mathbf{D}_\mathbf{x}$ is a matrix containing the spatial differential operators ∂_1, ∂_2 and ∂_3. D/Dt denotes the material time derivative, defined as $D/Dt = \partial/\partial t + \mathbf{v}^0 \cdot \boldsymbol{\nabla}$, where $\partial/\partial t$ is the time derivative in the reference frame and $\mathbf{v}^0 = \mathbf{v}^0(\mathbf{x})$ the space-dependent flow velocity of the material; the term $\mathbf{v}^0 \cdot \boldsymbol{\nabla}$ vanishes in non-moving media. For each application, there exists a real-valued diagonal matrix $\mathbf{K} = \mathbf{K}^{-1}$ such that $\mathbf{KAK} = \mathbf{A} = \mathbf{A}^T$, $\mathbf{KBK} = \mathbf{B}^T$ and $\mathbf{KD}_\mathbf{x}\mathbf{K} = -\mathbf{D}_\mathbf{x}^T$ (superscript T denotes transposition).

For mass diffusion of a species through a mixture, $\mathbf{u}^T = (Y, J_1, J_2, J_3)$ (with Y denoting the mass fraction of the species and J_i the mass flux relative to the mixture), $\mathbf{s}^T = (\dot{\omega}, 0, 0, 0)$ (with $\dot{\omega}$ the mass production rate), $\mathbf{A} = \rho\,\mathrm{diag}(1,0,0,0)$ (with ρ the mass density), $\mathbf{B} = \frac{1}{\rho\mathcal{D}}\,\mathrm{diag}(0,1,1,1)$ (with $\mathcal{D}$ the diffusion coefficient), $\mathbf{K} = \mathrm{diag}(1,-1,-1,-1)$ and

$$\mathbf{D}_\mathbf{x} = \begin{pmatrix} 0 & \partial_1 & \partial_2 & \partial_3 \\ \partial_1 & 0 & 0 & 0 \\ \partial_2 & 0 & 0 & 0 \\ \partial_3 & 0 & 0 & 0 \end{pmatrix}. \tag{1}$$

For other scalar diffusion processes the vectors and matrices are defined in a similar way.

For acoustic wave propagation in a moving attenuating fluid, $\mathbf{u}^T = (p, v_1, v_2, v_3)$ (with p the acoustic pressure and v_i the particle velocity), $\mathbf{s}^T = (q, f_1, f_2, f_3)$ (with q the volume injection rate and f_i the external force), $\mathbf{A} = \mathrm{diag}(\kappa, \rho, \rho, \rho)$ (with κ the compressibility and ρ the mass density), $\mathbf{B} = \mathrm{diag}(b^p, b^v, b^v, b^v)$ (with b^p and b^v the loss terms), $\mathbf{K} = \mathrm{diag}(1,-1,-1,-1)$ and $\mathbf{D}_\mathbf{x}$ again defined by equation (1). The spatial variations of the flow velocity $\mathbf{v}^0$ are assumed small in comparison with those of the particle velocity of the acoustic wave field (this assumption can be relaxed, but then the equations become more involved (Godin, 2006)).

For electromagnetic diffusion and/or wave propagation in a non-moving anisotropic medium, $\mathbf{u}^T = (\mathbf{E}^T, \mathbf{H}^T)$ (with $\mathbf{E}$ and $\mathbf{H}$ the electric and magnetic field vectors), $\mathbf{s}^T = -(\{\mathbf{J}^e\}^T, \{\mathbf{J}^m\}^T)$ (with $\mathbf{J}^e$ and $\mathbf{J}^m$ the external electric and magnetic current density vectors), $\mathbf{A} = \mathrm{blockdiag}(\boldsymbol{\epsilon}, \boldsymbol{\mu})$ (with $\boldsymbol{\epsilon}$ and $\boldsymbol{\mu}$ the permittivity and permeability tensors), $\mathbf{B} = \mathrm{blockdiag}(\boldsymbol{\sigma}^e, \boldsymbol{\sigma}^m)$ (with $\boldsymbol{\sigma}^e$ and $\boldsymbol{\sigma}^m$ the electric and magnetic conductivity tensors), $\mathbf{K} = \mathrm{diag}(-1,-1,-1,1,1,1)$ and

$$\mathbf{D}_\mathbf{x} = \begin{pmatrix} \mathbf{O} & \mathbf{D}_0^T \\ \mathbf{D}_0 & \mathbf{O} \end{pmatrix}, \mathbf{D}_0 = \begin{pmatrix} 0 & -\partial_3 & \partial_2 \\ \partial_3 & 0 & -\partial_1 \\ -\partial_2 & \partial_1 & 0 \end{pmatrix}. \tag{2}$$

For elastodynamic wave propagation in a solid, $\mathbf{u}^T = (\mathbf{v}^T, -\boldsymbol{\tau}_1^T, -\boldsymbol{\tau}_2^T, -\boldsymbol{\tau}_3^T)$ (with $\mathbf{v}$ and $\boldsymbol{\tau}_i$ the particle velocity and traction vectors), $\mathbf{s}^T = (\mathbf{f}^T, \mathbf{h}_1^T, \mathbf{h}_2^T, \mathbf{h}_3^T)$ (with $\mathbf{f}$ and $\mathbf{h}_i$ the external force and deformation rate vectors), and matrices $\mathbf{A}$, $\mathbf{B}$, $\mathbf{K}$ and $\mathbf{D}_\mathbf{x}$ defined in (Wapenaar & Fokkema, 2004).

For electroseismic wave propagation in a saturated porous solid (Pride, 1994), (Pride & Haartsen, 1996), $\mathbf{u}^T = (\mathbf{E}^T, \mathbf{H}^T, \{\mathbf{v}^s\}^T, -\boldsymbol{\tau}_1^T, -\boldsymbol{\tau}_2^T, -\boldsymbol{\tau}_3^T, \mathbf{w}^T, p^f)$ (with $\mathbf{w} = \varphi(\mathbf{v}^f - \mathbf{v}^s)$ the filtration velocity, φ the porosity, and superscripts s and f referring to the solid and fluid phase, respectively), $\mathbf{s}^T = (-\{\mathbf{J}^e\}^T, -\{\mathbf{J}^m\}^T, \mathbf{f}^T, \mathbf{0}^T, \mathbf{0}^T, \mathbf{0}^T, \{\mathbf{f}^f\}^T, 0)$, and matrices $\mathbf{A}$, $\mathbf{B}$, $\mathbf{K}$ and $\mathbf{D}_\mathbf{x}$ defined in (Wapenaar & Fokkema, 2004). Omitting $\mathbf{E}$, $\mathbf{H}$, $\mathbf{J}^e$ and $\mathbf{J}^m$ from $\mathbf{u}$ and $\mathbf{s}$ gives the field and source vectors for the Biot theory (Biot, 1956). On the other hand, omitting $\mathbf{w}$, p^f and $\mathbf{f}^f$ and reorganizing $\mathbf{B}$ results in the electrokinetic equations for a piezoelectric system (Auld, 1973).

In all cases, matrices $\mathbf{A}(\mathbf{x})$ and $\mathbf{B}(\mathbf{x})$ can be replaced by convolutional operators $\mathbf{A}(\mathbf{x},t)*$ and $\mathbf{B}(\mathbf{x},t)*$ to account for more general attenuation mechanisms. We define the Fourier transform of a time-dependent function $f(t)$ as $\hat{f}(\omega) = \int f(t)\exp(-j\omega t)\mathrm{d}t$, where j is the imaginary unit and ω denotes the angular frequency. Applying the Fourier transform to all terms in the matrix-vector equation (with $\mathbf{A}$ and $\mathbf{B}$ defined as convolutional operators) yields $\hat{\mathbf{A}}(j\omega + \mathbf{v}^0\cdot\boldsymbol{\nabla})\hat{\mathbf{u}} + \hat{\mathbf{B}}\hat{\mathbf{u}} + \mathbf{D}_\mathbf{x}\hat{\mathbf{u}} = \hat{\mathbf{s}}$.

3 RECIPROCITY THEOREM OF THE CONVOLUTION TYPE

In general, a reciprocity theorem interrelates two independent states in one and the same domain (de Hoop, 1966), (Fokkema & van den Berg, 1993). We consider two independent states that are distinguished by subscripts A and B. For an arbitrary spatial domain $\mathbb{D}$ with boundary $\partial\mathbb{D}$ and outward pointing normal vector $\mathbf{n}^T = (n_1, n_2, n_3)$, the convolution-type reciprocity theorem relating these two states reads (Wapenaar & Fokkema, 2004)

$$\int_\mathbb{D} \left[\hat{\mathbf{u}}_A^T\mathbf{K}\hat{\mathbf{s}}_B - \hat{\mathbf{s}}_A^T\mathbf{K}\hat{\mathbf{u}}_B\right]\mathrm{d}^3\mathbf{x} = \oint_{\partial\mathbb{D}} \hat{\mathbf{u}}_A^T\hat{\mathbf{M}}_1\hat{\mathbf{u}}_B\,\mathrm{d}^2\mathbf{x} + \int_\mathbb{D} \hat{\mathbf{u}}_A^T\hat{\mathbf{M}}_2\hat{\mathbf{u}}_B\,\mathrm{d}^3\mathbf{x}, \tag{3}$$

where $\hat{\mathbf{M}}_1 = \mathbf{K}\{\mathbf{N}_\mathbf{x} - \hat{\mathbf{A}}_A(\mathbf{v}_A^0\cdot\mathbf{n})\}$ and $\hat{\mathbf{M}}_2 = \mathbf{K}\{\hat{\mathbf{A}}_B(j\omega + \mathbf{v}_B^0\cdot\boldsymbol{\nabla}) - \hat{\mathbf{A}}_A(j\omega - \mathbf{v}_A^0\cdot\boldsymbol{\nabla}) + \hat{\mathbf{B}}_B - \hat{\mathbf{B}}_A\}$, with $\mathbf{N}_\mathbf{x}$ defined similar as $\mathbf{D}_\mathbf{x}$, but with ∂_i replaced by n_i (hence, $\mathbf{N}_\mathbf{x}$ obeys the symmetry relation $\mathbf{KN}_\mathbf{x}\mathbf{K} = -\mathbf{N}_\mathbf{x}^T$). We speak of a convolution-type reciprocity theorem because the multiplications in the frequency domain ($\hat{\mathbf{u}}_A^T\mathbf{K}\hat{\mathbf{s}}_B$ etc.) correspond to convolutions in the time domain.

4 GREEN'S MATRIX

In state A we replace the space- and frequency-dependent $L \times 1$ source vector $\hat{\mathbf{s}}_A(\mathbf{x},\omega)$ by a $L \times L$

frequency-independent point source matrix $\mathbf{I}\delta(\mathbf{x}-\mathbf{x}_A)$, where $\mathbf{I}$ is the identity matrix. Correspondingly, the $L\times 1$ field vector $\hat{\mathbf{u}}_A(\mathbf{x},\omega)$ is replaced by a $L\times L$ Green's matrix $\hat{\mathbf{G}}(\mathbf{x},\mathbf{x}_A,\omega)$. For example, the acoustic Green's matrix is given by

$$\hat{\mathbf{G}}(\mathbf{x},\mathbf{x}_A,\omega)=\begin{pmatrix}\hat{G}^{p,q} & \hat{G}^{p,f}_{,1} & \hat{G}^{p,f}_{,2} & \hat{G}^{p,f}_{,3}\\ \hat{G}^{v,q}_{1} & \hat{G}^{v,f}_{1,1} & \hat{G}^{v,f}_{1,2} & \hat{G}^{v,f}_{1,3}\\ \hat{G}^{v,q}_{2} & \hat{G}^{v,f}_{2,1} & \hat{G}^{v,f}_{2,2} & \hat{G}^{v,f}_{2,3}\\ \hat{G}^{v,q}_{3} & \hat{G}^{v,f}_{3,1} & \hat{G}^{v,f}_{3,2} & \hat{G}^{v,f}_{3,3}\end{pmatrix}(\mathbf{x},\mathbf{x}_A,\omega). \tag{4}$$

The superscripts refer to the type of observed wave field at $\mathbf{x}$ and the source type at $\mathbf{x}_A$, respectively; the subscripts denote the different components. Note that each column represents a field vector at $\mathbf{x}$ due to one particular source type at $\mathbf{x}_A$.

For state B we choose the medium parameters identical to those in state A (i.e., $\hat{\mathbf{A}}_B=\hat{\mathbf{A}}_A$, $\hat{\mathbf{B}}_B=\hat{\mathbf{B}}_A$) and we choose the flow velocity opposite to that in state A (i.e., $\mathbf{v}^0_B=-\mathbf{v}^0_A$), hence, $\hat{\mathbf{M}}_2$ vanishes. We replace the source vector $\hat{\mathbf{s}}_B(\mathbf{x},\omega)$ and the field vector $\hat{\mathbf{u}}_B(\mathbf{x},\omega)$ by $\mathbf{I}\delta(\mathbf{x}-\mathbf{x}_B)$ and $\hat{\mathbf{G}}_r(\mathbf{x},\mathbf{x}_B,\omega)$, respectively, where the subscript r refers to the reversed flow velocity. With these replacements, equation (3) becomes a reciprocity relation for the Green's matrix. The second term on the right-hand side vanishes due to the choice of the opposite flow velocities (flow-reversal theorem (Lyamshev, 1961), (Brekhovskikh & Godin, 1992), (Wapenaar & Fokkema, 2004)). When we choose $\mathbf{x}_A$ and $\mathbf{x}_B$ both in $\mathbb{D}$ and assume that outside a sphere with finite radius the medium is homogeneous, isotropic and non-flowing, then the boundary integral vanishes as well. This leaves the source-receiver reciprocity relation

$$\mathbf{K}\hat{\mathbf{G}}^T(\mathbf{x}_B,\mathbf{x}_A,\omega)\mathbf{K}=\hat{\mathbf{G}}_r(\mathbf{x}_A,\mathbf{x}_B,\omega). \tag{5}$$

Note that for non-flowing media the subscript r can be omitted.

5 RECIPROCITY THEOREM OF THE CORRELATION TYPE

We consider a modified version of the reciprocity theorem. For an arbitrary spatial domain $\mathbb{D}$ with boundary $\partial\mathbb{D}$ and outward pointing normal vector $\mathbf{n}$, the correlation-type reciprocity theorem reads (Wapenaar & Fokkema, 2004)

$$\int_{\mathbb{D}}\left[\hat{\mathbf{u}}_A^\dagger\hat{\mathbf{s}}_B+\hat{\mathbf{s}}_A^\dagger\hat{\mathbf{u}}_B\right]\mathrm{d}^3\mathbf{x}$$
$$=\oint_{\partial\mathbb{D}}\hat{\mathbf{u}}_A^\dagger\hat{\mathbf{M}}_3\hat{\mathbf{u}}_B\,\mathrm{d}^2\mathbf{x}+\int_{\mathbb{D}}\hat{\mathbf{u}}_A^\dagger\hat{\mathbf{M}}_4\hat{\mathbf{u}}_B\,\mathrm{d}^3\mathbf{x} \tag{6}$$

(superscript $\dagger$ denotes transposition and complex conjugation), where $\hat{\mathbf{M}}_3=\mathbf{N}_\mathbf{x}+\hat{\mathbf{A}}_A^\dagger(\mathbf{v}^0_A\cdot\mathbf{n})$ and $\hat{\mathbf{M}}_4=\hat{\mathbf{A}}_B(j\omega+\mathbf{v}^0_B\cdot\boldsymbol{\nabla})-\hat{\mathbf{A}}_A^\dagger(j\omega+\mathbf{v}^0_A\cdot\boldsymbol{\nabla})+\hat{\mathbf{B}}_B+\hat{\mathbf{B}}_A^\dagger$. We speak of a correlation-type reciprocity theorem because the multiplications in the frequency domain ($\hat{\mathbf{u}}_A^\dagger\hat{\mathbf{s}}_B$ etc.) correspond to correlations in the time domain.

6 GREEN'S MATRIX REPRESENTATION

We use equation (6) to derive a representation of the Green's matrix in terms of cross-correlations. To this end we replace the source vectors again by point source matrices and the field vectors by Green's matrices. We choose $\mathbf{x}_A$ and $\mathbf{x}_B$ again both in $\mathbb{D}$, but other choices are relevant as well (Slob *et al.*, 2006a), (Slob *et al.*, 2006b), (Slob & Wapenaar, 2006). This time we choose $\hat{\mathbf{A}}_B=\hat{\mathbf{A}}_A=\hat{\mathbf{A}}$, $\hat{\mathbf{B}}_B=\hat{\mathbf{B}}_A=\hat{\mathbf{B}}$ and $\mathbf{v}^0_B=\mathbf{v}^0_A=-\mathbf{v}^0$, so the Green's matrices in both states are defined for the situation of reversed flow. Next we use equation (5) as well as the symmetry relations for $\hat{\mathbf{A}}$, $\hat{\mathbf{B}}$ and $\mathbf{N}_\mathbf{x}$. Transposing both sides of the resulting equation yields

$$\hat{\mathbf{G}}(\mathbf{x}_B,\mathbf{x}_A,\omega)+\hat{\mathbf{G}}^\dagger(\mathbf{x}_A,\mathbf{x}_B,\omega)=$$
$$-\oint_{\partial\mathbb{D}}\hat{\mathbf{G}}(\mathbf{x}_B,\mathbf{x},\omega)\hat{\mathbf{M}}_5\hat{\mathbf{G}}^\dagger(\mathbf{x}_A,\mathbf{x},\omega)\,\mathrm{d}^2\mathbf{x}$$
$$+\int_{\mathbb{D}}\hat{\mathbf{G}}(\mathbf{x}_B,\mathbf{x},\omega)\hat{\mathbf{M}}_6\hat{\mathbf{G}}^\dagger(\mathbf{x}_A,\mathbf{x},\omega)\,\mathrm{d}^3\mathbf{x}, \tag{7}$$

with $\hat{\mathbf{M}}_5=\mathbf{N}_\mathbf{x}+\hat{\mathbf{A}}^\dagger(\mathbf{v}^0\cdot\mathbf{n})$ and $\hat{\mathbf{M}}_6=-(\underleftarrow{\nabla}\cdot\mathbf{v}^0-j\omega)2j\Im(\hat{\mathbf{A}})+\hat{\mathbf{B}}+\hat{\mathbf{B}}^\dagger$, where $\underleftarrow{\nabla}$ acts on the quantity left of it and $\Im$ denotes the imaginary part. Note that $\Im(\hat{\mathbf{A}})$ and $\hat{\mathbf{B}}+\hat{\mathbf{B}}^\dagger$ account for the attenuation of the medium. Since we used equation (5), the Green's matrices are now defined in a medium with flow velocity $+\mathbf{v}^0$ (or zero flow in case of a non-moving medium). Equation (7) is a general representation of the Green's matrix between $\mathbf{x}_A$ and $\mathbf{x}_B$ in terms of cross-correlations of observed fields at $\mathbf{x}_A$ and $\mathbf{x}_B$ due to sources at $\mathbf{x}$ on the boundary $\partial\mathbb{D}$ as well as in the domain $\mathbb{D}$. The inverse Fourier transform of the left-hand side is $\mathbf{G}(\mathbf{x}_B,\mathbf{x}_A,t)+\mathbf{G}^T(\mathbf{x}_A,\mathbf{x}_B,-t)$, from which $\mathbf{G}(\mathbf{x}_B,\mathbf{x}_A,t)$ is obtained by taking the causal part. The application of equation (7) requires independent measurements of the impulse responses of different types of sources at all $\mathbf{x}\in\mathbb{D}\cup\partial\mathbb{D}$. In the following we modify the right-hand side into a direct cross-correlation (i.e., without the integrals) of diffuse field observations at $\mathbf{x}_A$ and $\mathbf{x}_B$, the diffusivity being due to a distribution of uncorrelated noise sources. Following Snieder (Snieder, 2006a) we separately consider the situation for uncorrelated sources in $\mathbb{D}$ and on $\partial\mathbb{D}$.

7 UNCORRELATED SOURCES IN $\mathbb{D}$

The boundary integral vanishes when homogeneous boundary conditions apply at $\partial\mathbb{D}$ or, in case of infinite $\mathbb{D}$, when one or more elements of the loss matrices $\Im(\hat{\mathbf{A}})$ or $\hat{\mathbf{B}}+\hat{\mathbf{B}}^\dagger$ are non-zero throughout space. For these situations we consider a noise distribution $\hat{\mathbf{s}}(\mathbf{x},\omega)$ throughout $\mathbb{D}$, where $\hat{\mathbf{s}}$ is a vector with elements $\hat{s}_k$. We assume

that two noise sources $\hat{s}_k(\mathbf{x},\omega)$ and $\hat{s}_l(\mathbf{x}',\omega)$ are mutually uncorrelated for any $k \neq l$ and $\mathbf{x} \neq \mathbf{x}'$ in $\mathbb{D}$, and that their power spectrum is the same for all $\mathbf{x}$ and k, apart from a space- and frequency dependent excitation function. Hence, we assume that these noise sources obey the relation $\langle \hat{\mathbf{s}}(\mathbf{x}',\omega)\hat{\mathbf{s}}^\dagger(\mathbf{x},\omega)\rangle = \hat{\boldsymbol{\lambda}}(\mathbf{x},\omega)\delta(\mathbf{x}-\mathbf{x}')\hat{S}(\omega)$, where $\langle\cdot\rangle$ denotes a spatial ensemble average, $\hat{S}(\omega)$ the power spectrum of the noise, and $\hat{\boldsymbol{\lambda}}(\mathbf{x},\omega)$ is a diagonal matrix containing the excitation functions. We express the observed field vector at $\mathbf{x}_A$ as $\hat{\mathbf{u}}^{\mathrm{obs}}(\mathbf{x}_A,\omega) = \int_{\mathbb{D}} \hat{\mathbf{G}}(\mathbf{x}_A,\mathbf{x},\omega)\hat{\mathbf{s}}(\mathbf{x},\omega)\,\mathrm{d}^3\mathbf{x}$ (and a similar expression for $\hat{\mathbf{u}}^{\mathrm{obs}}(\mathbf{x}_B,\omega)$). Evaluating the cross-correlation of the observed fields yields

$$\langle \hat{\mathbf{u}}^{\mathrm{obs}}(\mathbf{x}_B,\omega)\{\hat{\mathbf{u}}^{\mathrm{obs}}(\mathbf{x}_A,\omega)\}^\dagger\rangle = \int_{\mathbb{D}} \hat{\mathbf{G}}(\mathbf{x}_B,\mathbf{x},\omega)\hat{\boldsymbol{\lambda}}(\mathbf{x},\omega)\,\hat{\mathbf{G}}^\dagger(\mathbf{x}_A,\mathbf{x},\omega)\hat{S}(\omega)\,\mathrm{d}^3\mathbf{x}. \quad (8)$$

Comparing this with the right-hand side of equation (7) (with vanishing boundary integral), we obtain

$$\{\hat{\mathbf{G}}(\mathbf{x}_B,\mathbf{x}_A,\omega) + \hat{\mathbf{G}}^\dagger(\mathbf{x}_A,\mathbf{x}_B,\omega)\}\hat{S}(\omega) = \langle \hat{\mathbf{u}}^{\mathrm{obs}}(\mathbf{x}_B,\omega)\{\hat{\mathbf{u}}^{\mathrm{obs}}(\mathbf{x}_A,\omega)\}^\dagger\rangle, \quad (9)$$

assuming $\hat{\boldsymbol{\lambda}}(\mathbf{x},\omega) = \hat{\mathbf{M}}_6(\mathbf{x},\omega)$. Hence, for those situations in which $\hat{\mathbf{M}}_6$ is a diagonal matrix with one or more non-zero elements (e.g. for scalar diffusion or acoustic wave propagation in an attenuating medium with either real-valued $\hat{\mathbf{A}}$ or zero flow velocity $\mathbf{v}^0$, for electromagnetic diffusion and/or wave propagation in a non-moving isotropic attenuating medium and, under particular conditions, for electrokinetic wave propagation in an isotropic porous or piezoelectric medium (Wapenaar & Fokkema, 2004)), the Green's matrix between $\mathbf{x}_A$ and $\mathbf{x}_B$ can be obtained from the cross-correlation of observations at those points, assuming that a distribution of uncorrelated noise sources is present in $\mathbb{D}$, with excitation function(s) proportional to the local loss function(s) on the diagonal of $\hat{\mathbf{M}}_6$. Equation (9) is a generalization of results obtained by Snieder for scalar diffusion (Snieder, 2006b) and for acoustic wave propagation in an attenuating medium (Snieder, 2006a).

8 UNCORRELATED SOURCES ON $\partial\mathbb{D}$

When $\mathbb{D}$ is finite and no homogeneous boundary conditions apply at $\partial\mathbb{D}$, the boundary integral in equation (7) does not vanish. Assuming the losses in $\mathbb{D}$ are small, the last integral can be ignored (see (Slob *et al.*, 2006a); (Slob *et al.*, 2006b); and (Slob & Wapenaar, 2006) for a discussion of the effects of ignoring this integral). Hence, under this condition equation (7) implies that the Green's matrix between $\mathbf{x}_A$ and $\mathbf{x}_B$ can be retrieved from cross-correlations of responses of independent impulsive sources on $\partial\mathbb{D}$ only (note that $\partial\mathbb{D}$ is not necessarily a closed surface: when the medium is 'sufficiently inhomogeneous' $\partial\mathbb{D}$ can be an open surface (Wapenaar, 2006a)). To make equation (7) suited for uncorrelated noise sources on $\partial\mathbb{D}$, matrix $\hat{\mathbf{M}}_5$ must be 'diagonalized' so that we can follow the same procedure as above. The term $\hat{\mathbf{A}}^\dagger(\mathbf{v}^0\cdot\mathbf{n})$ in $\hat{\mathbf{M}}_5$ is diagonal for scalar diffusion and for acoustic wave propagation in a flowing medium, whereas it vanishes in non-moving media. However, $\mathbf{N}_{\mathbf{x}}$ is not diagonal for any of the discussed applications. Diagonalization of the integral $-\oint_{\partial\mathbb{D}} \hat{\mathbf{G}}(\mathbf{x}_B,\mathbf{x},\omega)\mathbf{N}_{\mathbf{x}}\hat{\mathbf{G}}^\dagger(\mathbf{x}_A,\mathbf{x},\omega)\,\mathrm{d}^2\mathbf{x}$ involves decomposition of the sources at $\partial\mathbb{D}$ into sources for inward and outward propagating waves.

Following the approach discussed in (Wapenaar, 2004), (Wapenaar & Fokkema, 2006), assuming $\partial\mathbb{D}$ is far away from $\mathbf{x}_A$ and $\mathbf{x}_B$, we may approximate the integral (including the minus sign) by $\oint_{\partial\mathbb{D}} \hat{\mathbf{G}}^\phi(\mathbf{x}_B,\mathbf{x},\omega)\boldsymbol{\lambda}(\mathbf{x})\{\hat{\mathbf{G}}^\phi(\mathbf{x}_A,\mathbf{x},\omega)\}^\dagger\,\mathrm{d}^2\mathbf{x}$ + 'ghost', where 'ghost' refers to spurious events due to cross products of inward and outward propagating waves. When $\partial\mathbb{D}$ is irregular (which is the case when the sources are randomly distributed) these cross products do not integrate coherently and hence the spurious events are suppressed (Draganov *et al.*, 2006). When the medium at and outside $\partial\mathbb{D}$ is homogeneous and isotropic the spurious events are absent. Superscript ϕ refers to new source types at $\mathbf{x} \in \partial\mathbb{D}$ and $\boldsymbol{\lambda}(\mathbf{x})$ is a diagonal matrix containing normalization factors. For example, for elastodynamic waves in a solid (Wapenaar & Fokkema, 2006), $\hat{\mathbf{G}}^\phi(\mathbf{x}_A,\mathbf{x},\omega)$ is a 16×4 matrix, in which the columns represent the elastodynamic wave vectors observed at $\mathbf{x}_A$ due to P- and S-wave sources at $\mathbf{x}$ (the S-wave sources with three different polarizations), and the diagonal matrix is defined as $\boldsymbol{\lambda} = \mathrm{diag}(\frac{2}{\rho c_P}, \frac{2}{\rho c_S}, \frac{2}{\rho c_S}, \frac{2}{\rho c_S})$, where c_P and c_S are the P- and S-wave propagation velocities of the medium at and outside $\partial\mathbb{D}$.

Hence, assuming a distribution of uncorrelated noise sources $\hat{\mathbf{s}}^\phi(\mathbf{x},\omega)$ on $\partial\mathbb{D}$, we arrive in a similar way as above at equation (9), but this time with the observed field vector at $\mathbf{x}_A$ expressed as $\hat{\mathbf{u}}^{\mathrm{obs}}(\mathbf{x}_A,\omega) = \oint_{\partial\mathbb{D}} \hat{\mathbf{G}}^\phi(\mathbf{x}_A,\mathbf{x},\omega)\hat{\mathbf{s}}^\phi(\mathbf{x},\omega)\,\mathrm{d}^2\mathbf{x}$ (and a similar expression for $\hat{\mathbf{u}}^{\mathrm{obs}}(\mathbf{x}_B,\omega)$). In this form, equation (9) is a generalization of (Wapenaar, 2004), (Weaver & Lobkis, 2004), (van Manen *et al.*, 2005), (Wapenaar, 2006b), (Godin, 2006), (Slob *et al.*, 2006a), (Slob *et al.*, 2006b), (Slob & Wapenaar, 2006), (Snieder, 2006a), (Snieder, 2006b) to all field vectors described earlier. For example, for the electroseismic situation the (9,1)-element of $\mathbf{G}(\mathbf{x}_B,\mathbf{x}_A,t)$ is the vertical particle velocity of the solid phase at $\mathbf{x}_B$ due to an impulsive horizontal electric current source at $\mathbf{x}_A$.

According to equation (9) it is retrieved by correlating the 9th element of $\mathbf{u}^{\mathrm{obs}}(\mathbf{x}_B,t)$, i.e., the vertical velocity noise field at $\mathbf{x}_B$, with the first element of $\mathbf{u}^{\mathrm{obs}}(\mathbf{x}_A,t)$, being the horizontal electric noise field at $\mathbf{x}_A$ (actually a macroscopic sensor measures $v_3^s + w_3$ (Pride & Haartsen, 1996), so the cross-correlation of the measured vertical velocity and horizontal electric noise fields gives the sum of the (9,1)- and the (21,1)-elements of the Green's matrix).

9 CONCLUSION

We have derived a unified representation for Green's function retrieval by cross-correlation, which applies to diffusion phenomena, acoustic waves in flowing attenuating media, electromagnetic diffusion and wave phenomena, elastodynamic waves in anisotropic solids and electrokinetic waves in poro-elastic or piezoelectric media. The applications are found in 'remote sensing without a source', which includes observation of parameters such as flow, anelastic loss and the electrokinetic coupling coefficient.

Note added in proof: In another paper we derive Green's function representations for higher order linear scalar systems and discuss the connection with energy principles (Snieder *et al.*, 2006).

REFERENCES

Auld, B. A. 1973. *Acoustic fields and waves in solids.* Wiley-Interscience, New York.

Biot, M. A. 1956. Theory of propagation of elastic waves in a fluid-saturated porous solid: I. Low frequency range. *J. Acoust. Soc. Am.*, **28**, 168–178.

Brekhovskikh, L. M., & Godin, O. A. 1992. *Acoustics of layered media II. Point sources and bounded beams.* Springer, Berlin.

Campillo, M., & Paul, A. 2003. Long-range correlations in the diffuse seismic coda. *Science*, **299**, 547–549.

de Hoop, A. T. 1966. An elastodynamic reciprocity theorem for linear, viscoelastic media. *Appl. Sci. Res.*, **16**, 39–45.

de Hoop, M. V., & de Hoop, A. T. 2000. Wave-field reciprocity and optimization in remote sensing. *Proc. R. Soc. Lond., Series A.*, **456**, 641–682.

Derode, A., Larose, E., Campillo, M., & Fink, M. 2003. How to estimate the Green's function of a heterogeneous medium between two passive sensors? Application to acoustic waves. *Applied Physics Letters*, **83**(15), 3054–3056.

Draganov, D., Wapenaar, K., & Thorbecke, J. 2006. Seismic interferometry: reconstructing the Earth's reflection response. *Geophysics*, **71**, SI61–SI70.

Fokkema, J. T., & van den Berg, P. M. 1993. *Seismic applications of acoustic reciprocity.* Elsevier, Amsterdam.

Godin, O. A. 2006. Recovering the acoustic Green's function from ambient noise cross correlation in an inhomogeneous moving medium. *Phys. Rev. Lett.*, **97**, 054301–1–054301–4.

Lobkis, O. I., & Weaver, R. L. 2001. On the emergence of the Green's function in the correlations of a diffuse field. *J. Acoust. Soc. Am.*, **110**, 3011–3017.

Lyamshev, L. M. 1961. On some integral relationships in acoustics of moving medium. *Doklady Akademii Nauk*, **138**, 575–578.

Malcolm, A. E., Scales, J. A., & van Tiggelen, B. A. 2004. Extracting the Green function from diffuse, equipartitioned waves. *Phys. Rev. E.*, **70**, 015601(R)–1–015601(R)–4.

Pride, S. 1994. Governing equations for the coupled electromagnetics and acoustics of porous media. *Phys. Rev. B*, **50**, 15678–15696.

Pride, S. R., & Haartsen, M. W. 1996. Electroseismic wave properties. *J. Acoust. Soc. Am.*, **100**, 1301–1315.

Roux, P., Sabra, K. G., Kuperman, W. A., & Roux, A. 2005. Ambient noise cross correlation in free space: Theoretical approach. *J. Acoust. Soc. Am.*, **117**(1), 79–84.

Sánchez-Sesma, F. J., Pérez-Ruiz, J. A., Campillo, M., & Luzón, F. 2006. Elastodynamic 2D Green function retrieval from cross-correlation: Canonical inclusion problem. *Geophys. Res. Lett.*, **33**, L13305–1–L13305–6.

Slob, E., & Wapenaar, K. 2006. Generalized electromagnetic interferometric Greens function representations. *Phys. Rev. Lett.*, (withdrawn).

Slob, E., Draganov, D., & Wapenaar, K. 2006a. GPR without a source. *Page ANT.6 of: Eleventh International Conference on Ground Penetrating Radar.*

Slob, E., Draganov, D., & Wapenaar, K. 2006b. Interferometric electromagnetic Green's functions representations using propagation invariants. *Geoph. J. Int.*, (submitted).

Snieder, R. 2004. Extracting the Green's function from the correlation of coda waves: A derivation based on stationary phase. *Phys. Rev. E.*, **69**, 046610–1–046610–8.

Snieder, R. 2006a. Extracting the Green's function of attenuating acoustic media from uncorrelated waves. *J. Acoust. Soc. Am.*, (submitted).

Snieder, R. 2006b. Retrieving the Green's function of the diffusion equation from the response to a random forcing. *Phys. Rev. E.*, **74**, 046620–1–046620–4.

Snieder, R., Wapenaar, K., & Wegler, U. 2006. Unified Green's function retrieval by cross-correlation; connection with energy principles. *Phys. Rev. E.*, (submitted).

van Manen, D-J., Robertsson, J. O. A., & Curtis, A. 2005. Modeling of wave propagation in inhomogeneous media. *Phys. Rev. Lett.*, **94**, 164301–1–164301–4.

van Tiggelen, B. A. 2003. Green function retrieval and time reversal in a disordered world. *Phys. Rev. Lett.*, **91**, 243904–1–243904–4.

Wapenaar, K. 2004. Retrieving the elastodynamic Green's function of an arbitrary inhomogeneous medium by cross correlation. *Phys. Rev. Lett.*, **93**, 254301–1–254301–4.

Wapenaar, K. 2006a. Green's function retrieval by cross-correlation in case of one-sided illumination. *Geophys. Res. Lett.*, **33**, L19304–1–L19304–6.

Wapenaar, K. 2006b. Non-reciprocal Green's function retrieval by cross-correlation. *J. Acoust. Soc. Am.*, **120**, EL7–EL13.

Wapenaar, K., & Fokkema, J. 2004. Reciprocity theorems for diffusion, flow and waves. *A.S.M.E. Journal of Applied Mechanics*, **71**, 145–150.

Wapenaar, K., & Fokkema, J. 2006. Green's function representations for seismic interferometry. *Geophysics*, **71**, SI33–SI46.

Wapenaar, K., Draganov, D., Thorbecke, J., & Fokkema, J. 2002. Theory of acoustic daylight imaging revisited. *Pages 2269–2272 of: Soc. Expl. Geophys., Expanded Abstracts.*

Weaver, R. L., & Lobkis, O. I. 2001. Ultrasonics without a source: Thermal fluctuation correlations at MHz frequencies. *Phys. Rev. Lett.*, **87**, 134301–1–134301–4.

Weaver, R. L., & Lobkis, O. I. 2002. On the emergence of the Green's function in the correlations of a diffuse field: pulse-echo using thermal phonons. *Ultrasonics*, **40**, 435–439.

Weaver, R. L., & Lobkis, O. I. 2004. Diffuse fields in open systems and the emergence of the Green's function (L). *J. Acoust. Soc. Am.*, **116**(5), 2731–2734.

Weaver, R. L., & Lobkis, O. I. 2005. Fluctuations in diffuse field-field correlations and the emergence of the Green's function in open systems. *J. Acoust. Soc. Am.*, **117**(6), 3432–3439.

Improving the virtual source method by wavefield separation

K. Mehta[†], A. Bakulin[††], J. Sheiman[††], R. Calvert[††] & R. Snieder[†]
[†] *Center for Wave Phenomena, Department of Geophysics, Colorado School of Mines, Golden, CO 80401*
[††] *Shell International E & P Inc., 3737 Bellaire Blvd, Houston, TX 77001*

ABSTRACT
The virtual source method has recently been proposed to image and monitor below complex and time-varying overburden. The method requires surface shooting recorded at downhole receivers placed below the distorting or changing part of the overburden. Redatuming with the measured Green's function allows reconstruction of a complete downhole survey as if the sources were also buried at the receiver locations. Some challenges still need to be addressed in the virtual source method such as limited acquisition aperture and energy reflected downward from the overburden. We demonstrate that up-down wavefield separation can substantially improve the quality of virtual source data. First, it allows us to eliminate artifacts associated with the limited acquisition aperture typically used in practice. Second, it allows us to reconstruct a response in the absence of down-going multiples from the overburden. These improvements are illustrated on a synthetic dataset of a complex layered model modeled after the Fahud field in Oman, and on ocean bottom seismic data acquired in the Mars field in the deepwater Gulf of Mexico.

Key words: wavefield separation, multiple suppression, OBC, multi-component, dual-sensor summation

1 INTRODUCTION

The virtual source method (Bakulin and Calvert, 2004, 2006) is a technique to image and monitor below complex overburden without knowledge of overburden velocities or near-surface time-lapse changes. The virtual source method is closely related to seismic interferometry (Derode, et al., 2003; Schuster, et al., 2004; Snieder, 2004; Wapenaar, 2004; Wapenaar, et al., 2005); both use cross-correlation of the recorded wavefields at a given pair of receivers to estimate the Green's function between them. In practical applications challenges in virtual source method still need to be addressed. The goal of this study is to identify these challenges and demonstrate the usefulness of wavefield separation to overcome some of them.

The simplest approach to generating virtual source gathers is to cross-correlate the total wavefield recorded at the virtual source location with the total wavefield recorded at the receivers (Mehta, et al., 2006). The resultant virtual source gather includes all the responses between the virtual source and the receiver, some of which may not be of interest for geophysical applications. The current practice is to correlate the windowed direct arrival in the total wavefield recording at the virtual source with the total wavefield at the receivers (Bakulin and Calvert, 2006). This approach suppresses some of the unwanted responses as compared to the simplest approach. Neither one gives the true subsurface response for two reasons.

According to theory (Derode, et al., 2003; Bakulin and Calvert, 2006; Snieder, 2004; Wapenaar, 2004; Schuster, et al., 2004; Korneev and Bakulin, 2006), we get the true response between a given pair of receivers by correlating the wavefields recorded at the two receivers and summing the correlated signal over sources that populate a closed surface enclosing the two receivers. For geophysical applications, we cannot have sources all around the receivers; hence simple cross-correlation and summing over a subset of sources does not provide

the true response. Apart from the spurious events attributable to incomplete source aperture, both the approaches yield reflections from the overburden and the free-surface because both the up-going and the down-going waves are recorded at the receivers. These unwanted responses obscure the target reflections from beneath the virtual source and receivers.

Here, we attempt to suppress the artifacts caused by incomplete source aperture, and the reflections from the overburden and the free-surface. Up-down wavefield separation shows promise for improving virtual source data quality by removing the reflections from the overburden and non-physical events arising from incomplete source aperture. Similar up-down wavefield separation is done by Snieder et al. (2006b) in a different context applied to structural engineering. In the next section we illustrate this in a synthetic model, followed by an explanation of the need for wavefield separation before cross-correlating the recordings.

Apart from imaging below complex overburden, virtual source is also a powerful tool for time-lapse monitoring with permanently placed receivers. We apply the virtual source method to multi-component ocean-bottom cable (OBC) data recorded at the Mars field (*www.rigzone.com*), having 120 4-C sensors permanently placed on the sea-floor. We show in the final section how wavefield separation helps suppress the strong reflection from the sea-surface, hence unraveling the reflection response of the reservoir. This improves the repeatability for seismic monitoring by making the response independent of variations in the sea-level, sea temperature, source locations, and source signatures.

2 SYNTHETIC MODELING

Figure 1 shows vertical profiles of P- and S-wave velocities used for synthetic simulation by reflectivity modeling (Schmidt and Tango, 1986). The density varies between 2.1 and 2.5 g/cm^3. 161 sources (vertical forces) are placed, every 10 m, on the surface and 41 receivers are placed, every 10 m, in a horizontal well at a depth of 250 m. The objective is to create virtual sources along the horizonal well to suppress the distorting effects of the upper near surface (above 200 m), when trying to image the reservoir layers below. The complex overburden (i.e., the region above the receivers) consists of layers with extremely high velocity contrasts typical of the Middle East, and here modeled after the Fahud field in Oman.

If ideal redatuming is to be performed with seismic interferometry then the reconstructed response corresponds to a buried virtual source at any of the receivers. This response will contain reflections from the overburden layers as well as free-surface multiples.

Bakulin and Calvert (2006) showed how gating before cross-correlation can eliminate some of the overburden reflections. This makes the virtual source radiate predominantly downwards and provides cleaner response from deep target reflectors. Their approach, however, cannot suppress the free-surface and overburden-related multiples. Here we set a goal to completely eliminate from the virtual source data all the down-going multiples related to the overburden.

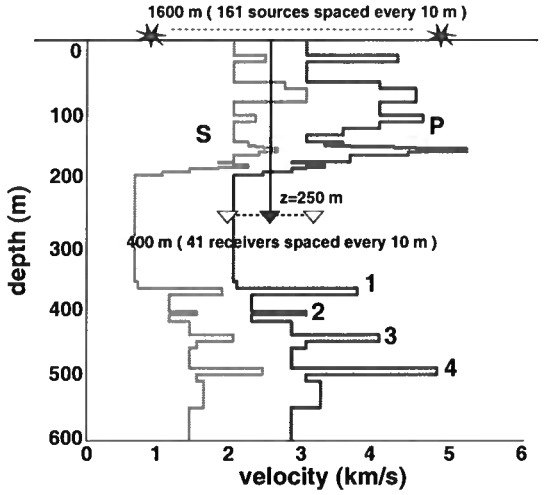

Figure 1. P- and S-wave velocity profiles and the acquisition geometry for a synthetic model inspired by Middle East field Fahud. 161 sources are spaced every 10 m on the surface, and 41 receivers are placed in a horizontal well at a depth of 250 m. Receiver spacing is 10 m.

Therefore, we benchmark the virtual source data against the "ground truth" response computed for a new model where all overburden above the well is replaced by a homogeneous half-space with the same velocities as just below the receivers (Figure 1).

We choose receiver 21 (middle receiver) as the virtual source, highlighted in red in Figure 1. The virtual source gather we generate should be equivalent to the response obtained by putting a physical source at the location of receiver 21. Figure 2 shows a comparison of the two responses. Figure 2a shows the virtual source gather generated by cross-correlating the total wavefield at the virtual source location (receiver 21) with the total wavefield at the receivers. Figure 2b shows the wavefield response of the receivers to a physical source (vertical force) at the virtual source location, after removing the laterally propagating shear waves. The laterally propagating shear waves are removed by using only the up-going energy at the receivers. For the rest of this paper, we refer to this response as the ground truth response. In addition to the four P-P reflection events, labeled 1 through 4 in Figure 1, which are present in both types of gather, the virtual source gather contains many other events.

For easier comparison we replot the ground truth response as shown in Figure 3. It shows the four P-P reflections labeled 1 through 4 and also an S-to-P con-

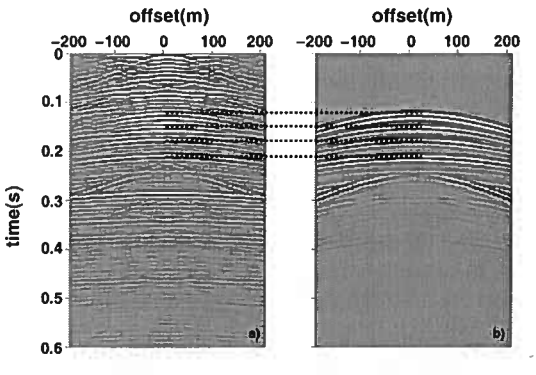

Figure 2. Figure (a) shows the virtual source gather generated by cross-correlating the total wavefield at the virtual source (receiver 21) with the total wavefield at the receivers. Figure (b) shows the shot gather generated by placing a physical source (vertical force) at the virtual source location (receiver 21) with a homogeneous half space above it. In Figure (b), the laterally propagating shear waves have been removed.

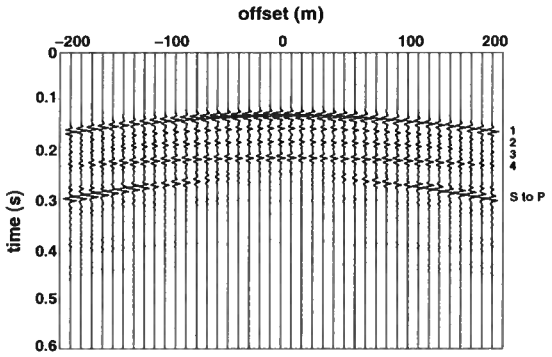

Figure 3. Ground truth response generated by putting a physical source (vertical force) at the virtual source location (receiver 21). The laterally propagating shear waves have been removed.

version. For further analysis we restrict ourselves to P-waves only. Figure 4 shows the virtual source gather, plotted in red, on top of the ground truth, plotted in black. As mentioned earlier, apart from the agreement in the reflection events, numerous other events exist in the virtual source gathers. Some of them are of physical nature (overburden-related response) and some are unphysical (artifacts arising from limited source aperture), but both represent unwanted responses, where the goal is to obtain only reflections from the subsurface. Next, we elaborate on their nature in layered media and demonstrate how wavefield separation can suppress both types of undesired response.

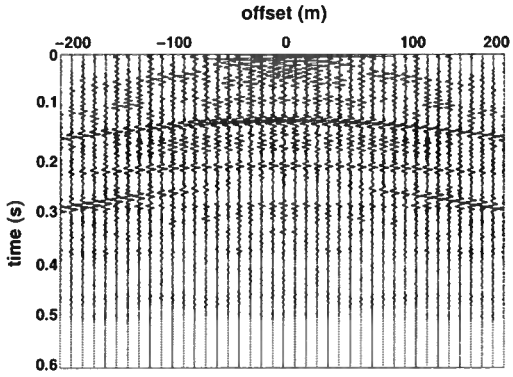

Figure 4. Black lines show the ground truth response. Red lines show the virtual source gather generated by cross-correlating the total wavefield at the virtual source (receiver 21) with the total wavefield at the receivers.

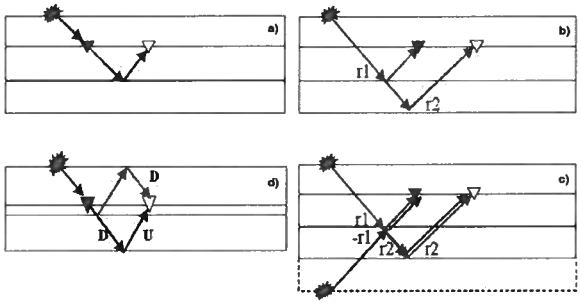

Figure 5. Depth-section cartoons explaining the need for wavefield separation. Figure (a) shows the source location that gives the stationary phase contribution for a physical arrival between the virtual source and the receiver. Figure (b) shows the source location that gives stationary phase contribution for a non-physical arrival between the virtual source and the receiver. Figure (c) shows the hypothetical source below the receivers, which, if present, would cancel the non-physical arrival. Figure (d) shows the presence of reflections from the overburden, in particular the free-surface multiples, here.

3 WAVEFIELD SEPARATION

Figure 5 shows depth-section cartoons for a three-layer model to illustrate the problem arising from incomplete source aperture and reflections coming from the overburden and the free-surface. In all the sub-figures, the red triangle is the virtual source and the yellow triangle is the receiver. They both are located at depth, and physical sources are excited at the surface. Figure 5a shows the source location along the surface that gives the stationary phase contribution (Snieder, et al., 2006a) for a physical arrival between the virtual source and the receivers as shown by the black arrows. By constitutive interference of the contributions from all other

sources, only this source contributes to the true response between the virtual source and the receiver.

If, however, the source is placed as shown in Figure 5b, the virtual source and the receiver will record the wavefield propagating along the red arrows. Snieder, et al. (2006a) explains that even though this source gives a stationary phase contribution, cross-correlation of the two wavefields does not correspond to any physical arrival between them. Hence this source does not contribute to the true response. Such arrivals contribute to spurious events in the virtual source gather. Snieder, et al. (2006a) also show that if a source were placed below the receivers, as shown in Figure 5c, the waves propagating along the blue arrows will cancel the contribution of the waves propagating along the red arrows and hence the spurious event will not be a part of the response. In geophysical applications, however, we do not have the luxury to put a source in the subsurface, as shown in the cartoon.

In order to remove these spurious events, we resort to wavefield separation. As shown in Figure 5b, the wavefield propagating along the red arrows, recorded by the virtual source and the receivers is up-going. By restricting the wavefield at the virtual source to be only down-going, we can suppress these spurious events.

Even though the waves at the virtual source are only down-going, we still record reflections from the overburden and the free-surface, as shown by the red arrows in Figure 5d. These correspond to physical arrivals and would be a part of the response if we had a physical source at the virtual source location. We can suppress these arrivals from the data by restricting the waves at the receivers to be only up-going. Hence, we get the subsurface response by correlating the down-going energy at the virtual source location with the up-going energy at the receivers. The idea is similar to Noah's deconvolution as suggested by Riley and Claerbout (1976). If such separation is achievable without distortions, it would represent an improvement over the current best practice of time-windowing the direct arrival at the virtual source location and correlating that with the total wavefield at the receivers (Bakulin and Calvert, 2006).

3.1 Windowing in time

Figure 6 shows the virtual source gather (in red) generated by cross-correlating the windowed direct arrival in the total wavefield at the virtual source with the total wavefield at the receivers. The windowed direct arrival is obtained by placing a time gate of 40 ms around the direct arrival. The reflections are preserved and compared to Figure 4 many spurious events are suppressed. The suppression results from restricting the energy at the virtual source location to be mostly down-going P-wave energy (in the form of direct arrival). Time-windowing the direct arrival thus improves the virtual source gather, although a better wavefield separation

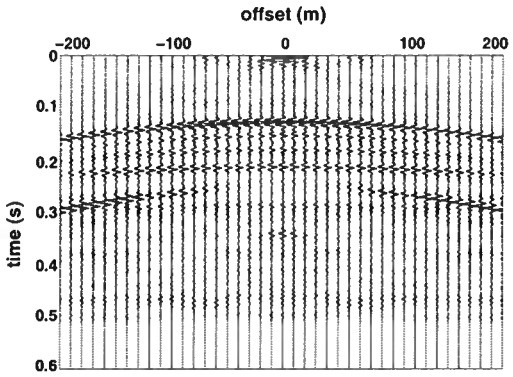

Figure 6. Black lines show the ground truth response. Red lines show the virtual source gather generated by cross-correlating the windowed direct arrival at the virtual source (receiver 21) with the total wavefield at the receivers.

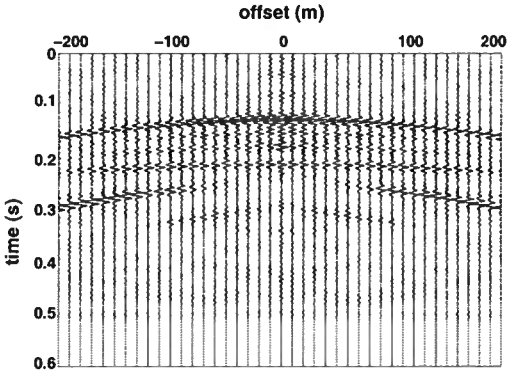

Figure 7. Black lines show the ground truth response. Red lines show the virtual source gather generated by cross-correlating the down-going waves at the virtual source (receiver 21) with the up-going waves at the receivers.

approach is to decompose the wavefield into up- and down-going waves.

3.2 Up-down separation

As demonstrated by the cartoons in Figure 5, we get the desired subsurface response by correlating the down-going energy at the virtual source location with the up-going energy at the receivers. Instead of time-windowing, we separate the wavefields into up- and down-going waves and use those for correlation. Figure 7 shows the virtual source gather (in red) generated by correlating the down-going waves at the virtual source with the up-going waves at the receivers. The spurious events are suppressed and the virtual source gather closely matches the ground truth response. Hence, wave-

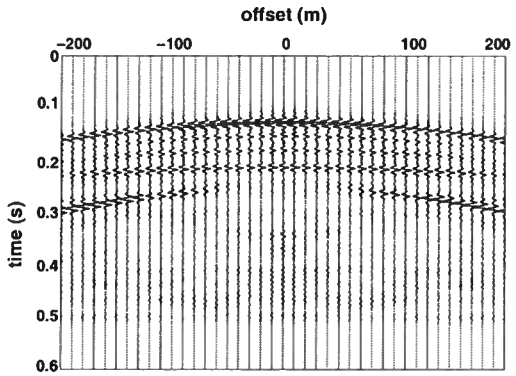

Figure 8. Black lines show the ground truth response. Red lines show the virtual source gather generated by cross-correlating the direct arrival windowed in the down-going waves at the virtual source (receiver 21) with the up-going waves at the receivers.

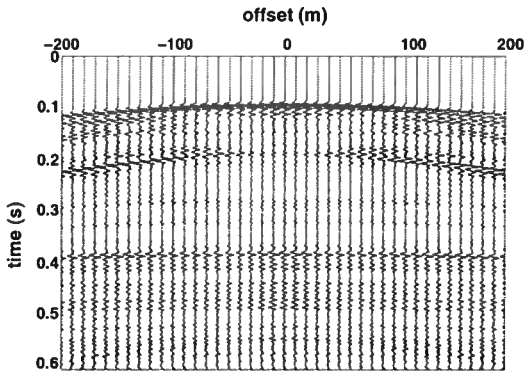

Figure 9. Comparison of the exact down-going waves (black lines) with the H-Z approximation (red lines).

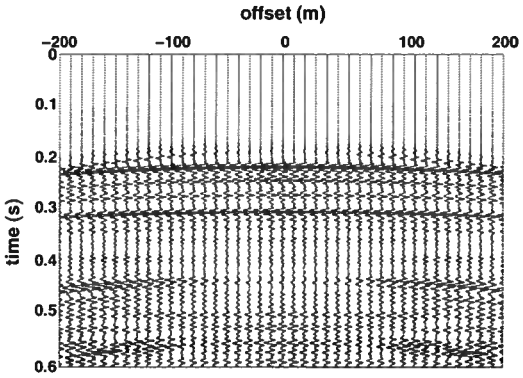

Figure 10. Comparison of the exact up-going waves (black lines) with the H+Z approximation (red lines).

field separation is indeed a promising tool for suppressing down-going multiples in the process of generating the virtual source gather.

The up-down separation and time-windowing can also be combined to generate the virtual source gather as shown in Figure 8. This virtual source gather is generated by correlating the direct arrival windowed in the down-going waves at the virtual source location with the up-going waves at the receivers. For this synthetic model it shows an improvement over Figure 7.

For field data this improvement will become prominent once we separate the recorded wavefield into up- and down-going waves. For the synthetic modeling, the modeling program separated the wave-field into up- and down-going waves. For layered media, wavefield separation for field data can be done by dual-sensor summation (e.g., Robinson, 1999). According to dual-sensor summation, given hydrophone (H) and vertical component geophone (Z) recording of vertically propagating waves at the same sensor location, the sum H+Z yields the up-going energy and the difference H-Z the down-going energy. Before we apply this to field data, we compare the exact down-going and up-going waves, for our synthetic model with waves separated by the H-Z and H+Z approximations respectively.

Figure 9 shows the exact down-going waves for the raw data (plotted in black) and obtained from H-Z (plotted in red). Similarly, Figure 10 shows the exact up-going waves for the raw data (plotted in black) and from H+Z (plotted in red). In each plot, the wavefields obtained in the two different ways are practically identical, suggesting that despite being strictly valid for zero-offset data in horizontally layered media, dual-sensor summation technique provides a reasonable separation of the wavefield into up- and down-going waves for all offsets at hand.

4 FIELD EXAMPLE: REDATUMING OCEAN-BOTTOM SEISMIC AT MARS

We demonstrate the improvement in the virtual source gathers due to wavefield separation using the data recorded for seismic monitoring of the Mars field located in the Gulf of Mexico. Figure 11 shows a cartoon of the acquisition geometry. The geometry consists of 364 air guns fired (spaced every 25 m) on the sea-surface, with 120 four-component sensors (spaced every 50 m) permanently placed on the sea floor at one kilometer depth. Sea level, water velocity and shot locations change slightly between repeat acquisitions even though receivers remain fixed on the seabed. This creates a problem for seismic monitoring aimed to detect small timeshifts and amplitude changes related to field depletion. The virtual source method allows us to redatum OBC data to the sea bed without knowing any of these factors. Redatumed data should correspond to fixed (virtual) source and fixed receiver and exhibit

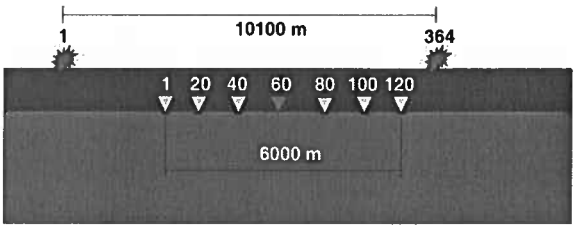

Figure 11. Cartoon showing the geometry of the Mars field OBC data acquisition. 120 receivers are spaced every 50 m on the sea-floor and 364 air guns (spaced every 25 m) are fired from the sea surface. Water depth in this cartoon is 1 km, close to that for the Mars field.

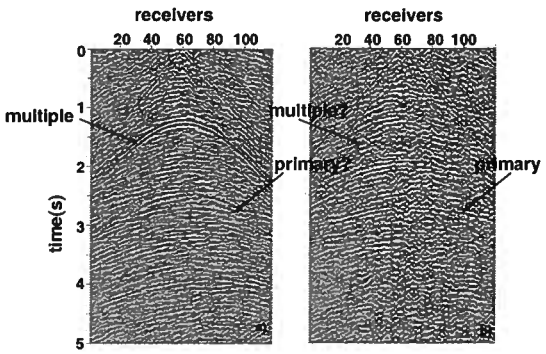

Figure 12. Virtual source gathers generated with receiver 60 as the virtual source. Figure (a) shows the virtual source gather generated by cross-correlating the total wavefields at both the virtual source and receiver locations. Figure (b) shows the virtual source gather generated by cross-correlating the down-going waves at the virtual source location with the up-going waves at the receivers. The label "multiple" refers to the reflection from the free-surface (overburden) and the label "primary" refers to a reflection from the subsurface. The "?" mark refers to the absence of the reflection event.

greatly improved repeatability between surveys. This was shown by Bakulin and Calvert (2006) for synthetic and real data of repeated vertical seismic profiles (VSP) acquired over time-varying overburden.

For the synthetic model, we demonstrated the improvement in the virtual source gathers by up-down separation. For the Mars field data, we use the dual-sensor summation technique for the separation of the wavefield into up- and down-going waves. We use these separate up- and down-going waves to generate the improved virtual source gathers.

We choose receiver 60 (middle receiver) as the virtual source and sum the correlation gather over all the sources. Figure 12a shows the virtual source gather, for the hydrophone component, generated by correlating the total wavefield recorded at the virtual source location with the total wavefield at the receivers. The

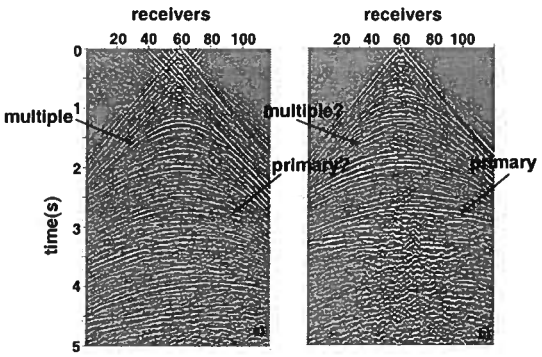

Figure 13. Virtual source gathers generated with receiver 60 as the virtual source. Figure (a) shows the virtual source gather generated by cross-correlating the direct arrival, windowed in the total wavefield at the virtual source, with the total wavefield at the receiver locations. Figure (b) shows the virtual source gather generated by cross-correlating the direct arrival, windowed in the down-going waves at the virtual source location, with the up-going waves at the receivers. The label "multiple" refers to the reflection from the free-surface (overburden) and the label "primary" refers to the reflection from the subsurface. The "?" mark refers to the absence of the reflection event.

most prominent reflection we see is the reflection from the sea-surface, labeled as "multiple". The arrow with the "primary?" mark is the location where we expect the strongest true reflection from the subsurface. Hence, even for a simple overburden, correlating the total wavefields gives a virtual source gather dominated by the reflection from the sea-surface.

Using the hydrophone and the vertical component geophone recording and the dual-sensor summation technique we separate the up- and down-going waves at all receivers. If instead of correlating the total wavefields, we correlate the down-going waves at the virtual source with the up-going waves at the receivers, we obtain virtual source gather shown in Figure 12b. The free-surface multiple is suppressed (highlighted by the arrow and "multiple?" mark). The reflections from the deeper subsurface are now visible and the strongest one is highlighted by an arrow and labeled as "primary." Although the reflections from the subsurface are visible, the virtual source gather is still noisy.

Figure 13a shows the virtual source gather obtained by the current best practice (Bakulin and Calvert, 2003, 2006): correlating the windowed direct arrival in the total wavefield at the virtual source location with the total wavefield at the receivers. The windowed direct arrival is obtained by placing a time gate of 400 ms around the direct arrival. Correlating the time windowed direct arrival makes the virtual source gather cleaner but the strongest reflection is still the free-surface multiple (labeled as "multiple"). To further improve the virtual source gather quality, we combine the up-down sepa-

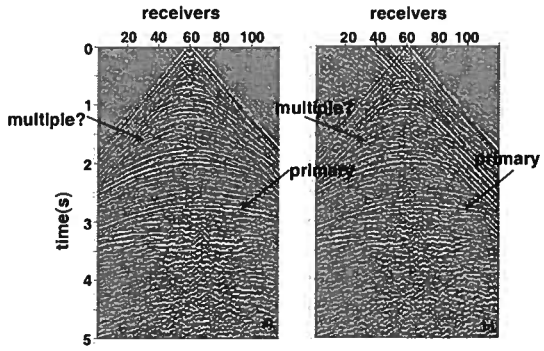

Figure 14. Virtual source gathers generated with receiver 60 as the virtual source. Figure (a) shows the virtual source gather generated by cross-correlating the direct arrival, windowed in the down-going waves at the virtual source location, with the up-going waves at the receivers. Figure (b) shows the virtual source gather generated by summing the *virtual source gathers*, generated for hydrophone and vertical component geophone: each of which is generated separately by cross-correlating the direct arrival, windowed in the total wavefield at the virtual source location, with the total wavefield at the receivers. The label "multiple" refers to the reflection from the free-surface (overburden) and the label "primary" refers to the reflection from the subsurface. The "?" mark refers to the absence of the reflection event.

ration and the time-windowing approach. As shown in Figure 13b, if we correlate the direct arrival, windowed in the down-going waves at the virtual source location, with the up-going waves at the receiver, the virtual source gather is cleaner and the true subsurface response (highlighted by the arrow and labeled as "primary") is clearly visible in the absence of the free-surface multiples. The free-surface multiple (labeled as "multiple?") is attenuated because we use only the up-going energy at the receivers. The early-time reflections are crisper in Figure 13b than in Figure 13a because we excluded any up-going energy that may have been left in the windowing approach. The near-offset jitter in Figure 13b around 3 to 4 s is the result of the wave scattering near the soft sea bottom. These scattered and mode-converted waves are sensed by the vertical component and show up in the virtual source gather when we include the vertical component for up-down wavefield separation.

We conclude that the combination of wavefield separation and gating produces the best of the responses [Figure 13b], as predicted by synthetic modeling. While wavefield separation restricts the radiation pattern of the virtual source to be strictly downward, additional gating imposes the virtual source to be P-wave and thus improves signal-to-noise ratio by eliminating unwanted shear-wave energy from the virtual source. This unwanted late energy might be used to generate virtual shear sources (Bakulin and Calvert, 2005).

Dual-sensor summation is strictly valid for zero-offset data over horizontally layered media. Therefore in many practical instances of large offsets or complex overburden structures in two or three dimensions it may fail to deliver separated wavefields with undistorted phase as required for virtual source generation. In cases such as for borehole observations below near surface, an alternative approach can be attempted to unravel an improved reflection response of the subsurface. First, one can generate two virtual source datasets using the current best practice, i.e. correlating the direct arrival, windowed in the total wavefield at the virtual source (VS), with the total wavefield at the receivers, both for the hydrophone (VS_H) and vertical component geophone (VS_Z) separately, and then extract the up-going waves ($VS_H + VS_Z$) for the downhole survey using dual-sensor summation applied to the virtual source data. Figure 14b, generated by such an alternative approach, reveals a gather similar in quality to our best response shown in Figure 14a [same as Figure 13b]. In Figure 14b, however, are distortions in early times and near the direct arrival because of windowing in the total wavefield instead of windowing in the down-going waves. As shown before, wavefield separation in the process of generating the virtual source gathers indeed gives the true subsurface response. This alternative approach with wavefield separation after generating the virtual source data, however, also gives reasonable reflection response and can be improved further by suitable combination of three-component (3-C) sources and 4-C geophones, i.e. by generating an elastic (vector) virtual source.

The up-down wavefield separation applied to the virtual source method suppresses the down-going multiples shown in the Figure 5. There are, however, waves that propagate downwards from the virtual source, reflect from the subsurface, propagate through the overburden and reflect back into the subsurface and are then sensed by the receivers as up-going waves. Such multiples are present in the virtual source data even after applying wavefield separation to the virtual source method.

5 CONCLUSIONS

The virtual source method as practiced to date can be improved upon to get mainly the reflection response from the deeper subsurface by using wavefield separation combined with gating of the direct arrival. Instead of correlating total wavefields as suggested by theory, in practice it is more beneficial to correlate down-going waves at the virtual source with the up-going waves at the receivers. In addition, time windowing or gating of the direct arrival in the down-going response further improves the signal-to-noise ratio.

Synthetic modeling in layered media inspired by the Fahud field in Oman reveals the nature of these improvements. Selecting down-going waves at the virtual source eliminates the reflections from the overburden and a free

surface; in other words it restricts the radiation pattern of the virtual sources to downward directions only. Using up-going waves at the receivers suppresses the free-surface multiples and spurious events arising from the inability to put sources surrounding the receivers. Combination of the two provides a response in the absence of downgoing energy from the overburden. Additional gating of the down-going response restricts the virtual source radiation pattern to predominantly P-waves and avoids contamination by shear energy. A field data example confirms that combination of wavefield separation and gating leads to a greatly improved signal-to-noise ratio on virtual source data and thus a cleaner reflection response of target horizons.

ACKNOWLEDGMENTS

We appreciate the comments from Jorge Lopez (Shell) and Ken Larner. We are grateful to Shell PDO colleagues Peter Engbers, Paul Matheny and Frank van Beek for stimulating discussions and for providing the data that inspired our synthetic model. We thank Shell for permission to show the Mars OBC data. We also thank the "Ministry of Oil and Gas, Oman" for permission to publish the paper.

REFERENCES

Bakulin, A., and R. Calvert, 2004, Virtual source: new method for imaging and 4D below complex overburden: 74th Annual Meeting, SEG, Expanded Abstracts, 2477-2480.

Bakulin, A., and R. Calvert, 2005, Virtual Shear Source: a new method for shear-wave seismic surveys: 75th Annual Meeting, SEG, Expanded Abstracts, 2633-2636.

Bakulin, A., and R. Calvert, 2006, The virtual source method: theory and case study: Geophysics, **71**, SI139-SI150.

Derode, A., E. Lacrose, M. Campillo, and M. Fink, 2003, How to estimate the Green's function for a heterogeneous medium between two passive sensors? Application to acoustic waves: Applied Physics Letters, **83**, 3054-3056.

Korneev, V., and A. Bakulin, 2006, On the fundamentals of the virtual source method: Geophysics, **71**, A13-A17.

Mehta, K., R. Snieder, R. Calvert and J. Sheiman, 2006, Virtual source gathers and attenuation of free-surface multiples using OBC data:implementation issues and a case study: 76th Annual Meeting, SEG, Expanded Abstracts, 2669-2673.

Riley, D. C., and J. F. Claerbout, 1976, 2-D multiple reflections: Geophysics, **41**, 592-620.

Robinson, E. A., 1999, Seismic Inversion and Deconvolution. Part B: Dual-sensor technology: Pergamon-Elsevier, Amsterdam, The Netherlands.

Schmidt, H., and G. Tango, 1986, Efficient global matrix approach to the computation of synthetic seismograms: Geophysical Journal of Royal Astronomical Society, **84**, 331–359.

Schuster, G. T., J. Yu, J. Sheng, and J. Rickett, 2004, Interferometric/daylight seismic imaging: Geophysics Journal International, **157** 838-852.

Snieder, R., 2004, Extracting the Green's function from the correlation of coda waves: A derivation based on stationary phase: Physics Review E., **69**, 046610.

Snieder, R., K. Wapenaar, and K. Larner, 2006a, Spurious multiples in interferometric imaging of primaries: Geophysics, **71**, SI65-SI78.

Snieder, R., J. Sheiman, and R. Calvert, 2006b, Equivalence of the virtual source method and wavefield deconvolution in seismic interferometry, Physics Review E, **73**, 066620.

Wapenaar, K., 2004, Retrieving the elastodynamic Green's function of an arbitrary inhomogeneous medium by cross-correlation: Physics Review Letters, **93**, 254301.

Wapenaar, K., J. Fokkema, and R. Snieder, 2005, Retrieving the Green's function by cross-correlation: a comparison of approaches: Journal of Acoustical Society of America, **118**, 2783-2786.

www.rigzone.com / data / projects / project_detail.asp ? project_id=27, Date of access: Dec 01, 2006.

Virtual source method applied to Mars field OBC data for time-lapse monitoring

K. Mehta[†], J. Sheiman[††], R. Snieder[†] & R. Calvert[††]
[†]*Center for Wave Phenomena, Department of Geophysics, Colorado School of Mines, Golden, CO 80401*
[††]*Shell International E & P Inc., 3737 Bellaire Blvd, Houston, TX 77001*

ABSTRACT
The virtual source method has recently been proposed to image and monitor below a complex and time-varying overburden. The method requires surface shooting recorded by subsurface receivers placed below the distorting or changing part of the overburden. Redatuming the recorded response to the receiver locations allows the reconstruction of a complete downhole survey as if the sources were also buried at the receiver locations. The ability to redatum the data independent of the knowledge of time-varying overburden velocities makes the virtual source method a valuable tool for time-lapse monitoring. We apply the virtual source method to the Mars field OBC data acquired in the deepwater Gulf of Mexico with 120 multi-component sensors permanently placed on the seafloor. Applying to the virtual source method, a combination of up-down wavefield separation and deconvolution of the correlation gather by the source power spectrum suppresses the influences of changes in the overburden (sea water), thus strengthening the virtual source method for time-lapse monitoring.

Key words: ocean-bottom cable, monitoring, wavefield separation, deconvolution, source power spectrum

1 INTRODUCTION

The virtual source method (Bakulin and Calvert, 2004, 2006) is a technique for imaging and monitoring below a complex overburden without knowledge of overburden velocities and near-surface changes. The virtual source method is closely related to seismic interferometry (Derode, et al., 2003; Schuster, et al., 2004; Snieder, 2004; Wapenaar, 2004; Bakulin and Calvert, 2005; Wapenaar, et al., 2005; Korneev and Bakulin, 2006; Snieder, et al., 2006a; Larose, et al., 2006; Curtis, et al., 2006). Theory states that cross-correlating the recording at a given reference receiver with the recorded data at any other receiver for all the sources and then summing the correlated data (correlation gather) over the physical sources gives a signal that represents the recording by the other receiver as if the reference receiver acted as a source (virtual source). Apart from imaging below a complex overburden, the virtual source method is a useful tool for time-lapse monitoring provided that the receivers are placed permanently below the time-varying overburden.

Time-lapse monitoring is a powerful tool for tracking changes in the subsurface. These changes include geomechanical phenomena associated with the migration of fluids. Conventionally, the changes can be tracked by observing the differences between data from two seismic surveys obtained over the surveillance period. Apart from changes in the subsurface caused by fluid flow, the difference in the two seismic surveys include changes in the overburden along with the acquisition discrepancies, which are both prominent and undesirable.

We apply the virtual source method to multi-component ocean-bottom cable (OBC) data acquired in the years 2004 and 2005 at the Mars field in deepwater Gulf of Mexico. The Mars field data are acquired by 120 multi-component sensors permanently placed on the seafloor 1 km deep and air guns shooting from the sea surface (Figure 1). A total of 364 air gun shots were fired along a line from the sea surface with a region of 40 missing shots because of the presence of platform above

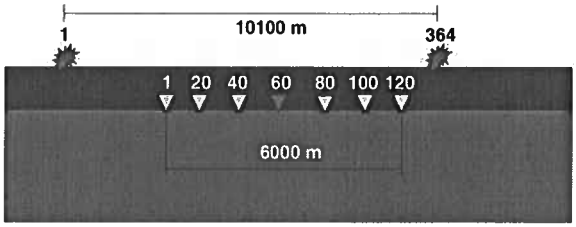

Figure 1. Depth model showing the geometry of the Mars field OBC data acquisition. 120 multi-component sensors (triangles) are permanently placed every 50 m on the seafloor. 364 air guns (stars), spaced every 25 m, are fired from the sea surface with a region of 40 missing shots, due to the presence of the platform, above receiver 80. Water depth for this cartoon is 1 km, roughly the depth for the Mars field.

receiver 80. The sensors are placed every 50 m and the shots are fired every 25 m.

The virtual source method is advantageous over the conventional seismic method in time-lapse monitoring at the Mars field because with virtual sources generated at each permanently placed receiver location the virtual source gathers obtained are independent of the variation in the overburden as well as acquisition discrepancies for the two surveys.

In section 2 we discuss the causes of non-repeatability in the overburden and reasons for using the virtual source method for time-lapse monitoring. In section 3 we compare the images obtained for the years 2004 and 2005 by migrating conventional seismic data and compute their difference to illustrate the causes of non-repeatability in the overburden (sea water). In section 4 we compare the images obtained by migrating virtual source data and study their differences. Section 5 illustrates the improvement in repeatability by incorporating wavefield separation in the virtual source method. Finally, we illustrate in section 6 that deconvolution of the correlation gather by the source power spectrum suppresses the influence of variations in the source power spectrum in the virtual source data.

2 WHY VIRTUAL SOURCE METHOD?

Time-lapse seismic monitoring is a useful tool for tracking changes in the subsurface associated with reservoir production. Along with the changes in the data at the reservoir level, there are prominent undesirable changes in the overburden that mask the changes of interest in the reservoir that one seeks to monitor. For the Mars field, the overburden consists of sea water. The variations in the overburden, therefore, include changes in sea water level, sea surface roughness, and sea water temperature and salinity. Redatuming of the data down to the receiver locations using virtual source method makes the survey independent of these variations in the sea water. Other causes of non-repeatability include acquisition discrepancies such as variations in the source location and source power spectrum. Source power spectrum varies not only for the two surveys but also with each shot location.

Let A and B be two receivers. The wavefields recorded by the receivers is, in the frequency domain, given by

$$\begin{aligned} U(\mathbf{r_A}, \mathbf{r_S}, \omega) &= S(\omega) G(\mathbf{r_A}, \mathbf{r_S}, \omega), \\ U(\mathbf{r_B}, \mathbf{r_S}, \omega) &= S(\omega) G(\mathbf{r_B}, \mathbf{r_S}, \omega), \end{aligned} \tag{1}$$

where $S(\omega)$ is the frequency-domain representation of the source wavelet, $G(\mathbf{r_A}, \mathbf{r_S}, \omega)$ is the Green's function for wave propagation from the source to receiver A, $G(\mathbf{r_B}, \mathbf{r_S}, \omega)$ is the Green's function for wave propagation from the source to receiver B and $\mathbf{r_S}$, $\mathbf{r_A}$ and $\mathbf{r_B}$ are the coordinates of the source and the two receivers A and B, respectively. Cross-correlation of the wavefields recorded by the two receivers A and B is, in the frequency domain,

$$\begin{aligned} U(\mathbf{r_A}, \mathbf{r_S}, \omega) U^*(\mathbf{r_B}, \mathbf{r_S}, \omega) &= |S(\omega)|^2 G(\mathbf{r_A}, \mathbf{r_S}, \omega) \\ & \quad G^*(\mathbf{r_B}, \mathbf{r_S}, \omega), \end{aligned} \tag{2}$$

where the asterisk indicates complex conjugate. Along with the correlation of the Green's functions, the right side of eq. (2) also contains the power spectrum of the source-time function. The cross-correlation is, therefore, independent of the phase spectrum of the source-time function. The power spectrum of the source pulse can be expected to differ for different shots as well as for different surveys. In order to remove the influence of varying source power spectrum, we deconvolve the correlation gather by the power spectrum of the source wavelet, if it is known with sufficient accuracy. We address this in section 6 of the paper.

3 CONVENTIONAL SEISMIC IMAGING

Mars field OBC data for the baseline survey was acquired October-November 2004. The repeat survey was carried out in June 2005. We first compare the conventional seismic images obtained from the two surveys. Conventional seismic data refers to wavefield excited by sources on the sea surface and recorded by the permanently placed sensors on the seafloor. To allow comparison with the seismic images generated after migrating the virtual source data, the conventional seismic data are downward continued to the seafloor using the water velocity and the virtual source method is not applied. We migrate the refocused conventional seismic data for the years 2004 and 2005 separately using Kirchoff depth migration. The depth images are then converted to time images (Figures 2a and 2b) using the Mars field velocity model generated by migration velocity analysis performed on the conventional seismic data. The time t=0 denotes the seafloor level. The gap just below the

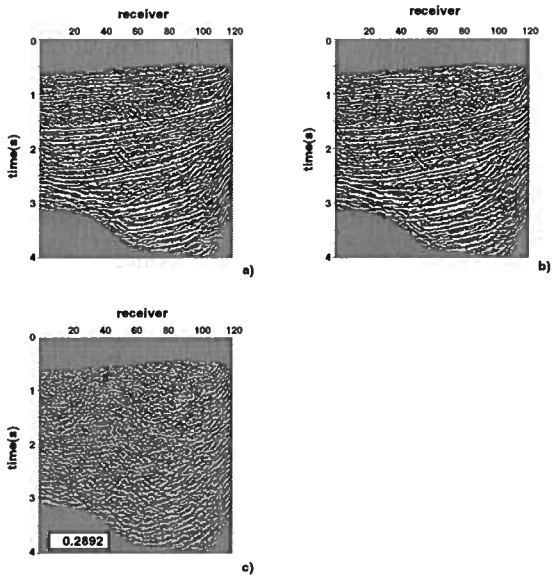

Figure 2. Images generated by migrating the conventional seismic data. Figure (a) is the image for the year 2004. Figure (b) is the image for the year 2005. Figure (c) is the difference of the two images, after time alignment, obtained on the same grey scale as that for Figures (a) and (b). The NRMS value is shown in the box in Figure (c).

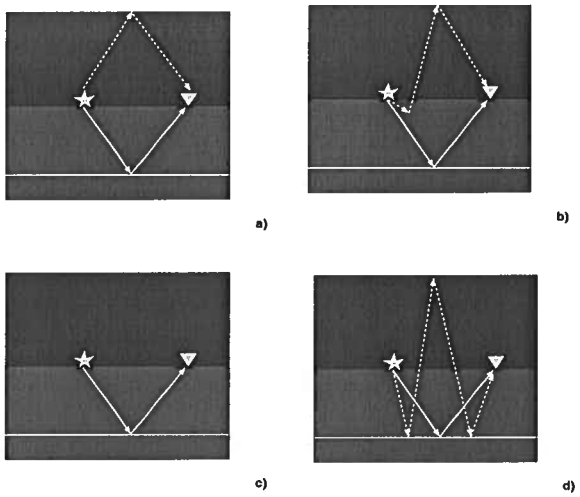

Figure 3. Ray paths corresponding to (a) conventional seismic data and virtual source data generated by correlating the total wavefield at the virtual source with the total wavefield at the receivers, (b) virtual source data generated by correlating the direct arrival windowed in the total wavefield at the virtual source with the total wavefield at the receivers, (c) data generated by correlating the down-going waves at the virtual source with the up-going waves at the receivers. Figure (d) is the cartoon of the ray paths of the multiple that propagates through the overburden even after applying wavefield separation to the virtual source method.

seafloor is due to blanking applied to the image gathers in order to mute data for which the opening angle at the reflection is large, which could lead to overly stretched shallow reflections.

Figure 2c is the difference of the two images. This difference is obtained after locally time-aligning these images to account for any geomechanical changes in the subsurface and to separate changes within the reservoir from its gross movement. The local time-alignment was done by correlating local windows of data both in time and space. There were no production-related subsurface changes at the reservoir level (around 3.5 s) between the two surveys over the surveillance period. Therefore, the differences (Figure 2c) are mainly due to variations in the overburden and to acquisition discrepancies. After being refocused at the seafloor, the waves propagate not only through the subsurface (solid rays in Figure 3a), but also through the time-varying overburden (dashed rays in Figure 3a). Variations in the overburden and acquisition contribute to the prominent undesirable differences observed in Figure 2c.

We quantify the repeatability using normalized root mean square amplitude (NRMS) of the difference of the images for the years 2004 and 2005. The NRMS of the difference is defined as

$$NRMS = \sqrt{\frac{< (M-B)^2 >}{< (M^2+B^2)/2 >}},$$

where 'B' represents the base survey (2004) and 'M' represents the monitor survey (2005). The symbols '<>' represents the average value over the region where NRMS is calculated. Decrease in the value of NRMS indicates improvement in the repeatability.

We calculate the NRMS for the entire seismic image. For the refocused conventional seismic data, the NRMS value is 0.2892. Table 1 shows the NRMS of the difference for the conventional seismic image as well as for the virtual source seismic images that will be discussed in the following sections.

4 THE VIRTUAL SOURCE METHOD

We generate different virtual source gathers with every receiver as the virtual source and, instead of migrating the refocused conventional seismic data, migrate the virtual source data generated for the years 2004 and 2005. For all the examples we use Kirchoff depth migration and then convert the depth image to a time image using the Mars field velocity model generated by migration velocity analysis on the conventional seismic data.

The simplest approach to generate a virtual source gather is to correlate the total wavefield at the virtual source with the total wavefield at the receivers (Mehta, et al., 2006). The images for the years 2004 and 2005 obtained by migrating virtual source data generated us-

Table 1. Comparison of the normalized root mean square amplitude (NRMS) values for different seismic images. 'Tot:tot' refers to the virtual source data generated by correlating total wavefield at the virtual source with the total wavefield at the receivers. 'Dir' refers to the direct arrival windowed in the total wavefield. 'Down' refers to the down-going waves. 'up' refers to the up-going waves. 'Down-dir' refers to the direct arrival windowed in the down-going waves. 'decon' refers to the deconvolution of the correlation gather by the source power spectrum. The corresponding figure number is mentioned in the second column.

Seismic image	Figure number	NRMS
Conventional seismic	2	0.2892
Tot:tot	4	0.3493
Dir:tot	5	0.3346
Down:up	6	0.2676
Down-dir:up	7	0.1770
Down:up:decon	9	0.1624
Down-dir:up:decon	10	0.1414

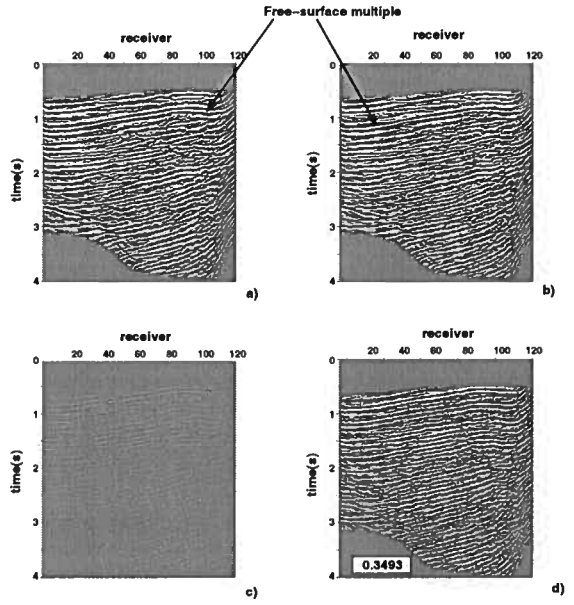

Figure 4. Images generated by migrating the virtual source data. Virtual source gathers are generated by correlating the total wavefield at the virtual source with the total wavefield at the receivers. Figure (a) is the image for the year 2004. Figure (b) is the image for the year 2005. Figure (c) is the difference of the two images, after time alignment, obtained on the same grey scale as that in Figures (a) and (b). Figure (d) is the difference of the image amplified by a factor of 10, on the same grey scale as that in Figures (a) and (b). The NRMS value is shown in the box in Figure (d).

ing this simplest approach are shown in Figures 4a and 4b, respectively. Figure 4c is the difference of the two images after local time-alignment. In order to highlight the features, we also show the difference image amplified by a factor of 10 in Figure 4d. The differences can be attributed to the waves propagating through the overburden (dashed rays in Figure 3a), which change between the two years because of the variations in the overburden. The acquisition discrepancies associated with the change in location of the source between the two years is, however, removed. The variation caused by differences in the source power spectrum [eq. (2)], nevertheless, still exists.

The NRMS of the difference for the virtual source data generated by the simplest approach is 0.3493. We believe this value is higher than the NRMS for the conventional seismic image because the pre-processing of conventional seismic data included suppression of the free-surface multiples. In contrast, the virtual source data generated using the simplest approach has the multiples that propagate through the time-varying overburden.

The images generated by the virtual source data (Figure 4a) have lower frequency content than that of the conventional seismic images (Figure 2a). The difference in frequency content is caused by the receivers and shots being placed along a line whereas the wave-propagation is three dimensional. Snieder, et al. (2006a) show that for such a geometry, the virtual source data need to be multiplied by a factor of $\sqrt{i\omega}$ (ω is the angular frequency), thus restoring the true frequency content. The pre-processing on the raw data involved band-limited spike deconvolution. In the virtual source data, the deconvolution of the correlation gather by the power spectrum of the source wavelet gives a zero-phase band-limited source pulse. Due to this discrepancy, the source-time function for the virtual source data multiplied by $\sqrt{i\omega}$ has a different frequency content compared to that of the conventional seismic data. The discrepancy between the frequency contents of the virtual source data and the conventional seismic data will, therefore, exist even after multiplying the virtual source data with the $\sqrt{i\omega}$ term. Hence, for the virtual source images that follows, we don't apply the $\sqrt{i\omega}$ term.

5 WAVEFIELD SEPARATION

The free-surface multiple are the response from the overburden and hence, are undesirable. They contaminate Figures 4a and 4b because we correlate the total wavefield at the virtual source with the total wavefield at the receivers, both of which contain those multiples. The dominant event is a simple reflection from the sea surface and are mainly down-going waves. If, instead of correlating the total wavefields, the down-going waves at the virtual source are correlated with the up-going waves at the receivers, the free-surface multiple along

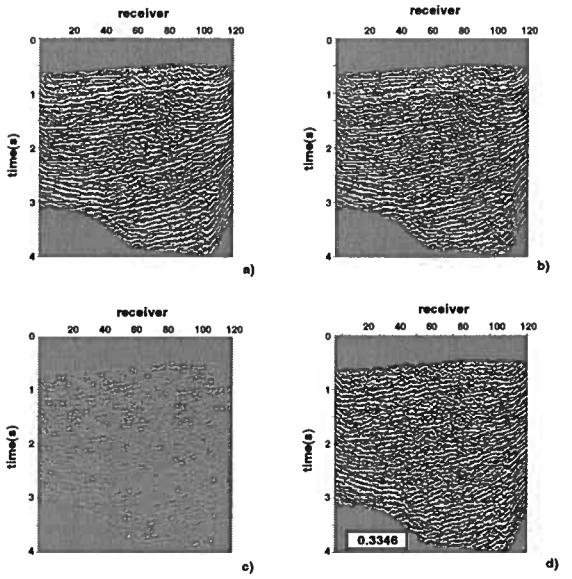

Figure 5. Same as Figure 4, but for virtual source gathers generated by correlating the direct arrival windowed in the total wavefield at the virtual source with the total wavefield at the receivers.

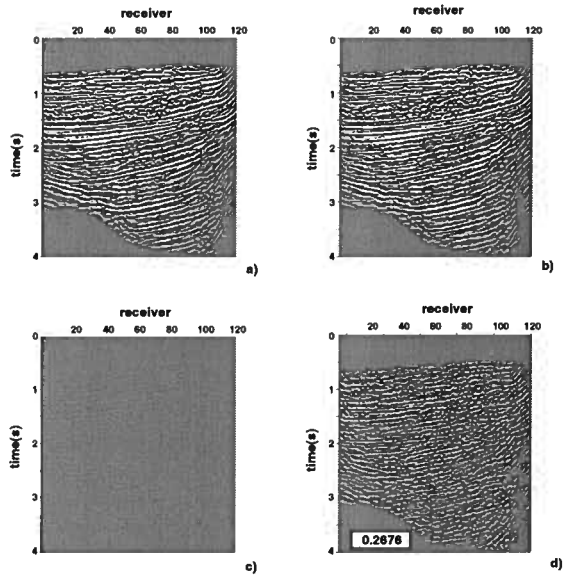

Figure 6. Same as Figure 4, but for virtual source gathers generated by correlating the down-going waves at the virtual source with the up-going waves at the receivers.

with other overburden reflections can be suppressed (Mehta, et al., 2007). Similar up-down wavefield separation is done by Snieder et al. (2006b) in a different context applied to structural engineering.

Before we discuss the wavefield separation into up and down-going waves, let us consider the image generated by migrating the virtual source data produced by the current practice. That approach to generating virtual source gather involves correlating the direct arrival windowed in the total wavefield at the virtual source with the total wavefield at the receivers (Bakulin and Calvert, 2004). By windowing the direct arrival at the virtual source, the virtual source is imposed to radiate predominantly downward thus, removing much of the overburden reflections but not all. The images for the years 2004 and 2005 obtained by migrating virtual source data, generated in that way are shown in Figures 5a and 5b, respectively. The free-surface multiple still dominates because instead of using only the up-going waves at the receivers, the total wavefield is used for correlation. Figure 5c is the difference of the images for the years 2004 and 2005 and Figure 5d is the difference image amplified by a factor of 10. Even after windowing of the direct arrival the virtual source data generated contain waves that still propagate through the overburden after reflecting from the near-seafloor (dashed rays in Figure 3b).

The NRMS of the difference for the virtual source data generated by the current practice is 0.3346. Similar to the simplest approach, this value is higher than the NRMS for the conventional seismic image because the pre-processing of conventional seismic data included suppression of the multiples. In contrast, the virtual source data generated using the current practice still have some multiples propagating through the time-varying overburden.

In order to make the virtual source data independent of the overburden, we follow the approach by Mehta, et al., 2007, and generate virtual source gathers by correlating the down-going waves at the virtual source with the up-going waves at the receivers. For OBC data, up-down separation of the wavefield is possible by dual-sensor summation (e.g., Robinson, 1999). Figure 6a and 6b are the images for the years 2004 and 2005 respectively, obtained by migrating virtual source data generated after wavefield separation into up- and down-going waves. Because the free-surface multiple, after reflecting from the free surface, is dominantly down-going energy, correlation of down-going waves at the virtual source with the up-going waves at the receivers suppresses the free-surface multiple and highlights, for example, reservoir events at around 3.5 s. The difference of the images (Figure 6c) for the years 2004 and 2005, amplified by 10 in Figure 6d is less noisy compared to Figures 5d and 4d.

The NRMS of the difference image after up-down wavefield separation reduced to 0.2676 (Table 1). The improved match in results for the two years compared to that for the simplest approach and current practice supports the improvement in repeatability after up-down wavefield separation. This improvement results because the waves now are those that propagate pre-

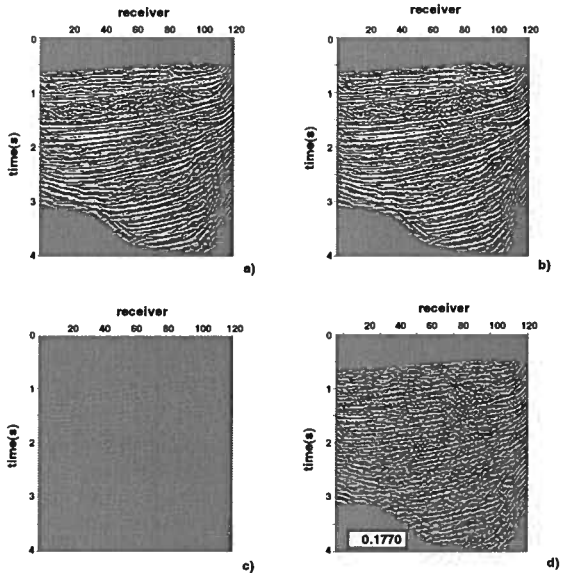

Figure 7. Same as Figure 4, but for virtual source gathers generated by correlating the direct arrival windowed in the down-going waves at the virtual source with the up-going waves at the receivers.

dominantly through the subsurface (solid rays in Figure 3c). Wavefield separation applied to the virtual source method has suppressed the down-going multiples propagating through the overburden, hence making the virtual source image less sensitive to overburden-related changes. The difference image still has some low-amplitude coherent events. These events could be weaker-amplitude multiples that are down-going at the virtual source, up-going at the receivers and yet still have propagated through the overburden (dashed rays in Figure 3d). These multiples cannot be suppressed even by applying wavefield separation to the virtual source method.

We can further reduce other sources of discrepancies in the time-lapse virtual source data by windowing the direct arrival in the down-going waves at the virtual source, instead of using all of the down-going waves. By windowing the direct arrival in the down-going waves, we are imposing a P-wave virtual source, hence suppressing the non-repeatability in the shear waves. The images for the years 2004 and 2005 obtained by migrating the resulting virtual source data are shown in Figures 7a and 7b, respectively and the differences are shown in Figures 7c and 7d. Compared to the images generated using the refocused conventional seismic data (Figures 2a and 2b), the images generated by the virtual source data preserves all the coherent reflectors and are less noisy.

Using up-down wavefield separation and windowing of the direct arrival at the virtual source has reduced the NRMS of the difference image to just 0.1770 (Table 1). Although the discrepancy in the shear waves is suppressed by windowing the direct arrival, the second-order multiples that propagate through the time-varying overburden (dashed rays in Figure 3d) still exist.

The improvement we have seen in the virtual source method by wavefield separation applied to the Mars field accounts for the variation in the sea water level, sea surface roughness, sea water temperature, salinity and source location. The variation in the source power spectrum [eq. (2)], however, still exist in all of the above images. We next address the correction for variation in the source power spectrum variation.

6 SOURCE POWER SPECTRUM VARIATION

The cross-correlation of the wavefields recorded by a given pair of receivers [eq. (2)] contains the power spectrum of the source pulse. To suppress the influence of the source power spectrum, and in particular its variation, the cross-correlated data (correlation gather) must be deconvolved by the source power spectrum, presuming that it is known or can be well approximated (Derode, et al., 2003; Schuster, et al., 2004; Snieder, 2004; Wapenaar, 2004; Wapenaar, et al., 2005). Typically, the source pulse varies not only between the two surveys but also among shots in a single survey. Since we use air guns as sources, variation in the source pulse is mainly due to changes in the air bubble, assuming that pre-processing of the two data sets attempted to equalize the source pulses. The equalization of the source pulse was done as follows. Small-offset traces were taken from each shot and the waves, in a time window of 400 ms around the direct arrival, were aligned. The length of the time window was chosen to be 400 ms to include the bubble. These aligned traces were then averaged, after which designative filters were derived to turn these responses into band-limited delta functions. The same procedure was applied to both the surveys to obtain the same desired band-limited delta function. This conventional pre-processing aimed to remove variations in the bubble sequence but was not sensitive enough to remove them completely.

The source power spectrum corresponds, in the time domain, to the auto-correlation of the source wavelet. The auto-correlation of the source wavelet present in the correlation gather varies from one shot to another because of changes in the residual bubble sequence. The variation of the auto-correlation of the source pulse (for receiver 90) as a function of source location for the years 2004 and 2005 is shown in Figures 8a and 8b, respectively. Each of the two figures is the auto-correlation of the direct arrival windowed in the down-going waves at receiver 90 for all the source locations. Down-going waves are used for correlation to avoid

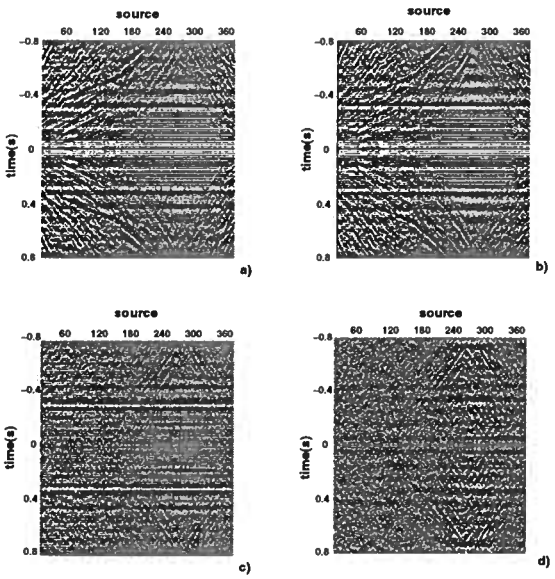

Figure 8. Variation of the auto-correlation of the source pulse corresponding to receiver 90 as a function of source location for 2004 (a) and 2005 (b). Figure (c) is the difference of the gathers in (a) and (b), obtained on the same grey scale as Figures (a) and (b). Figure (d) is the difference of the self-decons (convolution of the source power spectrum and filter that represents the inverse of the source power spectrum) for the years 2004 and 2005, on the same grey scale as Figures (a) and (b).

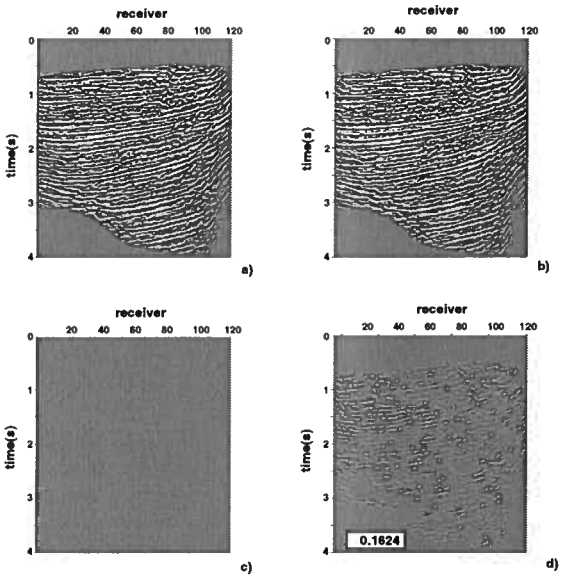

Figure 9. Same as Figure 7 but with deconvolution of the correlation gather by the source power spectrum before summation.

any near-seafloor reflection interfering with the auto-correlation of the source pulse. The auto-correlation of the source pulse varies not only between the two surveys but also between each source location. The event close to ± 0.35 s is attributable to the residual bubble sequence. Apart from the residual bubble, curved events are present for both causal and acausal times. These curved events correspond to the interference of reflected and refracted waves with the direct arrival for later times and larger offsets. Figure 8c is the difference in the auto-correlation of the source pulse for the years 2004 and 2005. The difference in the main lobe (close to time t=0) is negligible, suggesting that pre-processing adequately equalized the primary source pulses. The curved events also appear to diminish in the difference. The event occurring around ± 0.35 s, however, is the difference in the residual bubble sequence and is pronounced and consistent for every source location. This consistent difference could be due to the variation in the water temperature between the two surveys; the base survey was carried out in October and the repeat survey in June. Use of different air gun sources for the two surveys, different air gun pressures, different actual depths of source arrays (both surveys used the same nominal source depths), and discrepancies in the sea surface roughness could be other possible reasons for the systematic variation in the residual bubble.

The imprint of varying source power spectrum on the virtual source data can be removed by deconvolving each trace of the correlation gather by the power spectrum of the corresponding source. This is equivalent to applying a filter that represents the inverse of the source power spectrum. We refer to the convolution of the filter with the source power spectrum as *self-decon*. Figure 8d is the difference of self-decons for the years 2004 and 2005. Apart from the curved events representing the interference of other events with the direct arrival, the contribution of the systematic residual bubble variation is well suppressed. Hence, deconvolving the correlation gather by the source power spectrum suppresses the source power spectrum variations.

Migrated images, for the years 2004 and 2005, generated after applying both wavefield separation and deconvolution of the correlation gather by the source power spectrum are shown in Figures 9a and 9b, respectively with differences shown in Figures 9c and 9d. The virtual source data for these images are generated by correlating the down-going waves at the virtual source with the up-going waves at the receivers. The correlation gather is then deconvolved by the source power spectrum and summed over the physical sources. The improvement in the repeatability by combining up-down separation and deconvolution of the correlation gather with the auto-correlation of the source-time function is evident by the decrease in the NRMS to 0.1624 (Table 1).

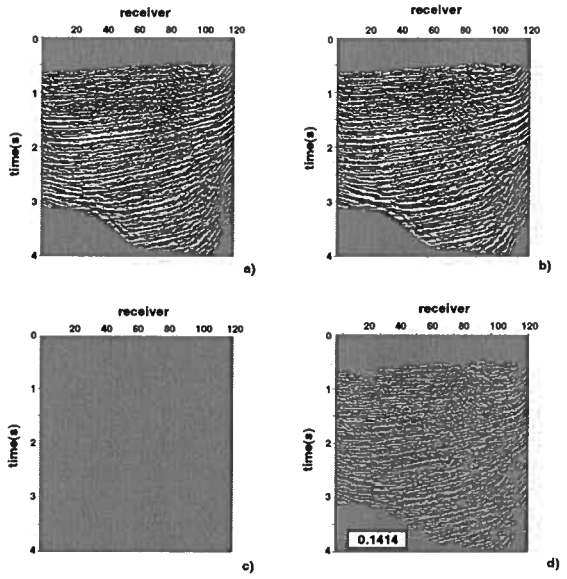

Figure 10. Same as Figure 9 but with the direct arrival windowed in the down-going waves at the virtual source.

The repeatability can be further improved by combining up-down separation, windowing of the direct arrival and deconvolution. The images in Figure 10 are obtained by migrating the virtual source data generated by combining up-down separation, windowing of the direct arrival, and deconvolution. The NRMS, after combining up-down separation, windowing the direct arrival and deconvolution, reduces from 0.1624 without windowing to just 0.1414.

7 CONCLUSION

Combination of up-down separation, windowing the direct arrival and deconvolution with the source power spectrum, improves the repeatability of the images created with the virtual source data. This makes the virtual source method a useful tool for time-lapse monitoring where the goal is to image changes just in the subsurface beneath the sources and the receivers. Up-down separation suppresses the first-order multiples from the time-varying overburden. Windowing the direct arrival in the down-going waves imposes a P-wave virtual source, hence suppressing the overburden-related variations in the shear waves. Finally, deconvolution of the correlation gather by the source power spectrum further suppresses the non-repeatability caused by variation in the source power spectrum. The progressively diminishing values of NRMS in the sequence of tests support our observation of improvement in time-lapse monitoring by applying wavefield separation and deconvolution to the virtual source method.

ACKNOWLEDGMENTS

We thank Shell for permission to show the Mars field OBC data and for the financial support through the GameChanger Program. We appreciate the critical comments from Ken Larner.

REFERENCES

Bakulin, A., and R. Calvert, 2004, Virtual source: new method for imaging and 4D below complex overburden: 74th Annual Meeting, SEG, Expanded Abstracts, 2477-2480.

Bakulin, A., and R. Calvert, 2005, Virtual Shear Source: a new method for shear-wave seismic surveys: 75th Annual Meeting, SEG, Expanded Abstracts, 2633-2636.

Bakulin, A., and R. Calvert, 2006, The virtual source method: theory and case study: Geophysics, **71**, SI139-SI150.

Curtis, A., P. Gerstoft, H. Sato, R. Snieder, and K. Wapenaar, 2006, Seismic interferometry - turning noise into signal: The Leading Edge, **25**, 1082-1092.

Derode, A., E. Lacrose, M. Campillo, and M. Fink, 2003, How to estimate the Green's function for a heterogeneous medium between two passive sensors? Application to acoustic waves: Applied Physics Letters, **83**, 3054-3056.

Korneev, V., and A. Bakulin, 2006, On the fundamentals of the virtual source method: Geophysics, **71**, A13-A17.

Larose, E., L. Margerin, A. Derode, B. van Tiggelen, M. Campillo, N. Shapiro, A. Paul, L. Stehly, and M. Tanter, 2006, Correlation of random wavefields: an interdisciplinary review: Geophysics, **71**, SI11-SI21.

Mehta, K., R. Snieder, R. Calvert and J. Sheiman, 2006, Virtual source gathers and attenuation of free-surface multiples using OBC data:implementation issues and a case study: 76th Annual Meeting, SEG, Expanded Abstracts, 2669-2673.

Mehta, K., A. Bakulin, J. Sheiman, R. Calvert and R. Snieder, 2007, Improving virtual source method by wavefield separation: Geophysics, Accepted.

Robinson, E. A., 1999, Seismic Inversion and Deconvolution. Part B: Dual-sensor technology: Pergamon-Elsevier, Amsterdam, The Netherlands.

Schuster, G. T., J. Yu, J. Sheng, and J. Rickett, 2004, Interferometric/daylight seismic imaging: Geophysics Journal International, **157** 838-852.

Snieder, R., 2004, Extracting the Green's function from the correlation of coda waves: A derivation based on stationary phase: Physics Review E., **69**, 046610.

Snieder, R., K. Wapenaar, and K. Larner, 2006a, Spurious multiples in interferometric imaging of primaries: Geophysics, **71**, SI65-SI78.

Snieder, R., J. Sheiman, and R. Calvert, 2006b, Equivalence of the virtual source method and wavefield deconvolution in seismic interferometry, Physics Review E, **73**, 066620.

Wapenaar, K., 2004, Retrieving the elastodynamic Green's function of an arbitrary inhomogeneous medium by cross-correlation: Physics Review Letters, **93**, 254301.

Wapenaar, K., J. Fokkema, and R. Snieder, 2005, Retrieving the Green's function by cross-correlation: a comparison of approaches: Journal of Acoustical Society of America, **118**, 2783-2786.

CWP-574

Virtual Real Source

Jyoti Behura
Center for Wave Phenomena, Department of Geophysics, Colorado School of Mines, Golden, CO 80401-1887, USA

ABSTRACT
Estimation of the seismic source signature is an important problem in reflection seismology. Existing methods of source signature estimation (statistical methods and well-log-based methods) suffer from several drawbacks. For example, assumptions of whiteness of the earth response, stationarity of the data, and the phase characteristics of the wavelet have no real theoretical justification and the extracted wavelets may not be reliable. Here, I introduce a method of extracting the source signature based on the theory of seismic interferometry, also known as the virtual source method. Interferometry can be used to extract the scaled impulse response between two receivers. This is the Green's function scaled by the power spectrum of the source wavelet. If a source location coincides with one of the receiver locations (not necessarily a zero-offset receiver), the recording at the other receiver would be the Green's function convolved with the source signature. The scaled impulse response, thus differs from the real recording by having an extra source term convolved with it. Deconvolving the real recording with the scaled impulse response gives the source signature, and so this method is named as "Virtual Real Source". Through modeling examples, I show that the Virtual Real Source method produces accurate source signatures even for complicated subsurface and source signatures. The quality of the extracted wavelet can be improved by using particular time windows and stacking wavelets extracted from different time windows. Source variability within a seismic survey does not pose any problems because interferometry averages the source signatures and the individual source signatures can be extracted reliably using this method. Source signature of each shot can be extracted reliably if they all have similar amplitude spectra even though their phase spectra might be completely different. This method of source signature estimation not only gives accurate traveltimes and amplitudes of reflection events, but also has the potential to solve other issues, such as finding source radiation patterns, measuring intrinsic attenuation, and estimating statics.

Introduction

Seismic source signature estimation is an important problem in reflection seismology. An accurate source signature deconvolved from the seismic data helps to correctly position reflectors and estimate reflection amplitudes. Amundsen (2000) notes that, "Areas where this knowledge (source signature) is potentially of great value are on board source array QC, deconvolution, multiple attenuation, tying reflection data to wells, modeling and inversion, AVO analysis, reservoir monitoring, and analysis of marine multicomponent recordings." A direct measurement of the source signature of an air gun (or an array of air guns) or a dynamite explosion can be made by recording the direct far-field wave from these sources after correcting for geometrical spreading. The recorded signal, however, might be contaminated with scattered waves and also might not even be the far-field signature. In offshore acquisition, air-gun arrays are often used instead of single air guns for various reasons. Dragoset (2000) points out that the disadvantage of using an array-like seismic source is that measuring the output is difficult. In this case, source-detector position is crucial and should be positioned such that it is equidistant from all the elements of the array. In land acquisition, it is normally impossible to measure the source signature of dynamite directly because of the difficult task of separating the direct wave from scattered waves (Ziolkowski, 1993).

Because of the challenges and high cost in measuring the source signature directly in the field, researchers have proposed alternative methods and algorithms to estimate the source signature. Source signature estimation based on statistical methods (Robinson and Trietel, 1980; Oldenburg et al., 1981; Hargreaves, 1992) suffer from several drawbacks. These methods assume the source signature to be minimum-phase, the earth response to be white, and the seismic data to be stationary. These assumptions have no real theoretical justification, making the extracted source signature unreliable. Methods based on well-logs are prone to errors as well. Other approaches involve linear and non-linear inversion (Landrø and Sollie, 1992; Amundsen, 1993; Landrø et al., 1994; Amundsen, 2000). These methods, however, need data to be recorded at a mini-streamer located below the source array and also assume that the scattered energy recorded by the mini streamer is negligible.

The above mentioned drawbacks and assumptions involved in source signature estimation call for a method of source signature extraction with a bare minimum of assumptions and requirements. Here I introduce a new and superior method for determination of the seismic source signature which is based on the principle of seismic interferometry. Through modeling examples, I show that this method produces accurate source signatures even for complicated subsurface structures and complex source signatures.

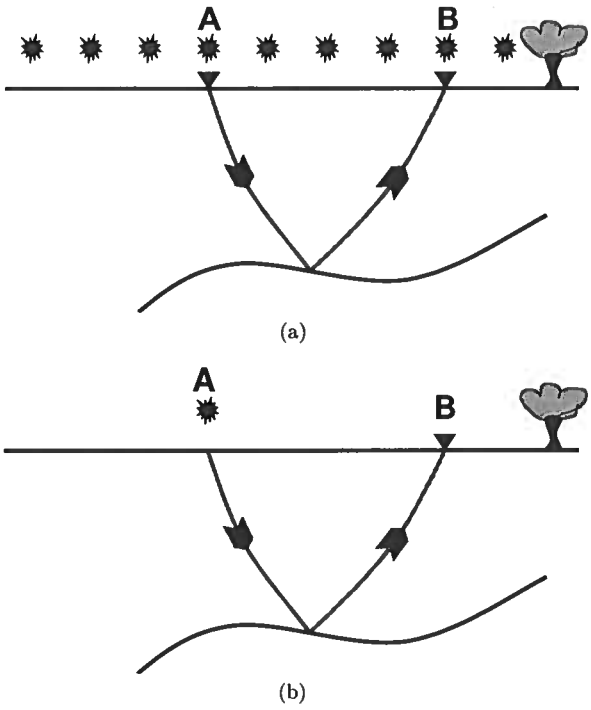

Figure 1. Scheme for (a) scaled impulse response and (b) real recording between two receiver locations A and B.

1 A SIMPLE IDEA

In seismic interferometry the Green's function between any two receiver locations can be computed by cross-correlating the receiver recordings due to random sources in the medium (Lobkis and Weaver, 2001; Derode et al., 2003a; Derode et al., 2003b; Snieder, 2004; Wapenaar, 2004; Weaver and Lobkis, 2004; Curtis et al., 2006). This principle has been applied to exploration seismology to remove overburden problems (Calvert et al., 2004; Mehta et al., 2006) and in imaging the subsurface(Schuster et al., 2004; Vasconcelos and Snieder, 2006).

I use seismic interferometry for extracting the Green's function between two receiver locations. Let us consider two receiver locations A and B as shown in Figure 1a. To determine the Green's function between these two receiver locations, the recordings at these two locations are cross-correlated for every source i.e. the two receiver gathers are cross-correlated. The cross-correlations are summed for all the shots to obtain the Green's function between the two receiver locations. This, however, is not the true Green's function, since it is scaled by the power spectrum of the source wavelet. This is the scaled impulse response and is given by:

$$U_{virt}(\omega) \quad = \quad |S(\omega)|^2 G(\omega), \tag{1}$$

where $U_{virt}(\omega)$ is the scaled impulse response, $S(\omega)$ is the seismic source wavelet, and $G(\omega)$ is the Green's function between A and B. Note that this wave field does not depend on the phase spectrum of the source.

Equation (1) is valid strictly for a closed source aperture, i.e. the true scaled impulse response between the two receivers can be obtained if there are sources on a closed surface surrounding the two receivers. In reality, the receivers are not usually surrounded by sources. This incomplete source aperture can result in some spurious events (Mehta et al., 2006) which can be removed through some special processing (K. Mehta, personal communication, 2007).

If location A also coincides with a shot location, then at receiver B there is a direct recording due to the shot at A (Figure 1b); this direct recording is given by

$$U_{real}(\omega) \quad = \quad S(\omega)G(\omega). \tag{2}$$

From the equations (1) and (2) it is clear that deconvolving the real recording (equation 2) with the scaled impulse response (equation 1) gives the true source signature. In practice, I perform this operation in the frequency domain by dividing the spectra of the two recordings

$$\left[\frac{U_{virt}(\omega)}{U_{real}(\omega)}\right]^* \quad = \quad S(\omega), \tag{3}$$

where $*$ represents the complex conjugate. To stabilize the deconvolution in equation (3), I use the following

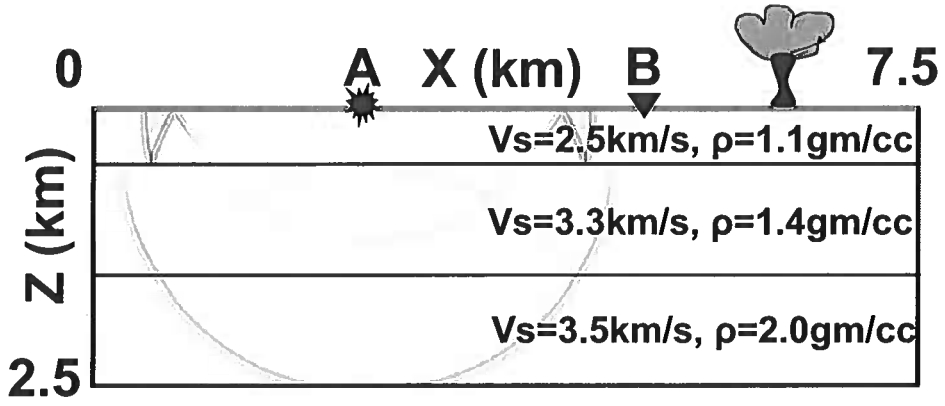

Figure 2. The 3-layer model used in the study. The SH-wavefront snapshot is shown at a particular instant of time.

estimator for the deconvolution instead

$$\left[\frac{U_{virt}(\omega)U^*_{real}(\omega)}{|U_{real}(\omega)|^2+\epsilon}\right]^* = S(\omega), \quad (4)$$

where the parameter ϵ is set to 0.01% of the average spectral power.

Thus, deconvolving the real recording with the scaled impulse response gives the source signature and so this method is named as "Virtual Real Source (VRS)". Note that the only requirement for this method is to have a receiver at the location previously occupied by the shot (the shot whose source signature we are interested in), but not necessarily a zero-offset receiver. This is a common scenario and is found in most seismic surveys. Apart from this requirement and the imperfect scaled impulse response due to an incomplete source aperture, there are no assumptions for this method to work; we do not need any prior information about the subsurface.

2 MODELING TESTS

Figure 2 shows a simple three-layer model used for testing the idea described in the previous section. The top boundary is a free-surface and the other three sides are absorbing boundaries. The shots are on the surface at an equal spacing of 10m spanning a total length of 7.5km. I do SH-wave modeling for this example and for all the examples that are to follow. The theory, however, is valid for all components of excitation and recording. The snapshot of the wavefront at a particular instant of time is shown in the figure. A 30Hz dominant frequency ricker wavelet is used as the source wavelet.

The wavelet extracted using VRS from the full record spanning over 5 seconds is given in Figure 3a. The true wavelet is also shown for comparison. The wavelet is well-recovered as can be seen from the good match in the waveform and initiation time. However, there are some spurious events after the main lobe which might be

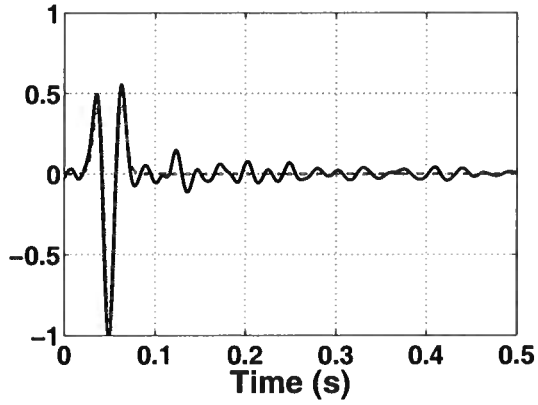

(a)

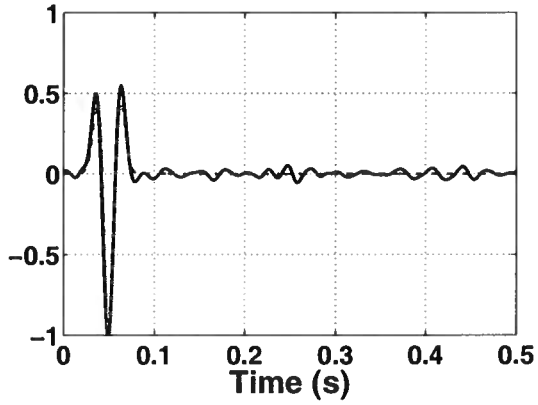

(b)

Figure 3. The true source signature (gray dashed line) and the wavelet extracted (black solid line) using (a) the full seismic record and (b) a windowing-stacking procedure.

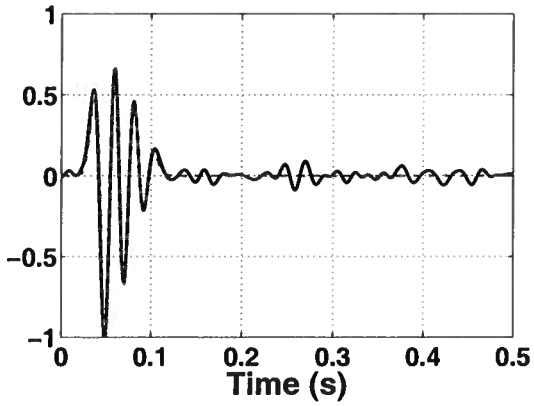

Figure 4. A more complex source signature (gray dashed line) and the signature extracted using Virtual Real Source (black solid line).

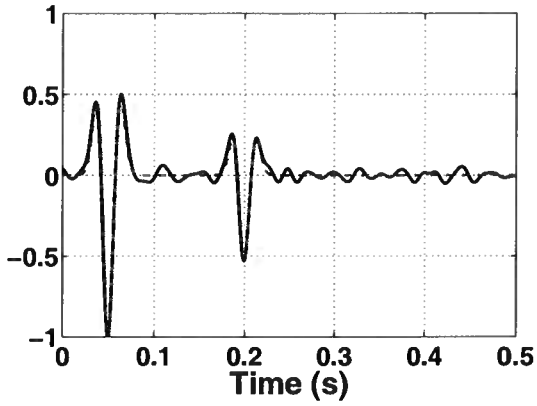

Figure 5. The true air-gun-type source signature (gray dashed line) and the extracted signature (black solid line).

caused due to the imperfect virtual source function. Extensive testing shows that some of these spurious events can be reduced by extracting the wavelet from a window of data. To further suppress the spurious events, wavelets can be extracted from different windows and then summed. Through this operation, only the true signals are stacked while the spurious events would be mis-stacked and thus suppressed. This is evident from Figure 3b where stacking of wavelets extracted from many windows has greatly improved the estimation of the source signature. The algorithm was tested on more complex models and in every case the source signature was extracted with acceptable accuracy.

Conventional methods for source signature estimation do not work well especially for complicated signatures. So this algorithm was tested extensively on complicated source signatures. Even for complicated wavelets, the method produced accurate results as evident from Figure 4. Another example of estimation of a complex source signature, similar to the air gun signature, is shown in Figure 5.

3 SOURCE VARIABILITY

Strictly this method of source signature estimation works well if all the sources are the same, i.e. they have the same source wavelet. But this is not usually the case in the field where source signatures can vary widely. What happens if the source signatures vary within the survey? A closer inspection of the interferometry process reveals that source variability does not pose a big problem. This is because after cross-correlations and summations, the source wavelet for the virtual source function, denoted by S_{avg} in equation (5), is an average over all source signatures (Snieder et al., 2007) which changes equation (1) to

$$U_{virt}(\omega) = |S_{avg}(\omega)|^2 G(\omega). \quad (5)$$

Equation (3) can now be rewritten as

$$\left[\frac{U_{virt}(\omega)}{U_{real}(\omega)}\right]^* = \left[\frac{|S_{avg}(\omega)|^2}{S(\omega)}\right]^* \quad (6)$$

$$= \left[\frac{|S_{avg}(\omega)|^2}{|S(\omega)|^2} S^*(\omega)\right]^* \approx S(\omega). \quad (7)$$

From equation (7) it is clear that if the amplitude spectrum of the source signature of interest does not deviate significantly from the average amplitude spectrum of all the source signatures in the survey (which is commonly the case in most surveys), then the source signature can be extracted accurately. All the phase information comes from the phase of the source signature of the shot we are interested in (denominator in equation 6).

3.1 Random-amplitude-spectra test

This is illustrated here with a couple of simple tests. For these tests a more complicated ten-layer model is used. The acquisition geometry, however, remains the same as the three-layer model used earlier. In the first test, the survey consists of sources differing in their amplitude spectra but having the same phase spectra. The amplitude spectra of all the sources is shown in Figure 6. Note that there is significant variation in amplitude spectrum of the sources. A receiver gather for the survey is shown in Fig 7 where we can also see the variation in source amplitude of the shots. The original and the extracted source signatures are shown in Figure 8. The source signature is recovered with good accuracy. In this case the amplitude spectra of all the sources gets averaged during cross-correlation and the scaled impulse response is given by equation (5). The closer the amplitude spectrum of the desired source signature is to the average

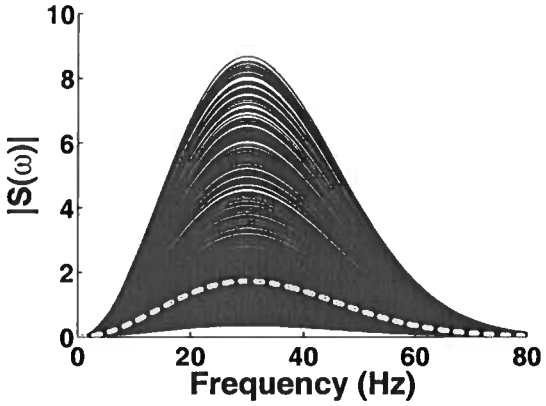

Figure 6. Amplitude spectra of the sources in the random-amplitude-spectra test. The gray dashed line is the average amplitude spectrum of all the sources.

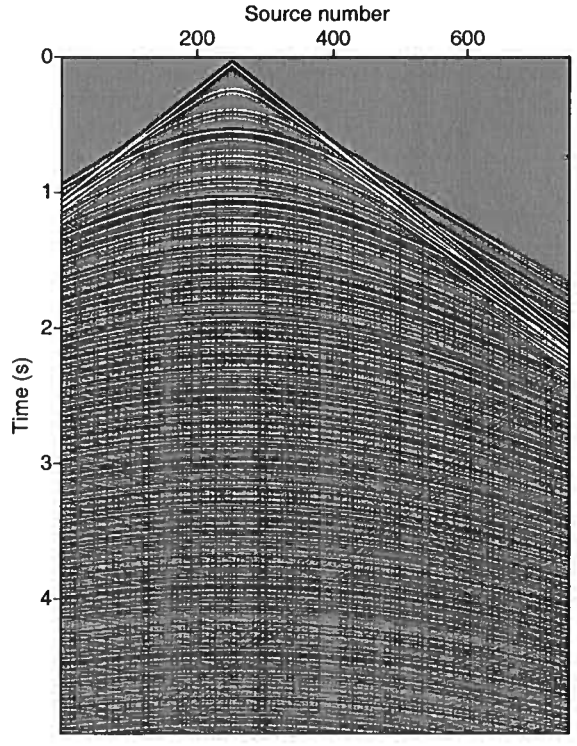

Figure 7. Receiver gather with the sources having different amplitude spectra but having the same phase spectrum.

amplitude spectrum, the more accurate will be the extracted source signature.

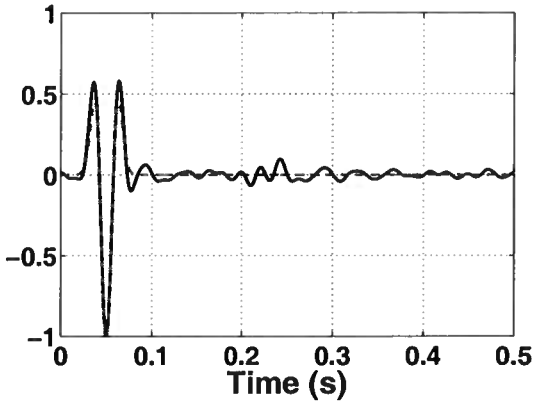

Figure 8. The true source signature (gray dashed line) and the extracted signature (black solid line) for a shot in the random-amplitude-spectra test.

3.2 Random-phase-spectra test

In the second test, the source signature changes phase changes randomly from one shot to the next, keeping the amplitude spectrum the same. A receiver gather from this survey is shown in Figure 9. As proved above, as long as all the sources have the same amplitude spectrum, every source signature can be extracted accurately. This is evident from Figure 10. It is clear from here that even for a complicated change in phase spectrum of the sources in the survey, the source signatures can be extracted reliably as long as they all have similar amplitude spectra.

In yet another test, the source signatures not only differ in phase spectra but also have different amplitude spectra. The survey consists of two types of sources differing in their amplitude spectra but have the same phase spectra. The peak amplitude of two-thirds of the total number of shots is five times the peak amplitude of the rest one-third of the shots. These two wavelets also have different initiation times and so differ in their phases. The original and the extracted source signatures are shown in Figures 11a and 11b. Both the source signatures are recovered with good accuracy. The extraction accuracy of the source signature in Figures 11b, however, is higher than the source in Figures 11a not only because of the larger number of sources for it but also because of its higher peak amplitude.

4 DISCUSSION AND CONCLUSION

Apart from the limited source aperture, there are no assumptions involved in source signature extraction using the Virtual Real Source method. No prior information about the subsurface or the seismic survey is needed. The only requirement for the method, however, is that the source location must coincide with a receiver loca-

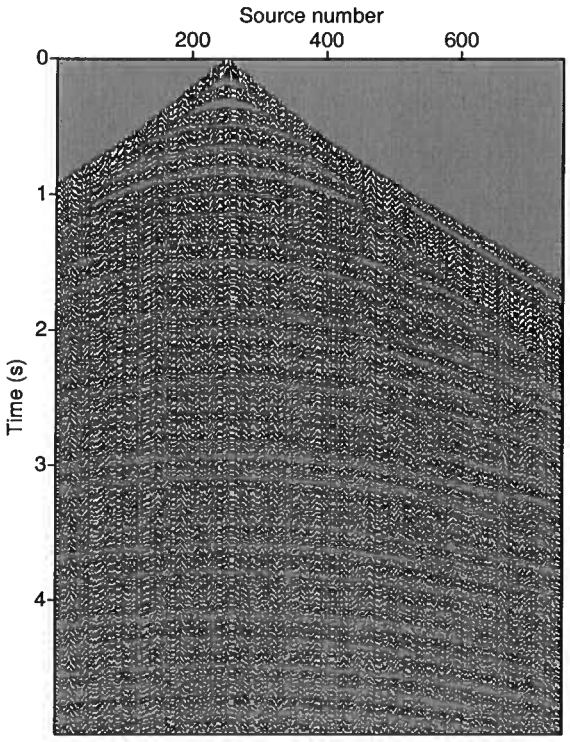

Figure 9. Receiver gather with the sources having different phase spectra but having the same amplitude spectrum.

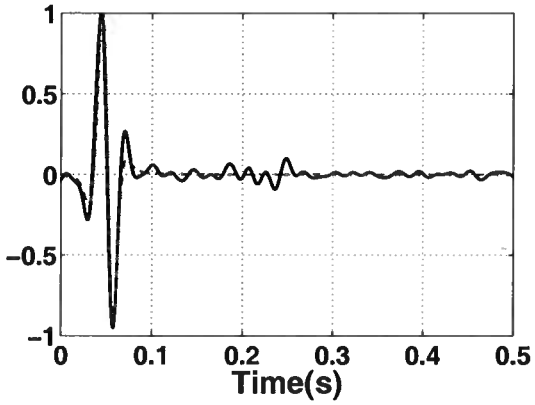

Figure 10. The true source signature (gray dashed line) and the extracted signature (black solid line) for a shot in the random-phase-spectra test.

tion. Note that we do not need a zero-offset receiver, rather a receiver location lie near the shot whose source signature we want to estimate. Even though only SH-wave propagation examples are shown in this paper, the method is valid for all components of excitation and recording. The Virtual Real Source method can extract

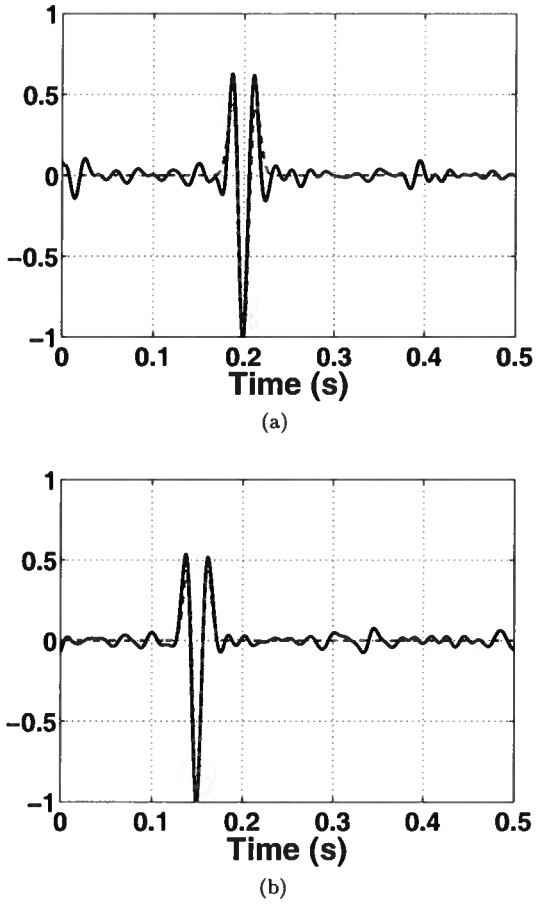

Figure 11. Normalized true source signature (gray dashed line) and extracted signature (black solid line) for (a) one-third of the shots and (b) the rest two-third of the total shots. The peak amplitude of the source signature in (b) is five times that of the source in (a).

source signatures accurately even if the phase spectra of the source signatures are completely different but as long as their amplitude spectra are similar. Because of the lack of any assumptions, Virtual Real Source works well for complicated sub-surfaces and complex source signatures. As already mentioned, it is important to keep in mind is that the quality of the extracted wavelet depends on the quality of the scaled impulse response. The true scaled impulse response between two receivers is obtained only when there is a full coverage of sources surrounding the receivers. This, however, is not the case in most seismic surveys. So for extracting the source signatures accurately, we need a large survey area and adequate coverage of sources and receivers. This method of seismic source signature estimation not only gives accurate traveltimes and amplitudes of reflection events, but also has the potential to solve other issues, such as finding source-receiver radiation patterns, measuring

attenuation, and estimating statics. The Virtual Real Source method can also be applied in crustal seismology to find the source signature of earthquakes. There might also be potential applications in other fields of science and technology dealing with wave propagation.

5 ACKNOWLEDGMENTS

I am grateful to Roel Snieder for all his suggestions and feedback on this work. I also thank Ken Larner for the many discussions on this topic. I am also grateful to Roel, Kurang, and Jia for correcting this manuscript and for the suggestions. I thank Jean-Paul Ampuero (ETH Zurich) and Matt Haney (Sandia National Laboratory) for helping me use SEM2DPACK, the 2D spectral element method tool used for modeling wave propagation in this study. The support for this work was provided by the Consortium Project on Seismic Inverse Methods for Complex Structures at CWP and by the Chemical Sciences, Geo-sciences, and Bio-sciences Division, Office of Basic Energy Sciences, U.S. Department of Energy.

REFERENCES

Amundsen, L., 1993, Estimation of source array signatures: Geophysics **58**, 1865–1869.

——, 2000, Linear inversion for source signatures from mini streamer data: The Leading Edge **19** , 40–43.

Calvert, R. W., A. Bakulin, and T. C. Joners, 2004, Virtual sources, a new way to remove overburden problems: EAGE Expanded Abstracts.

Curtis, A., P. Gerstoft, H. Sato, R. Snieder, and K. Wapenaar, 2006, Seismic interferometry – turning noise into signal: The Leading Edge **25**, 1082–1092.

Derode, A., E. Larose, M. Tanter, J. de Rosny, A. Tourin, M. Campillo, and M. Fink, 2003a, Recovering the Green's function from far-field correlations in an open scattering medium: Journal of Acoustical Society of America **113**, 2973–2976.

Derode, A., E. Larose, M. Campillo, and M. Fink, 2003b, How to estimate the Green's function for a heterogeneous medium between two passive sensors? Application to acoustic waves: Applied Physical Letters **83**, 3054–3056.

Dragoset, B., 2000, Introduction to air guns and air-gun arrays: The Leading Edge **19**, 892–897.

Hargreaves, N. D., 1992, Air-gun signatures and the minimum-phase assumption: Geophysics **57**, 263–271.

Landrø, M., and R. Sollie, 1992, Source signature determination by inversion: Geophysics **57**, 1633-1640.

Landrø, M., J. Langhammer, R. Sollie, L. Amundsen, and E. Berg, 1994, Source signature determination from mini streamer data: Geophysics **59**, 1261–1269.

Lobkis, O. I., and R. L. Weaver, 2001, On the emergence of Green's function in the correlations of a diffuse field: Journal of Acoustical Society of America **110**, 3011–3017.

Mehta, K., R. Snieder, R. Calvert, and J. Sheiman, 2006, Virtual source gathers and attenuation of free-surface multiples using OBC data: implementation issues and a case study: 76th Annual International Meeting, SEG, Expanded Abstracts **25**, 2669-2673.

Oldenburg, D. W., S. Levy, and K. P. Whittall, 1981, Wavelet estimation and deconvolution: Geophysics **46**, 1528–1542.

Robinson, E. A., and S. Treitel, 1980, Geophysical signal analysis: Prentice-Hall Inc.

Schuster, G. T., J. Yu, J. Sheng, and J. Rickett, 2004, Interferometric/daylight seismic imaging: Geophysical Journal International **157**, 838–852.

Snieder, R., 2004, Extracting the Green's function from the correlation of coda waves: A derivation based on stationary phase: Physical Review E. **69**, 046610.1-046610.8.

Snieder, R., K. Wapenaar, and K. Larner, 2006, Spurious multiples in interferometric imaging of primaries: Geophysics **71**, SI65-SI78.

Snieder, R., K. Wapenaar, and U. Wegler, 2007, Unified Green's function retrieval by cross-correlation; connection with energy principles: *Submitted to Physics Review E.*

Vasconcelos, I., and R. Snieder, 2006, Interferometric imaging by deconvolution: Theory and numerical examples: 76th Annual International Meeting, SEG, Expanded Abstracts **25**, 2416–2420.

Wapenaar, K., 2004, Retrieving the elastodynamic Green's function of an arbitrary inhomogeneous medium by cross correlation: Physical Review Letters **93**, 254301.

Weaver, R. L., and O. I. Lobkis, 2004, Diffuse fields in open systems and the emergence of the Green's function: Journal of Acoustical Society of America **116**, 2731–2734.

Ziolkowski, A., 1993, Determination of the signature of a dynamite source using source scaling, Part I: Theory: Geophysics **58**, 1174–1182.

Interferometry by deconvolution, Part I: Theory and numerical examples

Ivan Vasconcelos & Roel Snieder
Center for Wave Phenomena and Department of Geophysics, Colorado School of Mines, Golden, CO 80401

ABSTRACT

Interferometry allows us to synthesize data recorded at any two receivers into waves that propagate between these receivers as if one of them behaves as a source. This is typically accomplished by cross-correlations. Based on perturbation theory and representation theorems, we show that interferometry can also be done by deconvolutions for arbitrary media and multidimensional experiments. This is important for interferometry applications where the excitation is described by a complicated function. First, we derive a series expansion that proves that interferometry can be accomplished by deconvolution before source integration. This method, unlike using cross-correlations, yields only causal scattered waves that propagate between the receivers. We provide an analysis in terms of singly and multiply scattered waves. Because deconvolution interferometry shapes the zero-offset trace in the interferometric shot gather into a band limited spike centered at time equal zero, spurious arrivals are generated by the method. Here, we explain the physics behind these spurious arrivals and demonstrate the they usually do not map onto coherent structures in the image domain. We also derive an interferometry method that does deconvolution after source integration that is associated with existing interferometry techniques. Deconvolution after source integration yields both causal and acausal scattering responses, and it also introduces spurious events. Finally, we illustrate the main concepts of deconvolution interferometry and its differences with the correlation-based approach through stationary-phase analysis and with numerical examples.

Key words: interferometry, deconvolution, perturbation theory, scattering

1 INTRODUCTION

The main objective of seismic interferometry is to obtain the impulse response between receivers, without any knowledge about model parameters (Lobkis and Weaver, 2001; Weaver and Lobkis, 2004a; Wapenaar et al., 2004a). Typically, interferometry is implemented using by cross-correlations of recorded data (Curtis et al., 2006; Larose et al., 2006). Many of the formal proofs and arguments surrounding interferometry are based on cross-correlations. Proofs based on correlation-type representation theorems state the validity of interferometry for acoustic waves (Lobkis and Weaver, 2001; Weaver and Lobkis, 2004b), for elastic media (Wapenaar et al, 2004a and b, Draganov et al., 2006), and also for attenuative (Snieder, 2007) and perturbed media (Vasconcelos and Snieder, 2007). Other proofs of interferometry based on time-reversal were offered by Fink (2006), and by Bakulin and Calvert (2006) in their Virtual-Source methodology. Schuster et al. (2004) and Yu and Schuster (2006) use correlation-based interferometry imbedded within an asymptotic migration scheme to do interferometric imaging. Similarly, Snieder (2004) Sabra et al. (2004) and Snieder et al. (2006a) rely on the stationary-phase method to explain results from interferometry.

The field of interferometry expands beyond exploration seismology. There are examples of interferometry applications in many other fields such as ultrason-

ics (Malcolm et al., 2004; van Wijk, 2006), helioseismology (Rickett and Claerbout, 1999), global seismology (Shapiro et al., 2005; Sabra et al., 2005). Curtis et al. (2006) and Larose et al. (2006) give comprehensive interdisciplinary reviews of interferometry. As the understanding of interferometry progresses, finding more applications to the method is inevitable. For example, reservoir engineering may soon benefit from interferometry, as Snieder (2006) recently found that the principles of interferometry also hold for the diffusion equation. In an even more general framework, interferometry can be applied to a wide class of partial differential equations, with the examples of the Schrödinger or the advection equation (Wapenaar et al., 2006; Snieder et al., 2007). These findings might bring possibilities for interferometry within quantum mechanics, meteorology or mechanical engineering, for instance.

Our goal in this paper is to gain insight into interferometry from yet another point of view. Although interferometry is typically done by correlations, it is almost natural to wonder if it could be accomplished by deconvolutions. This issue was in fact raised by Curtis et al. (2006) as one of the standing questions within interferometry. We claim that interferometry can indeed be accomplished by deconvolutions for arbitrary, multidimensional media. In fact, there are already successful examples of deconvolution interferometry. Trampert et al. (1993) used deconvolution to extract the SH-wave propagator matrix and to estimate attenuation. Snieder and Şafak (2006) recovered the elastic response of a building using deconvolutions, and were able to explain their results using 1D normal-mode theory. Mehta and Snieder (2006) obtained the near-surface propagator matrix using deconvolutions from the recording of a teleseismic event in a borehole seismometer array.

In his early paper that spawned much of today's work on interferometry, Claerbout (1968) originally suggested the use of deconvolution to retrieve the Earth's 1D reflectivity response. He then turned to correlation because it tends to be a more stable operation. Loewenthal and Robinson (2000) showed that the deconvolution of dual wavefields can be used to change the boundary conditions of the original experiment to generate only up-going scattered waves at the receiver locations and to recover reflectivity. In a series of papers on free-surface multiple suppression, Amundsen and co-workers use inverse deconvolution-like operators designed to remove the free-surface boundary condition (e.g., Amundsen, 2001; Holvik and Amundsen, 2005). The topics of multiple suppression and interferometry are intrinsically related, precisely due to the manipulation of boundary conditions. This is explicitly pointed out by Berkhout and Verschuur (2006), by Mehta et al. (2006) and by Snieder et al. (2006b). Consequently, previous work on deconvolution-based multiple suppression is also related to the practice of interferometry. Since we seek to shed light on the physics behind deconvolution interferometry, we hope to bring yet another piece to the puzzle that connects interferometry and other geophysical applications. These applications may be the manipulation of boundary conditions for multiple suppression, passive and active imaging, time-lapse monitoring and others.

Using a combination of perturbation theory and representation theorems (as in Vasconcelos and Snieder, 2007), we first review interferometry by correlations. In our discussion on correlation-based interferometry, we restrict ourselves to key aspects which help understanding the meaning of deconvolution interferometry. In the Section that follows, we go through a derivation in which we represent deconvolution interferometry by a series similar in form to the Lippmann-Schwinger scattering series (Rodberg et al., 1967; Weglein et al., 2003). We first analyze the meaning of series terms of leading-order in the scattered wavefield, to then discuss the role of the higher-order terms of the deconvolution interferometry series. Next, we also demonstrate that interferometry can be accomplished by deconvolution after integration over sources, and compare the outcome of this method with deconvolution before source integration and with cross-correlation interferometry. Finally, using a single-layer model we illustrate the main concepts of deconvolution interferometry, while comparing it to its correlation-based counterpart. This is done by a stationary-phase analysis of the most prominent terms in deconvolution interferometry, and with a synthetic data example.

Although it is not our intention here to discuss a specific use for interferometry by deconvolution, we point out the this method will be of most use for interferometry applications that require the suppression of the source function. The paper by Vasconcelos and Snieder (2007b) is dedicated to a specific application of deconvolution interferometry, providing both numerical and field data examples in drill-bit seismic imaging. In particular, an important component of the broad-side imaging of the San Andreas fault at Parkfield presented by Vasconcelos et al. (2007a) would not have been possible without deconvolution interferometry (Vasconcelos and Snieder, 2007b). Apart from drill-bit seismics, a complicated source signal may be generated by the Earth itself. In the examples by Trampert et al. (1993), Snieder and Şafak (2006) and Mehta and Snieder (2006), deconvolution is necessary to suppress the incoming Earth signal, which contains arrivals of different modes, multiply scattered waves, etc. In the method by Loewenthal and Robinson (2000) the purpose of deconvolution is to collapse all down-going waves into a spike at zero time, leaving only the up-going Earth response. These are but examples of applications where deconvolution interferometry plays an important role.

2 THEORY OF INTERFEROMETRY

In this section we describe the theory of deconvolution interferometry through a perturbation theory approach. We begin by reviewing interferometry by cross-correlation in perturbed media. Next, we cover the derivation of deconvolution interferometry before summation over sources. Since such a derivation is done by a series expansion, we interpret the physical significance of the most prominent terms of the deconvolution interferometry series. On the following subsection, we discuss yet another option for interferometry where deconvolution is done after the summation over sources. Finally, we illustrate the physical significance of the the most prominent terms of the deconvolution interferometry series by providing an asymptotic analysis of these terms for a simplified toy model.

2.1 Review of interferometry by cross-correlations

Let the frequency-domain wavefield $u(\mathbf{r}_A, \mathbf{s}, \omega)$ recorded at $\mathbf{r}_A$ be the superposition of the unperturbed and scattered Green's functions $G_0(\mathbf{r}_A, \mathbf{s}, \omega)$ and $G_S(\mathbf{r}_A, \mathbf{s}, \omega)$, respectively, convolved with a source function $W(\mathbf{s}, \omega)$ associated with an excitation at $\mathbf{s}$, hence

$$u(\mathbf{r}_A, \mathbf{s}, \omega) = W(\mathbf{s}, \omega)\left[G_0(\mathbf{r}_A, \mathbf{s}, \omega) + G_S(\mathbf{r}_A, \mathbf{s}, \omega)\right] . \tag{1}$$

Although here and throughout the text we call G_S the *scattered wavefield*, formally G_S represents a wavefield perturbation. In our derivations, we rely on perturbation theory (Weglein et al., 2003; Vasconcelos and Snieder, 2007a), such that the quantities G_0 and u (or its impulsive version, G), respectively, represent background and perturbed wavefields that satisfy the equation for acoustic (Vasconcelos and Snieder, 2007a), elastic (Wapenaar et al., 2004a) and possibly attenuative waves (Snieder, 2007a), and may contain higher-order scattering and inhomogeneous waves. Both the background medium and the medium perturbation can be arbitrarily heterogenous and anisotropic. Also, $W(\mathbf{s}, \omega)$ may be a complicated function of frequency, and may vary as a function of $\mathbf{s}$.

The cross-correlation of the wavefields measured at $\mathbf{r}_A$ and $\mathbf{r}_B$ (equation 1) thus gives

$$C_{AB} = |W(\mathbf{s})|^2\, G(\mathbf{r}_A, \mathbf{s}) G^*(\mathbf{r}_B, \mathbf{s}) ; \tag{2}$$

where * denotes complex-conjugation. From equation 2, it follows that the cross-correlation C_{AB} depends on the power spectrum of $W(\mathbf{s})$. Note that we choose to omit the frequency dependence of equation 2 for the sake of brevity; we do the same with all of the other equations in this paper. Following the principle of interferometry (Lobkis and Weaver, 2001; Wapenaar et al, 2006), we integrate the cross-correlations in equation 2 over a surface Σ that includes all sources $\mathbf{s}$, giving

$$\oint_\Sigma C_{AB}\, d\mathbf{s} = \langle |W(\mathbf{s})|^2 \rangle \left[G(\mathbf{r}_A, \mathbf{r}_B) + G^*(\mathbf{r}_A, \mathbf{r}_B)\right] ; \tag{3}$$

where $\langle |W(\mathbf{s})|^2 \rangle$ is the source average of the power spectra (Snieder et al., 2007), and $G(\mathbf{r}_A, \mathbf{r}_B)$ and $G^*(\mathbf{r}_A, \mathbf{r}_B)$ are the causal and acausal Green's functions for an excitation at $\mathbf{r}_B$ and receiver at $\mathbf{r}_A$. Note that for equation 3 to hold G corresponds to the *pressure* response in acoustic media (e.g., Wapenaar and Fokkema, 2006). If G is the *particle velocity* response, the plus sign on the right-hand side of equation 3 is replaced by a minus sign (e.g., Wapenaar and Fokkema, 2006). Equation 3 has been derived by many other authors (e.g., Wapenaar et al., 2004b; Draganov et al., 2006) and it is not our intention here to restate it. Instead, we highlight the importance of the $\langle |W(\mathbf{s})|^2 \rangle$ term in equation 3.

The source average $\langle |W(\mathbf{s})|^2 \rangle$ may be a complicated function of frequency (or time), hence recovering the response between the receivers at $\mathbf{r}_A$ and $\mathbf{r}_B$ through equation 3 can be difficult. In the interferometry literature, most authors suggest deconvolving the power spectrum average $\langle |W(\mathbf{s})|^2 \rangle$ after the integration in equation 3 (Wapenaar et al., 2004a; Snieder et al., 2006; Fink, 2006). This assumes that an independent estimate of the source function is available. Indeed, in some applications such an estimate can be obtained (Mehta et al., 2007). There are many cases in which independent estimates of the source function are not a viable option. The second part of this paper (Vasconcelos and Snieder, 2007b) deals with a specific drill-bit seismic examples for which independent estimates of the source function are not available, and the correlation-based interferometry (equation 3) does not provide acceptable results. In the next two Sections we provide alternative interferometry methodologies that recover the impulse response between the receivers without the requirement of having independent estimates of the power spectrum of the source function.

In this paper we focus on understanding the physical meaning of interferometry by deconvolution, and its differences with its correlation-based counterpart. To do so it is necessary to review some of the physics behind cross-correlation interferometry in perturbed media. Thus, for the moment, it is convenient to assume a source function that is independent of the source position $\mathbf{s}$ ($W(\mathbf{s}) = W$) in equations 1, 2 and 3. Combining equations 1 and 2, we can expand C_{AB} into four terms:

$$\begin{aligned} C_{AB} &= u(\mathbf{r}_A,\mathbf{s})u^*(\mathbf{r}_B,\mathbf{s}) \\ &= \underbrace{u_0(\mathbf{r}_A,\mathbf{s})u_0^*(\mathbf{r}_B,\mathbf{s})}_{C_{AB}^1} + \underbrace{u_S(\mathbf{r}_A,\mathbf{s})u_0^*(\mathbf{r}_B,\mathbf{s})}_{C_{AB}^2} + \\ &+ \underbrace{u_0(\mathbf{r}_A,\mathbf{s})u_S^*(\mathbf{r}_B,\mathbf{s})}_{C_{AB}^3} + \underbrace{u_S(\mathbf{r}_A,\mathbf{s})u_S^*(\mathbf{r}_B,\mathbf{s})}_{C_{AB}^4}, \end{aligned} \tag{4}$$

where $u_0 = WG_0$ and $u_S = WG_S$ (see equation 1). The four terms, namely C_{AB}^1 through C_{AB}^4, can be inserted into equation 3, giving

$$\begin{aligned} \oint_\Sigma C_{AB}^1\, d\mathbf{s} + \oint_\Sigma C_{AB}^2\, d\mathbf{s} + \oint_\Sigma C_{AB}^3\, d\mathbf{s} + \oint_\Sigma C_{AB}^4\, d\mathbf{s} \quad &= |W|^2 \left[G_0(\mathbf{r}_A,\mathbf{r}_B) + G_S(\mathbf{r}_A,\mathbf{r}_B) + \right. \\ &\left. + G_0^*(\mathbf{r}_A,\mathbf{r}_B) + G_S^*(\mathbf{r}_A,\mathbf{r}_B)\right]. \end{aligned} \tag{5}$$

Each of the four integrals on the left-hand side of equation 5 has a different physical meaning. With the use of representation theorems, Vasconcelos and Snieder (2007a) have analyzed how each integral in equation 5 relates to the terms in the right-hand side of the equation. Note that for imaging purposes, we want to use only the u_S terms in equation 5. The first integral relates to the unperturbed terms in the right-hand side of equation 5 to give,

$$\oint_\Sigma u_0(\mathbf{r}_A,\mathbf{s})u_0^*(\mathbf{r}_B,\mathbf{s})\, d\mathbf{s} = |W|^2 \left[G_0(\mathbf{r}_A,\mathbf{r}_B) + G_0^*(\mathbf{r}_A,\mathbf{r}_B)\right]. \tag{6}$$

The relationship in equation 6 is not surprising because the unperturbed wavefields u_0 satisfy the unperturbed wave equation. Consequently, interferometry of the unperturbed wavefields on the left-hand side of equation 6 must yield the causal and acausal unperturbed wavefields between $\mathbf{r}_B$ and $\mathbf{r}_A$ (right-hand side of equation 6). A less obvious relationship between the terms in equation 5 (Vasconcelos and Snieder, 2007a) is that the dominant contribution to the causal scattered wavefield between $\mathbf{r}_B$ and $\mathbf{r}_A$ comes from the correlation between the unperturbed wavefield at $\mathbf{r}_B$ and the scattered wavefield at $\mathbf{r}_A$, that is,

$$\int_{\sigma_1} u_S(\mathbf{r}_A,\mathbf{s})u_0^*(\mathbf{r}_B,\mathbf{s})\, d\mathbf{s} \approx |W|^2\, G_S(\mathbf{r}_A,\mathbf{r}_B); \tag{7}$$

where σ_1 is a portion of Σ that yields stationary contributions to $G_S(\mathbf{r}_A,\mathbf{r}_B)$. Vasconcelos and Snieder (2007a) argue that this relationship holds for most types of experiments in exploration seismology (surface seismic, many VSP experiments, etc.). Equation 7 is an approximate relationship because it neglects the influence of a volume integral that provides a correction for medium perturbations that sit in the stationary paths of the unperturbed waves that propagate from the sources $\mathbf{s}$ to the receiver at $\mathbf{r}_B$ (Vasconcelos and Snieder, 2007a). In the context of seismic imaging, the extraction of $G_S(\mathbf{r}_A,\mathbf{r}_B)$ is the objective of interferometry. Equation 7 is not only important for the separation of the scattered waves that propagate between $\mathbf{r}_B$ and $\mathbf{r}_A$, but also because it can be used to show that deconvolution interferometry is capable of recovering the response between any two receivers.

An important requirement for the successful application of interferometry is that there must be waves propagating at all directions at each receiver location. Many authors refer to this condition as *equipartioning* (Weaver and Lobkis, 2004; Larose et al, 2006), while others simply mention the necessity of having many sources closely distributed around a closed surface integral, such as in equation 3. In real-life exploration experiments, however, it is impossible to surround the subsurface with sources. As a consequence we end up with only a partial source integration, instead of the closed surface integration necessary for equation 3 to hold. As was pointed out by Snieder et al. (2006) for simplified 1D models, truncation of the surface integral may lead to the introduction of spurious events in the final interferometric gathers. This holds for general 3D models as well, and it can be easily verified provided that

$$\int_{\sigma_1} C_{AB}\, d\mathbf{s} + \int_{\sigma_2} C_{AB}\, d\mathbf{s} = |W|^2 \left[G(\mathbf{r}_A,\mathbf{r}_B) + G^*(\mathbf{r}_A,\mathbf{r}_B)\right], \tag{8}$$

where σ_1 and σ_2 are surface segments of Σ, such that $\sigma_1 \cup \sigma_2 = \Sigma$. Now, suppose that in an actual field experiment we could only acquire data with waves excited over the surface σ_1 (such as in equation 7). Then, as we can see from equation 8, the integration over all available sources (the integral over σ_1) results in the desired response (right-hand side of equation 8) minus the integral over σ_2. In this case, if the integral over σ_2 is non-zero (i.e., there are stationary contributions associated with sources placed over σ_2), then the data synthesized from interferometry over σ_1 would

contain spurious events associated the missing sources over σ_2. Although this at first glance may seem like a practical limitation of the method of interferometry, in reality the lack of primary sources in the subsurface is somewhat compensated by multiple scattering, or by reflections below the region of interest (Wapenaar, 2006; Halliday et al., 2007). In field experiments, some of the desired system equipartioning may be achieved with longer recording times, making up for some of the missing sources over σ_2. Because this is a model-dependent problem, it is impossible in practice to pre-determine what the influence of missing sources will be, and to what extent longer recording times make up for these sources.

2.2 Deconvolution before summation over sources

As we have seen in the previous Section, the cross-correlation of the wavefields $u(\mathbf{r}_A,\mathbf{s})$ and $u(\mathbf{r}_B,\mathbf{s})$ contains the power spectrum of the excitation function (equation 2). Instead deconvolution of $u(\mathbf{r}_A,\mathbf{s})$ with $u(\mathbf{r}_B,\mathbf{s})$ gives

$$D_{AB} = \frac{u(\mathbf{r}_A,\mathbf{s})}{u(\mathbf{r}_B,\mathbf{s})} = \frac{u(\mathbf{r}_A,\mathbf{s})\,u^*(\mathbf{r}_B,\mathbf{s})}{|u(\mathbf{r}_B,\mathbf{s})|^2} = \frac{G(\mathbf{r}_A,\mathbf{s})\,G^*(\mathbf{r}_B,\mathbf{s})}{|G(\mathbf{r}_B,\mathbf{s})|^2}\,, \tag{9}$$

Now the source function $W(\mathbf{s})$ (equation 1) is canceled by the deconvolution process. Although no multidimensional deconvolution interferometry approach has been presented to date, it is intuitive to proceed with the integration

$$\oint_\Sigma D_{AB}\,d\mathbf{s} = \oint_\Sigma \frac{G(\mathbf{r}_A,\mathbf{s})\,G^*(\mathbf{r}_B,\mathbf{s})}{|G(\mathbf{r}_B,\mathbf{s})|^2}\,d\mathbf{s}\,, \tag{10}$$

to mimic the procedure of interferometry by cross-correlation (equation 3). The existing proofs for the validity of interferometry by cross-correlation (equation 3) are not immediately applicable to interferometry by deconvolution. For example, the use of representation theorems (e.g., Wapenaar et al., 2004a; Wapenaar et al., 2006; Vasconcelos and Snieder, 2007a) is unpractical for the spectral ratio of wavefields. Also, stationary-phase evaluation of the integral in equation 10 for a specified model (such as in Snieder et al., 2006) is compromised by the presence of $|G(\mathbf{r}_B,\mathbf{s})|^2$ in the numerator. Despite being zero-phase, $|G(\mathbf{r}_B,\mathbf{s})|^2$ contains cross-terms between unperturbed and scattered wavefields (see below) which make the denominator in equation 10 a highly oscillatory function that cannot be accounted for by the stationary-phase method (Bleistein and Handelsman, 1975).

Our solution to evaluating the integral in equation 10 is to expand the denominator in a power series, which then allows us to give a physical interpretation to deconvolution interferometry. The next two Sections cover the derivations of this series expansion and the subsequent interpretation of its physical significance.

2.2.1 Contributions to first-order in the scattered wavefield

We focus our discussion on the terms that make the most prominent contributions to the deconvolution interferometry integral in equation 10. First, we rewrite the deconvolution in equation 9 as

$$\begin{aligned} D_{AB} = \frac{C_{AB}}{|G(\mathbf{r}_B,\mathbf{s})|^2} &= \frac{1}{|G(\mathbf{r}_B,\mathbf{s})|^2}\,[G_0(\mathbf{r}_A,\mathbf{s})G_0^*(\mathbf{r}_B,\mathbf{s}) + G_S(\mathbf{r}_A,\mathbf{s})G_0^*(\mathbf{r}_B,\mathbf{s}) + \\ &\quad + G_0(\mathbf{r}_A,\mathbf{s})G_S^*(\mathbf{r}_B,\mathbf{s}) + G_S(\mathbf{r}_A,\mathbf{s})G_S^*(\mathbf{r}_B,\mathbf{s})]\,; \end{aligned} \tag{11}$$

where we explicitly identify the relationship between deconvolution and the cross-correlation of $G(\mathbf{r}_B,\mathbf{s})$ with $G(\mathbf{r}_B,\mathbf{s})$, here denoted by C_{AB}. As in equation 4, the numerator in equation 9 yields four terms as shown in the right-hand side of equation 11. The next step in our derivation is to express $|G(\mathbf{r}_B,\mathbf{s})|^{-2}$ as

$$\begin{aligned} \frac{1}{|G(\mathbf{r}_B,\mathbf{s})|^2} &= \frac{1}{[G_0(\mathbf{r}_B,\mathbf{s}) + G_S(\mathbf{r}_B,\mathbf{s})]\,[G_0^*(\mathbf{r}_B,\mathbf{s}) + G_S^*(\mathbf{r}_B,\mathbf{s})]} \\ &= \frac{1}{\left[|G_0(\mathbf{r}_B,\mathbf{s})|^2 + G_0(\mathbf{r}_B,\mathbf{s})G_S^*(\mathbf{r}_B,\mathbf{s}) + G_S(\mathbf{r}_B,\mathbf{s})G_0^*(\mathbf{r}_B,\mathbf{s}) + |G_S(\mathbf{r}_B,\mathbf{s})|^2\right]}\,; \end{aligned} \tag{12}$$

which shows that the numerator in equation 10 contains the power spectra of the unperturbed and scattered wavefields, as well as cross-terms between these two wavefields. If we assume the wavefield perturbations to be small ($|G_S|^2 << |G_0|^2$), the last term in the denominator of equation 12 can be dropped, hence

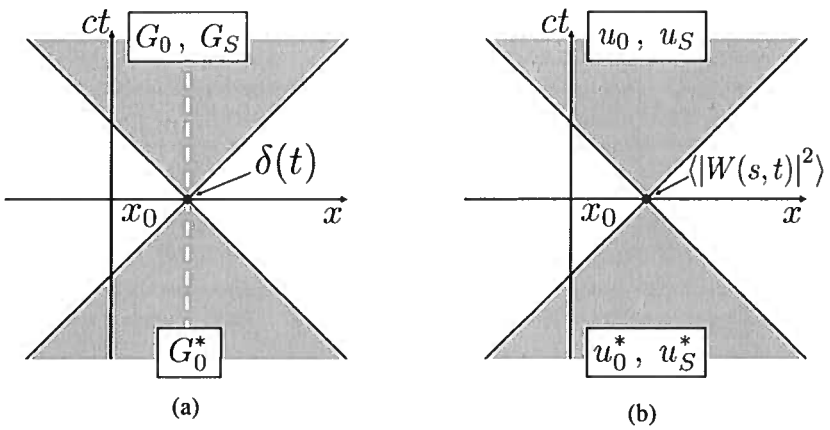

Figure 1. Representation of the wavefields that result from (a) deconvolution and (b) correlation interferometry. We refer to this representation as *light cones*. The medium is 1D with a wavespeed c. x_0 is the location of the pseudo-source. The grey-shaded areas represent the regions where the wavefields are nonzero. Away from these areas the wavefields are equal to zero. The wavefield produced by deconvolution interferometry in (a) is zero also along the dashed white line, for $t \neq 0$. In the time-domain, the excitation in (a) is given by $\delta(t)$, while in (b) it is given by $\langle|W(s,t)|^2\rangle$. The white text boxes indicate what type of wavefields propagate in the causal and acausal light cones of (a) and (b).

$$|G(\mathbf{r}_B,\mathbf{s})|^{-2} \approx \frac{1}{|G_0(\mathbf{r}_B,\mathbf{s})|^2 \left[1 + \frac{G_0(\mathbf{r}_B,\mathbf{s})\, G_S^*(\mathbf{r}_B,\mathbf{s})}{|G_0(\mathbf{r}_B,\mathbf{s})|^2} + \frac{G_S(\mathbf{r}_B,\mathbf{s})\, G_0^*(\mathbf{r}_B,\mathbf{s})}{|G_0(\mathbf{r}_B,\mathbf{s})|^2}\right]}, \tag{13}$$

By inspecting the denominator, it follows that equation 13 can be expanded in a power series in $G_S/G_0 + G_S^*/G_0^*$. From this expansion, taking terms only up to first order in the wavefield perturbations gives

$$|G(\mathbf{r}_B,\mathbf{s})|^{-2} \approx \frac{1}{|G_0(\mathbf{r}_B,\mathbf{s})|^2}\left[1 - \frac{G_S(\mathbf{r}_B,\mathbf{s})}{G_0(\mathbf{r}_B,\mathbf{s})} - \frac{G_S^*(\mathbf{r}_B,\mathbf{s})}{G_0^*(\mathbf{r}_B,\mathbf{s})}\right]. \tag{14}$$

After inserting equation 14 into the integral in equation 10 and keeping only the terms which are linear in the wavefield perturbations G_S, we get

$$\oint_\Sigma D_{AB}\, d\mathbf{s} = \underbrace{\oint_\Sigma \frac{G_0(\mathbf{r}_A,\mathbf{s})G_0^*(\mathbf{r}_B,\mathbf{s})}{|G_0(\mathbf{r}_B,\mathbf{s})|^2}\, d\mathbf{s}}_{D_{AB}^1} + \underbrace{\oint_\Sigma \frac{G_S(\mathbf{r}_A,\mathbf{s})G_0^*(\mathbf{r}_B,\mathbf{s})}{|G_0(\mathbf{r}_B,\mathbf{s})|^2}\, d\mathbf{s}}_{D_{AB}^2} - \underbrace{\oint_\Sigma \frac{G_S(\mathbf{r}_B,\mathbf{s})G_0(\mathbf{r}_A,\mathbf{s})G_0^*(\mathbf{r}_B,\mathbf{s})}{G_0(\mathbf{r}_B,\mathbf{s})}\, d\mathbf{s}}_{D_{AB}^3}. \tag{15}$$

Equation 15 shows that, to leading order in the scattered wavefield, the deconvolution integral in equation 10 can be represented by the integrals D_{AB}^1 through D_{AB}^3. In fact, equation 15 is a Born-like approximation (e.g., Weglein et al., 2003) of equation 10. In contrast with the term $|G(\mathbf{r}_B,\mathbf{s})|^2$ in equation 10, the term $|G_0(\mathbf{r}_B,\mathbf{s})|^2$ in equation 15 does not contain cross-terms between unperturbed and scattered wavefields. Therefore, $|G_0(\mathbf{r}_B,\mathbf{s})|^2$ is a slowly-varying zero-phase function of $\mathbf{s}$. This means that only the numerators determine the stationary contributions to the integrals in the right-hand side of equation 15. This property allows the direct comparison between the phases of the integrands in equations 15 and the terms in equation 5.

Physical insights into deconvolution interferometry come from observing that the integrands of the D_{AB}^1 and D_{AB}^2 terms (equation 15) have the same phase as the C_{AB}^1 and C_{AB}^2 terms in equations 4 and 5. Based on these observations, and on equation 6 (Vasconcelos and Snieder, 2007a), we can conclude that D_{AB}^1 provides the causal and acausal unperturbed wavefield that propagates from $\mathbf{r}_B$ to $\mathbf{r}_A$. More importantly, since the integrand of D_{AB}^2 and C_{AB}^2 have the same phase, the term D_{AB}^2 gives the causal scattered waves that are excited at $\mathbf{r}_B$ and recorded at $\mathbf{r}_A$.

In the process of deriving equation 15 from equations 10, 11 and 14, the terms that carry the same phase as C_{AB}^3 and C_{AB}^4 cancel with the products of C_{AB}^1 and C_{AB}^2 with the G_S^*/G_0^* term. This cancelation implies that interferometry by deconvolution does not recover the acausal scattering response between the two receivers.

Note that the acausal scattered waves are attenuated in deconvolution interferometry even for a closed surface integral (equation 15), or for an equipartioned system. This is a difference with what is obtained with interferometry by cross-correlation, which does recover the acausal scattering response between the receivers (equation 3).

The term D^3_{AB} has no counterpart in correlation interferometry. In a zero-offset interferometric experiment, that is $\mathbf{r}_A = \mathbf{r}_B$, the integrands of D^3_{AB} and D^2_{AB} have the same phase. In that case, the stationary traveltimes that come from integrating D^3_{AB} are the same as the ones coming from D^2_{AB}. These traveltimes correspond to scattered waves for a zero-offset experiment at $\mathbf{r}_B$. Given that D^3_{AB} and D^2_{AB} have opposite sign (equation 15), their contributions cancel when $\mathbf{r}_A = \mathbf{r}_B$. As the offset between the two receivers increases, the stationary traveltimes from D^3_{AB} and D^2_{AB} become increasingly different. As we shall discuss in more detail in Section 2.4, the stationary traveltimes from D^3_{AB} at finite offsets does not correspond to physical events for real wavefields excited at $\mathbf{r}_B$ and recorded at $\mathbf{r}_A$. Because of this we refer to terms such as D^3_{AB} as *spurious events*. Next, we explain the origin of the spurious arrivals in deconvolution interferometry.

Indeed, setting $\mathbf{r}_A = \mathbf{r}_B$ in equation 10 yields, in the time domain, a delta function at zero time. In deconvolution interferometry, scattered waves must cancel at zero-offset. This is a boundary condition imposed on the interferometric experiment where we excite waves at $\mathbf{r}_B$ and record them at $\mathbf{r}_A$. The consequence of this boundary condition is the creation of spurious events such as D^3_{AB} that cancel scattered waves that arrive at zero-offset with finite traveltimes. Note that these spurious arrivals are different from the ones that may result from the truncation of the surface integral (equation 8), and exist even for a closed surface of sources or in an equipartioned system (equation 15). Truncation of the surface integral in deconvolution interferometry will have the same effect as in interferometry by cross-correlation (see previous Section).

In Figure 1, we summarize the physical meaning of deconvolution interferometry and compare it to the correlation-based approach. The type of wavefield representation in Figure 1 comes from the theory of special relativity (Ohanian and Ruffini, 1994). According to the causality principle, no wave in Figure 1 can move faster than the medium wavespeed c (which for the sake of argument we assume to be constant). Hence, an excitation that occurs at x_0 and $t = 0$ influences only the causal grey-shaded regions in Figure 1, and it is influenced by the acausal grey-shaded regions. In special relativity theory, these grey-shaded areas are called *light cones*: the causal grey-shaded regions are the *future light cones*, while the acausal ones are the *past light cones*. From equation 9, it follows that $D_{BB} = 1$ (i.e., when $\mathbf{r}_A = \mathbf{r}_B$). In this case, deconvolution interferometry yields $G(\mathbf{r}_B, \mathbf{r}_B) = 1$ in the frequency domain, which translates to

$$G(\mathbf{r}_B, \mathbf{r}_B, t) = \delta(t) \tag{16}$$

in the time domain. Hence, in deconvolution interferometry, the time-domain excitation is given by $\delta(t)$ (Figure 1a). This excitation influences all of the causal light cone of interferometry by deconvolution, except at $x = x_0$ for $t > 0$, where the wavefield is zero (equation 16). Likewise, the condition given by equation 16 states that the pseudo-source in deconvolution interferometry is influenced by all events of the past light cone, except for the ones at $x = x_0$ and $t < 0$. The pseudo-source in deconvolution interferometry generates the unperturbed impulse response $G_0(x, x_0, t)$ and the impulsive scattered waves $G_S(x, x_0, t)$, as indicated in the future light cone of Figure 1a. This pseudo-source, obtained by deconvolution, is influenced only by unperturbed waves in its past light cone, which pertain to impulsive wavefield $G^*_0(x, x_0, t)$. This observation holds for terms from the deconvolution interferometry series (after the expansion of equation 10) of any order in the scattered wavefield, as we demonstrate in the next Section.

In correlation interferometry (Figure 1b), the excitation at $t = 0$ is given by $\langle |W(s,t)|^2 \rangle$, where $s = x_0$ for the pseudo-source synthesized by interferometry. This excitation generates the unperturbed wavefield $u_0(x, x_0, t)$ and the perturbation $u_S(x, x_0, t)$ in the future light cone in Figure 1b. The acausal waves in $u^*_0(x, x_0, t)$ and $u^*_S(x, x_0, t)$ present in the past light cone of correlation interferometry influence the excitation at $x = x_0$ and $t = 0$. Therefore, unlike in deconvolution interferometry (Figure 1b), x_0 is influenced by the acausal scattered waves in correlation interferometry (Figure 1b). Note that $u_0(x, x_0, t)$ and $u_S(x, x_0, t)$ (and their acausal counterparts) are not impulsive. Another difference with the deconvolution approach is that correlation interferometry influences $x = x_0$ for $t > 0$, and is influenced by waves at $x = x_0$ for $t < 0$ (Figure 1b). Although the light cone representations in Figure 1 are valid for one-dimensional homogeneous media, it can be generalized to higher dimensions (Ohanian and Ruffini, 1994) and to inhomogeneous media. These generalizations, however, are not necessary to our discussion on the physics of interferometry.

Finally, we rely on Figure 2 to summarize the physics of the extra boundary condition imposed by deconvolution interferometry (equation 16). From this condition (equation 16), it follows that $G(\mathbf{r}_B, \mathbf{r}_B, t) = 0$ when $t \neq 0$, which is represented by the dashed white line in Figures 1a and 2a. If G is the *pressure* response, we refer to this boundary condition in the interferometric experiment as the *free point* boundary condition. We use this term because the physical meaning of this boundary is analogous to that of a *free surface* boundary condition (where pressure is equal to zero), but in-

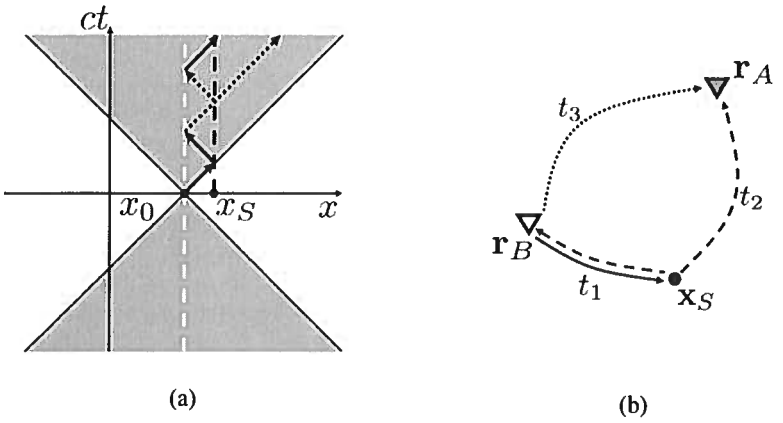

(a) (b)

Figure 2. Illustrations of the *free point* boundary condition in deconvolution interferometry. (a) provides an interpretation of the free point boundary condition for 1-dimensional media with wavespeed c, using the light cone representation (as in Figure 1a). x_0 is the location of the pseudo-source (and of the free point) and x_S is the location of a point scatterer. The arrows represent waves, excited by the source in x_0, propagating in the medium. Waves denoted with solid arrows propagate with opposite polarity with respect to waves represented by dotted arrows. The wavefield is equal to zero at the dashed white line, and the black vertical line indicates the region of influence of the medium perturbation at x_S. (b) illustrates the free point boundary condition in a 3D inhomogeneous acoustic medium. The pseudo-source, located at $\mathbf{r}_B$, is shown with the white triangle. The receiver is represented by the grey triangle at $\mathbf{r}_A$. The medium perturbation is a point scatterer at $\mathbf{x}_S$, here denoted by the black circle. The solid arrow depicts a direct wave excited at $\mathbf{r}_B$. This wave is scattered at $\mathbf{x}_S$ and propagates toward $\mathbf{r}_A$ and $\mathbf{r}_B$, as shown by the dashed arrows. The dotted arrow denotes a free point scattered wave that is recorded at $\mathbf{r}_A$. Waves represented by dashed and dotted arrows have opposite polarity. t_1 through t_3 are the traveltimes of waves that propagate from $\mathbf{r}_B$ to $\mathbf{x}_S$, $\mathbf{x}_S$ to $\mathbf{r}_A$, and $\mathbf{r}_B$ to $\mathbf{r}_A$, respectively.

stead it only applies to a *point* in space (in this case, $\mathbf{r}_B$). When G stands for the *particle velocity* response, the condition in equation 16 has the effect of *clamping* the point $\mathbf{r}_B$, so that it cannot move for $t \neq 0$. In that case, we refer to equation 16 as the *clamped point* boundary condition. Throughout this paper, we use the term *free point* when referring to the condition given by equation 16, since in previous equations G is represents pressure waves (e.g., equations 3 and 6). The boundary condition imposed by deconvolution interferometry in elastic media is different than that we discuss here, as shown by Vasconcelos and Snieder (2007b).

The effect of the free point boundary condition in a 1D homogeneous medium is illustrated by Figure 2a. The medium is perturbed by a scatterer at x_S. According to our interpretation of Figure 1a, the medium perturbations occurs at $t = 0$, so the black dashed line in Figure 2a shows that the medium perturbation only influences the future light cone in Figure 2a. Starting at $x = x_0$ and $t = 0$, the arrows in Figure 2a describe the path of a wave that propagates toward the scatterer at x_S, bounces off the scatterer to be then scattered again at the free point at $x = x_0$. This wave keeps on scattering infinite times between x_S and x_0. As in the free surface boundary condition, the free point at x_0 reflects waves with a reflection coefficient equal to -1. Note that the waves in Figure 2a change polarity at each bounce off the free point at x_0.

The extension of the free point concept to 3D inhomogeneous media is shown in Figure 2b. In this example, deconvolution interferometry is conducted for receivers at $\mathbf{r}_A$ and $\mathbf{r}_B$, as in equation 10. The receiver at $\mathbf{r}_B$ acts as a pseudo-source (white triangle in the Figure). The medium perturbation is the point scatterer at $\mathbf{x}_S$. The pseudo-source at $\mathbf{r}_B$ sends a direct wave (solid arrow in Figure 2b), with traveltime t_1 toward the scatterer. After this direct wave scatters at $\mathbf{x}_S$, it propagates back to $\mathbf{r}_B$ and toward $\mathbf{r}_A$ (dashed arrows), where it is recorded. This recorded singly scattered wave corresponds to the D^2_{AB} term in equation 15, with traveltime $t = t_1 + t_2$. When it arrives at $\mathbf{r}_B$, the wave backscattered at $\mathbf{x}_S$ scatters once more because of the free point boundary condition. The free-point scattered wave (dotted arrow) then travels directly to $\mathbf{r}_A$, where it is recorded at $t = 2t_1 + t_3$. This arrival corresponds to the D^3_{AB} term in equation 15. When $\mathbf{r}_A = \mathbf{r}_B$, $t_2 = t_1$ and $t_3 = 0$, and the singly scattered and free-point scattered waves have the same traveltime. This agrees with our previous discussion on the phase of the terms in equation 15. For a fixed $\mathbf{r}_B$ and varying $\mathbf{r}_A$, the traveltime of the free-point scattered wave is only controlled by t_3, since t_1 stays constant. Note that t_3 is also the traveltime of the direct wave that travels from $\mathbf{r}_B$ to $\mathbf{r}_A$, which is in turn given by the D^1_{AB} term in equation 15. Since the term D^3_{AB} is controlled by the direct wave traveltime t_3 for a fixed $\mathbf{r}_B$, it has the same move-

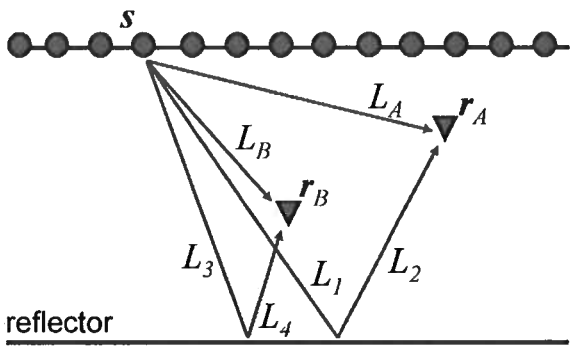

Figure 3. A simple model gain intuitive understanding about the physical meaning of the terms in equation 15. Receivers are imbedded in an acoustic homogeneous space containing a single reflector, bounded by a perfectly absorbing surface. Only direct and single-scattered waves are considered. Sources are depicted by circles on the surface, the two receivers are represented by triangles. L_A, L_B and L_1 through L_4 are the lengths of the ray segments. The reflection coefficient r is constant with respect to both position and incidence angle.

out as the direct wave in an interferometric shot gather with a pseudo-source at $\mathbf{r}_B$. Figure 2b illustrates only one of the many free point scattered waves produced by deconvolution interferometry.

Although the presence of spurious events such as D^3_{AB} (equation 15) may appear to be a problem for imaging interferometric gathers that result from deconvolution, we show in the Sections to come that these spurious events typically are not mapped onto coherent reflectors. What is most important is that interferometry by deconvolution is capable of successfully recovering the causal scattering response between any two receivers, as shown by the D^2_{AB} term.

2.2.2 Higher-order terms

In the previous section we limited our analysis to the terms of first order in G_S. Here, we analyze the higher-order terms. The full deconvolution series resulting from the expansion of equation 11 is

$$D_{AB} = \frac{C_{AB}}{|G_0(\mathbf{r}_B,\mathbf{s})|^2}\sum_{n=0}^{\infty}\left(-\frac{G_S(\mathbf{r}_B,\mathbf{s})}{G_0(\mathbf{r}_B,\mathbf{s})}-\frac{G^*_S(\mathbf{r}_B,\mathbf{s})}{G^*_0(\mathbf{r}_B,\mathbf{s})}\right)^n. \tag{17}$$

As shown in Appendix A, a physical analysis of the terms in equation 17 allows us to simplify it to

$$D_{AB} \approx \frac{G(\mathbf{r}_A,\mathbf{s})}{G_0(\mathbf{r}_B,\mathbf{s})}+\frac{C_{AB}}{|G_0(\mathbf{r}_B,\mathbf{s})|^2}\sum_{n=1}^{\infty}(-1)^n\left(\frac{G_S(\mathbf{r}_B,\mathbf{s})}{G_0(\mathbf{r}_B,\mathbf{s})}\right)^n. \tag{18}$$

In this equation, the first term yields physical unperturbed and scattered waves that propagate between $\mathbf{r}_B$ and $\mathbf{r}_A$, while the second term accounts for the effect of the free point boundary condition in deconvolution interferometry. The objective of the simplification in equation 18 is to keep only the terms that have non-zero phase which bring the most prominent contributions to the series in equation 17. The approximation that leads to equation 18 involves neglecting terms from equation 17 which are zero-phase or that yield arrivals with negligible amplitudes (see Appendix A). Note that the acausal terms proportional to $(G^*_S/G^*_0)^n$ in equation 17 are not present in equation 18 because they cancel in the $n \to \infty$ limit (see Appendix A). This cancellation determines that the point x_0 in Figure 1a is not influenced by acausal scattered waves (see discussion in Section 2.2.1). The first term in equation 18 gives the terms D^1_{AB} and D^2_{AB} in equation 15. The term D^3_{AB} is obtained by the product of C^1_{AB} and the first term of the sum in equation 18. It is important to note that terms of a given order in the scattered wavefield come from different values of n in equation 18. Let us take, for example,

$$T_1^{2^{nd}} = -G_S(\mathbf{r}_A,\mathbf{s})\,G^*_0(\mathbf{r}_B,\mathbf{s})\left(\frac{G_S(\mathbf{r}_B,\mathbf{s})}{G_0(\mathbf{r}_B,\mathbf{s})}\right) \tag{19}$$

and

$$T_2^{2^{nd}} = G_0(\mathbf{r}_A,\mathbf{s})\,G^*_0(\mathbf{r}_B,\mathbf{s})\left(\frac{G_S(\mathbf{r}_B,\mathbf{s})}{G_0(\mathbf{r}_B,\mathbf{s})}\right)^2 \tag{20}$$

where T_i^o represents a given term T_i from equation 18 of order o in the scattered wavefield G_S. $T_1^{2^{nd}}$ and $T_2^{2^{nd}}$ are the most prominent terms which are of second-order in the scattered wavefield, where $T_1^{2^{nd}}$ comes from $n = 1$ while $T_2^{2^{nd}}$ comes from $n = 2$. When $\mathbf{r}_A = \mathbf{r}_B$, $T_1^{2^{nd}}$ and $T_2^{2^{nd}}$ will give rise to arrivals with twice the traveltimes of $G_S(\mathbf{r}_A,\mathbf{r}_B)$. Since these two terms have opposite polarity (equations 19 and 20), their contributions cancel. Likewise the terms

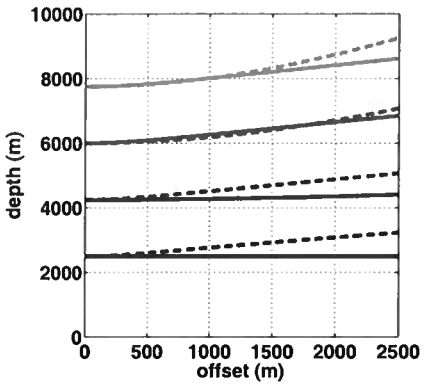

Figure 4. Depths obtained by shot-profile migration of stationary traveltimes of deconvolution interferometry terms with varying receiver-to-receiver offset. Black lines correspond to the terms that are of leading order in the scattered wavefield (see Section 2.2.1). The black solid line represents migrated depths from traveltimes associated to the D^2_{AB} term (equation 15); whereas the black dashed line pertains to the D^3_{AB} term (also equation 15). The curves colored in blue, red and green are associated respectively to terms which are quadratic, cubic and quartic with respect to scattered waves. For a given order in the scattered waves, we show only the two terms that have strongest amplitude. Of the blue curves, the solid curve relates to the $T_1^{2^{nd}}$ in equation 19 and the dashed one pertains to $T_2^{2^{nd}}$ (equation 20). The imaged depths computed from the $T_1^{3^{rd}}$ (equation 21) and $T_2^{3^{rd}}$ (equation 22) stationary traveltimes are shown by the solid and dashed red lines, respectively. Although the quartic terms related to the green curves are not explicitly shown in the text, they come from the deconvolution interferometry series in equation 18 for n equal to 3 and 4.

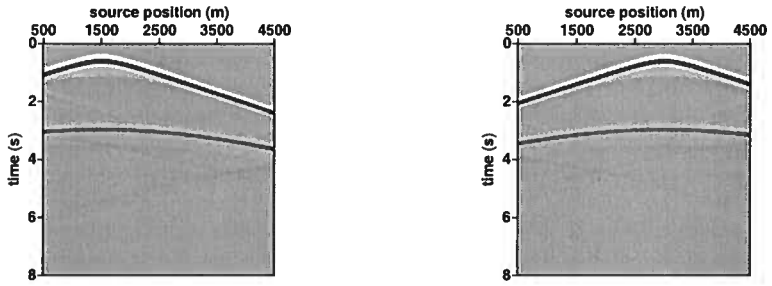

(a) (b)

Figure 5. Common receiver gathers for receivers placed at (a) 1500 m and at (b) 3000 m.

$$T_1^{3^{rd}} = G_S(\mathbf{r}_A,\mathbf{s})\,G_0^*(\mathbf{r}_B,\mathbf{s})\left(\frac{G_S(\mathbf{r}_B,\mathbf{s})}{G_0(\mathbf{r}_B,\mathbf{s})}\right)^2 \qquad (21)$$

and

$$T_2^{3^{rd}} = -\,G_0(\mathbf{r}_A,\mathbf{s})\,G_0^*(\mathbf{r}_B,\mathbf{s})\left(\frac{G_S(\mathbf{r}_B,\mathbf{s})}{G_0(\mathbf{r}_B,\mathbf{s})}\right)^3 \qquad (22)$$

result in traveltimes that are three times those of $G_S(\mathbf{r}_A,\mathbf{r}_B)$ when $\mathbf{r}_A = \mathbf{r}_B$. $T_1^{3^{rd}}$ and $T_2^{3^{rd}}$ are the most prominent terms from the series in equation 18 which are of third-order in the wavefield perturbations. They come respectively from setting $n = 2$ and $n = 3$ in equation 18. The phase of of any the higher-order terms in deconvolution interferometry (second term in equation 18; e.g., equations 19 through 22) can be physically explained by the interactions of the free point at $\mathbf{r}_B$ (equations 10 and 16) with the waves scattered by the medium perturbation. In the example of Figure 2b, the higher-order spurious multiples arise from multiple scattering between the scatterer at $\mathbf{x}_S$ and the free point at $\mathbf{r}_B$.

As we demonstrate with our numerical example, some of these higher-order spurious terms (such as in equations 19 through 22) may be present in the deconvolution interferometry integrand. Hence, it is important to understand to what extent these terms present a challenge to the proper imaging from interferometry by deconvolution. We investigate this in the next Sections.

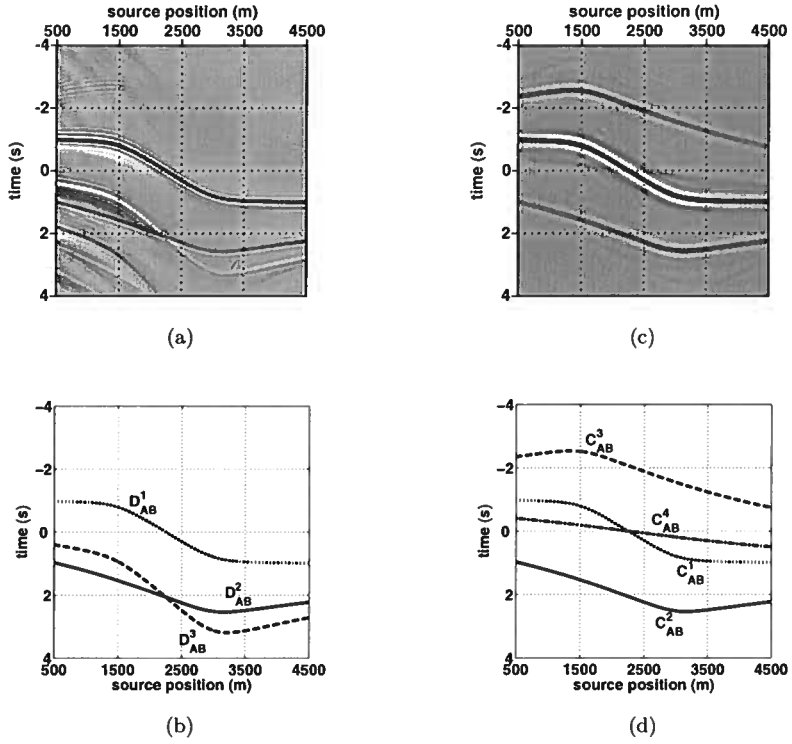

Figure 6. Deconvolution and cross-correlation gathers for the first and last receivers, whose lateral positions are, respectively, 1500 and 3000 m. (a) displays the deconvolution gather obtained from deconvolving the modeled common-receiver gathers, whereas (b) shows ray-theoretical traveltimes for the terms in equation 15, computed according to integrands in equation 15 in Section 2.4. Analogous to (a), (c) is the cross-correlation gather generated from source-by-source correlation of the two receiver gathers. (d) shows the asymptotic traveltimes corresponding the phase of the integrands in equation 5.

2.3 Deconvolution after summation over sources

Using the deconvolution approach described by equation 10 is not the only option for doing interferometry without independent estimates of the source function. The deconvolution of $u(\mathbf{r}_A, \mathbf{s})$ and $u(\mathbf{r}_B, \mathbf{s})$ is equal to

$$D_{AB} = \frac{u(\mathbf{r}_A, \mathbf{s})\, u^*(\mathbf{r}_B, \mathbf{s})}{u(\mathbf{r}_A, \mathbf{s})\, u^*(\mathbf{r}_B, \mathbf{s})} = \frac{C_{AB}}{C_{BB}}, \tag{23}$$

where C_{BB} is the auto-correlation of $u(\mathbf{r}_B, \mathbf{s})$. In the previous Section we summed this result over all sources. Interferometry can be done as in the previous Section, or we can first integrate over sources, and then compute the spectral ratio

$$\frac{\oint_\Sigma C_{AB}\, d\mathbf{s}}{\oint_\Sigma C_{BB}\, d\mathbf{s}} = \frac{G(\mathbf{r}_A, \mathbf{r}_B) + G^*(\mathbf{r}_A, \mathbf{r}_B)}{\oint_\Sigma C_{BB}\, d\mathbf{s}}. \tag{24}$$

The ratio on the left-hand side of the equation cancels the contribution of the wavelet $\langle |W(\mathbf{s})|^2 \rangle$ (equation 3). No independent estimate of the source function is required. Other authors have suggested approaches similar to the one in equation 24. The pilot-trace approach used in drill-bit seismology (e.g., Poletto and Miranda, 2004; Rector and Marion, 1991) uses auto-correlations of the accelerometer recordings or geophone data to built a deconvolution operator (Vasconcelos and Snieder, 2007b). The Virtual Source method (Bakulin and Calvert, 2006; Schuster and Zhou, 2006) also relies on a deconvolution analogous to the one in equation 24.

As we did with the cross-correlation in equation 4, we can expand C_{BB} and integrate it over sources, giving:

$$\oint_\Sigma C_{BB}\, d\mathbf{s} = \oint_\Sigma C^1_{BB}\, d\mathbf{s} + \oint_\Sigma C^2_{BB}\, d\mathbf{s} + \oint_\Sigma C^3_{BB}\, d\mathbf{s} + \oint_\Sigma C^4_{BB}\, d\mathbf{s} \tag{25}$$

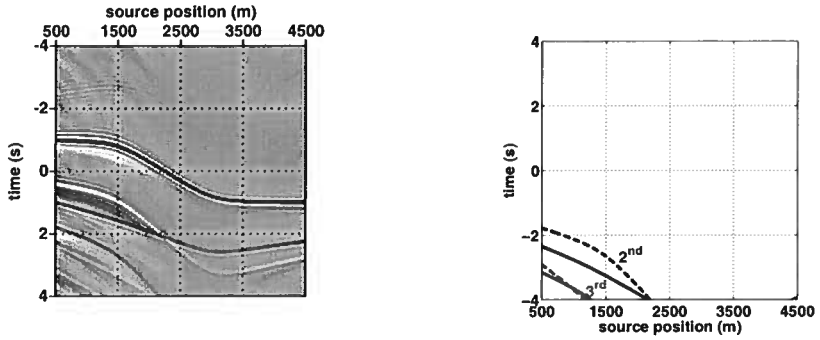

(a) (b)

Figure 7. Deconvolution interferometry terms which are nonlinear in the scattered wavefield. The left panel shows the integrand of the deconvolution interferometry integral (equation 10),computed from finite-difference modeling (same as in Figure 6a). In (b), the traveltimes corresponding to the second order terms T_1^{2nd} and T_2^{2nd} (equations 19 and 20) are shown respectively with solid and dashed blue curves; while the solid and dashed red curves come from T_1^{3rd} and T_2^{3rd} (equations 21 and 22), respectively. The curves in (a) correspond to the curves of the same color and type in Figure 4.

From the integration of the four terms on the right-hand side of equation 25, we can write

$$\frac{1}{\oint_\Sigma C_{BB}\, ds} = \frac{1}{\left[|G_0(\mathbf{r}_B,\mathbf{r}_B)|^2 + \oint_\Sigma C_{BB}^2\, ds + \oint_\Sigma C_{BB}^3\, ds + |G_S(\mathbf{r}_B,\mathbf{r}_B)|^2\right]}\,; \tag{26}$$

where the denominator contains zero-phase terms (the power spectra), as well as the causal and acausal zero-offset scattered wavefield $u_S(\mathbf{r}_B,\mathbf{r}_B)$. Using the weak perturbation approximation ($|G_0|^2 >> |G_S|^2$), we can approximate

$$\left[\oint_\Sigma C_{BB}\, ds\right]^{-2} \approx \frac{1}{|G_0(\mathbf{r}_B,\mathbf{r}_B)|^2\left[1 + \frac{1}{|G_0(\mathbf{r}_B,\mathbf{r}_B)|^2}\oint_\Sigma C_{BB}^2\, ds + \frac{1}{|G_0(\mathbf{r}_B,\mathbf{r}_B)|^2}\oint_\Sigma C_{BB}^3\, ds\right]} \tag{27}$$

which gives us an expression of the same form as equation 13. Hence, we can expand equation 27 in a power series of the same form as in our previous discussions (see equations 13, 14 and 17). Considering only the very first term of the series expansion, it gives

$$\frac{\oint_\Sigma C_{AB}\, ds}{\oint_\Sigma C_{BB}\, ds} \approx \frac{G(\mathbf{r}_A,\mathbf{r}_B) + G^*(\mathbf{r}_A,\mathbf{r}_B)}{|G_0(\mathbf{r}_B,\mathbf{r}_B)|^2}\,. \tag{28}$$

This expression shows that deconvolving the integral over C_{AB} by the integral over C_{BB} recovers both the causal and acausal response at $\mathbf{r}_A$ for waves excited at $\mathbf{r}_B$. This response is scaled by the power spectrum of the zero-offset unperturbed wavefield. Note that equation 28 is approximate. Other terms of the series expansion of equation 27 yield cross-correlations and convolutions between causal and acausal $u(\mathbf{r}_A,\mathbf{r}_B)$ and $u_S(\mathbf{r}_B,\mathbf{r}_B)$. Since, after Vasconcelos and Snieder (2007a),

$$\int_{\sigma_1} C_{BB}^2\, ds = \int_{\sigma_1} G_S(\mathbf{r}_B,\mathbf{s})G_0^*(\mathbf{r}_B,\mathbf{s})\, ds \approx G_S(\mathbf{r}_B,\mathbf{r}_B)\,, \tag{29}$$

and

$$\int_{\sigma_1} C_{BB}^3\, ds = \int_{\sigma_1} G_0(\mathbf{r}_B,\mathbf{s})G_S^*(\mathbf{r}_B,\mathbf{s})\, ds \approx G_S^*(\mathbf{r}_B,\mathbf{r}_B)\,. \tag{30}$$

Other terms arising from the expansion of equation 27 are bound to be small because not only they are products between G and G_S terms, but also because they are divided by $|G_0(\mathbf{r}_B,\mathbf{r}_B)|^{2n}$ (with $n = 2,3,4,\ldots$).

2.4 Example: asymptotic analysis of deconvolution interferometry

In Section 2.2 we discussed some of the physics behind the terms in deconvolution interferometry based on their integral representation. Here we illustrate the ideas in the previous Sections using asymptotics. We use these asymptotic methods to investigate the spurious arrivals in imaging gathers produced by deconvolution interferometry (see Section 2.2). Although it is necessary to restrict this type of analysis to simple models, the observations provide useful insight into the physics of our problem. Snieder et al. (2006) used the same kind of asymptotic analysis to study the terms arising from interferometry by cross-correlations (e.g., equation 4). They also characterized spurious multiples that come from a limited source integration (see discussion concerning equation 8). Since our approach is analogous to that in Snieder et al. (2006), we do not reproduce all steps in their derivation. Some of these steps are reproduced in Appendix B.

The toy model we use is that of a single reflector in a homogeneous medium (Figure 3). The unperturbed wavefields $u_0(\mathbf{r}_{A,B},\mathbf{s})$ consist of the direct waves while $u_S(\mathbf{r}_{A,B},\mathbf{s})$ are the single-reflected waves. We use the far-field acoustic Green's functions in equation B1 to represent the ray-geometric arrivals in Figure 3. If we rewrite the term D^1_{AB} in equation 15 according to equation B1 we get

$$D^1_{AB} = \frac{1}{(4\pi L_B)^2}\int \frac{e^{ik(L_A-L_B)}}{L_A L_B}dxdy\,, \qquad (31)$$

where the integral over $\mathbf{s}$ (equation 15) has been converted to the integration over the lateral coordinates x and y (representing the surface plane). The stationary-phase evaluation (see Appendix A) of the integral in equation 31 gives

$$D^1_{AB} = \frac{nc}{32\pi^2 L_B^2\, cos\psi}\,\frac{G_0(\mathbf{r}_A,\mathbf{r}_B)}{(-i\omega)}\,; \qquad (32)$$

with the acoustic wavespeed c, and n representing sources per unit area (Snieder et la., 2006). A straight raypath connecting $\mathbf{r}_A$, $\mathbf{r}_B$ and the surface determines the stationary source position that gives equation 32. The angle defined between this stationary ray and the vertical defines the angle ψ. $G_0(\mathbf{r}_A,\mathbf{r}_B)$ is the unperturbed Green's function, in this case a direct wave, propagating from $\mathbf{r}_B$ to $\mathbf{r}_A$. Equation 32 is consistent with our interpretation of the term D^1_{AB} in Section 2.2.1. The $(-i\omega)^{-1}$ in equation 32 indicates that after interferometry it is necessary to perform a time-domain differentiation to obtain the Green's function (Snieder et al., 2006). This is a correction factor commonly found in interferometry (e.g., Wapenaar et al., 2004a; van Wijk et al., 2006): it compensates for the source integration, and it depends on which type of Green's function is considered (Wapenaar et al, 2004b). Although for simplicity we have not explicitly kept the $i\omega$ factors in the integrals in previous Sections, the exact forms of those expressions also have $i\omega$ factors (Vasconcelos and Snieder, 2007a).

The term D^2_{AB} of equation 15 for our model reduces with equation B1 to the integral

$$D^2_{AB} = \frac{r}{(4\pi L_B)^2}\int \frac{e^{ik(L_1+L_2-L_B)}}{(L_1+L_2)\,L_B}dxdy\,, \qquad (33)$$

which is has a form similar to that of equation 31. This integral can also be evaluated with the stationary phase method, giving

$$D^2_{AB} = \frac{nc}{32\pi^2 L_B^2\, cos\psi}\,\frac{G_S(\mathbf{r}_A,\mathbf{r}_B)}{(-i\omega)}\,; \qquad (34)$$

where r is the constant reflection coefficient at the interface in Figure 3. The stationary source point that results in equation 34 is associated with a raypath that starts at the surface, passes through $\mathbf{r}_B$, specularly reflects off the interface and is recorded at $\mathbf{r}_A$. Since the stationary raypaths that give equations 32 and 34 are different, the corresponding values of the obliquity factor $cos\psi$ are also different. The stationary-phase evaluation of D^2_{AB} (equation 33) results in $G_S(\mathbf{r}_A,\mathbf{r}_B)$: a causal singly reflected wave excited at $\mathbf{r}_B$ and recorded at $\mathbf{r}_A$.

Next, we consider the asymptotic behavior of the D^3_{AB} term (equation 15). Using the Green's functions in equation B1, D^3_{AB} is given by

$$D^3_{AB} = -\frac{r}{(4\pi L_B)^2}\int \frac{e^{ik[(L_3+L_4-L_B)-(L_A-L_B)]}}{(L_3+L_4)\,L_A L_B^2}dxdy\,. \qquad (35)$$

If $\mathbf{r}_A = \mathbf{r}_B$, the phase of the integrand in equation 35 is the same as in equation 33, so the resulting stationary-phase evaluation of D^3_{AB} is proportional to $G_S(\mathbf{r}_B,\mathbf{r}_B)$. This supports the physical interpretation of D^3_{AB} provided in Section 2.2.1, where we argue that for $\mathbf{r}_A = \mathbf{r}_B$ the terms D^3_{AB} and D^1_{AB} have the same phase and give the zero-offset scattered-wave traveltimes. For $\mathbf{r}_A \neq \mathbf{r}_B$, D_{AB} is not associated to any stationary paths that would exist for a real excitation placed at $\mathbf{r}_B$ without the free point boundary condition (equation 16).

The main objective in studying the spurious terms such as D^3_{AB} is to determine their influence in imaging data from deconvolution interferometry. Hence, we proceed with a numerical asymptotic analysis of the spurious arrivals. Once we specify a model such as the one in Figure 3, we compute the ray-based traveltimes of each spurious arrival for all source positions, according to equation 18. From the maxima of the phases of each spurious event, we determine their corresponding stationary traveltime and source position. We did this for a fixed position $\mathbf{r}_B$ as a function of a laterally-varying $\mathbf{r}_A$. Given the receiver positions, stationary traveltimes and model parameters, we predict the migrated depth

of any given term (e.g., D^2_{AB}) through common-shot migration (Bleistein et al., 2001). The result of this analysis is shown in Figure 4. The geometry and model parameters used in the computations in Figure 4 are the same as in the numerical model we discuss in the next Section. For these computations, $\mathbf{r}_A$ and $\mathbf{r}_B$ are kept at the same constant depth level.

Only the term D^2_{AB} represents physical scattered waves in Figure 4. As expected, D^2_{AB} is mapped at the same depth for all offsets, as shown by the solid black line in the Figure. On the other hand, the spurious terms in Figure 4 map to depths that increase with increasing offset. This suggests that when a sufficiently large range of offsets is used, most spurious events interfere destructively when imaged. The only exception is the term $T_1^{2^{nd}}$, whose mapped depth varies slowly with offset. We suspect that this might be because the phase of $T_1^{2^{nd}}$ is equivalent to twice the phase of the integrand of D^2_{AB} (equation 15), thus representing artifact multiples arising from convolving $u_S(\mathbf{r}_A, \mathbf{r}_B)$ with itself.

If only a short offset aperture is available (e.g., in the offset range 0 to 500 m in Figure 4), the spurious multiples may add constructively in the final image. We argue that even if spurious events in Figure 4 map to image they will not be very prominent because they are of higher order in the scattered wavefield. In addition, these terms should cancel close to zero-offset because of the free point boundary condition imposed by deconvolution interferometry (see discussion in Section 2.2.1). This boundary condition requires the zero-offset wavefield to be zero at finite times (see Section 2.2.1). Indeed, solid and dashed lines of a common color in Figure 4 pertain to terms that have opposite polarity.

Note that at zero-offset (Figure 4), 2^{nd}-order spurious events map at twice the depth of the physical reflector relative to the receivers (receiver depth is 750 m); 3^{rd}-order events map at three times that depth, and so on. This observation relates to the remarks made about the zero-offset traveltimes expected for the higher-order terms in Section 2.2.2.

3 NUMERICAL EXAMPLE

The model we use is composed of a water layer with a wavespeed of 1500 m/s. A flat, horizontal interface was placed at 2500 m depth. The contrast at the interface is produced by a velocity step from 1500 to 2200 m/s, with a constant background density of 1000 kg/m^3. The receivers were positioned in a horizontal line at 750 m depth, starting at lateral position $x = 1500$ m and ending at 3000 m, with increments of 25 m. The source line was also horizontal at a depth of 400 m, ranging from $x = 500$ m to 4500 m, with increments of 50 m. The data was modeled by 2D acoustic finite-differencing with absorbing boundary conditions. Figure 5 shows that the data consists of direct and single-reflected waves. As in the previous Section, we refer to these waves as $u_0(\mathbf{r}_{A,B}, \mathbf{s})$ and $u_S(\mathbf{r}_{A,B}, \mathbf{s})$, respectively.

First, we use the data in Figure 5 to analyze the integrands in equations 3 and 10. The deconvolution of the wavefield in Figure 5a with the wavefield in Figure 5b yields Figure 6a, while the cross-correlation yields Figure 6c. The deconvolution gather (Figure 6a) displays causal term D^2_{AB}, while both causal (C^2_{AB}) and acausal (C^3_{AB}) contributions are present in the cross-correlation gather (Figure 6c). This confirms our claim that deconvolution interferometry gives mostly causal scattering contributions (see Section 2.2.1). The term C^4_{AB} also does not have a corresponding term in the deconvolution gather, as was predicted by equation 15. Also, the waveforms in Figure 6a are sharper than those in Figure 6c because deconvolution suppresses the source function. We use a *water-level regularization* method to do deconvolutions. For a brief discussion on this method see Appendix A in Vasconcelos and Snieder (2007b).

The arrival times predicted with perturbation theory (bottom plots in Figure 6) provide an accurate representation of the modeled results in the top panels of Figure 6. In particular, the deconvolution series (equation 18, Figure 6b) describes well the most prominent terms in deconvolution interferometry (equation 10, Figure 6a). As predicted by theory, the terms D^2_{AB} and D^3_{AB} have opposite polarity. The extrema of the curves in Figure 6 are stationary source positions. Thus, the stationary traveltime of each term is the time associated to the extremum of its curve in Figure 6. The stationary traveltimes from D^1_{AB} and C^1_{AB} are $t = \pm 1$ s, representing causal and acausal direct waves. D^2_{AB} and C^2_{AB} result in a stationary time of approximately 2.5 s, which coincides with the traveltime of a causal single-scattered wave. In previous Sections we showed that the stationary traveltimes given by D^2_{AB} and D^3_{AB} only coincide when $\mathbf{r}_A = \mathbf{r}_B$. Since in Figure 6 $\mathbf{r}_A \neq \mathbf{r}_B$, the stationary time of D^3_{AB} is different from that of D^2_{AB}.

There are other events present in the lower left-hand corner of Figure 6a which are not present in Figure 6b. These events are described by higher-order terms of the deconvolution series (equation 18). Figure 7 shows how the events are described by terms of second and third order in the scattered wavefield. The events corresponding to third-order terms have considerably smaller amplitude than the ones related to second-order terms. Second-order terms are in turn weaker than the leading-order terms (Figure 6a). A decrease in the power of the events with increasing order in the perturbed wavefield is expected, given the form of equation 18. These examples confirm the accuracy of the deconvolution series in describing the character of the integrand in deconvolution interferometry (equation 10).

The integration over sources (e.g., equations 3 and 10) corresponds to the horizontal stack of the plots in Figures 6a and c. Stacking, for example, Figure 6c results in a single trace that represents a wavefield ex-

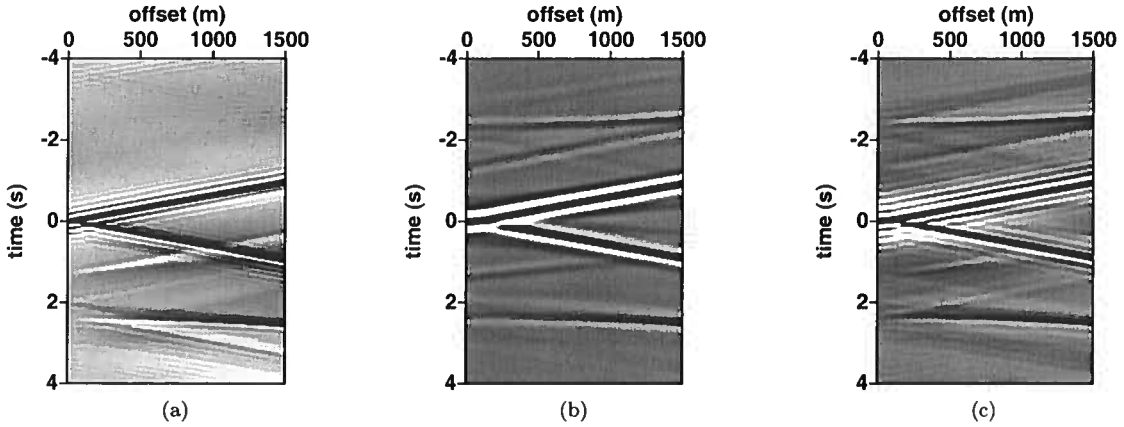

Figure 8. Pseudo-shot (interferometric) gathers with the shot positioned at the receiver at 1500 m. The gather in (a) is obtained by deconvolution before stacking (equation 10), (b) is generated by cross-correlations (equation 3) and (c) is given by deconvolution after summation over sources (equation 24). Source integration of the gathers in Figures 6a and c yield the last trace in (a) and (b), respectively.

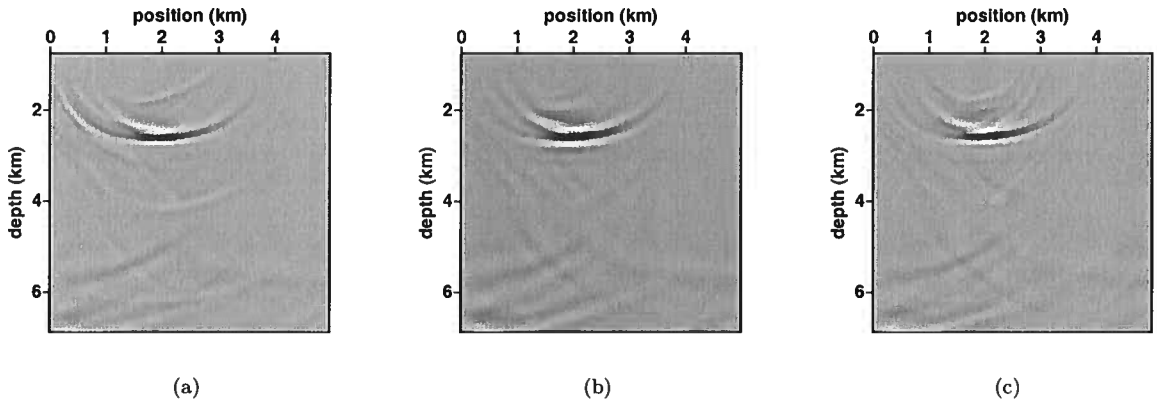

Figure 9. Shot-profile wave-equation migrated images of the virtual shot gathers in Figure 8. In this figure, (a), (b) and (c) are the images obtained from migrating the gathers in Figure 8a, b and c, respectively. The true depth of the target interface is 2500 m. The shot is placed at 1.5 km and receivers cover a horizontal line from 1.5 to 3.0 km.

cited at a lateral position of 1500 m and recorded at 3000 m. We create an interferometric shot gather with a pseudo-shot placed at 1500 m by computing and stacking all of the deconvolution and cross-correlation gathers (Figures 6a and c) for the receiver fixed at 1500 m but varying the lateral position of the other receiver from 1500 to 3000 m. The interferometric shot gathers are shown in Figure 8.

All gathers in Figure 8 show both causal and acausal direct waves. Only the gathers produced from cross-correlation (Figure 8b) and deconvolution after stack (Figure 8c) show causal and acausal reflections, agreeing with equations 3 and 28. The interferometric gather produced from deconvolution interferometry (Figure 8a) indeed only shows the causal scattered wave. The first-order term D^3_{AB} (equation 15) can be seen in Figure 8a with opposite polarity and slower moveout compared to the physical reflection. The reflection and the D^3_{AB} spurious events converge at zero-offset where they cancel. As observed in Figure 8a, this is due to the effect of the free point boundary condition (equation 16) imposed by the deconvolution of wavefields before source integration (see Section 2.2.1). As in Figure 8a, the zero-offset trace of the gather in Figure 8c consists of a band-limited spike at 0 s. This can be verified by setting $C_{AB} = C_{BB}$ in equation 24. In contrast

to Figure 8a, Figure 8c does not contain the spurious events produced by the free point boundary condition present when deconvolving the wavefields before source integration. There are other events which are related to the truncated source integration (see Section 2.1). These are, for example, the upward-sloping linear events appearing between the direct arrivals and the reflections in all three gathers.

The images obtained by shot-profile migration of the gathers in Figure 8 are shown in Figure 9. The shot-profile migration was done by wavefield extrapolation, with a split-step Fourier extrapolator. The reflector is placed at the correct depth in all three images. Also, all three images are remarkably similar, despite the differences between the gathers in Figure 8. The similarity between the images comes from the fact that the spurious events in deconvolution interferometry have a negligible effect in images made from offset-dependent data. Based on Figure 4, we argue in Section 2.4 that the spurious events produced by deconvolution interferometry typically do not map onto coherent reflectors. This justifies the absence of spurious reflectors in Figure 9a. In Figure 9, we can also appreciate the effect of deconvolution (Figures 9a and c) in compressing the waveform relative to cross-correlation (Figure 9b).

4 DISCUSSION AND CONCLUSIONS

By representing recorded wavefields as a superposition of direct and scattered wavefields, we derived a series expansion yielding terms that follow from performing deconvolution interferometry on receiver gathers before summing over sources. This derivation suggests that interferometry by deconvolution before stacking over sources gives only the causal scattered wavefield as if one of the receivers acted as a source. Because deconvolution interferometry requires the zero-offset wavefield to be zero at nonzero times, it generates spurious events to cancel scattered arrivals at zero-offset. We refer to this condition as the *free point* boundary condition at the pseudo-source location. With a simple model we illustrate this by using asymptotic approximations to the terms in deconvolution interferometry using the stationary-phase method. We also argue that interferometry can also be accomplished by deconvolution after summation over sources, which would yield terms analogous to correlation-based interferometry.

Numerical examples with impulsive source data showed that deconvolution interferometry can successfully retrieve the causal response between two receivers. This response can be used to build interferometric shot gathers which in turn can be imaged. Imaging of deconvolution interferometric shot gathers proved to practically eliminate the spurious arrival generated by the deconvolution method. Indeed, our numerical asymptotic analysis suggests that the deconvolution-related spurious events add destructively in the imaging of offset-variable data. It may be possible to create a reverse-time imaging scheme that results in an image free of spurious artifacts. We believe this could be done from the proper manipulation of boundary conditions in numerical modeling by the finite-difference method (Biondi, 2006). Although our assessment of the spurious events is model dependent, we believe that our observations also hold for more complicated models (see Part II of this article).

Ideally, we want interferometry to give us the best possible representation of the impulse response between two given receivers. Cross-correlation interferometry yields an accurate representation of the waves propagating between the receivers, but it requires an estimate of the power spectrum of the wavelet for it to give an impulsive response. Deconvolution interferometry yields an impulsive response, but it does so at the cost of generating artifacts. Another option is to design an inverse filter to do interferometry (Sheiman, personal communication, 2006). For example, the inverse filter may require the zero-offset trace in the pseudo-shot with a pre-determined band-limited pulse. This inverse filter does not require any knowledge about the model, and its output would be described the deconvolution series discussed here. If there is some knowledge about the model, the inverse filter may be designed to replicate an estimate of a desired wavefield (e.g., Amundsen, 2001). In this case, the output of the inverse filter will approximate an impulsive version of cross-correlation interferometry. We associate the form of the deconvolution interferometry series to that of scattering series such as the Lippman-Schwinger series (Rodberg et al., 1967; Weglein et al. 2003). Forward and inverse scattering series serve, for instance, as the basis to methodologies in imaging and multiple suppression (Weglein et al., 2003). In analogy to scattering-based approaches, it is possible to express the deconvolution interferometry series in forward and inverse forms as well. Hence, an inverse deconvolution interferometry series may be designed for the imaging of pseudo-shots generated by deconvolution interferometry.

The results we present here are consistent with previous deconvolution interferometry results. Although there is no explicit source integration in the work of Snieder and Şafak (2006) and of Mehta et al. (2007a), their results agree with our representation of deconvolution interferometry before integration over sources. In the 1D models, such as used by Snieder and Şafak (2006) and Mehta et al. (2007a), the excitation produced by teleseismic events was naturally in the stationary path between the receivers. This excludes the need for a full 3D source integration as in equation 10. Moreover, we argue that the application commonly referred to as *receiver function* (e.g., Shen et al. 1998, Mehta et al., 2007b) in global seismology is a direct application of deconvolution interferometry. With the same type of 1D layered model as in Snieder and Şafak (2006) and of

Mehta et al. (2007a), the receiver functions consist on the deconvolution of a radial receiver component with the vertical component of the same receiver. This, in interferometry terms, yields a zero-offset trace that corresponds to an excitation in the vertical direction whose wavefield is recorded in the radial direction. Also, like in Snieder and Şafak (2006) and Mehta et al. (2007a), no source integration is required because in the 1D model all incoming waves are in the stationary wave-path.

It is important to point out other perhaps less obvious relationships between our work and that of other authors. With an elegant derivation and examples, Loewenthal and Robinson (2000) show that deconvolutions between measured dual wavefields (e.g., particle velocity and pressure) can be used for model-independent redatuming and for recovering reflectivity. Their derivation, in fact, is a proof of the application of deconvolution interferometry for dual wavefields. Amundsen (2001) designs deconvolution-type inverse operators to strip the influence of the water layer in marine data, at the same time performing free-surface multiple attenuation and estimating reflectivity. In a companion paper, Holvik and Amundsen (2005) use representation theorems of the same type as discussed in Section 2.1 along with deconvolution for elastic wavefield decomposition and multiple elimination. These papers are intimately related to deconvolution interferometry as we propose it. We advocate that the proper choice and manipulation of the wavefield pair u_0 and u_S give rise to different applications, with the example of dual wavefields by Loewenthal and Robinson (2001) or the boundary-condition approach by Amundsen (2001) and Holvik and Amundsen (2005). We also use these examples to highlight the potential of deconvolution-based interferometry in recovering data with amplitudes consistent with the subsurface reflectivity function.

There are other important potential applications for deconvolution interferometry. As we summarized in Figure 1, deconvolution interferometry gives only causal wavefield perturbations, while unperturbed waves are present at both positive and negative times. For an ideal source coverage, the subtraction of the acausal wavefield from deconvolution interferometry from its causal response results only in wavefield perturbations. This idea may be useful for processing data from time-lapse experiments, as well as for pre-processing procedures such as direct- or surface-wave suppression. In the context of imaging, we highlight that in the cross-correlation imaging condition (Claerbout, 1985; Sava, 2006), the correlation serves the purpose of reproducing a zero-offset pseudo-shot experiment placed on top of a reflector (after extrapolating data to the reflector position). This is a direct application of the concept of correlation interferometry (e.g., Wapenaar and Fokkema). We believe that deconvolution interferometry can also be used to impose deconvolution imaging conditions (e.g., Muijs et al., 2007) that help to construct images whose amplitudes are an estimate of subsurface reflectivity (Bleistein et al., 2001).

Our goal here was to demonstrate the feasibility of using deconvolutions to recover the impulse response between receivers. Nonetheless, deconvolution interferometry has proven to be an important tool for interferometric imaging from complicated excitation. The Earth itself may be the cause of complicated source functions, as in the case of Snieder and Şafak (2006) and of Mehta et al. (2007a). When using internal multiples for imaging, Vasconcelos et al. (2007b) found deconvolution interferometry to be necessary. In other applications the complicated character of the excitation may be related to the source itself. One such example is drill-bit seismology. When independent measures of the drill-bit stem noise are not available, deconvolution interferometry is necessary. This is the focus of the next part of this manuscript (Vasconcelos and Snieder, 2007b). Here, we highlight the physical differences between three interferometric methods: 1) deconvolution before source integration, 2) cross-correlations and 3) deconvolution after source integration. The comparison between methods 1) and 2) serves the purpose of providing the reader with information that allows one to relate the new content in this manuscript to much of the existing literature about interferometry. The understanding of the methods 2) and 3) provides the basis for the discussion about the specific use of deconvolution interferometry in drill-bit seismic imaging, which is the subject of the second part of our study (Vasconcelos and Snieder, 2007b).

5 ACKNOWLEDGEMENTS

We thank the NSF (grant EAS-0609595) and the sponsors of the consortium for Seismic Inverse Methods for Complex Structures for their financial support. We are grateful to Kurang Mehta (CWP), Rodney Calvert and Jon Sheiman (both Shell) for insightful discussions and suggestions throughout this project. I.V. thanks Art Weglein for a private lecture on the inverse scattering series that inspired many of the ideas in this paper.

REFERENCES

L. Amundsen. Elimination of free-surface related multiples without need of the source wavelet. *Geophysics*, 66:327-341, 2001.

A. Bakulin and R. Calvert. The virtual source method: Theory and case study. *Geophysics*, 71:SI139-SI150, 2006.

A.J. Berkhout and D.J. Verschuur. Imaging of multiple reflections. *Geophysics*, 71:SI209-SI220, 2006.

B. Biondi. 3D Seismic Imaging. *Investigations in Geophysics, 14, Society of Exploration Geophysicists*, 240 pages, 2006.

N. Bleistein and R.A. Handelsman. Asymptotic expansions of integrals. *Dover, New York*, 1975.

N. Bleistein, J.K. Cohen and. J.W. Stockwell Jr. Mathematics of Multidimensional Seismic Imaging, Migration, and Inversion. *Springer, New York*, 2001.

J.F. Claerbout. Synthesis of a layered medium from its acoustic transmission response. *Geophysics*, 33:264–269, 1968.

J.F. Claerbout. Imaging the Earth's Interior. *Balckwell Publishing*, 1985.

A. Curtis, P. Gerstoft, H. Sato, R. Snieder and K. Wapenaar. Seismic interferometry - turning noise into signal. *The Leading Edge*, 25:1082–1092, 2006.

D. Draganov, K. Wapenaar and J. Thorbecke. Seismic interferometry: Reconstructing the earths reflection response. *Geophysics*, 71:SI61-SI70, 2006.

M. Fink. Time-reversal acoustics in complex environments. *Geophysics*, 71:SI151-SI164, 2006.

E. Holvik and L. Amundsen. Elimination of the overburden response from multicomponent source and receiver seismic data, with source designature and decomposition into PP-, PS-, SP-, and SS-wave responses. *Geophysics*, 70:S43-S59, 2005.

V. Korneev and A. Bakulin. On the fundamentals of the virtual source method. *Geophysics*, 71:A13-A17, 2006.

D. Halliday, A. Curtis, D. van Mannen and J. Robertsson. Interferometric surface wave (ground roll) isolation and removal. *submitted to Geophysics*, 2007.

E. Larose, L. Margerin, A. Derode, B. van Tiggelen, M. Campillo, N. Shapiro, A. Paul, L. Stehly and M. Tanter. Correlation of random wavefields: An interdisciplinary review. *Geophysics*, 71:SI11-SI21, 2006.

O.I. Lobkis and R.L. Weaver. On the emergence of the Green's function in the correlations of a diffuse field. *J. Acoust. Soc. Am.*, 110:3011-3017, 2001.

D. Loewenthal and E.A. Robinson. On unified dual wavefields and Einstein deconvolution. *Geophysics*, 65:293–303, 2000.

A. Malcolm, J. Scales and B.A. van Tiggelen. Extracting the Greens function from diffuse, equipartitioned waves. *Physical Review E*, 70:015601, 2004.

D. van Manen, A. Curtis, and J.O.A. Robertsson. Interferometric modeling of wave propagation in inhomogeneous elastic media using time reversal and reciprocity. *Geophysics*, 71:SI47-SI60, 2006.

K. Mehta, R. Snieder, R. Calvert and J. Sheiman. Virtual source gathers and attenuation of free-surface multiples using OBC data:implementation issues and a case study. *Soc. Explor. Geophys. Expand. Abs.*, 2669–2673, 2006.

K. Mehta, R. Snieder and V. Graizer. Extraction of near-surface properties for a lossy layered medium using the propagator matrix. *Geophys. J. Intl.*, in press, 2007.

K. Mehta, R. Snieder and V. Graizer. Down-hole receiver function: a case study. *Bull. Seism. Soc. Am.*, submitted, 2007.

R. Muijs, J.O.A. Robertsson and K. Holliger. Prestack depth migration of primary and surface-related multiple reflections: Part I Imaging. *Geophysics*, 72:S59-SI69, 2006.

H. Ohanian and R. Ruffini. Gr avitation and Spacetime. *Norton & Co.,New York*, 2nd Edition, 1994.

F. Poletto and F. Miranda. Seismic while drilling, fundamentals of drill-bit seismic for exploration. *Handbook of Geophysical Exploration*, Vol 35, 2004.

J.W. Rector III and B.P. Marion. The use of drill-bit energy as a downhole seismic source. *Geophysics*, 56:628-634, 1991.

J.E. Rickett and J.F. Claerbout. Acoustic daylight imaging via spectral factorization; helioseismology and reservoir monitoring. *The Leading Edge*, 19:957–960, 1999.

L.S. Rodberg and R.M. Thaler. Introduction to the Quantum Theory of Scattering. *Academic Press, New York*, 1967.

K.G. Sabra, P. Roux and W.A. Kuperman . Arrival-time structure of the time-averaged ambient noise cross-correlation function in an oceanic waveguide. *J. Acoust. Soc. Am.*, 117:164–174, 2004.

K.G. Sabra, P. Gerstoft, P. Roux, W.A. Kuperman and M. Fehler. Surface-wave tomography from microseisms in Southern California. *Geophys. Res. Let.*, 32:L14311, 2005.

P. Sava. Time-shift imaging condition in seismic migration. *Geophysics*, 71:S209–S217, 2006.

G.T. Schuster, F. Followill, L.J. Katz, J. Yu, and Z. Liu. Autocorrelogram migration: Theory. *Geophysics*, 68:1685-1694, 2004.

G.T. Schuster and M. Zhou. A theoretical overview of model-based and correlation-based redatuming methods. *Geophysics*, 71:SI103-SI110, 2006.

N.M. Shapiro, M. Campillo, L. Stehly, and M.H. Ritzwoller. High-resolution surface-wave tomography from ambient seismic noise. *Science*, 307:1615-1618, 2005.

Y. Shen, A.F. Sheehan, K.G. Dueker, C. de Groot-Hedlin and H. Gilbert. Mantle Discontinuity Structure Beneath the Southern East Pacific Rise from P-to-S Converted Phases. *Science*, 280:1232–1235, 1998.

R. Snieder. Extracting the Green's function from the correlation of coda waves: A derivation based on stationary phase. *Phys. Rev. E.*, 69:046610, 2004.

R. Snieder and E. Şafak. Extracting the building response using seismic interferometry; theory and application to the Millikan library in Pasadena, California. *Bull. Seismol. Soc. Am.*, 96:586-598, 2006.

R. Snieder, K. Wapenaar and K. Larner. Spurious multiples in seismic interferometry of primaries. *Geophysics*, 71:SI111-SI124, 2006a.

R. Snieder, J. Sheiman and R. Calvert. Equivalence of the virtual-source method and wave-field deconvolution in seismic interferometry. *Phys. Rev. E*, 73:066620, 2006b.

R. Snieder. Retrieving the Greens function of the diffusion equation from the response to a random forcing. *Phys. Rev. E*, 74:046620, 2006.

R. Snieder. Extracting the Greens function of attenuating heterogeneous acoustic media from uncorrelated waves. *J. Acoust. Soc. Am.*, in press, 2007.

R. Snieder, K. Wapenaar, and U. Wegler. Unified Green's function retrieval by cross-correlation; connection with energy principles. *Phys. Rev. E*, 75:036103, 2007.

J. Trampert, M. Cara and M. Frogneux. *SH* propagator matrix and Q_s estimates from borehole- and surface-recorded earthquake data. *Geophys. J. Intl.*, 112:290–299, 1993.

I. Vasconcelos and R. Snieder. On representation theorems and seismic interferometry in perturbed media. *Geophysics*, in preparation, 2007a.

I. Vasconcelos and R. Snieder. Interferometry by deconvolution, Part II: application to drill-bit seismic imaging. *Geophysics*, in preparation, 2007b.

I. Vasconcelos, R. Snieder, S.T. Taylor, P. Sava, J.A. Chavarria and P. Malin. High Resolution Imaging of the San Andreas Fault at Depth. *Science*, in preparation, 2007a.

I. Vasconcelos, R. Snieder and B. Hornby. Imaging with internal multiples from subsalt VSP data: examples of controlled illumination in interferometry experiments. *Geophysics*, in preparation, 2007b.

K. Wapenaar. Retrieving the elastodynamic Green's function of an arbitrary inhomogeneous medium by cross correlation. *Phys. Rev. Lett.*, 93:254301, 2004.

K. Wapenaar, J. Thorbecke, and D. Dragonov. Relations between reflection and transmission responses of three-dimensional inhomogeneous media. *Geophys. J. Int.*, 156:179–194, 2004.

K. Wapenaar. Green's function retrieval by cross-correlation in case of one-sided illumination. *Geophys. Res. Lett.*, 33:L19304, 2006.

K. Wapenaar, E. Slob, and R. Snieder. Unified Green's Function Retrieval by Cross Correlation. *Phys. Rev. E.*, 97:234301, 2006.

R.L. Weaver and O.I. Lobkis. Ultrasonics without a source: Thermal fluctuation correlations and MHz frequencies. *Phys. Rev. Lett.*, 87:134301–1/4, 2001.

R.L. Weaver and O.I. Lobkis. Diffuse fields in open systems and the emergence of the Green's function. *J. Acoust. Soc. Am.*, 116:2731–2734, 2004.

A.B. Weglein, F.V. Araújo, P.M. Carvalho, R.H. Stolt, K.H. Matson, R.T. Coates, D. Corrigan, D.J. Foster, S.A. Shaw, and H. Zhang. Inverse scattering series and seismic exploration. *Inverse Problems*, 19:R27–R83, 2003.

K. van Wijk. On estimating the impulse response between receivers in a controlled ultrasonic experiment. *Geophysics*, 71:SI79-SI84, 2006.

J. Yu and G.T. Schuster. Crosscorrelogram migration of inverse vertical seismic profile data. *Geophysics*, 71:S1-S11, 2006.

APPENDIX A: PHYSICAL ANALYSIS OF THE DECONVOLUTION INTERFEROMETRY SERIES

According to the derivation in Section 2.2.1, the deconvolution in equation 9 can be expressed in series form

$$D_{AB} = \frac{C_{AB}}{|G_0(\mathbf{r}_B,\mathbf{s})|^2} \sum_{n=0}^{\infty} \left(- \frac{G_S(\mathbf{r}_B,\mathbf{s})}{G_0(\mathbf{r}_B,\mathbf{s})} - \frac{G_S^*(\mathbf{r}_B,\mathbf{s})}{G_0^*(\mathbf{r}_B,\mathbf{s})} \right)^n . \tag{A1}$$

The objective of this appendix is to reproduce the steps and physical approximations that simplify the series in equation A1. Let us first consider the $n = 2$ term in the summation in equation A1, which is

$$S_2 = \left(- \frac{G_S(\mathbf{r}_B,\mathbf{s})}{G_0(\mathbf{r}_B,\mathbf{s})} - \frac{G_S^*(\mathbf{r}_B,\mathbf{s})}{G_0^*(\mathbf{r}_B,\mathbf{s})} \right)^2 \tag{A2}$$

Substituting this term in the expansion of $|G(\mathbf{r}_B,\mathbf{s})|^{-2}$ (equation 13) gives, to second order in G_S,

$$\begin{aligned} |G(\mathbf{r}_B,\mathbf{s})|^{-2} \approx & \frac{1}{|G_0(\mathbf{r}_B,\mathbf{s})|^2} \left[1 - \frac{G_S(\mathbf{r}_B,\mathbf{s})}{G_0(\mathbf{r}_B,\mathbf{s})} - \frac{G_S^*(\mathbf{r}_B,\mathbf{s})}{G_0^*(\mathbf{r}_B,\mathbf{s})} \right] \\ & + \frac{1}{|G_0(\mathbf{r}_B,\mathbf{s})|^2} \left[\left(\frac{G_S(\mathbf{r}_B,\mathbf{s})}{G_0(\mathbf{r}_B,\mathbf{s})} \right)^2 + \left(\frac{G_S^*(\mathbf{r}_B,\mathbf{s})}{G_0^*(\mathbf{r}_B,\mathbf{s})} \right)^2 + 2 \frac{|G_S(\mathbf{r}_B,\mathbf{s})|^2}{|G_0(\mathbf{r}_B,\mathbf{s})|^2} \right] , \end{aligned} \tag{A3}$$

where the very last term is zero-phase. When $|G_0|^2 >> |G_S|^2$, the zero-phase term in equation A3 can be neglected because it does not contribute with any new arrival. Equation A3 thus simplifies to

$$|G(\mathbf{r}_B,\mathbf{s})|^{-2} \approx \frac{1}{|G_0(\mathbf{r}_B,\mathbf{s})|^2} \left[1 - \frac{G_S(\mathbf{r}_B,\mathbf{s})}{G_0(\mathbf{r}_B,\mathbf{s})} - \frac{G_S^*(\mathbf{r}_B,\mathbf{s})}{G_0^*(\mathbf{r}_B,\mathbf{s})} + \left(\frac{G_S(\mathbf{r}_B,\mathbf{s})}{G_0(\mathbf{r}_B,\mathbf{s})} \right)^2 + \left(\frac{G_S^*(\mathbf{r}_B,\mathbf{s})}{G_0^*(\mathbf{r}_B,\mathbf{s})} \right)^2 \right] ; \tag{A4}$$

for which the actual contribution from $n = 2$ to the sum in equation A1 is

$$S_2 \approx \left(\frac{u_S(\mathbf{r}_B,\mathbf{s})}{u_0(\mathbf{r}_B,\mathbf{s})} \right)^2 + \left(\frac{u_S^*(\mathbf{r}_B,\mathbf{s})}{u_0^*(\mathbf{r}_B,\mathbf{s})} \right)^2 , \tag{A5}$$

instead of the full S_2 term in equation A2. Applying the same rationale for the simplification of S_2 to the $n = 3$ term from the summation in equation A1 gives

$$S_3 = \left(- \frac{G_S(\mathbf{r}_B,\mathbf{s})}{G_0(\mathbf{r}_B,\mathbf{s})} - \frac{G_S^*(\mathbf{r}_B,\mathbf{s})}{G_0^*(\mathbf{r}_B,\mathbf{s})} \right)^3 . \tag{A6}$$

S_3 can be expressed in terms of S_2, such that

$$S_3 = S_2 \times \left(- \frac{G_S(\mathbf{r}_B,\mathbf{s})}{G_0(\mathbf{r}_B,\mathbf{s})} - \frac{G_S^*(\mathbf{r}_B,\mathbf{s})}{G_0^*(\mathbf{r}_B,\mathbf{s})} \right) . \tag{A7}$$

Using the simplified S_2 (equation A5) in evaluating S_3 gives

$$S_3 \approx - \left(\frac{G_S(\mathbf{r}_B,\mathbf{s})}{G_0(\mathbf{r}_B,\mathbf{s})} \right)^3 - \left(\frac{G_S^*(\mathbf{r}_B,\mathbf{s})}{G_0^*(\mathbf{r}_B,\mathbf{s})} \right)^3 - \frac{|G_S(\mathbf{r}_B,\mathbf{s})|^2}{|G_0(\mathbf{r}_B,\mathbf{s})|^2} \frac{G_S(\mathbf{r}_B,\mathbf{s}) G_0^*(\mathbf{r}_B,\mathbf{s})}{|G_0(\mathbf{r}_B,\mathbf{s})|^2} - \frac{|G_S(\mathbf{r}_B,\mathbf{s})|^2}{|G_0(\mathbf{r}_B,\mathbf{s})|^2} \frac{G_S^*(\mathbf{r}_B,\mathbf{s}) G_0(\mathbf{r}_B,\mathbf{s})}{|G_0(\mathbf{r}_B,\mathbf{s})|^2} \tag{A8}$$

The last two terms of S_3 in the above equation are not zero-phase. Note also that despite being nonzero phase, the phase of these terms is the same of other terms of lower order. For example, the term $\left(|G_S|^2 / |G_0|^4\right) G_S\, G_0^*$ has the same phase as the integrand in the D_{AB}^2 term in equation 15, but with weaker amplitude and opposite polarity. Because they do not result in new arrivals and have weak amplitudes, we drop the last two terms in equation A8 and reduce S_3 to

$$S_3 \approx -\left(\frac{G_S(\mathbf{r}_B,\mathbf{s})}{G_0(\mathbf{r}_B,\mathbf{s})}\right)^3 - \left(\frac{G_S^*(\mathbf{r}_B,\mathbf{s})}{G_0^*(\mathbf{r}_B,\mathbf{s})}\right)^3. \tag{A9}$$

Any S_n term of the summation in equation A1 can be written in terms of S_{n-1} in the same form of equation A7. Analogously to equation A8, any S_n will yield four terms from which two terms can be dropped according to the same rationale we use to neglect the last two terms in equation A8. Thus, by induction, the summation in equation A1 simplifies to

$$\sum_{n=0}^{\infty}\left(-\frac{G_S(\mathbf{r}_B,\mathbf{s})}{G_0(\mathbf{r}_B,\mathbf{s})} - \frac{G_S^*(\mathbf{r}_B,\mathbf{s})}{G_0^*(\mathbf{r}_B,\mathbf{s})}\right)^n \approx 1 + \sum_{n=1}^{\infty}(-1)^n\left[\left(\frac{G_S(\mathbf{r}_B,\mathbf{s})}{G_0(\mathbf{r}_B,\mathbf{s})}\right)^n + \left(\frac{G_S^*(\mathbf{r}_B,\mathbf{s})}{G_0^*(\mathbf{r}_B,\mathbf{s})}\right)^n\right]. \tag{A10}$$

Using this simplified summation in the deconvolution series gives

$$D_{AB} \approx \frac{C_{AB}}{|G_0(\mathbf{r}_B,\mathbf{s})|^2}\left(1 + \sum_{n=1}^{\infty}(-1)^n\left[\left(\frac{G_S(\mathbf{r}_B,\mathbf{s})}{G_0(\mathbf{r}_B,\mathbf{s})}\right)^n + \left(\frac{G_S^*(\mathbf{r}_B,\mathbf{s})}{G_0^*(\mathbf{r}_B,\mathbf{s})}\right)^n\right]\right). \tag{A11}$$

The term-by-term expansion of the equation above is such that for any given value of n, the terms

$$D_{AB,\text{terms}} = (-1)^n\left(\frac{G_S^*(\mathbf{r}_B,\mathbf{s})}{G_0^*(\mathbf{r}_B,\mathbf{s})}\right)^n\left(\underbrace{G_0(\mathbf{r}_A,\mathbf{s})G_S^*(\mathbf{r}_B,\mathbf{s})}_{C_{AB}^2} + \underbrace{G_S(\mathbf{r}_A,\mathbf{s})G_S^*(\mathbf{r}_B,\mathbf{s})}_{C_{AB}^4}\right) \tag{A12}$$

cancel, for $n+1$, with the terms

$$D_{AB,\text{terms}} = (-1)^{n+1}\left(\frac{G_S^*(\mathbf{r}_B,\mathbf{s})}{G_0^*(\mathbf{r}_B,\mathbf{s})}\right)^{n+1}\left(\underbrace{G_0(\mathbf{r}_A,\mathbf{s})G_0^*(\mathbf{r}_B,\mathbf{s})}_{C_{AB}^1} + \underbrace{G_S(\mathbf{r}_A,\mathbf{s})G_0^*(\mathbf{r}_B,\mathbf{s})}_{C_{AB}^3}\right); \tag{A13}$$

which in the limit $n \to \infty$ leaves only the contribution of the causal ratio G_S/G_0 to D_{AB} in equation A11. The cancelation of the terms proportional to the acausal ratio G_S^*/G_0^* (highlighted by equations A12 and A13) is responsible for the absence of acausal terms having the same phase as C_{AB}^3 and C_{AB}^4 (equation 4) in deconvolution interferometry (equation 15). Because of these successive cancelations, we arrive to

$$D_{AB} \approx \frac{G_0(\mathbf{r}_A,\mathbf{s})G_0^*(\mathbf{r}_B,\mathbf{s})}{|G_0(\mathbf{r}_B,\mathbf{s})|^2} + \frac{G_S(\mathbf{r}_A,\mathbf{s})G_0^*(\mathbf{r}_B,\mathbf{s})}{|G_0(\mathbf{r}_B,\mathbf{s})|^2} + \frac{C_{AB}}{|G_0(\mathbf{r}_B,\mathbf{s})|^2}\sum_{n=1}^{\infty}(-1)^n\left(\frac{G_S(\mathbf{r}_B,\mathbf{s})}{G_0(\mathbf{r}_B,\mathbf{s})}\right)^n, \tag{A14}$$

which, in compact form, gives

$$D_{AB} \approx \frac{G(\mathbf{r}_A,\mathbf{s})}{G_0(\mathbf{r}_B,\mathbf{s})} + \frac{C_{AB}}{|G_0(\mathbf{r}_B,\mathbf{s})|^2}\sum_{n=1}^{\infty}(-1)^n\left(\frac{G_S(\mathbf{r}_B,\mathbf{s})}{G_0(\mathbf{r}_B,\mathbf{s})}\right)^n. \tag{A15}$$

We present this approximate deconvolution series as a tool to identify the most prominent events within the integrand of the deconvolution interferometry integral (equation 10). Equation A14 is also useful in the description of the kinematics of deconvolution interferometry terms, as we discuss in the main text. If one seeks to describe the result of deconvolution interferometry with a more accurate dynamic behavior, the original series in equation A1 is more appropriate.

APPENDIX B: STATIONARY-PHASE EVALUATION OF LEADING ORDER TERMS

The wavefields shown in Figure 3 can be described by the ray-geometric impulse responses

$$\begin{aligned} u_0(\mathbf{r}_{A,B},\mathbf{s}) &= G_0(\mathbf{r}_{A,B},\mathbf{s}) = -\frac{e^{ik|\mathbf{r}_{A,B}-\mathbf{s}|}}{4\pi|\mathbf{r}_{A,B}-\mathbf{s}|}\,, \text{ and} \\ u_S(\mathbf{r}_{A,B},\mathbf{s}) &= G_S(\mathbf{r}_{A,B},\mathbf{s}) = -r\frac{e^{ik\left(|\mathbf{r}^{sr}_{A,B}-\mathbf{r}_{A,B}|+|\mathbf{s}-\mathbf{r}^{sr}_{A,B}|\right)}}{4\pi\left(|\mathbf{r}^{sr}_{A,B}-\mathbf{r}_{A,B}|+|\mathbf{s}-\mathbf{r}^{sr}_{A,B}|\right)}\,; \end{aligned} \tag{B1}$$

where $\mathbf{r}^{sr}_{A,B}$ are the specular reflection points for the receiver-source pairs $(\mathbf{r}_{A,B},\mathbf{s})$. G_0 and G_S are the far-field acoustic Green's functions we use to describe u_0 and u_S, respectively. In our model, $\mathbf{s}=(x,y,z=0)$ and $\mathbf{r}_{A,B}=(x_{A,B},y_{A,B}=0,z_{A,B})$. The distances in the phases and denominators in equation B1 can be expressed in terms of the corresponding ray-lengths in Figure 3. Using the Green's functions in equation B1 to express D^1_{AB} (equation 15) we get

$$D^1_{AB} = \frac{1}{(4\pi L_B)^2}\int \frac{e^{ik(L_A-L_B)}}{L_A L_B}dxdy\,, \tag{B2}$$

where $\varphi = ik\,(L_A-L_B)$ is the phase of the integrand. The source position that gives a stationary contribution to the integral in equation B2 satisfies

$$0=\frac{\partial\varphi}{\partial y}=\frac{y}{L_A}-\frac{y}{L_B}\,; \tag{B3}$$

and

$$0=\frac{\partial\varphi}{\partial x}=\frac{x-x_A}{L_A}-\frac{x-x_B}{L_B}=\sin\psi_A-\sin\psi_B\,, \tag{B4}$$

where ψ_A and ψ_B is the angle defined between the direct wave and the vertical at receivers A and B. It follows from equations B3 and B4 that the stationary point for the source in the D^1_{AB} term satisfies (Snieder et al., 2006)

$$\psi_A=\psi_B=\psi \qquad \text{and} \qquad y=0\,. \tag{B5}$$

It is expected that the stationary contribution for all terms comes from sources at $y=0$ because $y_{A,B}=0$ and the model is a flat reflector in a homogeneous and isotropic medium. The condition $\psi_A=\psi_B$ (equation B5) states that the stationary source is the one that sends a direct wave which is first recorded at $\mathbf{r}_B$ and goes straight to $\mathbf{r}_A$. This is the same stationary condition as for the C^1_{AB} term of Snieder et al. (2006).

To approximate the integral in equation B2 with the stationary-phase method we must evaluate, at the stationary point, the second derivatives

$$\begin{aligned} \frac{\partial^2\varphi}{\partial x^2} &= \frac{z_A^2}{L_A^3}-\frac{z_B^2}{L_B^3}=\frac{z_A^2}{L_A^2}\frac{1}{L_A}-\frac{z_B^2}{L_B^2}\frac{1}{L_B} \\ &= \cos^2\psi\left(\frac{1}{L_A}-\frac{1}{L_B}\right)\,, \end{aligned} \tag{B6}$$

and

$$\frac{\partial^2\varphi}{\partial y^2}=\frac{L_A^2}{L_A^3}-\frac{L_B^2}{L_B^3}=\frac{1}{L_A}-\frac{1}{L_B}\,. \tag{B7}$$

Based on these second derivatives, the stationary-phase approximation (Bleistein and Handelsman, 1975) to equation B2 is

$$D^1_{AB} = \frac{n}{(4\pi L_B)^2}\frac{1}{(4\pi)^2}\frac{\exp\left(ik\left(L_A - L_B\right)\right)}{L_A L_B} \quad \times e^{-i\pi/4}\sqrt{\frac{2\pi}{k}}\frac{1}{\sqrt{\cos^2\psi\left(\frac{1}{L_B}-\frac{1}{L_A}\right)}} \times e^{-i\pi/4}\sqrt{\frac{2\pi}{k}}\frac{1}{\sqrt{\frac{1}{L_B}-\frac{1}{L_A}}}, \tag{B8}$$

where $k = \frac{\omega}{c}$. At the stationary source point, where $\psi_A = \psi_B$, the distance $L_A - L_B$ is equivalent to the distance $|\mathbf{r}_A - \mathbf{r}_B|$. Thus, in the stationary-phase approximation, D^1_{AB} is given by

$$D^1_{AB} = \frac{nc}{32\pi^2 L_B^2 cos\psi}\frac{G_0(\mathbf{r}_A, \mathbf{r}_B)}{(-i\omega)}\,. \tag{B9}$$

From the derivation above, the stationary-phase evaluation of D^1_{AB} is completely analogous to the evaluation of C^1_{AB} (equation 4) in Snieder et al. (2006). Since the same occurs with the term D^2_{AB}, we refrain from reproducing the steps of its stationary-phase approximation in this paper, and refer the readers to Snieder et al. (2006) for these steps.

Interferometry by deconvolution, Part II: Application to drill-bit seismic data

Ivan Vasconcelos & Roel Snieder
Center for Wave Phenomena and Department of Geophysics, Colorado School of Mines, Golden, CO 80401

ABSTRACT

In the practice of Seismic-While-Drilling (SWD), the goal is to determine the subsurface impulse response from drill-bit noise records. Most of the existing SWD technologies rely on pilot sensors and/or models to predict the drill-bit source function, which is then removed from the data. Deconvolution interferometry successfully recovers the impulse response between receivers from drill-bit noise without the need for an independent estimate of the drill-bit source function. We give a general review of current SWD methods in the context of cross-correlation interferometry, followed by a comparison of these methods with deconvolution interferometry. Unlike other SWD processing methods, interferometry does not require knowledge about the drill-bit position. We heuristically extend the concept of interferometry by deconvolution to multi-component data in elastic media. In elastic media, the radiation pattern of the interferometric pseudo-source are influenced by the radiation properties of the bit. This dependence is a function of the medium properties and of the distance between the bit and the recording sensors. Interferometry by deconvolution is of most use to SWD applications where pilot records are absent or provide unreliable estimates of the bit excitation. With a numerical SWD subsalt example, we show that deconvolution interferometry provides an impulsive image of the subsurface that cannot be obtained by correlations without an estimate of the source autocorrelation. This numerical example also illustrates the potential of SWD and deconvolution interferometry for passive imaging in deep-water subsalt environments. Finally, we validate the use of deconvolution interferometry in processing field SWD data acquired at the San Andreas Fault Observatory at Depth (SAFOD). Since no pilot records were available for these data, deconvolution outperforms correlation in obtaining an interferometric image of the San Andreas Fault zone at depth.

Key words: seismic-while-drilling, deconvolution interferometry, borehole seismics

1 INTRODUCTION

The recording of drilling noise can be used for seismic imaging (Rector and Marion; 1991). In the majority of seismic-while-drilling applications (e.g., Poletto and Miranda, 2004) the data acquisition and imaging geometries fall under the category of reverse VSP (RVSP) experiments, where knowledge of the position of the drill-bit is required. With the autocorrelogram migration method, Schuster et al. (2004) and Yu et al. (2004) recognized that interferometry could be applied to SWD data without any knowledge of the drill bit position. Recently, Poletto and Petronio (2006) used interferometry to characterize fault zones ahead of a tunnel being drilled.

Interferometry is a proven methodology for the recovery of the impulse response between any two receivers from measurements of uncorrelated noise. This can be accomplished in diffuse fields by cross-correlating the data recorded by two receivers (Lobkis and Weaver, 2001; Larose et al., 2006). Wapenaar (2004) and Wape-

naar et al. (2004) provided general proofs that cross-correlations of deterministic wavefields excited by uncorrelated noise result in the impulse response between receivers for arbitrary media. When the measured data is excited by correlated noise sources, the result from cross-correlation interferometry contains the source power spectrum (Snieder et al., 2006a; Wapenaar and Fokkema, 2006; Vasconcelos and Snieder, 2007a). In the specific case of SWD applications, the drill-bit noise signal (and its power spectrum) is a long and complicated source-time function with a narrow band signature (Poletto and Miranda, 2004). Hence, the extraction of an impulsive response from the application of cross-correlation interferometry to SWD data requires an additional processing step. This is the removal of the source signature (Wapenaar and Fokkema, 2006).

As shown by Vasconcelos and Snieder (2007a), interferometry can also be accomplished by deconvolution. One advantage of deconvolution interferometry over its correlation counterpart is that it removes the source function without the need for an extra processing step. The main objective of this paper is to validate deconvolution interferometry as a method to recover impulsive signals from drill-bit noise without the need for an independent estimate of the drill-bit excitation function.

There are many existing examples of successful applications of SWD technology. Most of the SWD methods rely on the so-called pilot sensors to independently estimate the drill-bit excitation (Rector and Marion, 1991; Haldorsen et al. 1994; Poletto and Miranda, 2004). Without relying on pilot records, Miller et al. (1990) design multichannel weighting deconvolution filters based on statistical assumptions about the source function. The monograph by Poletto and Miranda (2004) provides a comprehensive description of pilot deconvolution technologies. Some pilot-based SWD methods deconvolve the bit excitation directly from the recorded data (e.g., Haldorsen et al., 1994) while most methodologies rely on cross-correlations (e.g., Rector and Marion, 1991; Poletto and Miranda, 2004). There is a close connection between correlation-based SWD methods and cross-correlation interferometry, which we highlight in this paper. Pilot-based SWD technologies can be elaborate; the more sophisticated pilot recordings may use dual-field sensors (Poletto et al., 2004) or accelerometers mounted close to the drill-bit (Poletto and Miranda, 2004). Recognizing that pilot records are imperfect estimates of the drill-bit excitation, Poletto et al. (2000) present a statistical technique that further optimizes pilot deconvolution. We promote the use of deconvolution interferometry for the cases where pilot signals are absent or provide poor estimates of the drill-bit excitation. As described by Poletto and Miranda (2004), examples of data for which pilot deconvolution can be unsuccessful are those excited by deep drilling wells, deviated wells, or when the drill-bit is below strong geologic contrasts (e.g., below salt).

The majority of SWD experiments constitute RVSP geometries (Rector and Marion, 1991; Poletto and Miranda, 2004). Drilling noise has also been used for imaging ahead of the drill-bit (i.e., "Look-Ahead" VSP) as shown by Armstrong et al. (2000) and Malusa et al. (2002). Armstrong et al. (2000) showed examples of drill-bit imaging in the deep-water Gulf of Mexico. Most SWD experiments are conducted onshore with roller-cone drill-bits (Poletto and Miranda, 2004). Deep-water offshore applications of SWD technology, such as described by Armstrong et al. (2000), are rare. One of the reasons why deep-water offshore SWD is uncommon is that pilot records yield poor representations of the bit excitation in these conditions (Poletto and Miranda, 2004). With the numerical experiment in this paper we demonstrate the potential of interferometry by deconvolution for treating passive recordings of drilling noise in deep-water subsalt environments.

We first review SWD methods based on correlations and pilot deconvolution in the context of interferometry. Next, we describe the role of deconvolution interferometry (Vasconcelos and Snieder, 2007a) in extracting the impulse response between receivers from drilling noise. Within this description, we discuss the applications of the concepts presented by Vasconcelos and Snieder (2007a) to elastic media, and elaborate on how the drill-bit radiation properties influence the recovered elastic response. With a numerical example using the *Sigsbee* salt model, we compare the performance of deconvolution and correlation interferometry in passive drill-bit imaging. Finally, we present the results of using deconvolution interferometry for the imaging of the San Andreas Fault zone from SWD data acquired at Parkfield, CA.

2 DRILL-BIT SEISMIC IMAGING AND DECONVOLUTION INTERFEROMETRY

2.1 The practice of seismic-while-drilling

The frequency-domain wavefield measured at $\mathbf{r}_A$ excited by a working drill-bit at $\mathbf{s}$ is given by

$$u(\mathbf{r}_A, \mathbf{s}, \omega) = W(\mathbf{s}, \omega)\, G(\mathbf{r}_A, \mathbf{s}, \omega)\,, \qquad (1)$$

where $G(\mathbf{r}_A, \mathbf{s}, \omega)$ is the impulse response between $\mathbf{s}$ and $\mathbf{r}_A$, and $W(\mathbf{s}, \omega)$ is the drill-bit excitation function. For brevity, we omit the dependence on the angular frequency ω in subsequent equations. As in most exploration imaging experiments, the objective of drill-bit seismology is to image the subsurface from its impulse response, G, which needs to be obtained from equation 1. The main issue for successful imaging from drill-bit noise is removing the imprint of the source function

W (Rector and Marion, 1991; Haldorsen et al., 1994; Poletto and Miranda, 2004). The first complication imposed by drill-bit excitation is that the source is constantly active; in other words, the source pulse is as long as the total recording time of the data. Additionally, the drill-bit is a source of coherent noise that is dominated by specific vibrational modes associated with the drilling process (Poletto, 2005a). These strong drilling-resonant modes give the time-domain drill-bit signature a predominantly monochromatic character. Apart from the coherent vibrations, weaker random vibrations that occur during drilling make the drill-bit signal wide-band (Poletto, 2005a). We illustrate these issues in our sub-salt example, where we provide a numerical model for the drill-bit excitation.

Current interferometric approaches to processing drill-bit noise records rely on correlations (e.g., Schuster et al.; 2004, Yu et al., 2004; Poletto and Miranda, 2004). The cross-correlation of wavefields measured at $\mathbf{r}_A$ and $\mathbf{r}_B$ is, in the frequency domain, given by

$$\begin{aligned} C_{AB} &= u(\mathbf{r}_A,\mathbf{s})\, u^*(\mathbf{r}_B,\mathbf{s}) \\ &= |W(\mathbf{s})|^2\, G(\mathbf{r}_A,\mathbf{s})\, G^*(\mathbf{r}_B,\mathbf{s})\,; \end{aligned} \tag{2}$$

where * stands for complex conjugation. It follows from this expression that the cross-correlation is influenced by the power spectrum of the drill-bit source function. In the time domain, the power spectrum in equation 2 corresponds to the autocorrelation of the drill-bit source-time function. This autocorrelation, despite being zero phase, is similar in character to the excitation $W(\mathbf{s},t)$: a long, complicated waveform with a monochromatic appearance.

In the majority of drill-bit processing methods presented to date, the removal of the drill-bit source function in equation 1 (or of its autocorrelation, equation 2) relies on an independent estimate of the drill-bit excitation. This estimate typically comes in the form of the so-called *pilot record* or *pilot trace* (e.g., Rector and Marion, 1991; Poletto and Miranda, 2004). The pilot records are the data acquired by accelerometers placed in the rig/drill-stem structure. The most common form of pilot sensor mount is at the top of the drill-string. Pilot sensors may also consist of *dual-wavefield* sensors that measure displacement and strain waves (Poletto et al., 2004). The positioning and the type of sensors used in acquiring pilot records depends on the specific SWD application. Poletto and Miranda (2004) provide a detailed explanation of the different types of pilot sensor technologies and their applications.

Within the literature on SWD, there are different descriptions of the signal acquired by the pilot sensors. Most of these descriptions are based on deterministic physical models for wave propagation in the rig/stem/bit system (Rector, 1992; Rector and Hardage, 1992; Haldorsen et al., 1994; Poletto and Miranda, 2004). Poletto et al. (2000) and Poletto and Miranda (2004) propose a statistical approach for the description of the drill bit signal. Since for the purpose of deconvolution interferometry we do not require a particular description of the pilot signal, it is convenient to express it in the general form

$$P(\mathbf{r}_d,\mathbf{s}) = W(\mathbf{s})\, T_d(\mathbf{r}_d,\mathbf{s})\,; \tag{3}$$

T_d is the transfer function of the drill-stem and rig assembly, and $\mathbf{r}_d$ is the location of the pilot sensor in the assembly. This transfer function includes reflection and transmission coefficients of the rig/stem/bit system, drill-string multiples, etc (Poletto and Miranda, 2004). The autocorrelation of the pilot signal in equation 3 gives

$$C_{PP} = |W(\mathbf{s})|^2\ |T_d(\mathbf{r}_d,\mathbf{s})|^2\ . \tag{4}$$

From this autocorrelation, and with additional knowledge about T_d, it is possible to design a filter $\mathcal{F}$, of the form

$$\mathcal{F}\,(C_{PP}) \approx \frac{1}{|W(\mathbf{s})|^2}\,. \tag{5}$$

We use the notation $\mathcal{F}\,(C_{PP})$ to indicate that $\mathcal{F}$ is a function of the autocorrelation C_{PP}. The deterministic (Rector, 1992; Rector and Hardage, 1992; Haldorsen et al., 1994; Poletto and Miranda, 2004) or statistical (Poletto et al., 2000; Poletto and Miranda, 2004) descriptions of T_d aim to remove its influence (equation 3) in the design of the filter $\mathcal{F}$. We present $\mathcal{F}$ as an approximation of $|W(\mathbf{s})|^{-2}$ in equation 5 because the theories that are used to eliminate the influence of T_d are approximate (e.g., Rector and Hardage, 1992; Poletto and Miranda, 2004). Multiplying the filter $\mathcal{F}$ (equation 5) by the cross-correlation in equation 2 gives

$$\mathcal{F}\,C_{AB} \approx G(\mathbf{r}_A,\mathbf{s})G^*(\mathbf{r}_B,\mathbf{s})\,. \tag{6}$$

According to this equation, $\mathcal{F}$ removes the power spectrum of the drill-bit excitation from the correlation in equation 2. The application of $\mathcal{F}$ is what is referred to as *pilot deconvolution* (Poletto and Miranda, 2004). The SWD RVSP methods rely on the cross-correlations of geophone data (equation 1) with the pilot signal (equation 3) to determine the time delay of waves that propagate between the drill-bit and the receivers (e.g. Rector and Marion, 1991; Poletto and Miranda, 2004). Note that for these methods it is necessary to know the drill-bit position $\mathbf{s}$. Although the most common applications of SWD RVSP correlate pilot and geophone signals (equation 2 correlates geophone signals), the removal of the drill-bit source function is done by pilot deconvolution in a manner analogous to the one presented here.

Following the principles of interferometry (e.g., Lobkis and Weaver, 2001; Wapenaar and Fokkema, 2006), the source average of the cross-correlations in

equation 2 gives

$$\oint_{\Sigma} C_{AB}\, d\mathbf{s} \;=\; \langle |W(\mathbf{s})|^2 \rangle \left[G(\mathbf{r}_A, \mathbf{r}_B) + G^*(\mathbf{r}_A, \mathbf{r}_B) \right] ; \tag{7}$$

the integration is done over a closed surface Σ that includes all sources $\mathbf{s}$ (Vasconcelos and Snieder, 2007a). According to equation 7, the source average of the cross-correlations gives the superposition of the causal and acausal impulse responses between $\mathbf{r}_A$ and $\mathbf{r}_B$. This response is shaped by the source average of the excitation spectrum $\langle |W(\mathbf{s})|^2 \rangle$. When using the noise from a single drill-bit, source integration reduces to a line integral, rather than an integration over a surface. This is not necessarily an issue for interferometry from drill-bit noise for two reasons. The first reason is that the desired response (right-hand side of equation 7) is obtained if the drill-bit samples the stationary source points that give rise to the target arrivals (Snieder et al., 2006a; Wapenaar and Fokkema, 2006). The second reason is that the long recording times employed in drill-bit acquisition can help sampling multiply scattered waves. These waves may make up for some of the missing sources that are required by the integration in equation 7 (Wapenaar, 2006; Vasconcelos and Snieder, 2007a), depending on the scattering properties of the medium.

The processing of SWD data with correlation interferometry as in equation 7 does not require knowledge of the drill-bit position $\mathbf{s}$. This was observed by Schuster et al. (2004), who, along with the companion paper by Yu et al. (2004), first proposed the use of interferometry by correlation for imaging from drill-bit noise. Although not explicitly referring to interferometry, Poletto and Miranda (2004) promote the stack of cross-correlations over long listening times. In the context of drilling, listening times in the order of days translate to varying the drill-bit position $\mathbf{s}$. Hence, in general, the stack of long listening times mentioned by Poletto and Miranda (2004) is equivalent to an integration over $\mathbf{s}$ (equation 7).

The term $\langle |W(\mathbf{s})|^2 \rangle$ in equation 7 plays the same role $|W(\mathbf{s})|^2$ in equation 2. The average of the excitation power spectra constitutes, in the time domain, a long zero-phase waveform with a monochromatic character. The removal of this waveform can also be achieved using the pilot record (equation 3). Poletto and Miranda (2004) recognize that pilot deconvolution can be done before or after stacking over long time records (which is equivalent to stacking over $\mathbf{s}$). From integrating the pilot autocorrelation (equation 4) over sources $\mathbf{s}$ we get

$$\oint_{\Sigma} C_{PP}\, d\mathbf{s} \;=\; \langle |W(\mathbf{s})|^2 \rangle \langle |T_d(\mathbf{r}_d, \mathbf{s})|^2 \rangle \,. \tag{8}$$

$\langle |T_d(\mathbf{r}_d, \mathbf{s})|^2 \rangle$ is the source average of the transfer function T_d (equation 3). Given that a model that describes T_d is available (e.g., Rector and Hardage, 1992; Poletto and Miranda, 2004), the result of integral in equation 9 can be used to build a filter such as

$$\mathcal{F}_{av}\left(\langle C_{PP} \rangle \right) \approx \frac{1}{\langle |W(\mathbf{s})|^2 \rangle} ; \tag{9}$$

where $\langle C_{PP} \rangle$ is the source average represented by the integral in equation 9. Applying the filter $\mathcal{F}_{av}$ to the integral in equation 7 gives

$$\mathcal{F}_{av}\left[\oint_{\Sigma} C_{AB}\, d\mathbf{s} \right] \approx G(\mathbf{r}_A, \mathbf{r}_B) + G^*(\mathbf{r}_A, \mathbf{r}_B) ; \tag{10}$$

where the influence of the drill-bit source signature is removed. This is a general representation of pilot deconvolution for the correlation-based interferometry of drill-bit noise records. After pilot deconvolution, interferometry by correlations of SWD data yields the causal and acausal impulse response for waves excited at $\mathbf{r}_B$ and recorded at $\mathbf{r}_A$. Poletto and Miranda (2004) give a comprehensive review of pilot deconvolution methods. Note that the filtering of equation 7 by $\mathcal{F}_{av}$ involves deconvolving the source integral of C_{AB} by the source integral of C_{PP}. This approach is similar in concept to deconvolution interferometry after source integration described by Vasconcelos and Snieder (2007a).

There are a number of different approaches to processing SWD data. Most of them rely on cross-correlation (e.g. Rector and Marion; Poletto and Miranda, 2004). Some of these correlation-based processing techniques (e.g., RVSP techniques) require knowledge of the drill-bit position $\mathbf{s}$, and apply pilot deconvolution in a manner similar to that in equations 5 and 6. Another approach to treating drilling noise records is to use a source average of the cross-correlations (Poletto and Miranda, 2004; Schuster et al., 2004; Yu et al., 2004) as in equations 7 through 10. Although we describe SWD processing by the correlation of recordings made by geophones at two arbitrary locations $\mathbf{r}_A$ and $\mathbf{r}_B$, some SWD applications rely on correlations between pilot and geophone signals (Poletto and Miranda, 2004). Methods based on pilot trace correlations are affected by the drill-bit source function in the same way it affects methods based on geophone correlations. Therefore, the pilot deconvolution discussion above also applies to SWD processing by correlating pilot and geophone traces (Poletto and Miranda, 2004). The majority of SWD technologies rely on the acquisition of pilot records to remove the drill-bit source function.

2.2 Deconvolution interferometry

We present interferometry by deconvolution as an alternative to processing drill-bit noise records. A detailed description of the method and physics of deconvolution interferometry is given by Vasconcelos and Snieder (2007a). Here, we rely on the key concepts of that work to highlight the differences between interferometry by

deconvolution and other techniques in SWD data processing. We extend the physical interpretation of deconvolution interferometry given by Vasconcelos and Snieder (2007a) heuristically to elastic media for the special case of single-scattered waves. This extension is necessary for the discussion on the processing of the SAFOD SWD data.

Consider the deconvolution of the wavefield measured at $\mathbf{r}_A$ (equation 1) with the wavefield recorded at $\mathbf{r}_B$, given by

$$\begin{aligned} D_{AB} &= \frac{u(\mathbf{r}_A,\mathbf{s})}{u(\mathbf{r}_B,\mathbf{s})} = \frac{u(\mathbf{r}_A,\mathbf{s})\,u^*(\mathbf{r}_B,\mathbf{s})}{|u(\mathbf{r}_B,\mathbf{s})|^2} \\ &= \frac{G(\mathbf{r}_A,\mathbf{s})\,G^*(\mathbf{r}_B,\mathbf{s})}{|G(\mathbf{r}_B,\mathbf{s})|^2}\,. \end{aligned} \tag{11}$$

This deconvolution cancels the drill-bit source spectrum $|W(s)|^2$, present in cross-correlation (equation 2). Note that this cancelation occurs without the need for an independent estimate of $W(\mathbf{s})$. The next step in deconvolution interferometry is to mimic its correlation-based counterpart (see equation 7) and integrate equation 11 over all sources $\mathbf{s}$. The impulsive wavefields G are taken as a superposition of an unperturbed wavefields G_0 and wavefield perturbations G_S (Vasconcelos and Snieder, 2007a). The perturbations G_S can be interpreted as the waves scattered by the medium (Vasconcelos and Snieder, 2007a; Weglein et al., 2003). In this context, Vasconcelos and Snieder (2007a) expanded the deconvolution in equation 11 into a power series over $G_S(\mathbf{r}_B,\mathbf{s})/G_0(\mathbf{r}_B,\mathbf{s})$. After integrating over $\mathbf{s}$ and keeping the terms that are linear in the scattered waves G_S, we get

$$\begin{aligned} \oint_\Sigma D_{AB}\,d\mathbf{s} &= \underbrace{\oint_\Sigma \frac{G_0(\mathbf{r}_A,\mathbf{s})G_0^*(\mathbf{r}_B,\mathbf{s})}{|G_0(\mathbf{r}_B,\mathbf{s})|^2}\,d\mathbf{s}}_{D^1_{AB}} \\ &+ \underbrace{\oint_\Sigma \frac{G_S(\mathbf{r}_A,\mathbf{s})G_0^*(\mathbf{r}_B,\mathbf{s})}{|G_0(\mathbf{r}_B,\mathbf{s})|^2}\,d\mathbf{s}}_{D^2_{AB}} \\ &- \underbrace{\oint_\Sigma \frac{G_S(\mathbf{r}_B,\mathbf{s})G_0(\mathbf{r}_A,\mathbf{s})G_0^*(\mathbf{r}_B,\mathbf{s})}{G_0(\mathbf{r}_B,\mathbf{s})}\,d\mathbf{s}}_{D^3_{AB}}\,. \end{aligned} \tag{12}$$

Following the interpretation of Vasconcelos and Snieder (2007a), the term D^1_{AB} recovers $G_0(\mathbf{r}_A,\mathbf{r}_B)$ and $G_0^*(\mathbf{r}_A,\mathbf{r}_B)$, which are the causal and acausal unperturbed impulse responses for waves excited at $\mathbf{r}_B$ and recorded at $\mathbf{r}_A$. The term D^2_{AB} yields $G_S(\mathbf{r}_A,\mathbf{r}_B)$ that describes causal scattered waves propagating from $\mathbf{r}_B$ to $\mathbf{r}_A$. Recovering $G_S(\mathbf{r}_A,\mathbf{r}_B)$ from D^2_{AB} is the objective of deconvolution interferometry with the purpose of imaging scattered waves. The last term in equation 12 describes a spurious arrival that arises from the *clamped point* boundary condition imposed by deconvolution interferometry (Vasconcelos and Snieder, 2007a).

As noted above, using deconvolution according to equation 11 to process SWD data does not require an independent estimate of the drill-bit source function. This is the first and main difference between deconvolution interferometry and the majority of correlation-based methods used in SWD data processing. Apart from being an alternative method for treating data from standard SWD experiments, interferometry by deconvolution would be particularly useful when pilot records are either unavailable or are poor estimates of the drill-bit excitation function. Poletto and Miranda (2004) provide examples of when pilot recordings yield unreliable estimates of the drill-bit source function. This is the case, for example, when transmission along the drill-string is weak, when the drilling well is deep (in the order of several thousands of feet), or when the drilling well is deviated or when two or more nearby wells are drilling simultaneously with the well that is equiped with pilot sensors. From the standpoint of removing the excitation function, none of these cases is an issue for deconvolution interferometry, as they are for pilot deconvolution. This is because equation 11 holds regardless of the complexity of the excitation (equation 1).

As in interferometry methods based in correlation (Schuster et al., 1994; Yu and Schuster, 2004), knowledge of the drill-bit position $\mathbf{s}$ is not necessary for the processing of SWD data by deconvolution interferometry. The only requirement for the successful application of deconvolution interferometry is that the drill-bit must occupy the stationary source locations that give rise to targeted scattered waves propagating between the receivers (Vasconcelos and Snieder, 2007a; Snieder et al, 2006). Analogously to the method originally proposed by Schuster et al. (2004) for the imaging of drill-bit noise, it is possible to use deconvolution interferometry to reconstruct primary arrivals from free-surface ghost reflections.

So far we have only discussed SWD processing and deconvolution interferometry for acoustic media. Now we extend some of these concepts to elastic media, with the objective of applying interferometry by deconvolution to multicomponent data. The conclusions drawn in our previous discussions on removal of the drill-bit source function, pilot deconvolution and deconvolution interferometry also hold for elastic media. Here, the goal is to understand what is the result of combining different receiver components when performing deconvolution interferometry. We start by defining $G^{(i,k)}(\mathbf{r}_A,\mathbf{s})$ as the elastic frequency-domain impulse response excited by the k-th component of the source at $\mathbf{s}$, and recorded by the i-th component of the receiver at $\mathbf{r}_A$. For our purposes it is not necessary to specify whether the Green's functions $G^{(i,k)}$ pertain to stress or to strain waves (Wapenaar, 2004; Wapenaar and Fokkema, 2006). We refer to component orientations according to the 1-, 2- and 3-directions in Figure 1. Next, we take the deconvolution

$$D_{A^iB^j} = \frac{u^{(i,k)}(\mathbf{r}_A,\mathbf{s})}{u^{(j,k)}(\mathbf{r}_B,\mathbf{s})} = \frac{G^{(i,k)}(\mathbf{r}_A,\mathbf{s})\,G^{(j,k)*}(\mathbf{r}_B,\mathbf{s})}{\left|G^{(j,k)}(\mathbf{r}_B,\mathbf{s})\right|^2}, \tag{13}$$

where $u^{(i,k)} = W\ G^{(i,k)}$ is the recorded data. As in equation 11, the source function W cancels. It follows from equation 13 that $D_{A^iB^j}$ is the deconvolution of the i-th component of the receiver at $\mathbf{r}_A$ with the j-th component of the receiver at $\mathbf{r}_B$. We treat $G^{(i,k)}$ as the superposition of the unperturbed wavefield $G_0^{(i,k)}$ and the scattered waves $G_S^{(i,k)}$ (as in Vasconcelos and Snieder, 2007a). The source integral of equation 13 can be expressed in the same three-term form of equation 12. We call $D^2_{A^iB^j}$ the elastic term analogous to D^2_{AB}. The is term can be expressed as

$$\begin{aligned} D^2_{A^iB^j} &= \int_{\sigma_1} \frac{G_S^{(i,k)}(\mathbf{r}_A,\mathbf{s})G_0^{(j,k)*}(\mathbf{r}_B,\mathbf{s})}{\left|G_0^{(j,k)}(\mathbf{r}_B,\mathbf{s})\right|^2}\,d\mathbf{s} \\ &\approx \mathcal{K}\,G_S^{(i,j)}(\mathbf{r}_A,\mathbf{r}_B)\,. \end{aligned} \tag{14}$$

where $\mathcal{K}$ is a constant. Following the reasoning given by Vasconcelos and Snieder (2007a) in interpreting equation 12, $\left|G_0^{(j,k)}(\mathbf{r}_B,\mathbf{s})\right|^2$ is a slowly varying function of $\mathbf{s}$, and its source average effectively gives a constant. The phase of the integrand in equation 14 is controlled by the numerator (Vasconcelos and Snieder, 2007a). In equation 14, σ_1 is a segment of Σ that contains the stationary source locations that give rise to the desired waves in $G_S^{(i,j)}(\mathbf{r}_A,\mathbf{r}_B)$ (Vasconcelos and Snieder, 2007a and 2007b). Analogously to D^2_{AB} (Vasconcelos and Snieder, 2007a), the term $D^2_{A^iB^j}$ yields causal scattered waves that propagate from $\mathbf{r}_B$ to $\mathbf{r}_A$. Equation 14 states that the scattered waves described by $G_S^{(i,j)}(\mathbf{r}_A,\mathbf{r}_B)$ are excited by j-th component of a pseudo-source at $\mathbf{r}_B$ and are recorded by the i-th component of the receiver at $\mathbf{r}_B$. As in the acoustic case (equation 12), the scattered waves in the second line of equation 14 are the objective of interferometry.

According to the Green's function representation of Wapenaar and Fokkema (2006), the full elastodynamic reconstruction of $G^{(i,j)}(\mathbf{r}_A,\mathbf{r}_B)$ using cross-correlations requires a summation over the index k when integrating over sources, and the separation of P- and shear-wavefields at the surface of integration. Draganov et al. (2006) validate the elastodynamic interferometric reconstruction described by Wapenaar and Fokkema (2006) with a numerical example for a heterogeneous model. Although deconvolution interferometry (Vasconcelos and Snieder, 2007a) has not been formally extend to elastic media, we expect that the elastodynamic reconstruction of $G_S^{(i,j)}(\mathbf{r}_A,\mathbf{r}_B)$ by deconvolution interferometry also requires a summation over the index k. Note that in equation 14, we do not perform a summation over the index k as in the approach by Wapenaar and Fokkema (2006). In practice, this means that the integral in the first line of equation 14 only yields a partial reconstruction of $G_S^{(i,j)}(\mathbf{r}_A,\mathbf{r}_B)$ (second line of equation 14). In the case of single-scattered waves reconstructed from the interference of transmission and reflection responses (such as the data examples we provide in this paper), the partial reconstruction of $G_S^{(i,j)}(\mathbf{r}_A,\mathbf{r}_B)$ by the use of equation 14 can yield events with correct kinematics but distorted amplitudes (Draganov et al., 2006). As we discuss here with our field data example, a kinematically-consistent reconstruction of single-scattered waves using equation 14 is sufficient for the structural delineation of fault reflectors at the San Andreas fault zone (Vasconcelos et al., 2007a).

It is known that the deconvolution of any signal with itself results in a delta function ($\delta(t)$) in the time domain. For the acoustic case in equation 11, this is accomplished by setting $\mathbf{r}_A = \mathbf{r}_B$, which in turn gives the zero-offset trace in deconvolution interferometry. Vasconcelos and Snieder (2007a) showed that the time-domain zero-offset response in deconvolution interferometry is given by $G(\mathbf{r}_B,\mathbf{r}_B,t) = \delta(t)$ in arbitrary media. Since deconvolved waves satisfy the same homogeneous wave equation as the original waves (Snieder et al., 2006b), spurious arrivals are generated by deconvolution interferometry to cancel scattered waves that arrive at zero-offset at nonzero times. This represents the effect of an extra boundary condition in deconvolution interferometry experiments: the point $\mathbf{r}_B$ behaves, for the *particle velocity* impulse response, like a *clamped point* in the medium (see discussion in Vasconcelos and Snieder, 2007a). In our elastic case, setting $\mathbf{r}_A = \mathbf{r}_B$ and $i = j$ in equation 13 results in unity, this translates to the time-domain condition

$$D_{B^iB^i}(t) = \delta(t)\,. \tag{15}$$

This condition does not hold if the receivers at $\mathbf{r}_B$ and $\mathbf{r}_A$ measure different field quantities, i.e., one receiver measures stress while the other measures strain. Equation 15 holds for arbitrarily inhomogeneous and anisotropic media. The condition in equation 15 sets a different type of boundary condition than those discussed by Vasconcelos and Snieder (2007a) for the acoustic case. While deconvolution interferometry *clamps* the point $\mathbf{r}_B$ for $t \neq 0$ in acoustic media, in elastic media only the i-th component of the wavefield deconvolution is clamped for $t \neq 0$. Clarifying the physical meaning of the boundary condition imposed by deconvolution interferometry in elastic media is beyond the scope of this paper, and is the subject of future research.

Analogously to interferometry by correlation (Wapenaar and Fokkema, 2006; Draganov et al., 2006), it follows from equations 13 and 14 that the orientation of the pseudo-source in deconvolution interferometry is dictated by the choice of component of the receiver at $\mathbf{r}_B$ that is used for deconvolution. The choice of component of the receiver at $\mathbf{r}_A$ controls the orientation of the recording component in the interferometric experiment.

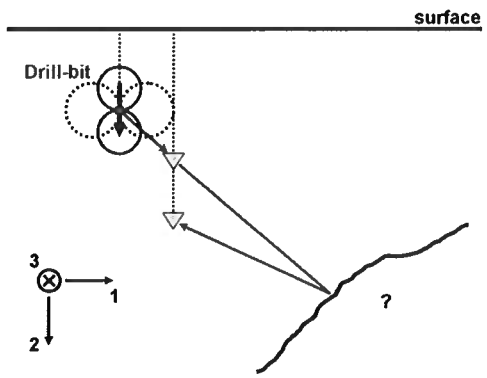

Figure 1. Illustration of drill-bit interferometry in elastic media. The red dot indicates a drill-bit position that yields a stationary contribution to waves that propagate between the receivers (light blue triangles). Red arrows shows the raypaths of pure-mode stationary arrivals. The blue arrow represents the oscillatory point-force excitation that describes the drill-bit source function. Solid and dashed blue circles denote the P- and S-wave radiation patterns, respectively. These radiation patterns follow the description of drill-bit radiation by Poletto (2005a). Receiver components, numbered 1 through 3, are oriented according to the vectors in the lower left-hand corner of the Figure. The medium consists of a homogeneous and isotropic half-space with an irregular reflector

From elastic wave theory (Aki and Richards, 1980), the analysis of point-source radiation shows that a single source component generates impulse responses in all three receiver components, depending on the medium properties and on the source/receiver geometry. Because deconvolved waves satisfy the same homogeneous wave equations as the original experiment (Snieder et al., 2006b), the radiation pattern of the pseudo-source synthesized from deconvolution interferometry is controlled by the radiation pattern of the original physical experiment.

In SWD experiments, the drill-bit can be approximately described by an oscillatory force oriented in the local direction of the well (Rector and Hardage, 1992; Poletto, 2005a). Figure 1 portrays a schematic 2D representation of the drill-bit far-field radiation pattern in homegeneous and isotropic media. The radiation pattern shown in Figure 1 is similar to the point-force radiation pattern (Aki and Richards, 1980), except that the amount of drill-bit energy that converts into shear-waves (mostly SV-waves) is considerably larger than that from a traditional point-force source (Rector and Hardage, 1992; Poletto, 2005a). In Figure 1, we depict a drill-bit and instrumented well geometry that is consistent with the SAFOD case study, which we discuss in one of the next Sections. The receiver that acts as a pseudo-source in Figure 1 radiates waves according to the its recorded transmitted wavefield (see red arrows in the Figure). The wave modes and polarizations of the transmitted waves are dictated by the bit radiation pattern and the source/receiver geometry (Poletto, 2005a; Aki and Richards, 1980). The physical excitation in Figure 1 is associated to a vertically-oriented drill-bit point-force, whose radiation pattern (Rector and Hardage, 1992; Poletto, 2005a) is illustrated in the Figure. According to the geometry and bit radiation pattern in Figure 1, the direct waves recorded by the top receiver are P- and S-waves polarized in the source/receiver plane. Hence, using the same notation as in equations 13 through 14 and assuming the receivers measure only the far-field response, interferometry in the context of Figure 1 recovers $G_S^{(i,2)}(\mathbf{r}_A, \mathbf{r}_B)$. Also, the response $G_S^{(i,2)}(\mathbf{r}_A, \mathbf{r}_B)$ is zero for $i = 3$ because SH-wave excitation (polarized in the 3-direction) from a drill-bit source is negligible in the conditions of Figure 1. From the drill-bit radiation pattern, we see that waves propagating along the stationary path depicted by Figure 1 (red arrows) carry both P- and shear-wave energy. The discussion surrounding Figure 1 illustrates how the radiation properties of the pseudo-source recovered from interferometry depend on the drill-bit excitation in SWD experiments. This dependence is model-dependent, and becomes more complicated with the introduction of heterogeneity and anisotropy.

3 SUBSALT NUMERICAL EXAMPLE

The drill-bit imaging numerical experiment we present here is conducted with the 2D *Sigsbee* salt model (Figure 2). In this experiment, we place a long 100-receiver downhole array below the salt canopy, in a 45° deviated well. The first receiver is placed at $x = 14630$ m and $z = 4877$ m , and the last receiver is at $x = 16139$ m and $z = 6385$ m. The receivers are evenly spaced; and x and z translate to the lateral and depth coordinates in Figure 2, respectively. The borehole array records the drilling noise from a vertical well placed at $x = 14478$ m (Figure 2). The drill-bit noise is recorded for a drill-bit depth interval that ranges from $z = 4572$ m to $z = 6705$ m. The objective of this numerical experiment is to show interferometry can recover, from drill-bit noise, up-going single-scattered waves that propagate between the receivers, such as the one represented by the raypath in Figure 2 (represented by the dashed arrow). The up-going scattered waves recovered by interferometry of drill-bit noise can be used to image the *Sigsbee* structure from below.

To replicate drill-bit wave excitation in the numerical experiment, we first modeled 200 evenly-spaced shots within the drilling interval of interest. These shots were modeled by an acoustic finite difference method

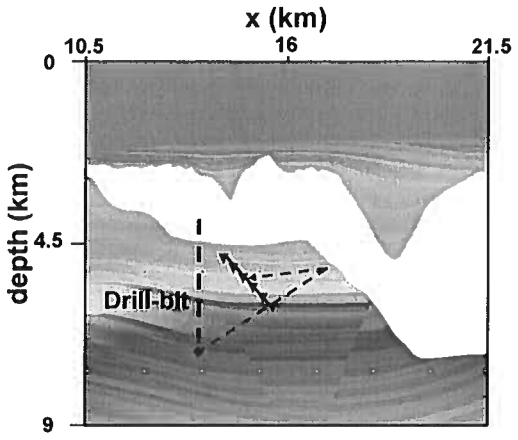

Figure 2. Structure of *Sigsbee* model and schematic acquisition geometry of the drill-bit experiment. The colors in the model denote acoustic wavespeed. The dashed black line indicates a well being drilled, which excites waves in the medium. The waves are recorded in a deviated instrumented well, inclined 45° with respect to the vertical direction. The solid line with triangles represents the instrumented well. The dashed arrow illustrates a stationary contribution to singly reflected waves that can be used to image the salt flank from the drilling noise.

(Claerbout, 1985). Next, we convolved the shots with a 60 second-long model of the drill-bit excitation (Figure 3). The model for the drill-bit excitation is that of a roller-cone bit (Polleto, 2005a). We add band-limited noise (see Figure 3) to the model by Poletto and Miranda (2004) to make the drill-bit signal wide-band. Similar to the numerical example in Poletto and Miranda (2004), the bit and drilling parameters we used in our model are listed in the caption of Figure 3. The excitation function in Figure 3 represents the portion of the drilling energy that is radiated in the rock formation (Poletto 2005a, Poletto and Miranda, 2004).

Figure 3a shows the power spectrum of the modeled bit signal, while Figure 3b shows a portion of the drill-bit source function in the time-domain. As discussed in the previous Section, the time-domain drill-bit excitation has a narrow-band character (Figure 3b) because the source power spectrum is dominated by vibrational drilling modes (Poletto, 2005a; Poletto and Miranda, 2004). This behavior is also present in the data recorded by the borehole receivers. The common receiver gather from receiver 50 in Figure 4a shows that the simulated data is dominated by the character of the drill-bit excitation function (Figure 3b). The records in Figure 4a depict a moveout that characterizes the direct-wave arrival from the drill-bit. The weak events with positive slopes in the left-hand portion of Figure 4a are salt-bottom reflections from when the drill-bit is close to the bottom of the salt (see geometry in Figure 2).

Interferometry of recorded data such as in Figure 4a results in pseudo-shot gathers as in Figures 4b and c. The use of deconvolution interferometry as shown in the left-hand side of equation 12 (Vasconcelos and Snieder, 2007a) for a fixed $\mathbf{r}_B$ at receiver 50 results in Figure 4b. The pseudo-shot gather in Figure 4c is obtained from correlation interferometry (equation 7; e.g., Draganov et al., 2006) for the same geometry as Figure 4b. Although both Figures 4b and c represent waves excited by a pseudo-source at receiver 50, the wavefield in Figure 4b is approximately impulsive, while the data in Figure 4c is dominated by the autocorrelation of the drill-bit source function. Because the excitation function is canceled in deconvolution interferometry (Vasconcelos and Snieder, 2007a; equation 11), the pseudo-source in Figure 4 is impulsive. The source power spectrum in equation 2 results, in the time-domain, in the dominant reverberation in the pseudo-shot generated by correlation (Figure 4c). When pilot sensors are available, pilot deconvolution methods (e.g., Rector and Marion, 1991; Poletto and Miranda, 2004) can be employed to remove the source autocorrelation from data such as in Figure 4c (equation 10).

Many of the features of the deconvolution pseudo-shot gather in Figure 4b are explained by the theory presented by Vasconcelos and Snieder (2007a); the interferometric shot gather generated by deconvolutions shows causal and acausal direct waves, and causal scattered arrivals. According to Vasconcelos and Snieder (2007a), the zero-offset trace obtained by deconvolution interferometry is a band-limited delta function at $t = 0$. This can also be observed in Figure 4 for the trace at receiver 50 (i.e., the zero-offset trace). The presence of this delta function at zero-offset imposes the so-called *clamped point* boundary condition in acoustic media (Vasconcelos and Snieder, 2007a). Because of this boundary condition, the gather in Figure 4 contains spurious arrivals. The visual identification of these arrivals in the gather is not straightforward because the recorded wavefield is complicated, given the model complexity (Figure 2). These spurious arrivals, however, typically do not translate into image artifacts (Vasconcelos and Snieder, 2007a).

Given the acquisition geometry in this numerical experiment (Figure 2), there is a point, to the left-hand side of the receivers, where drill-bit position aligns with the array direction. This drill-bit position samples a source stationary point for the direct waves that travel between the receivers. At this stationary position, the drill-bit excites waves that travel straight down the receiver array. These waves are responsible for the recovery of the direct-wave events with positive slopes in Figure 4. With the drilling geometry shown in Figure 2 the drill-bit never reaches a position where it aligns with the receivers to the right-hand side of the array. Therefore, the drill-bit does not sample a stationary source point that emits waves that travel directly upward along the

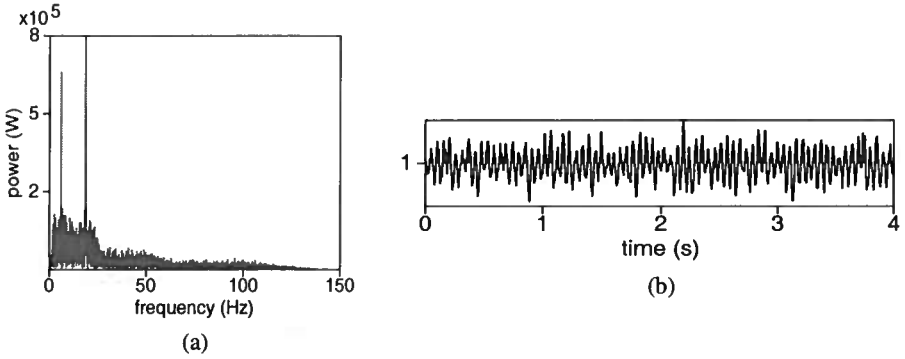

Figure 3. Numerical model of the drill-bit excitation. (a) shows the power spectrum of the drill-bit source function. Note that although it is wide band, the power spectrum of the source function in (a) has pronounced peaks that correspond to vibrational drilling modes. (b) is the drill-bit source function in the time-domain. We show only the first 4 s of the 60 second-long drill-bit source function used in the modeling. The assumed drill-bit is a tri-cone bit an outer diameter of 0.35 m, an inner diameter of 0.075 m and a density of 7840 kg/m^3. Each cone is comprised of three teeth rows as in the example by Poletto and Miranda (2004). Drill-string P-wave velocity is of 5130 m/s. The drilling was modeled with a weight on bit of 98 kN, torque on bit of 6 kNm, 60 bit revolutions per minute, a rate of penetration of 10 meters per hour and four mud pumps with a rate of 70 pump strikes per minute.

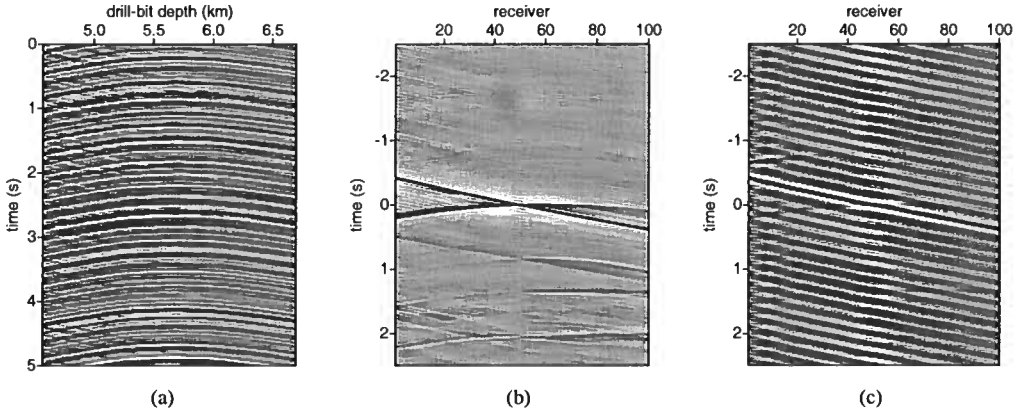

cc

Figure 4. (a) Synthetic drill-bit noise records at receiver 50. Only 5 s out of the 60 s of recording time are shown. The narrow-band character of the records is due to influence of specific drilling modes (Figure 3a). (b) Deconvolution-based interferometric shot gather with the pseudo-source located at receiver 50. (c) Pseudo-shot gather resulting from cross-correlation with same geometry as (b). Receiver 1 in (a) and (b) is the shallowest receiver of the borehole array (Figure 2).

receiver array. Hence, the direct-wave events with negative slopes in the pseudo-shot gather (Figure 4b) have a distorted curved moveout instead of the correct linear moveout shown by the direct waves that have positive slopes. A similar phenomenon was observed by Mehta et al. (2006), who show that the distortions caused by poor source sampling over stationary source positions can be attenuated by tapering the ends of the integrand in equation 7.

We generate interferometric shot gathers such as the ones in Figures 4b and c for pseudo-sources at each of the receivers in the array. This yields 100 pseudo-shots, which are recorded by the 100-receiver array. We use shot-profile wave-equation migration to image the interferometric data. The migration is done by wavefield extrapolation with the spilt-step Fourier method (Biondi, 2006). The wavefield extrapolation is done in a rectangular grid conformal to the receiver array, where the extrapolation steps are taken in the direction perpendicular to the array. Figure 5 displays the images obtained from migrating the pseudo-shot gathers from

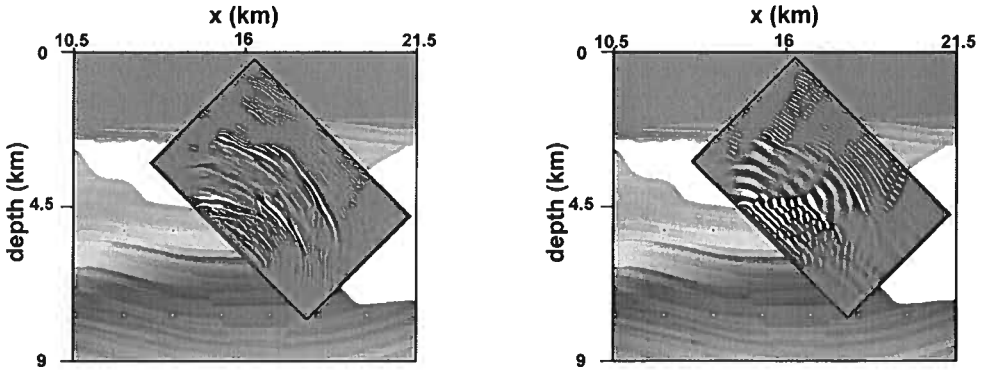

(a) (b)

Figure 5. Images obtained from drill-bit noise interferometry. The images, in grey scale, are superposed on the Sigsbee model in Figure 2. Panel (a) is the image obtained from shot-profile wave-equation migration of pseudo-shot gathers generated from deconvolution interferometry (such as in Figure 4b). The image in (b) is the result of migrating correlation-based interferometric shot gathers. The red lines in the images represent the receiver array.

deconvolution interferometry (Figure 5a), and from the correlation-based method (Figure 5b).

In interferometric experiments, the image aperture is dictated by the geometry of the receiver array (red lines in Figure 5). The positioning of physical sources that are used in interferometry along with the medium properties control the actual subsurface illumination that is achieved by interferometry. When the sources completely surround the receivers, the interferometric pseudo-source radiates energy in all directions, similarly to a real physical source (Wapenaar and Fokkema, 2006; Larose et al., 2006). When the physical excitation generated by the sources is one-sided (Wapenaar, 2006; Vasconcelos and Snieder, 2007a), pseudo-source radiation is uneven. Therefore, that the subsurface illumination in the images in Figure 5 is controlled by the illumination given by the original drill-bit/receiver geometry. In our case, the illumination given by interferometric shots is different from that obtained by placing real physical sources at the receiver locations; hence, the resulting image from these active shots would be different, in terms of illumination, from those in Figure 5. This is an important distinction between the imaging interferometric pseudo-shots and imaging actual shots placed at the receiver locations. We have to make this distinction because the physical sources in the experiment (Figure 2) do not constitute the closed surface required for equations 7 and 12 to hold.

Comparing the images in Figure 5 with the Sigsbee model in Figure 2, shows that the image from deconvolution interferometry (Figure 5a) provides a better representation of the subsurface structure than does the image from correlation interferometry (Figure 5b). The salt reflectors (top and bottom) are better resolved in in Figure 5a than they are in Figure 5b. Also, it is possible to identify subsalt sediment reflectors in Figure 5a which are not visible in Figure 5b. The reflectors in Figure 5a are well resolved because deconvolution interferometry successfully suppresses the drill-bit source function when generating pseudo-shot gathers (Figure 4). The image from deconvolution interferometry does not present severe distortions due to the spurious arrivals characteristic of deconvolution pseudo-shot gathers (Vasconcelos and Snieder, 2007a). As discussed by Vasconcelos and Snieder (2007a), these spurious events typically do not map onto coherent reflectors on shot-profile migrated images like the one in Figure 5a. The image from correlation interferometry (Figure 5b) portrays a distorted picture of the Sigsbee structure (Figure 2) because the correlation-based pseudo-shot gathers are dominated by the power spectrum of the drill-bit excitation (Figure 4c; equation 7). The narrow-bandcharacter of the drill-bit source (Figures 3b, 4a and 4c) is responsible for the "ringy" appearance of the image in Figure 5b.

Drill-bit imaging technology based on pilot recordings (e.g., Rector and Marion, 1991; Haldorsen et al., 1994; Poletto and Miranda, 2004) provides images that are accurate representations of subsurface geology, such as the image in Figure 5a. In the context of SWD, deconvolution interferometry is an alternative processing methodology that does neither require an inde-

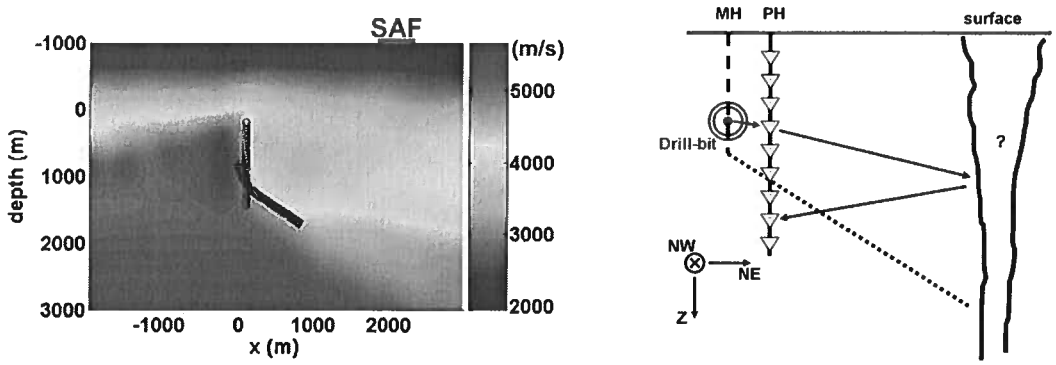

Figure 6. Panel (a) shows the large-scale structure of the P-wave velocity field (velocities are colorcoded) at Parkfield, CA. The circles in (a) indicate the location of the sensors of the SAFOD pilot-hole array used for the recording of drilling noise. The SAFOD MH is denoted by the triangles. The location of the SAFOD drill site is depicted by the star. Depth is with respect to sea level, the altitude at SAFOD is of approximately -660 m. Panel (b) shows the schematic acquisition geometry of the downhole seismic-while-drilling (SWD) SAFOD dataset. Receivers are indicated by the light-blue triangles. The structures outlined by black solid lines to the right-hand side of the figure represent a target fault. As indicated by (b), receivers are oriented in the Z-(or downward vertical), NE- and NW-directions. (b) also shows a schematic stationary path between the drill-bit and two receivers. Both panels represent Southwest to Northeast (from left to right) cross-sections at Parkfield.

pendent estimate of the drill-bit source function, nor any assumptions of wave propagation within the drill-string. We present the Sigsbee SWD numerical example with the intention of modeling a situation where pilot recordings are absent or would yield a poor representation of the drill-bit excitation. Our numerical example also demonstrates that deconvolution interferometry can also be used for passive drill-bit imaging, where no knowledge about the drill-bit position is required.

4 SAFOD DRILL-BIT DATA

The San Andreas Fault Observatory at Depth (SAFOD) is located at Parkfield, CA. Its objective is to actively study the San Andreas Fault (SAF) zone from borehole data, as well as to monitor the fault zone activity. SAFOD consists of two boreholes, the Pilot-Hole (PH) and the Main-Hole (MH). The geometry of the PH and MH relative to the to surface trace of the SAF is displayed in Figure 6a. The data we analyze consists of the noise excited by the drilling of the MH, recorded by the 32-receiver array permanently placed in the PH. The geologic context of this experiment and the full interpretation of the results we show here, along with active-shot seismic data, are presented in Vasconcelos et al. (2007a). We focus here on the use of deconvolution interferometry to obtain an image of the SAF, and on the differences between the deconvolution- and correlation-based approaches in the processing of the SAFOD SWD data.

The main objective of the SAFOD borehole SWD experiment is to provide broadside illumination of the SAF that is not possible from surface measurements. Figure 6b illustrates how single reflections from the SAF can potentially be recovered by the drilling noise records measured at the SAFOD PH array. The stationary path indicated by the red and black arrows in Figure 6b shows that the interference between the drill-bit direct arrivals with fault-scattered waves can be used to reconstruct primary fault reflections propagating between the receivers. Because the distance between the MH and PH is only in the order of 10 meters (Boness and Zoback, 2006), the drill-bit only gives stationary contributions to waves emanating from a given receiver when drilling next to that receiver. This is an important consideration in identifying which portion of the recorded data is useful for processing (see below).

The acquisition of the SAFOD PH drill-bit noise records began in June 2004, and continued until late August 2004 (Taylor et al., 2006). The MH intersected the PH on July 15th (Figure 6a). The drill-bit noise recorded after the MH crossed the PH is not of interest for our interferometry purposes because, unlike the drill-bit positions illustrated by Figure 6b, it does not yield stationary contributions that give primary fault reflections that propagate between the receivers. Due to field instrumentation issues (S. T. Taylor, 2006; personal communication), most of the data recorded by the PH array before July 15th consists of electrical noise only. A window of approximately 20 hours prior to the intersection of the PH by the MH coincides with the portion of the PH data for which the instrumentation problem was fixed. The data acquired within this window are used in the analysis we show here.

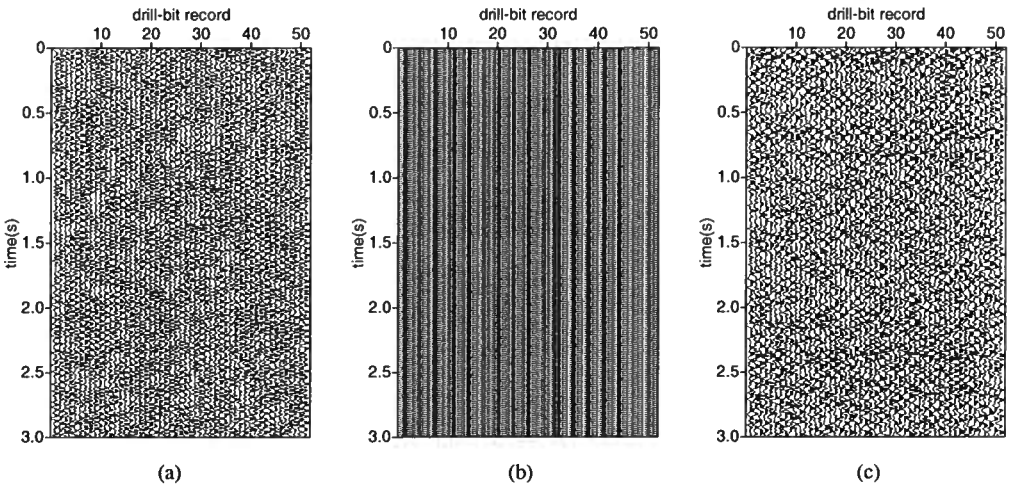

Figure 7. Drill-bit noise records from the SAFOD Pilot-Hole. Because the drill-bit is closest to receiver 26, the data recorded at this receiver, shown by panel (a), is not contaminated by electrical noise. For the same drill-bit position, panel (b) shows the data recorded at receiver 23. Panel (c) shows the result of filtering the electrical noise from the data in panel (b). These data show the first 3 s of the full records (which are 60 s long). For the records shown here, the drill-bit position is practically constant. These data are from the vertical component of recording.

According to the MH drilling records, the depth interval that was sampled by the usable drill-bit data extends from approximately 350 m to 450 m (in the scale in Figure 6a). We use the data recorded in this interval to generate interferometric shot records. Within the 350-450 m bit interval, the drill-bit passes by the PH receiver 26. Since the stationary contributions of the sources to recovering primary reflections from the SAF only occur when the bit is next to a receiver, the data recorded by receiver 26 in the depth interval of 350-450 m can be used as the filter for interferometry. This translates to setting $\mathbf{r}_B$ in equations 7, 12 or 13 to the coordinates of receiver 26. Hence, out of the 32 receivers of the SAFOD PH array, it is only possible to create interferometric shot gathers with a pseudo-source at receiver 26.

A small portion of the recorded data is shown in Figure 7. The data in Figure 7a are from the vertical component of receiver 26, while the data in Figures 7b and c correspond to receiver 23. Since the records shown in Figure 7 are subsequent recordings of the drill-bit noise of 1 minute duration (of which only the first 3 s are shown in Figure 7), the drill-bit position for the records in the Figure is practically constant. The data recorded by receiver 26 shown in Figure 7a are low-pass filtered to preserve signal up to 75 Hz. A similar filter, preserving frequencies up to 55Hz, is applied to the original data from receiver 23 in Figure 7b, resulting in the data in Figure 7c. The data recorded by receiver 23 (Figure 7b) is heavily contaminated by electrical noise, at frequencies of 60, 120 and 180 Hz. This electrical noise is practically negligible in the data from receiver 26, as shown by Figure 7 where the 60 Hz monochromatic oscillation cannot be seen. Because the bit is close to receiver 26, the drilling noise is louder than the electrical noise in Figure 7a. After low-pass filtering, the data from receiver 23 (Figure 7c) shows a similar character to that from receiver 26 (Figure 7a). As discussed in previous sections (and illustrated by Figure 3), the SAFOD drill-bit noise data shows a narrow-band character, typical of the vibrational modes from drilling. The drilling of the SAFOD MH was done with a roller-cone bit.

A critical issue with the processing of the SAFOD SWD data is that pilot records are not available. Drill-string accelerometers were not placed in the SAFOD rig until August 2004 (Taylor et al., 2006), after the acquisition of the SAFOD PH data we process here. Since no pilot records are available, pilot-based SWD processing (Rector and Marion, 1991; Haldorsen et al., 1994; Poletto and Miranda, 2004) cannot be applied to the PH drill-bit data. Thus, these data are a natural candidate for the application of deconvolution interferometry. Figure 8 shows four pseudo-shot gathers derived from deconvolution interferometry using different combinations of receiver components (see equations 13 through 14). We only display the traces for receivers 15 through 32 in Figure 8 because electric noise in receivers 1-14 prevents the recovery of coherent signals. Before computing the pseudo-shots in Figures 8 and 9, all data were low-passed to preserve frequencies up to 55 Hz. For the interferometry, we divide each minute-long record into two 30-second long traces. With approximately 20 hours of recording time, the resulting traces in the pseudo-shot records are the result of stacking in the order of 2000 de-

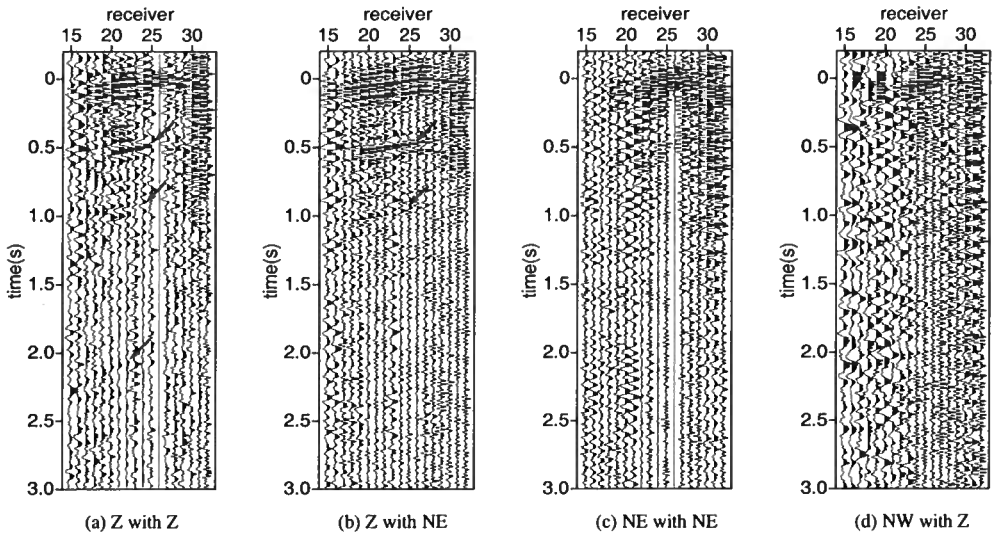

Figure 8. Pseudo-shot gathers from deconvolution interferometry. In these gathers, receiver 26 acts as a pseudo-source. Each panel in the Figure is the result of deconvolving different combinations of receiver components: the deconvolution of the Z- with Z-components yields (a), Z- with NE-components give (b), NE- with NE-components result in (c), and NW- with Z-components yield (d). Physically, panel (a) shows waves recorded by the vertical component for a pseudo-shot at receiver 26, excited by a vertical point-force. (b) is also the vertical component for a pseudo-shot at PH-26, but unlike the wavefield in (a), it represents waves excited by a point-force in the NE-direction. Likewise, (c) pertains to both excitation and recording in the NE-direction, while waves in (d) are excited by a vertical point-force and are recorded in the NW-direction. The red arrows show reflection events of interest. Note that receiver 32 is the shallowest receiver in the SAFOD PH array (Figure 6). Receiver spacing is of 40 m. The component orientations we use here are the same as those in Figure 6b.

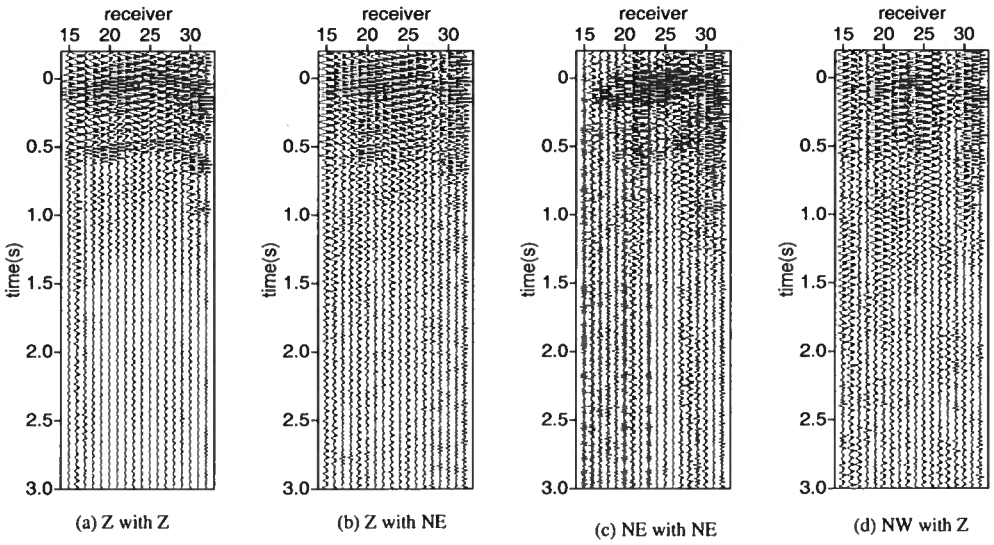

Figure 9. Pseudo-shot gathers from correlation interferometry. Here, each panel is associated to the correlation of the same receiver components as in the corresponding panels in Figure 8. The physical interpretation of excitation and recording directions is the same as for Figure 8. Unlike the data in Figure 8, the source function in these data is given by the autocorrelation of the drill-bit excitation.

convolved or correlated traces (see equations 7 and 12). For a discussion on our numerical implementation of deconvolution, see Appendix A.

The panels in Figure 8 show that combining different components in deconvolution interferometry yields different waveforms. Scattered arrivals, indicated by red arrows, can be identified in Figures 8a and b, but not in c and d. The first reason for the difference between the results in the four panels of the Figure lies in equations 13 through 14. According to these equations, deconvolving data recorded in the i-component with data recorded by the j-component results in the interferometric impulse response recorded by the i-component and excited by the j-component. This means that the data in Figure 8a represents a vertical excitation at receiver 26 recorded by the vertical component at all receivers. Likewise, Figure 8b represents a vertical excitation and the recording of data in the Northeast direction (NE-component). Similar interpretations follow for the other two panels in the Figure, and are given in the Figure caption.

In Section 2.2, we discuss the influence of the drill-bit radiation properties on the radiation pattern of the pseudo-source synthesized by interferometry. The radiation characteristics of the pseudo-source together with signal-to-noise ratio in different recording components of the receiver away from the drill-bit (and from receiver 26) is also responsible for the differences between the panels of Figure 8. Because coherent arrivals can be seen in Figures 8a and b, two conclusions can be drawn. First, the signal-to-noise ratio in the vertical component (Z-component) of the receivers is sufficiently high to record scattered waves. Second, Figure 8a shows that the recorded drill-bit direct wave has nonzero polarization in the Z-direction. This is caused by the fact that the pseudo-source radiation is controlled by the radiation pattern of the bit (Section 2.2), and this case most of the energy radiated by the bit is polarized in the vertical direction.

Since Figure 8b shows coherent events (indicated by red arrows) that are reconstructed from energy recorded by the Northeast component, it follows that the direct-wave response from the bit excitation has a nonzero polarization component in the NE-direction as well. In these data, receiver 26 records drill-bit direct waves polarized both in the Z- and NE-directions because the receiver is in the bit's near-field (the PH and MH are a few meters apart). The measured near-field response to an excitation in the Z-direction (the drilling direction is close to vertical) is polarized both in the vertical and in-plane horizontal components (Aki and Richards, 1980; Tsvankin, 2001). The waves scattered from the SAF have far-field polarization because the fault zone is approximately 2 km away from the PH. The lack of scattered signals in Figures 8c and d are mostly have a poor signal-to-noise ratio in the the Northeast and Northwest components (NE- and NW-components) of the receivers far from the bit.

The zero-offset trace (the trace at receiver 26) in Figures 8a and c is a band-limited delta function centered at $t = 0$. This is a demonstration of the deconvolution interferometry boundary condition in equation 15. The acoustic counterpart of this boundary condition generates introduces spurious arrivals in the pseudo-shot gathers (Vasconcelos and Snieder, 2007a). In Figure 8a, we do not observe pronounced spurious arrivals associated with the scattered events (marked by red arrows). As highlighted in Section 2.2, the boundary condition in equation 15 does not have the same physical meaning as in the acoustic case (Vasconcelos and Snieder, 2007). A thorough understanding of the physical meaning of equation 15 is beyond the scope of this paper.

The pseudo-shot gathers in Figure 8 were generated by deconvolution interferometry while the ones in Figure 9 are the result of correlation interferometry (e.g., Wapenaar, 2004; Draganov et al., 2006). Analogously to the observations made in the previous Section, the correlation-based interferometric shot gathers (Figure 9) are influenced by the autocorrelation of the drill-bit source function, giving them a monochromatic appearance. The scattered events seen in Figures 8a and b cannot be identified in Figures 9a and b. In a more standard SWD processing routine, the autocorrelation of the source function could be removed from the data in Figure 9 by means of pilot deconvolution (Rector and Marion, 1991; Poletto and Miranda, 2004). We reiterate that this type of processing is not possible in our case because pilot records are not available.

Together with geologic information from the MH data and with an active shot acquired by sensors in the MH, Vasconcelos et al. (2007a) associated the event arriving with a zero-offset time of approximately $t = 1.0$ s (second arrow from top) in Figures 8a and b to the primary P-wave reflection from the SAF. The event at 0.5 s (marked by top arrow) is the reflection from a blind fault zone that was intercepted by the SAFOD MH (Solum et al., 2006; Boness and Zoback, 2006). The bottom arrow in Figure 8a indicates a an event with approximately 2.0 s of zero-offset time that whose slope is determined by shear-wave velocity. We interpret this arrival as a pure-mode shear-wave reflection from the SAF. Since only the pseudo-shots in Figures 8a and b present physically meaningful arrivals, we only show migrated images from these two panels.

The migration of the pseudo-shot data was done with the same methodology as in the Sigsbee numerical example. We use shot-profile migration by wavefield extrapolation (Biondi, 2006), where the extrapolation steps are taken in the horizontal coordinate away from the SAFOD PH (Figure 6). Migrated images are shown in Figure 10. The images of the pseudo-shots from deconvolution interferometry (left panels) show

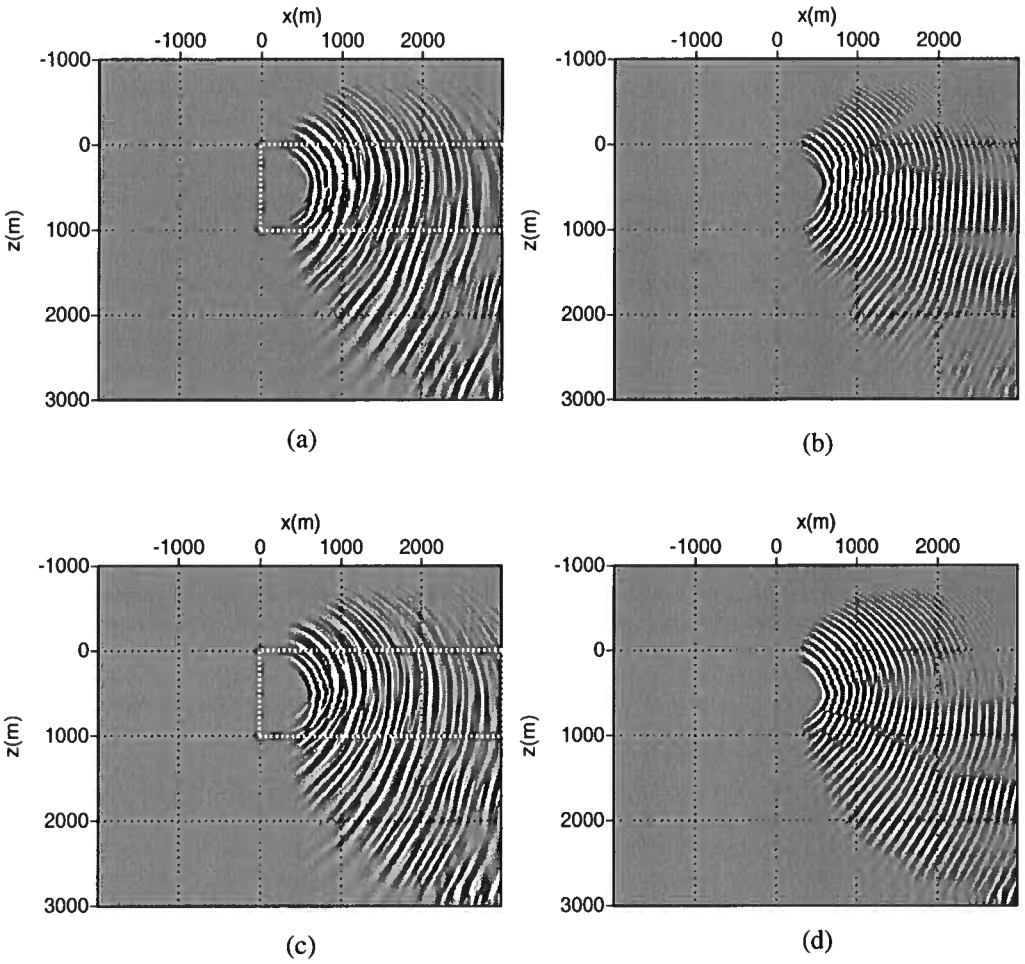

Figure 10. Shot-profile wave-equation images of interferometric shot gathers with a pseudo-source at receiver 26. The left panels are the result migrating pseudo-shot gathers from deconvolution interferometry while the panels on the right result from cross-correlation. The migration of the data in Figure 8a and b gives panels (a) and (c), respectively. Analogously, panels (b) and (d) are obtained from migrating the data in Figures 9a and b. The yellow boxes outline the subsurface area that is physically sampled by P-wave reflections. The data were migrated with the velocity model in Figure 6a.

reflector-like features that cannot be identified on the images from correlation interferometry (right panels). The images from correlation-based pseudo-shots have a narrow-band character that is similar to that of the pseudo-shots themselves, caused by the presence of the autocorrelation of the drill-bit excitation function (Figure 9). This is the same phenomenon we show in the images from the Sigsbee model (Figure 5), with the difference that the Sigsbee images are produced from 100 pseudo-shots. Because the SAFOD images result from migrating a single shot, the reflectors are curved toward the edges of the images (top and bottom of images in Figure 10) due to effect of the migration operator and the relatively small aperture of the receiver array used to reconstruct the data.

The final image from the SAFOD SWD data was obtained by stacking the top images with the bottom ones in Figure 10. We do this with the intention of enhancing the reflectors that are common in both images. The final SAFOD images are shown in Figure 11. Figure 11 only shows the portion of the images that yield physically meaningful reflectors, which is highlighted by the yellow rectangles in Figures 10a and c. The image from deconvolution interferometry (Figure 11a) shows reflectors that cannot be seen in the image from correlation interferometry (Figure 11b). Vasconcelos et al (2007) show that the reflector at $x \approx 2000$ m indicated

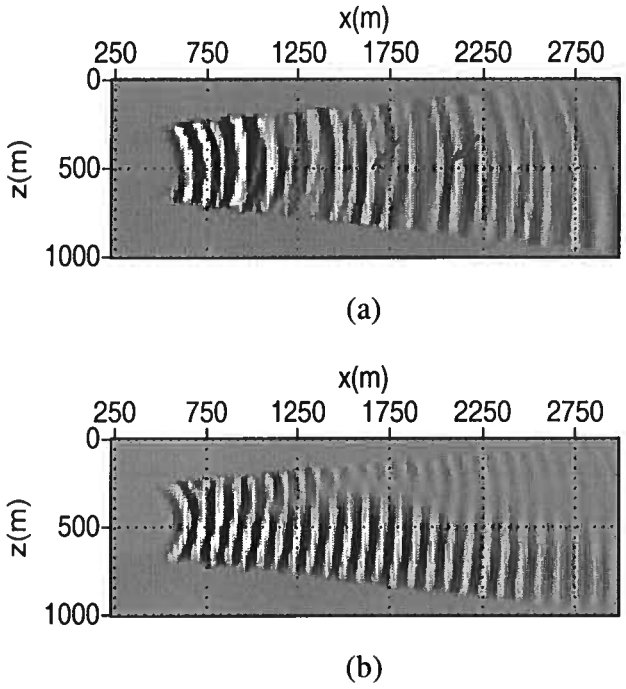

Figure 11. Final images from the interferometry of the SAFOD drill-bit noise recordings. The image in (a) is the result of stacking the images from deconvolution interferometry in Figures 10a and c. The right-hand side arrow shows the location of San Andreas Fault reflector. The other arrow highlights the reflector associated to a blind fault zone at Parkfield. The stack of the images from correlation interferometry in Figures 10b and d gives the image in (b). We muted the portion of the stacked images that is not representative of physical reflectors. The area of the image in (a) and (b) corresponds to the area bounded by yellow boxes in Figure 10.

by the right arrow coincides with the contact of the SAF with metamorphic rocks to the Northeast. The reflector at $x \approx 1600$ m coincides with a possibly active blind fault zone at Parkfield. The observations made by Vasconcelos et al. (2007) are based on the data we present here together with active-shot data measured at the MH and with fault intersection locations from the MH (Solum et al, 2006; Boness and Zoback, 2006).

5 DISCUSSION AND CONCLUSIONS

We present the method of interferometry by deconvolution, described by Vasconcelos and Snieder (2007a), as an alternative to the processing of seismic-while-drilling (SWD) data. In these types of datasets, the signature of the drill-bit source function complicates the recovery of the subsurface response (e.g., Poletto and Miranda, 2004). Most SWD processing methods rely on the so-called pilot sensors to obtain an independent estimate of the drill-bit excitation that is used to remove the drill-bit source function (Rector and Marion, 1991; Haldorsen et al., 1994; Poletto and Miranda, 2004). Here, we review SWD methods based on pilot recordings in the context of seismic interferometry by cross-correlations (e.g., Poletto and Miranda, 2004; Draganov et al., 2006). The method of deconvolution interferometry is capable of recovering the subsurface response from SWD data without the need for an independent estimate of the drill-bit excitation. Additionally, the knowledge about the drill-bit position is not a requirement for the application of interferometry (see also Schuster et al., 2004), as it is for other SWD applications (e.g., Poletto and Miranda, 2004). Interferometry requires, however, that the drill-bit must sample the source stationary points that give rise to the target scattered waves (Vasconcelos and Snieder, 2007a; Snieder et al, 2006).

Extending concepts presented by Vasconcelos and Snieder (2007a), we discuss the application of deconvolution interferometry in elastic media. With physical arguments we state that the interferometric response obtained by the deconvolution of the i-component of a given receiver by the j-component of another receiver results in single-scattered waves that propagate between

these two receivers. These waves are the impulse response from a j-oriented point-force excitation at one of the receivers, recorded by the i-component at the other receiver. Because the deconvolved data satisfies the same wave equation as the original physical experiment, the radiation properties of the drill-bit (Poletto, 2005a) determine the radiation pattern of the pseudo-source synthesized by interferometry. In the case of receivers positioned far from the drill-bit and highly heterogeneous media, deconvolution interferometry can potentially extract a response that is closer to a full elastic response, as discussed by Wapenaar and Fokkema (2006).

Our numerical experiment with the *Sigsbee* model seeks to reproduce a passive subsalt SWD experiment where pilot recordings are absent. Using modeled drill-bit noise (Poletto, 2005a), we produce images of the Sigsbee salt canopy from the receiver array sitting below the salt. The image from deconvolution interferometry provides a reliable representation of the structure in the model because the deconvolution removes the drill-bit excitation function from the data. When distorted by the dominant vibrational modes of the drill-bit source function, the image from correlation interferometry gives a poorer representation of the model structure when compared with the deconvolution image. The choice of the Sigsbee model shows the feasibility of the passive application of drill-bit imaging in subsalt environments. SWD typically is not done in such environments because the wells are deeper than they are onshore, and the transmission through the drill-string is weaker which makes rig pilot records unreliable estimates of the drill-bit excitation (Poletto and Miranda, 2004). Additionally, many subsalt wells are drilled with PDC bits, which radiate less energy than the roller-cone bit (Poletto, 2005a). The signal from PDC bits is thus difficult to measure from the surface or from the sea bottom. This difficulty can be overcome with downhole receiver arrays, as in our example. Although we used a model for a roller-cone bit, we expect results of deconvolution interferometry of noise records from PDC bits (Poletto 2005a) to be similar to ours .

Using field data acquired at the Pilot Hole of the San Andreas Fault Observatory at Depth (SAFOD), we validate the method of deconvolution interferometry in recovering the impulse response between receivers from drill-bit noise records. The SAFOD SWD data are ideal for the application of deconvolution interferometry because pilot recordings are not available. From interferometry by deconvolution, we synthesize scattered waves that propagate from receiver 26 toward the other receivers that are not visible in pseudo-shot gathers from correlation interferometry. Single-scattered P-waves were obtained mostly by the deconvolution of the vertical component of recording of the PH receivers, with the vertical and Northeast components of receiver 26. Shot-profile migration of the interferometric shots generated by deconvolution yield coherent reflectors. From the images presented here together with active-shot data and fault intersection locations from the MH, Vasconcelos et al. (2007a) identified the San Andreas Fault reflector as well as a possibly active blind fault at Parkfield, CA. Their conclusions rely on the processing we describe here, where interferometry by deconvolution plays an important role in imaging the fault reflectors (Vasconcelos and Snieder, 2007a).

More than just an alternative to processing SWD data as it is typically acquired, deconvolution interferometry opens possibilities for using passive measurements of drill-bit or rig noise for imaging. Poletto (2005b) provides a thorough comparison between drill-bit and conventional seismic sources. The fact that seismic interferometry techniques do not require knowledge about the source position allows for pseudo-acquisition geometries that cannot be accomplished by standard SWD experiments. The geometries in of the Sigsbee and SAFOD datasets presented in this paper are examples of non-conventional acquisition that can be treated by interferometric techniques. The use of the free-surface ghosts to reconstruct primary reflections that propagate between receivers (Schuster et al., 2004; Yu et al., 2004) is another example where deconvolution interferometry can also be applied. Interferometry of internal multiples (Vasconcelos et al., 2007b) can potentially be accomplished from SWD as well. The passive imaging from working drill-bits could help in the monitoring of fields in environmentally sensitive areas, where active seismic experiments are compromised. These areas now become more of a concern as the search for unconventional reservoirs increases. One such area is the Tempa Rossa field in Italy (D'Andrea et al., 1993). While active seismic activity in this field is hindered by environmental regulations, its future production is expected to reach 50000 oil barrels per day. Environment-friendly seismic monitoring of oil fields like Tempa Rossa could potentially be accomplished with recordings of the field's drilling activity and with deconvolution interferometry.

6 ACKNOWLEDGEMENTS

This research was financed by the NSF (grant EAS-0609595) and by the sponsors of the Consortium for Seismic Inverse Methods for Complex Structures at the Center for Wave Phenomena. Tom Taylor (Duke University; presently at VS Fusion) provided us with the SAFOD data, and his help was vital in identifying which portion of the data could be used in our processing. Peter Malin (Duke University) gave us the orientations of the PH receivers. The velocity model we used to migrate the data was given to us by Andres Chavarria (P/GSI). The equipment and acquisition of the SAFOD SWD data were donated by Schlumberger. We thank Flavio Poletto for visiting CWP during the 2006 Sponsor Meeting, when he kindly shared his expertise in drill-bit noise

processing with us. I.V. thanks Doug Miller and Jakob Haldorsen (both Schlumberger) for discussions about SWD processing and deconvolution interferometry.

REFERENCES

K. Aki and P.G. Richards. Quantitative seismology. *Freeman Co., San Francisco*, 1980.

P. Amstrong, L. Nutt and R. Minton. Drilling Optimization Using Drill-bit Seismic in the Deepwater Gulf of Mexico. *IADC/SPE Drilling Conference*, IADC/SPE 59222, 2000.

A. Bennia and N.S. Nahman. Deconvolution of causal pulse and transient data. *IEEE Transactions on Instrumentation and Measurement*, 39:933–939, 1990.

N.L. Boness and M.D. Zoback. A multiscale study of the mechanisms controlling shear velocity anisotropy in the San Andreas Fault Observatory at Depth. *Geophysics*, 71:F131–F146, 2006.

J.F. Claerbout. Imaging the Earth's Interior. *Balckwell Publishing*, 1985.

R.W. Clayton and R.A. Wiggins. Source shape estimation and deconvolution of teleseismic body waves. *Geophys. J. R. Astron. Soc.*, 47:151–177, 1976.

S. D'Andrea, R. Pasi, G. Bertozzi and P. Dattilo. Geological model, advanced methods help unlock oil in Italy's Apennines. *Oil and Gas Journal*, 91:53–57, 1993.

D. Draganov, K. Wapenaar and J. Thorbecke. Seismic interferometry: Reconstructing the earths reflection response. *Geophysics*, 71:SI61-SI70, 2006.

J.B.U. Haldorsen, D.E. Miller and J.J. Walsh. Walk-away VSP using drill noise as a source. *Geophysics*, 60:978-997, 1994.

E. Larose, L. Margerin, A. Derode, B. van Tiggelen, M Campillo, N. Shapiro, A. Paul, L. Stehly and M. Tanter. Correlation of random wavefields: An interdisciplinary review. *Geophysics*, 71:SI11-SI21, 2006.

O.I. Lobkis and R.L. Weaver. On the emergence of the Green's function in the correlations of a diffuse field. *J. Acoust. Soc. Am.*, 110:3011-3017, 2001.

M. Malusa, F. Poletto and F. Miranda. Prediction ahead of the bit by using drill-bit pilot signals and reverse vertical seismic profiling (RVSP). *Geophysics*, 67:1169-1176, 2002.

K. Mehta, R. Snieder, R. Calvert and J. Sheiman. Virtual source gathers and attenuation of free-surface multiples using OBC data:implementation issues and a case study. *Soc. Explor. Geophys. Expand. Abs.*, 2669–2673, 2006.

D. Miller, J. Haldorsen and C. Kostov. Methods for deconvolution of unknown source signatures from unknown waveform data. *US Patent*, 4 922 362, 1990.

F. Poletto, F.L. Rocca and L. Bertelli. Drill-bit signal separation for RVSP using statistical independence. *Geophysics*, 65:1654-1659, 2000.

F. Poletto, M. Malusa, F. Miranda and U. Tinivella. Seismic-while-drilling by using dual sensors in drill strings. *Geophysics*,69:1261-1271, 2004.

F. Poletto and F. Miranda. Seismic while drilling, fundamentals of drill-bit seismic for exploration. *Handbook of Geophysical Exploration*, Vol 35, 2004.

F. Poletto. Energy balance of a drill-bit seismic source, part 1: Rotary energy and radiation properties. *Geophysics*, 70:T13-T28, 2005a.

F. Poletto. Energy balance of a drill-bit seismic source, part 2: Drill bit versus conventional seismic sources. *Geophysics*, 70:T29-T44, 2005b.

F. Poletto and L. Petronio. Seismic interferometry with a TBM source of transmitted and reflected waves. *Geophysics*, 71:SI85-SI93, 2006.

M. Porsani and B. Ursin. Mixed-phase deconvolution and wavelet estimation. *The Leading Edge*, 19:76-79, 2000.

M. Porsani and B. Ursin. Direct multichannel predictive deconvolution. *Geophysics*, 72:H11-H27, 2007.

L. Qu, P.S. Routh and K. Ko. Wavelet deconvolution in a periodic setting using cross-validation. *IEEE Signal Processing Letters*, 13:232-235, 2006.

J.W. Rector and B.P. Marion. The use of drill-bit energy as a downhole seismic source. *Geophysics*, 56:628-634, 1991.

J.W. Rector and B.A. Hardage. Radiation pattern and seismic waves generated by a working roller-cone drill bit. *Geophysics*, 57:1319-1333, 1992.

J.W. Rector. Noise characterization and attenuation in drill bit recordings. *J. Seis. Expl.*, 1:379-393, 1992.

G.T. Schuster, F. Followillz, L.J. Katz, J. Yu, and Z. Liu. Autocorrelogram migration: Theory. *Geophysics*, 68:16851694, 2004.

R. Snieder, K. Wapenaar and K. Larner. Spurious multiples in seismic interferometry of primaries. *Geophysics*, 71:SI111-SI124, 2006a.

R. Snieder, J. Sheiman and R. Calvert. Equivalence of the virtual-source method and wave-field deconvolution in seismic interferometry. *Phys. Rev. E*, 73:066620, 2006b.

R. Snieder, K. Wapenaar, and U. Wegler. Unified Green's function retrieval by cross-correlation; connection with energy principles. *Phys. Rev. E.*, 75:036103, 2007.

J.G. Solum, S.H. Hickman, D.A. Lockner, D.E. Moore, B.A. van der Pluijm, A.M. Schleicher and J.P. Evans. Mineralogical characterization of protolith and fault rocks from the SAFOD Main Hole. *Geophys. Res. Let.*, 33:L21314, 2006.

S.T. Taylor, P. Malin, E. Shalev, J.B.U. Haldorsen, R. Coates, and C. Stolte. Drill bit seismic imaging of the San Andreas Fault System at SAFOD. *Soc. of Expl. Geophys. Exp. Abstr.*, 24:2657–2660, 2005.

I. Tsvankin. Seismic Signatures and Analysis of Reflection Data in Anisotropic Media. *Handbook of Geophysical Exploration*, Vol 29, 2001.

I. Vasconcelos and R. Snieder. Interferometry by deconvolution: theory and numerical examples. *Phys. Rev. Lett.*, in preparation, 2007a.

I. Vasconcelos and R. Snieder. On representation theorems and seismic interferometry in perturbed media. *Phys. Rev. Lett.*, in preparation, 2007b.

I. Vasconcelos, R. Snieder, S.T. Taylor, P. Sava, J.A. Chavarria and P. Malin. High Resolution Imaging of the San Andreas Fault at Depth. *Science*, submitted, 2007a.

I. Vasconcelos, R. Snieder and B. Hornby. Imaging with internal multiples from subsalt VSP data: examples of target-oriented interferometry. *Geophysics*, in preparation, 2007b.

K. Wapenaar. Retrieving the elastodynamic Green's function of an arbitrary inhomogeneous medium by cross correlation. *Phys. Rev. Lett.*, 93:254301, 2004.

K. Wapenaar, J. Thorbecke, and D. Dragonov. Relations

between reflection and transmission responses of three-dimensional inhomogeneous media. *Geophys. J. Int.*, 156:179–194, 2004.

K. Wapenaar. Green's function retrieval by cross-correlation in case of one-sided illumination. *Geophys. Res. Lett.*, 33:L19304, 2006.

K. Wapenaar, E. Slob, and R. Snieder. Unified Green's Function Retrieval by Cross Correlation. *Phys. Rev. E.*, 97:234301, 2006.

K. Wapenaar and J. Fokkema. Green's function representations for seismic interferometry. *Geophysics*, 71:SI133-SI146, 2006.

G.M. Webster. Deconvolution. *Geophysics reprint series*, Vol. 1, 1978.

A.B. Weglein, F.V. Araújo, P.M. Carvalho, R.H. Stolt, K.H. Matson, R.T. Coates, D. Corrigan, D.J. Foster, S.A. Shaw, and H. Zhang. Inverse scattering series and seismic exploration. *Inverse Problems*, 19:R27–R83, 2003.

J. Yu, L.J. Katz, F. Followill, H. Sun and G.T. Schuster. Autocorrelogram migration: IVSPWD test. *Geophysics*, 68:297307, 2004.

APPENDIX A: SHORT NOTE ON DECONVOLUTION

Our numerical application of deconvolution is based on the so-called *water level* deconvolution (Clayton and Wiggins, 1976), given by

$$D_{AB} = \frac{u(\mathbf{r}_A,\mathbf{s})}{u(\mathbf{r}_B,\mathbf{s})} = \frac{u(\mathbf{r}_A,\mathbf{s})\,u^*(\mathbf{r}_B,\mathbf{s})}{|u(\mathbf{r}_B,\mathbf{s})|^2 + \epsilon\langle|u(\mathbf{r}_B,\mathbf{s})|^2\rangle}, \tag{A1}$$

where $\langle|u(\mathbf{r}_B,\mathbf{s})|^2\rangle$ is the an average of the power spectrum of the data measured at $\mathbf{r}_B$. The factor ϵ is a free-parameter that we choose by visually inspecting the output of the deconvolution in equation A1. When ϵ is too large, the denominator becomes a constant and the result of the deconvolution approximates the result of cross-correlation (equation 2). When ϵ is too small the deconvolution becomes unstable. An optimal value of ϵ results in the desired deconvolved trace with weak random noise associated to the water level regularization (Clayton and Wiggins, 1976).

There are other deconvolution approaches that yield better results than the water-level deconvolution method. For deconvolution references in the exploration geophysics literature, we refer to the article collection edited by Webster (1981) and to the work of Porsani and Ursin (Porsani and Ursin, 2000; Porsani and Ursin, 2007). In the signal processing field, the work of Bennia and Nahman (1996) and Qu et al. (2006) are examples of deconvolution methods that are relevant to SWD processing.

Broadside imaging of the San Andreas fault system at depth

I. Vasconcelos, R. Snieder*, S. T. Taylor†, J. A. Chavarria‡, & P. Sava*

* *Center for Wave Phenomena, Department of Geophysics, Colorado School of Mines, Golden, CO 80401, USA*
† *Earth and Ocean Sciences Division, Duke University, Durham, NC 27708, USA*
‡ *Paulsson Geophysical Services, Inc., Brea, CA 92821*

ABSTRACT

The San Andreas Fault Observatory at Depth provides perhaps the most comprehensive set of data on the structure and dynamics of the San Andreas fault. We use two independent experiments recorded by the seismometer arrays of the SAFOD Pilot and Main Holes to resolve the localized structure of the San Andreas fault zone and of an intermediate fault zone at depth. From Pilot Hole recordings of the drilling noise coming from the Main Hole, we reconstruct the waves that propagate between the Pilot Hole sensors and use them to image the fault zone structure. The use of correlated drilling noise leads to a high-resolution image of a major transform fault zone. Another independent image is generated from the detonation of a surface explosive charge recorded at a large 178-sensor array placed in the Main Hole. The images reveal the San Andreas fault as well as an active blind fault zone that could potentially rupture. This is confirmed by two independent methods. The structure and the activity of the imaged faults is of critical importance to understanding the current stress state and activity of the San Andreas fault system.

Key words: San Andreas Fault, VSP, seismic-while-drilling, deconvolution interferometry, reverse-time migration

1 THE SAFOD PROJECT

The San Andreas Fault Observatory at Depth (SAFOD) was conceived to closely study and monitor the earthquake dynamics and structure of the San Andreas Fault (SAF) at Parkfield, CA (http://www.icdp-online.de/sites/sanandreas/index/index.html). Characterizing the structure and dynamics of the SAF strike-slip system is crucial for understanding the geodynamics of transform plate boundaries and their associated seismicity. In particular, the SAF at Parkfield has historically been seismically active, with seven catalogued earthquakes of magnitude six approximately (Bakun and McEvilly, 1984; Roeloffs and Langbein, 1994); the latest one occurred in September 2004 (Kerr, 2006).

Consisting of a vertical borehole, the Pilot Hole (PH), and of a deviated well that intersects the SAF, the Main Hole (MH), SAFOD is designed to sample and monitor the SAF system from within the subsurface at Parkfield. Together with surface observations, data from SAFOD already contributed greatly to the understanding of the SAF system at Parkfield. Figure 1a is a scaled schematic cartoon that summarizes and connects results from several publications that analyze data from the SAFOD site. Much of the information on the surface geology and on the basement and sedimentary structures at Parkfield comes from geologic mapping (Rymer et al., 2003) and from surface refraction (Catchings et al., 2003) and reflection (Hole et al., 2001; Catchings et al., 2003) seismic data. The lateral delineation of the Salinian granite to the SW of the SAF has also been inferred from magnetotelluric (Unsworth et al., 2000; Unsworth and Bedrosian, 2004) measurements and from joint inversion of gravity and surface seismic data (Figure 1b; Roecker et al., 2004; and Thurber et al., 2004).

Analysis of PH rock samples (Solum et al., 2004) and of their in-situ physical properties (Boness and Zoback, 2004) helped determine the lithology and the stress state around the PH. Likewise, recent studies of rock samples from drilling (Solum et al., 2006) and well-logs (Boness and Zoback, 2006) from the MH have shed light on the subsurface geology along the SAFOD MH. It was not until 2006 that the SAFOD MH first intersected the SAF (Figure 1a), and the upcoming coring of the SAF system during the Phase 3 drilling of the MH (summer 2007) promises to bring important information on the internal composition of the SAF.

Previous to the drilling of the SAFOD MH, microseismic events along with surface active-shots recorded at the PH seismometer array were used to make some of the first images of the SAF at depth (Chavarria et al., 2003) which also contributed much to our understanding of the subsurface geology at Parkfield (Figure 1a). As a continuation of the subsurface imaging at Parkfield, we use drilling noise recorded at the PH and an active-shot experiment recorded at the SAFOD MH to obtain high-resolution images of the SAF system between depths of 0 to approximately 1.5 km (from sea level; this corresponds to approximately 0.6 to 2.1 km from the surface). These images help to resolve the wave-scattering structures associated to the SAF as well as at least one other heavily faulted zone between the SAFOD drilling site and the SAF. Images such as the ones we present here are critical for the development of detailed models of the SAF plate and earthquake dynamics.

2 IMAGING THE SAF FROM PASSIVE AND ACTIVE SEISMIC DATA

The SAFOD data we use were acquired in two experiments. The first experiment was carried out in July 2004, when the SAFOD PH receiver array (Figure 1b) was switched on to constantly monitor the drilling noise during the early stages of the drilling of the SAFOD MH. We used the drill-bit noise recordings of the SAFOD PH array to create an image of the SAF. In a second independent experiment, conducted in 2005, a large 178-receiver array was placed in the SAFOD MH (Figure 1b) to record the active shooting of an 80-pound explosive charge placed at the surface near the SAFOD MH. We also used this shot record to image the SAF. These two experiments differ not only on the geometry of the data acquisition (i.e., source and receiver positioning), but also in the physical character of the excitation that generates the recorded waves. To account for the differences between the PH and the MH data, we applied different processing to each dataset and to subsequently produce the images. Figure 2 provides schematic representations of the data acquisition geometry for the PH drill-bit noise recordings and for the MH active-shot experiment.

To create an image of the SAF zone from the drill-bit noise records we rely on the concept of seismic interferometry (Curtis et al., 2006; Larose et al., 2006). Interferometry recovers the response between any two receivers in an arbitrarily heterogeneous and anisotropic medium as if a source was placed at one of the receiver locations(Lobkis and Weaver, 2001; Snieder et al., 2006). We only briefly highlight the issues of interferometry that are of particular concern to the processing of the SAFOD PH drilling noise records.

Typically, interferometry makes use of cross-correlations between recorded data to recover waves propagating between receivers (Lobkis and Weaver, 2001). By doing so, the recovered receiver response includes an average of the power spectra of the excitations(Lobkis and Weaver, 2001, Snieder et al., 2006). Removing the contribution of the source power spectrum is an issue when recovering signals from drill-bit noise because in this case the wave-generation mechanism is constantly active, and the spectrum is heavily dominated by specific vibration modes associated to the drilling process (Poletto and Miranda, 2004). An example of this behavior from SAFOD PH-array records can be found in Figure 4a.

It is possible, however, to remove the drill-bit source signature from drilling noise records (Poletto and Miranda, 2004). The standard industry practice is to estimate the drill-bit signature by placing accelerometers on the drill-stem (Poletto and Miranda, 2004; Rector and Marion, 1991). This estimate is then used to extract the drill-bit noise signature from the cross-correlations of the recorded data, leaving only the approximate impulse response of the Earth (Lobkis and Weaver, 2001; Poletto and Miranda, 2004). Following this accelerometer-based approach, drill-bit imaging has been previously applied to surface recordings of MH drilling noise at Parkfield (Taylor et al., 2005). In our case, such accelerometer recordings are not available. As an alternative to interferometry by cross-correlations, we used an interferometry technique based on deconvolutions (Vasconcelos and Snieder, 2007). This technique synthesizes the response between receivers from incoherent excitations as if one of the receivers acted as a pseudo-source, while canceling the effect of the drill-bit source signature without the need for drill-stem accelerometers.

In Figure 3a we show the result from processing approximately 17 hours of drilling noise records into a shot record with a pseudo-source at receiver PH-26. With the pseudo-source centered at 0 s, PH-26 acts as the pseudo-shot responsible for the excitation of waves (Vasconcelos and Snieder, 2007). Figure 3a shows the direct wave that propagates from receiver PH-26 and is recorded at the other receivers. The reflection events highlighted in Figure 3a are caused by faults in the SAF system. The data in Figure 3a represents waves excited by a vertically-oriented force (see Figure 4). In addition, we are also able to recover the excitation at receiver PH-26

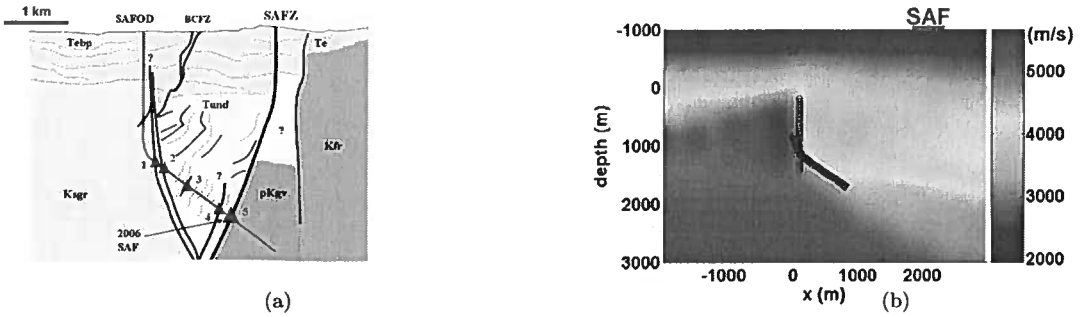

Figure 1. Panel (a) shows our current knowledge of the structure of the San Andreas fault system at Parkfield, CA. The main geologic formations are indicated by different colors and by their corresponding acronyms, these are: the Tertiary Ethegoin (Te), Tertiary Ethegoin-Big Pappa (Tebp), Tertiary undifferentiated (Tund), Cretaceous Franciscan rocks (Kfr), Cretaceous Salinian Granite (Ksgr), and the pre-Cretaceous Great Valley (pKgv). The SAFOD main-hole (MH) is indicated by the blue solid line. Black solid lines in (a) represent faults. BCFZ refers to the Buzzard Canyon Fault zone. The areas where the finer-scale structure of the SAF system were unknown are indicated by question marks. The red triangles, numbered 1 through 5, show approximate locations of intersections of the MH with major zones of faulting (Solum et al., 2006). Triangle number 5 represents the point where the MH penetrated the SAF in 2006. Panel (b) shows the large-scale structure of the P-wave velocity field (velocities are colorcoded) that approximately corresponds to the schematic representation in (a). The circles in (b) indicate the location of the sensors of the SAFOD pilot-hole array used here for the recording of drilling noise. The SAFOD MH array, used in the active-shot experiment, is indicated by the triangles. The location of the active shot is depicted by the star. Depth is with respect to sea level, the altitude at SAFOD is of approximately −660 m.

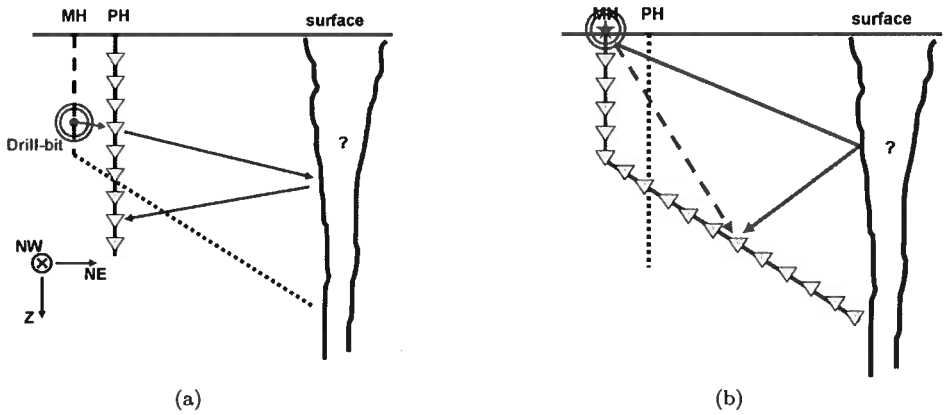

Figure 2. Schematic acquisition geometries of SAFOD data. Receivers are indicated by the light-blue triangles. The structures outlined by black solid lines to the right-hand side of the figure represent a target fault. (a) shows the acquisition geometry of the downhole seismic-while-drilling (SWD) dataset. It consists of multiple 60 second-long recordings of drill-bit noise excited at different depths, recorded at 32 3-component receivers in the PH. As indicated by (a), receivers are oriented in the Z-(or downward vertical), NE- and NW-directions. (a) also shows a schematic stationary path between the drill-bit and two receivers. Interferometry recovers only the portion of the propagation path represented by black arrows in (a). The active-shot geometry in (b) is comprised of 178 3-component receivers placed in the MH. The dashed red arrow in (b) represents all waves that propagate towards the NE (right-hand side of the figure), while the solid red line represents all waves going toward SW (left-hand side of (b)). The inclination of the deviated portion of the MH is of about 45° with respect to the vertical. The receiver components of the SAFOD MH array are co-oriented with those of the PH array, whose orientations are shown in (a).

associated to a Northeast-oriented force (see Figure 4c). The SAFOD interferometric image we will discuss here is a product from imaging the pseudo-shots at PH-26 excited by forces oriented both in the vertical and in the Northeast (NE) directions.

Unfortunately, out of almost two months of recording drilling noise at the PH array, only about a day and a half of the data is useable for interferometry purposes due to data acquisition problems. Within this time window, the drill-bit is closest to receiver PH-26 (the dis-

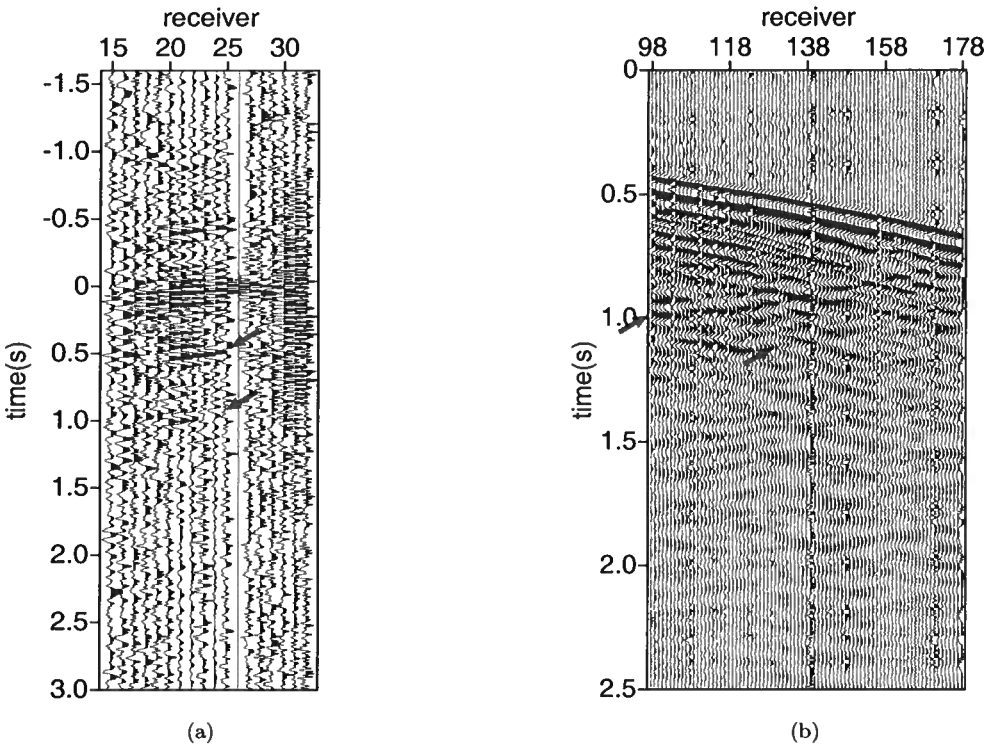

(a) (b)

Figure 3. (a) Vertical component of the interferometric shot gather for a pseudo-shot position at pilot-hole receiver PH-26. Red arrows indicate reflections of interest. The reflection event that arrives at approximately 1.0 s at receiver PH-24 is interpreted to correspond to a P-wave reflection from the SAF zone. Due to the noise levels, only a subset of the 32 receivers of the PH array is sensitive to the incoming signals from the SAF zone. (b) Data recorded by the vertical component of motion in the SAFOD MH array from the active-shot experiment. The red arrows indicate two left-sloping events that are associated to P-wave reflections from faults within the SAF system.

tance between the MH and PH at that depth is of only a few meters). It is at this drill-bit position that we find the most prominent contribution from the waves excited by the drill-bit for the reconstruction of the waves that propagate between receiver PH-26 and the remaining receivers. We refer to this point as a stationary position for the drill-bit source (Snieder et al., 2006). To recover signals propagating between receivers, it is necessary to have physical sources at the stationary points that link a pair of receivers to a target reflector (Snieder et al., 2006). The only drill-bit stationary point sampled within the good-quality PH records recovers waves that emanate from receiver PH-26. This restriction limits the area of the SAF zone from which we can produce a physically meaningful image to the area shown in Figure 6a.

The shot gather from the SAFOD MH active-shot experiment (Figure 3b) shows a reflection as a left-sloping event arriving at main-hole receiver MH-98 at approximately 1.0 s (indicated by the top-most arrow). Another weaker left-sloping event that arrives at approximately 1.2 s at receiver MH-98 (lower-most arrow) is associated with a P-wave reflection from the SAF zone. Since the receivers MH-98 to MH-178 are in the deviated, deeper-most portion of the SAFOD MH (see Figure 1b), right-sloping events are mostly associated with right-going waves, whereas left-sloping events are associated with left-going waves (see also Figure 2b). This observation only holds for a subset of the receivers of the large 178-receiver MH array: the ones which lie in the deviated portion of the MH. These would be receivers MH-98 through MH-178 (Figure 3b), whose locations are shown in Figure 1b. For the purpose of imaging the SAF system from the MH array, it is important to discern between right- and left-going waves in the data because fault reflection information for this acquisition geometry is predominantly contained in left-going waves. With frequency-wavenumber filtering (Biondi, 2006), we extract only the left-sloping events from Figure 3b. We use only these events to image the SAF zone.

The process of mapping data such as in Figure 3

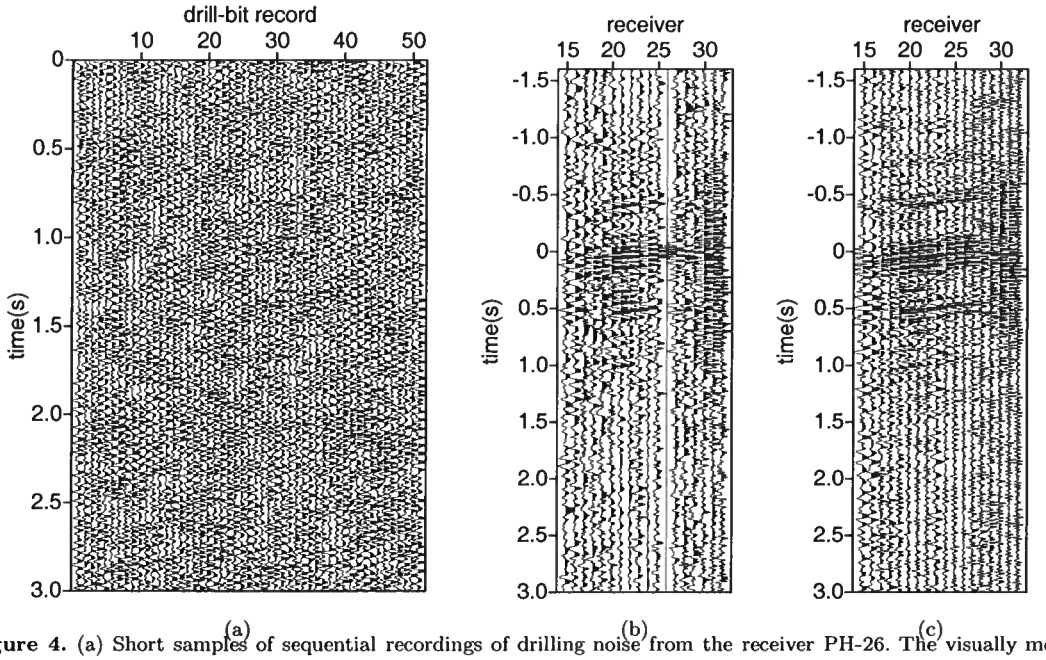

Figure 4. (a) Short samples of sequential recordings of drilling noise from the receiver PH-26. The visually monochromatic character of the records is due to drilling vibrational modes. (b) Vertical component of the interferometric shot gather for a pseudo-shot position at pilot-hole receiver PH-26. The recording at (b) represents waves excited by a vertical point-force. (c) is also the vertical component for a pseudo-shot at PH-26, but unlike the wavefield in (b), it represents waves excited by a point-force in the NE-direction. The complicated character of the drilling noise in (a) is attenuated by the interferometry procedure that produces the data in (b) and in (c). Note that receiver PH-32 is the shallowest receiver in the SAFOD PH array (see Figure 1b in main text).

into a subsurface image (Figure 6) is what we refer to as *imaging* or *migration*. Imaging typically requires a velocity model of the subsurface; the one we use is shown in Figure 1b. This model was estimated from surface seismic tomography (Thurber et al., 2004). We do the imaging of the PH and MH data (Figure 3) with two different methodologies. For imaging from the PH data we use the technique of shot-profile migration by wavefield extrapolation (Biondi, 2006). The wavefield extrapolation is done by the split-step fourier phase-shift plus interpolation method. The MH active-shot data in Figure 3b is imaged by *reverse-time migration* (Biondi, 2006).

3 HIGH-RESOLUTION IMAGES AND THE SAF

The images from the SAFOD PH and MH arrays are shown in Figures 6a and b (also in Figures S3a and b). The interferometric image from PH array (Figures 6a and S3a) provides a different area of "illumination" of the subsurface than the active-shot image from the MH array (Figures 6b and S3b). This is a consequence of the differences in the acquisition geometry of these two experiments. The images displaying all subsurface positions corresponding to the velocity model in Figure 1b are shown in the support Figure 5. A numerical model was build for the MH active-shot data to aid us in understanding what is the subsurface area that could be illuminated by the active-shot experiments, as well as what would be the character of image artifacts caused by waves diffracted by the Salinian granite. From the portion of the synthetic image that showed physically meaningful reflectors we chose the area of illumination of the SAFOD MH image in Figure 6b. The support Figure 7 shows the results from the numerical modeling of the SAFOD MH active-shot data.

Since both images are built from single-shot data (a pseudo-shot in the PH interferometric data and the active-shot in the MH data), they are prone to artifacts associated with the limited illumination (Biondi, 2006). Additionally, the method of interferometry by deconvolutions may produce image artifacts (Vasconcelos and Snieder, 2007). It is thus critical to establish which reflectors in the images in Figure 6 (and in Figure 5) pertain to actual faults or interfaces in the subsurface.

We rely on two independent criteria to gain insight into which reflectors in Figure 6 (and in Figure 5) represent real faults and/or interfaces. The first criterion is based on the consistency of events between different images. Note that all of the available images were gener-

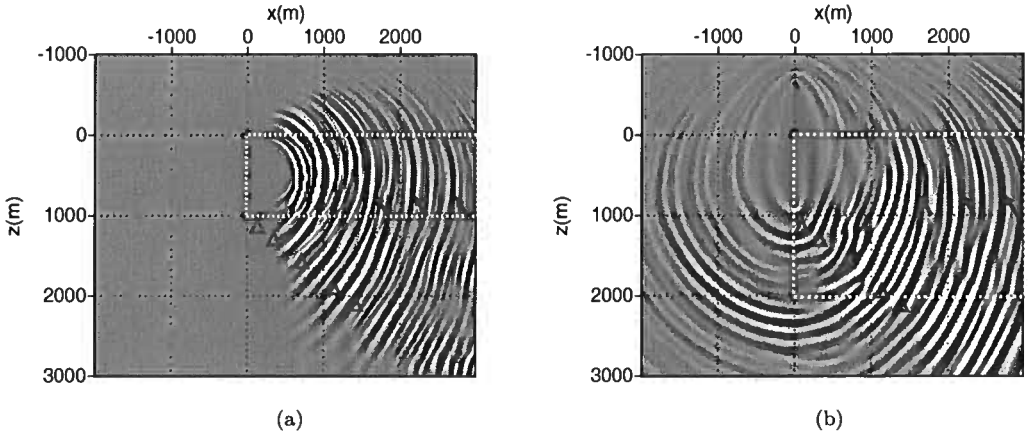

Figure 5. (a) Image obtained from stacking the results of migrating the SAFOD interferometric shot gathers in Figures S4c and d. After migrating only the left-going waves from the SAFOD MH active-shot data (Figure 2b in main text), we obtain the image in (b). The red arrows point to features that are common to both images. These features are the same as indicated by the red arrows and numbers 1 through 3 in main-text Figure 3. The dashed yellow boxes in (a) and in (b) highlight the portions of the images that are shown in main-text Figures 3a and 3b, respectively. Both yellow boxes in fact represent the subsurface area that is physically sampled by P-wave reflections, which in turn depends on the acquisition geometry of each experiment (see Figure S2). The red triangles show the approximate locations where the SAFOD MH intersected major fault zones (see main text Figure 1b). Distances in the x-axis in (a) and (b) are with respect to the location of the SAFOD drill site at the surface. The surface trace of the SAFz is at approximately $x = 2000$ m.

ated from independent experiments. In our case, on one hand we have the drilling noise recordings at the PH array, and on the other hand we have the the active-shot MH data. The images from Chavarria et al. (2003) (Figure 6) come from PH recordings of both surface active shots and microseismicity from the SAF. Not only were the data in these three experiments different, but also the corresponding images were generated by distinct methodologies. Consequently, reflectors that are consistent in two or more images are likely to be representative of actual subsurface structures.

The second criterion for interpreting reflectors in Figure 6 is the correlation between the location of fault zone intersections at the SAFOD main-hole (Solume et al., 2006) and the position of reflectors which are consistent in two or more images. The position of the five main fault zones intersected by the MH are shown schematically in Figure 1a and are superposed on the full images from the SAFOD PH and MH arrays in the support Figure 5. The comparison between MH fault intersections (Solum et al., 2006;Boness and Zoback, 2006) and reflectors in the images (Figure 5) is not always straight forward because the subsurface area illuminated by the images does not coincide with the MH well-path. Despite this difficulty, we provide our interpretation of the correlation between the MH fault intersections and imaged reflectors based on the overlay of these data (Figure 5) and on our current conceptual geologic model of the subsurface at SAFOD (Figure 1a).

In the interferometric image from the PH drilling noise records (Figure 6a) we highlight four distinct reflection events. The events 1 through 3 coincide both in the interferometric and active-shot images (Figures 6a and b, respectively; see support also Figure 5). Reflector 2 (Figure 6) is associated with the SAF, because its lateral position coincides with the lateral position of the surface trace of the SAF (marked by a vertical solid line at 0 km in the background images in Figure 6). In both the PH and MH images, the position of reflector 2 is consistent with the scattering zone associated with the SAF zone from Chavarria et al. (2003). Even though our images of the SAF (reflector 2, Figure 6) do not illuminate the fault all the way to its point of intersection with the SAFOD MH, the change in dip of the SAF in the active-shot image at approximately 1100 m depth is consistent with the intersection of the MH with fault zone 4 (Figures 1a and S3b). Since the anomaly that represents the SAF in the image by Chavarria et al. (2003) is caused by direct-wave energy coming from microseismicity within the SAF, the relative positioning between the SAF reflector in the MH active-shot image and the corresponding reflector in the background image suggests that reflector 2 may be due to P-wave energy scattered at the contact of the Franciscan rocks to the NE with the SAF zone to the SW (Solum et al., 2006; Boness and Zoback, 2006). The PH interferometric and MH active-shot images resolve structures larger than approximately 75 to 100 m in size, presenting higher resolution when compared to the previous images of the SAF at Parkfield (Hole et al., 2003; Chavarria et al.,

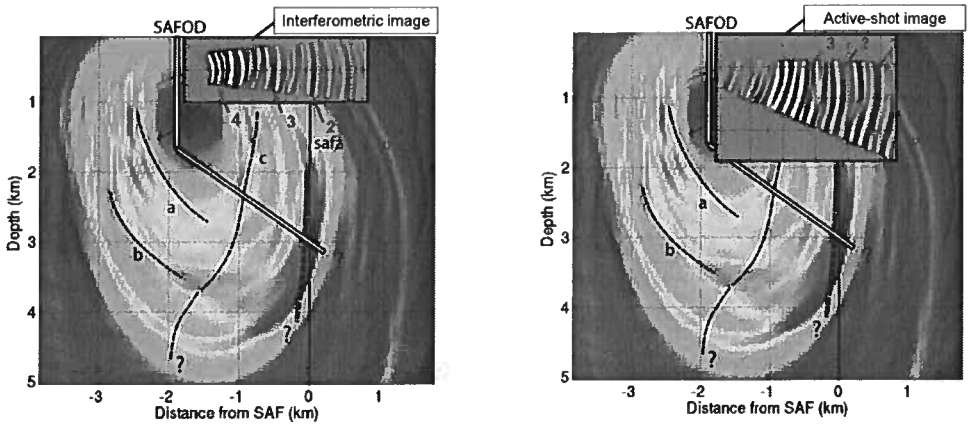

(a) (b)

Figure 6. Images from the drill-bit noise recordings and from the active-shot experiment (in grey-scale, outlined by black-boxes). These images are overlayed on the result obtained from Chavarria et al. (2003). The overlay in (a) is the interferometric image from the SAFOD PH array, compiled after synthesizing drilling noise records into a pseudo-shot at the location of receiver PH-26. (b) shows an overlay of the image obtained from reverse-time imaging of the active-shot recorded at the SAFOD MH. The arrows mark the most prominent reflectors in the images. The reflectors numbered 1 through 3 coincide in both images. Reflectors 2 and 3, and possibly 4 are associated with fault zones. The SAF zone is visible at reflector 2 in both images. The location of the SAFOD MH in the background color images is schematic, since the MH was drilled after the work by Chavarria et al. (2003) was published. See also Figures S3a and S3b for the full images from the drill-bit noise recordings and active-shot data.

2003). The geometry of our experiments (especially of the PH drill-bit records) is ideal for the broadside imaging of the SAF, complementing the previous Parkfield experiments (Hole et al., 2003; Chavarria et al., 2003).

Although the reflector 1 is consistent between the PH interferometric image and the MH active-shot image, we do not associate it to any known faults. The reason for this is that there is no surface trace of a fault at the location of reflector 1; nor has a major fault zone yet been intersected by the SAFOD MH after the SAF. If reflector 1 is indeed an artifact produced from the imaging procedures applied to both the PH and the MH data, it was not reproduced by the numerical modeling of the SAFOD MH data. Since the modeling in Figure 7 was acoustic (accounting only for P-wave propagation), reflector 1 could be due to erroneous imaging of recorded P-to-S converted waves. Note that our imaging procedures also assume that the medium is acoustic, so any recorded converted waves will be imaged as artifact reflectors placed farther than their P-wave counterparts. This, we believe, is what happens to reflector 1; a P-to-S converted reflection perhaps related to the SAF P-wave reflector at reflector 2 (Figure 6).

The fact that reflector 4 can only be seen in the PH interferometric image is not necessarily inconsistent with the MH image because even if the reflector pertained to a physical event, its location makes it mostly invisible for the MH active-shot image (the reflector is located between the shot and most of the receivers in the MH array). The location of reflector 4 in Figure 5a suggests a possible correspondence with the SAFOD MH intersection with fault zone number 2 (Figures 1a and S3a). If such a correspondence is true, then reflector 4 is likely to represent the contrast between the Salinian granite and the sediments, which is bordered by fault zone 2 (Figure 1a).

Reflector 3 in Figure 6 is also associated with a fault zone. It is present in both the PH interferometric and in the MH active shot images, and its location coincides with the scattered energy observed by Chavarria et al. (2003) in their P-wave migration images (see Figure 3C and 3B of their paper). We associate this reflector with fault intersection number 4 (Figure 1a) in the SAFOD MH array (Solum et al., 2006; Boness and Zoback, 2006). The location of the fault intersection is close to the portion of the fault illuminated by the MH active-shot image (see Figure 5b). Also, the fault image dips in the SW direction towards the point of intersection between the SAFOD MH and fault number 4 (Figures 1a and S3b). The location of this fault zone at reflector 3 coincides with a well-resolved localized cluster of microseismic events detected both by surface records

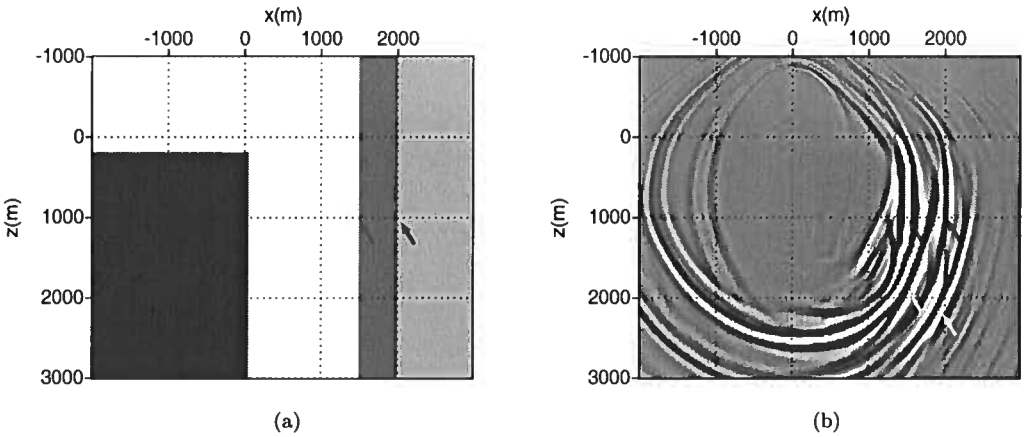

Figure 7. Acoustic numerical modeling of the SAFOD MH active-shot data. (a) shows the structure of the reflectivity model used to generate the synthetic data. The velocity model used is the same as the one used for imaging (Figure 1b in main text). The black block in the reflectivity model in (a) represents the Salinian granite (see Figure 1a in main text), whereas the grey structures to the left of the model generate two vertical fault-like features. After applying the same imaging procedure as for the field SAFOD MH data (Figure 5), we end up with the image in (b). The red arrows mark the position of the target reflectors both in the model (a) and in the image (b). The reflections of waves generated by the diffraction of energy in the corner of the granite block appear as image artifacts (marked by yellow arrows). Without the numerical model, these artifacts could potentially be misinterpreted as dipping fault structures. The objective of the numerical modeling is not to closely replicate all features of the data (Figure 2b in main text). Instead, the objective of the model is two-fold: it helps us understand which portion of the subsurface is "illuminated" by P-wave reflections in the active-shot experiment, and it gives us an idea of how P-waves that are diffracted and/or guided by the granite structure may appear in the image.

(Nadeau et al., 2004) and by the PH array (Oye et al., 2004). The images in Figure 6 show considerably higher resolution than the previous images from Chavarria et al. (2003) in imaging the intermediate fault zone corresponding to fault number 4 (Figure 1a). The imaging of this intermediate fault zone (and its subsequent intersection at the SAFOD PH) is important to the understanding of the structure of the SAF system, especially because there is no trace of this fault system at the surface. Since it is a blind fault (Yeats and Hutfile, 1995; Talebian et al., 2004), determining the activity status of fault 3 is critical in assessing its seismogenic risk. The existence of this feature interpreted from two independent observations provides the basis for a better fault zone understanding and its hazard assessment. Unknown blind faults have been the cause of major fatal earthquakes, such as the 1994 Northridge earthquake (Yeats and Hutfile, 1995) and the 2003 Bam earthquake in Iran (Talebian et al., 2004).

The dip of the SAF reflector and of the intermediate fault reflector support the interpretation of the SAF system being structurally characterized by a flower structure (Figure 1a). Previous surface seismic profiling also suggested the presence of intermediate fault zones (Hole et al., 2001) such as the one confirmed here. It remains to be understood whether this intermediate faulting is associated with the same flower structure as the SAF, potentially representing an earlier trace or an active branch of the SAF, or if these secondary faults belong to a separate flower structure (Chavarria et al., 2003). According to Solum et al. (2006), well casing deformation was only observed at fault intersection 5 (associated to the SAF, Figure 1a). The other four fault zones showed no signs of fault activity since so far there was no casing deformation associated to them. If the imaged intermediate fault zone (reflector 3, Figure 6) is indeed an inactive fault zone, it might well represent an earlier trace of the SAF. On the other hand, the clusters of microseismic activity previously observed (Nadeau et al., 2004; Oye et al., 2004) are likely associated to the imaged blind fault zone (reflector 3, Figure 6), which suggests that this fault zone is likely to be an active part of the current SAF system.

Other important factors for understanding fault activity and seismogenic potential are fault zone mineralogy, fluid content and pore-pressure. It has been previously suggested that there may be high-pressured fluids within the SAF zone at Parkfield (Unsworth et al., 2000; Unsworth and Bedrosian, 2004; Chavarria et al., 2003). Both the SAF reflector and reflector 3 in Figure 6 are consistent with the lateral positioning of the known low resistivity anomaly inferred by magnetotelluric soundings at Parkfield (Unsworth et al., 2000; Unsworth and Bedrosian, 2004). Indeed, the analysis of the inferred fault material from the SAF and from the imaged intermediate fault zone (Solum et al., 2006) shows a high

concentration of clay minerals, which are typically associated with low resistivity materials and with fluid-rich rocks. Furthermore, the analysis of rocks from the deeper SAF Solum et al. (2006) also showed the presence of serpentine, a mineral that could potentially generate fluid seals within the SAF leading to the creation of high-pressured fluid pockets inside the fault (Unsworth et al., 2000; Unsworth and Bedrosian, 2004). From the available seismic data, it is not yet possible to determine if the observed fault reflections are caused by fault-trapped fluids, by the contrast in material properties across the faults (Solum et al., 2006) or by a combination of these factors.

Nonetheless, the understanding of the structure of the SAF system has gained much from the imaging from the PH drill-bit noise and the MH active-shot experiments conducted at SAFOD. Our current images from these experiments not only provide better resolution in the structural definition of the faults within the SAF, but were also played a decisive role in the characterization of a blind fault zone between the SAFOD PH and the SAF. The high-resolution structural characterization of the SAF system is critical to the understanding of fault-growth and earthquake mechanics at Parkfield. The results we present here prove that imaging from noise can be crucial for illuminating complex fault zones in areas where observations from active experiments are insufficient. With the help of further continuous coring and analysis of fault material from the SAFOD MH Phase 3 drilling (to be conducted Summer 2007), the nature of the observed fault reflections will be perhaps better understood.

4 ACKNOWLEDGEMENTS

This research was supported through grant EAS-0609595 of the NSF. We also acknowledge the partial support of the sponsors of the Seismic Inverse Methods for Complex Structures consortium at the Center for Wave Phenomena, Colorado School of Mines. Schlumberger donated the equipment and funds for the acquisition of PH drill-bit data. Paulsson Geophysical Services, Inc. (P/GSI), acquired and donated the MH active-shot data. We thank Peter Malin (Duke University) for intermediating the data exchange, and for providing the orientation of the Pilot Hole receivers.

REFERENCES

W.H. Bakun and T.V. McEvilly. Recurrence models and Parkfield, California earthquakes. *J. Geoph. Res.*, 89:3051–3058, 1984.

B. Biondi. 3D Seismic Imaging. *Investigations in Geophysics, 14, Society of Exploration Geophysicists*, 240 pages, 2006.

N.L. Boness and M.D. Zoback. Stress-induced seismic velocity anisotropy and physical properties in the SAFOD Pilot Hole in Parkfield, CA. *Geophys. Res. Let.*, 31:L15S17, 2004.

N.L. Boness and M.D. Zoback. A multiscale study of the mechanisms controlling shear velocity anisotropy in the San Andreas Fault Observatory at Depth. *Geophysics*, 71:F131–F146, 2006.

R.D. Catchings, M.R. Goldman, M.J. Rymer, G. Gandhok, and G.S. Fuis. Data Report for the Main Line of the PSINE Seismic Survey Across the San Andreas Fault and the SAFOD Site Near Parkfield, California. *USGS Open-file Report*, 03-04:30, 2003.

R.D. Catchings, M.J. Rymer, and M.R. Goldman. Subsurface Structure of the San Andreas Fault Zone Near SAFOD From High-resolution Seismic Images. *Geophys. Res. Abs.*, 5:07861, 2003.

J.A. Chavarria, P. Malin, R.D. Catchings and E. Shalev. A look inside the San Andreas fault at Parkfield through vertical seismic profiling. *Science*, 302:1746–1748, 2003.

A. Curtis, P. Gerstoft, H. Sato, R. Snieder and K. Wapenaar. Seismic interferometry - turning noise into signal. *The Leading Edge*, 25:1082–1092, 2006.

J.A. Hole, R.D. Catchings, K.C. St. Clair, M.J. Rymer, D. A. Okaya, and B. J. Carney. Steep-Dip Seismic Imaging of the Shallow San Andreas Fault Near Parkfield *Science*, 294:1513–1515, 2001.

R. A. Kerr. Parkfield keeps secrets after long awaited quake. *Science*, 306:206–207, 2006.

E. Larose, L. Margerin, A. Derode, B. van Tiggelen, M Campillo, N. Shapiro, A. Paul, L. Stehly and M. Tanter. Correlation of random wavefields: An interdisciplinary review. *Geophysics*, 71:SI11-SI21, 2006.

O.I. Lobkis and R.L. Weaver. On the emergence of the Green's function in the correlations of a diffuse field. *J. Acoust. Soc. Am.*, 110:3011-3017, 2001.

R.M. Nadeau, A. Michelini, R.A. Uhrhammer, D. Dolenc and T.V. McEvilly. Detailed kinematics, structure and recurrence of micro-seismicity in the SAFOD target region. *Geophys. Res. Let.*, 31:L12S08, 2004.

V. Oye, J.A. Chavarria and P. Malin. Determining SAFOD area microearthquake locations solely with the Pilot Hole seismic array data. *Geophys. Res. Let.*, 31:L12S10, 2004.

F. Poletto and F. Miranda. Seismic while drilling, fundamentals of drill-bit seismic for exploration. *Handbook of Geophysical Exploration*, Vol 35, 2004.

J.W. Rector III and B.P. Marion. The use of drill-bit energy as a downhole seismic source. *Geophysics*, 56:628-634, 1991.

S. Roecker, C. Thurber and D. McPhee. Joint inversion of gravity and arrival time data from Parkfield: New constraints on structure and hypocenter locations near the SAFOD drill site. *Geophys. Res. Let.*, 31:L12S04, 2004.

E. Roeloffs and J. Langbein. The earthquake prediction experiment at Parkfield, California. *Reviews of Geophysics*, 32:315–336, 1994.

M.J. Rymer, R.D. Catchings and M.R. Goldman. Structure of the San Andreas fault as revealed by surface geologic mapping and high-resolution seismic profiling near Parkfield, California. *Geophys. Res. Abstr.*, 5, 13:513, 2003.

R. Snieder, K. Wapenaar and K. Larner. Spurious multiples in seismic interferometry of primaries. *Geophysics*, 71:SI111-SI124, 2006.

J.G. Solum and B.A. van der Pluijm. Phyllosilicate mineral assemblages of the SAFOD Pilot Hole and comparison with an exhumed segment of the San Andreas Fault System. *Geophys. Res. Let.*, 31:L15S19, 2004.

J.G. Solum, S.H. Hickman, D.A. Lockner, D.E. Moore, B.A. van der Pluijm, A.M. Schleicher and J.P. Evans. Mineralogical characterization of protolith and fault rocks from the SAFOD Main Hole. *Geophys. Res. Let.*, 33:L21314, 2006.

M. Talebian, E.J. Fielding, G.J. Funning, M. Ghorashi, J. Jackson, H. Nazari, B. Parsons, K. Priestley, P.A. Rosen, R. Walker, and T.J. Wright. The 2003 Bam (Iran) earthquake: Rupture of a blind strike-slip fault. *Geophys. Res. Let.*, 31:L11611, 2004.

S.T. Taylor, P. Malin, E. Shalev, J.B.U. Haldorsen, R. Coates, and C. Stolte. Drill bit seismic imaging of the San Andreas Fault System at SAFOD. *Soc. of Expl. Geophys. Exp. Abstr.*, 24:2657–2660, 2005.

C. Thurber, S. Roecker, H. Zhang, S. Baher and W. Ellsworth. Fine-scale structure of the San Andreas fault zone and location of the SAFOD target earthquakes. *Geophys. Res. Let.*, 31:L12S02, 2004.

I. Vasconcelos and R. Snieder. Interferometry by deconvolution, Part I: theory and numerical examples. *in preparation*, 2007.

M. Unsworth, P. Bedrosian, M. Eisel, G. Ebert and W. Siripunvaraporn. Along strike variations in the electrical structure of the San Andreas Fault at Parkfield, CA. *Geophys. Res. Let.*, 27:3021–3024, 2000.

M. Unsworth and P. Bedrosian. Electrical resistivity at the SAFOD site from magnetotelluric exploration. *Geophys. Res. Let.*, 31:L12S05, 2004.

R.S. Yeats and G.J. Hutfile. The Oak Ridge fault system and the 1994 Northridge earthquake. *Nature*, 373:418–420, 1995.

The Leading Edge, v25, September 2006

Seismic anisotropy of a building

David Thompson[1] & Roel Snieder[2]
[1] *University of Leeds, United Kingdom*
[2] *Center for Wave Phenomena and Department of Geophysics, Colorado School of Mines, Golden, CO 80401*

ABSTRACT
The Department of Geophysics at the Colorado School of Mines has an international exchange program for undergraduate students with the University of Leeds, Delft University of Technology, Imperial College, and the University of Leoben. Exchange student David Thompson from Leeds carried out a brief research project with Roel Snieder to investigate the anisotropic mechanical properties of a building using seismic interferometry. The results of this project, which are largely of a didactic nature, were published in *The Leading Edge, September 2006.*

Key words: interferometry, anisotropy, structural engineering

Introduction

The Robert A. Millikan Library is a reinforced concrete building located on the campus of the California Institute for Technology in Pasadena, CA. The building has been frequently studied by earthquake engineers since it was first instrumented in the late 1960. The recording system inside the library has been periodically improved ever since, until the current setup was achieved in 2000. At present, 19-bit real-time seismometers record continuous measurements at 200 Hz on each of the 10 floors and also in the basement. These seismometers measure the response of the library in the North-South direction (on both the east and west side of the building) and in the East-West direction.

Seismic Anisotropy

The phenomenon of shear-wave splitting occurs when a linearly polarized shear- wave passes through a seismically anisotropic medium. When this occurs, the wave is split into slow and fast shear-waves which are polarized orthogonal to each other. Splitting is typically observed in global seismology, occurring in the upper mantle due to the crystal lattice structure of olivine. It is not confined to this area though, and any medium of seismic anisotropy has the potential to cause shear-wave splitting. By looking at the cross section of the Library and noticing its structural differences in the two orientations, it was speculated that seismic anisotropy may be present in our investigation.

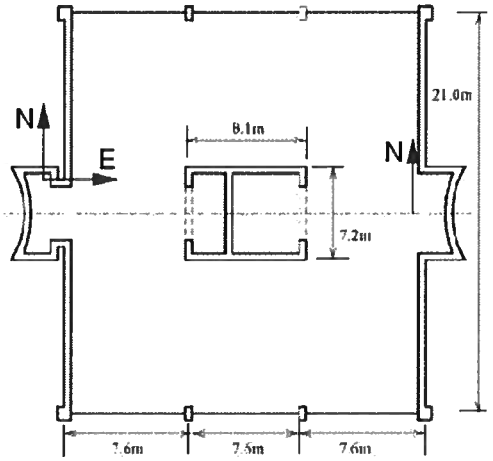

Figure 1. Cross section of the Millikan Library with location of seismometers.

Applying Seismic Interferometry

Previous studies have used actual earthquakes, and also a synchronised shaker permanently located on the roof, to study the response of the building due to excitation.

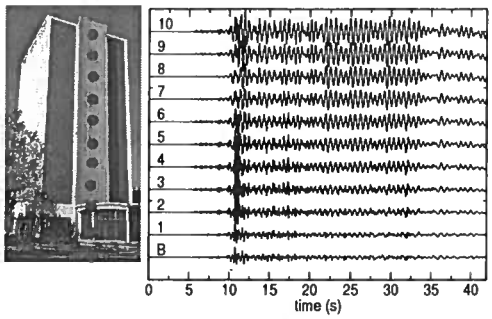

Figure 2. Response of the building due to excition.

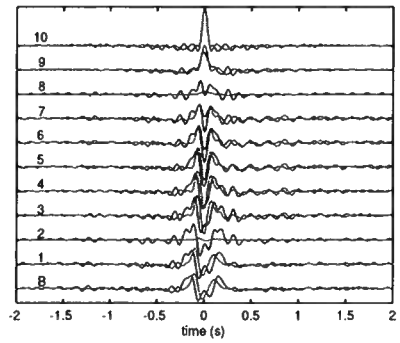

Figure 3. Deconvolved waveforms for the North-South direction on the East side of the building (Red) and East-West direction (blue).

In our studies, we use seismic interferometry to analyze the data in the 3 orientations due to the Yorba Linda earthquake of 3rd September, 2002. A typical approach using this method would be to analyze the correlations of the recorded traces, but our approach is to look at the deconvolution of recorded traces at different floors.

It is possible to deconvolve all of the floors with any single floor, each giving a different type of waveform. We concentrate on the deconvolutions with respect to the trace at the top floor (floor 10). This simplifies the problem by making the building response independent of its ground coupling at the base. By deconvolving all floors with respect to the trace at the 10th floor, surprisingly simple waveforms are produced. These deconvolved waveforms are acausal (non-zero for $t < 0$) and comprise of a single up-going and down-going wave. By picking the peaks of the waveforms and plotting them against time, an estimate of the shear wave velocity inside the building can be obtained.

The hypothesis that shear-wave splitting would be present was proved correct by the contrast between shear wave velocities in the East-West direction and in the North-South direction. Below are the results for each of the orientations:

- North-South direction, East side of building = 385 ms-1
- East-West direction = 286 ms-1.

This corresponds to a splitting coefficient of 15 percent.

Seismic anisotropy is clearly a characteristic of the Millikan Library. The waves produced by excitation appear to travel faster in the North-South direction as opposed to the East-West direction. The symmetry axes of the building align with the orientations of the accelerometers (East-West and North-South respectively), hence there is no need to perform an Alford rotation to decompose the split shear waves into their fast and slow directions.

Studying Abroad

Deciding to study abroad for a year at the Colorado School of Mines has opened up several new doors for my geophysical career. The school provides a number of different opportunities, and greatly encourages, undergraduate research. The teaching style and environment promoted by the Department of Geophysics allows undergraduates to pursue research topics in several different areas, and in many cases, studies which they have chosen and designed themselves.

The study which we have carried out gave me an excellent insight into how post-graduate research is done. The experience which I have gained during my time in the United States will serve me well when making decisions regarding my future after graduation.

For students of geophysics the opportunity to study abroad, like the one which the University of Leeds has given me, would be highly recommended. The field is truly an international community, and an experience like this provides an excellent head-start to becoming part of it.

Suggested Reading

Snieder, R. and E. Şafak, Extracting the building response using seismic interferometry: Theory and application to the Millikan library in Pasadena, California, *Bulletin of the Seismological Society of America*, **96**, 586-598.